REPORT SRL-08-F-1990

DEVELOPMENT OF AN ALL SOLID STATE 6 kHz PULSE GENERATOR FOR DRIVING FREE ELECTRON LASER AMPLIFIERS

Prepared by

Dr. Daniel Birx

SCIENCE RESEARCH LABORATORY, INC.
15 Ward Street
Somerville, MA 02143
(617) 547-1122

16 July 1990

FINAL TECHNICAL REPORT

Period for July 15, 188 to July 14, 1990

Contract Number N00014-88-C-0398

APPROVED FOR PUBLIC RELEASE; DISTRIBUTION UNLIMITED

Prepared for

OFFICE OF NAVAL RESEARCH
800 North Quincy Street
Arlington, VA 22217-5000

"The views and conclusions contained in this document are those of the authors and should not be interpreted as necessarily representing the official policies, either expressed or implied, of the Strategic Defense Initiative Organization or U.S. Government."

Unclassified
SECURITY CLASSIFICATION OF THIS PAGE

REPORT DOCUMENTATION PAGE

Form Approved OMB No. 0704-0188

1a. REPORT SECURITY CLASSIFICATION: Unclassified	1b. RESTRICTIVE MARKINGS: N/A
2a. SECURITY CLASSIFICATION AUTHORITY	3. DISTRIBUTION/AVAILABILITY OF REPORT: approved for public release; distribution unlimited
2b. DECLASSIFICATION/DOWNGRADING SCHEDULE	
4. PERFORMING ORGANIZATION REPORT NUMBER(S): SRL-08-F-1990	5. MONITORING ORGANIZATION REPORT NUMBER(S)
6a. NAME OF PERFORMING ORGANIZATION: Science Research Laboratory; 6b. OFFICE SYMBOL (If applicable)	7a. NAME OF MONITORING ORGANIZATION: Office of Naval Research, Department of Navy
6c. ADDRESS (City, State, and ZIP Code): 15 Ward Street, Somerville, MA 02143	7b. ADDRESS (City, State, and ZIP Code): 800 N. Quincy Street, Arlington, VA 22217
8a. NAME OF FUNDING/SPONSORING ORGANIZATION: Strategic Defense Initiative Org.; 8b. OFFICE SYMBOL (If applicable)	9. PROCUREMENT INSTRUMENT IDENTIFICATION NUMBER: N00014-88-C-0398
8c. ADDRESS (City, State, and ZIP Code): Pentagon, Washington, DC	10. SOURCE OF FUNDING NUMBERS: PROGRAM ELEMENT NO. / PROJECT NO. / TASK NO / WORK UNIT ACCESSION NO.

11. TITLE (Include Security Classification)
Development of an All Solid State 6 kHz Pulse Generator for Driving Free Electron Laser Amplifiers

12. PERSONAL AUTHOR(S)
Dr. Daniel Birx

13a. TYPE OF REPORT	13b. TIME COVERED	14. DATE OF REPORT (Year, Month, Day)	15. PAGE COUNT
Final	FROM 7/15/88 TO 7/14/90	16 July 1990	191

16. SUPPLEMENTARY NOTATION

17. COSATI CODES			18. SUBJECT TERMS (Continue on reverse if necessary and identify by block number)
FIELD	GROUP	SUB-GROUP	

19. ABSTRACT (Continue on reverse if necessary and identify by block number)

Five new, all-solid-state pulse generators have been designed to meet ~~CBFEL~~ the requirements for an efficient, reliable pulsed power source to drive free electron laser amplifiers. Four of these have been constructed and tested. These SCR-commutated, nonlinear magnetic pulse compressors will be fully-compatible with present high power SDIO induction linac driven free electron ~~laser~~ designs developed by LLNL/TRW.

By employing SCRs rather than thyratron commutators, these pulsers should provide a significant increase in reliability over the current generation pulsed power drivers proposed as drivers for Free Electron Lasers. SCR-commutated nonlinear magnetic pulse compressors, SNOMAD-I, II, IV and V have been successfully tested at SRL. The goals of this research effort have been realized. A line of cost effective, reliable, efficient, all-solid-state induction linac drivers has now been developed. We will discuss the details of their design in the following report. (RH)

20. DISTRIBUTION/AVAILABILITY OF ABSTRACT: ☐ UNCLASSIFIED/UNLIMITED ☒ SAME AS RPT. ☐ DTIC USERS	21. ABSTRACT SECURITY CLASSIFICATION: Unclassified
22a. NAME OF RESPONSIBLE INDIVIDUAL	22b. TELEPHONE (Include Area Code) / 22c. OFFICE SYMBOL

DD Form 1473, JUN 86 — Previous editions are obsolete. — SECURITY CLASSIFICATION OF THIS PAGE

Unclassified

TABLE OF CONTENTS

LIST OF ILLUSTRATIONS

LIST OF ILLUSTRATIONS CONTINUED

LIST OF ILLUSTRATIONS CONTINUED

LIST OF TABLES

SECTION 1

1.0 INTRODUCTION

In previous induction linac designs, production of the high power drive pulsers could only be accomplished with gas discharge switches. These devices were unreliable and incapable of operating at high duty factors or repetition rates. Nonlinear magnetic pulse compressors have greatly alleviated this problem. However, thyratrons are still used to supply the input commutation for these nonlinear magnetic pulse compressors and represent a weak link in establishing the required reliability and maintainability of induction linacs at high repetition rates. The use of nonlinear magnetic pulse compressor technology has greatly eased the dI/dt problems for the thyratrons, but the high average current still leads to a tube life which may be unacceptable with respect to reliability and maintenance and which drive the projected operating cost of the GBFEL accelerator.

SCR-commutated drivers promise to remove thyratrons entirely from the system but current research has shown that this path requires a complete redesign of the pulse compression circuit. Nonlinear magnetic pulser compressors are themselves resonant circuits. The basic principle underlying nonlinear magnetic driver operation involves using a saturable core which is an inductor in a resonant circuit. The circuit is designed to allow the core of the next stage to saturate before a significant fraction of the energy stored in the capacitors of the previous stage is transferred. This nonlinear saturation phenomenon shifts the resonant frequency of this resonant circuit by the square root of the permeability shift as the core saturates. These stages are typically cascaded (Fig. 1) and energy is coupled faster and faster from one stage to the next. These circuits are efficient at transferring power in both directions since they act not only to upshift the frequency in the forward direction thereby providing temporal compression, but also downshift the frequency of a voltage pulse as it cascades back up the chain in the reverse direction. The energy which reflects from the mismatched laser load can propagate back up the chain to the SCR commutator. If this reverse voltage pulse arrives with the SCR partially recovered, then localized junction recommutation can occur resulting in punch through and

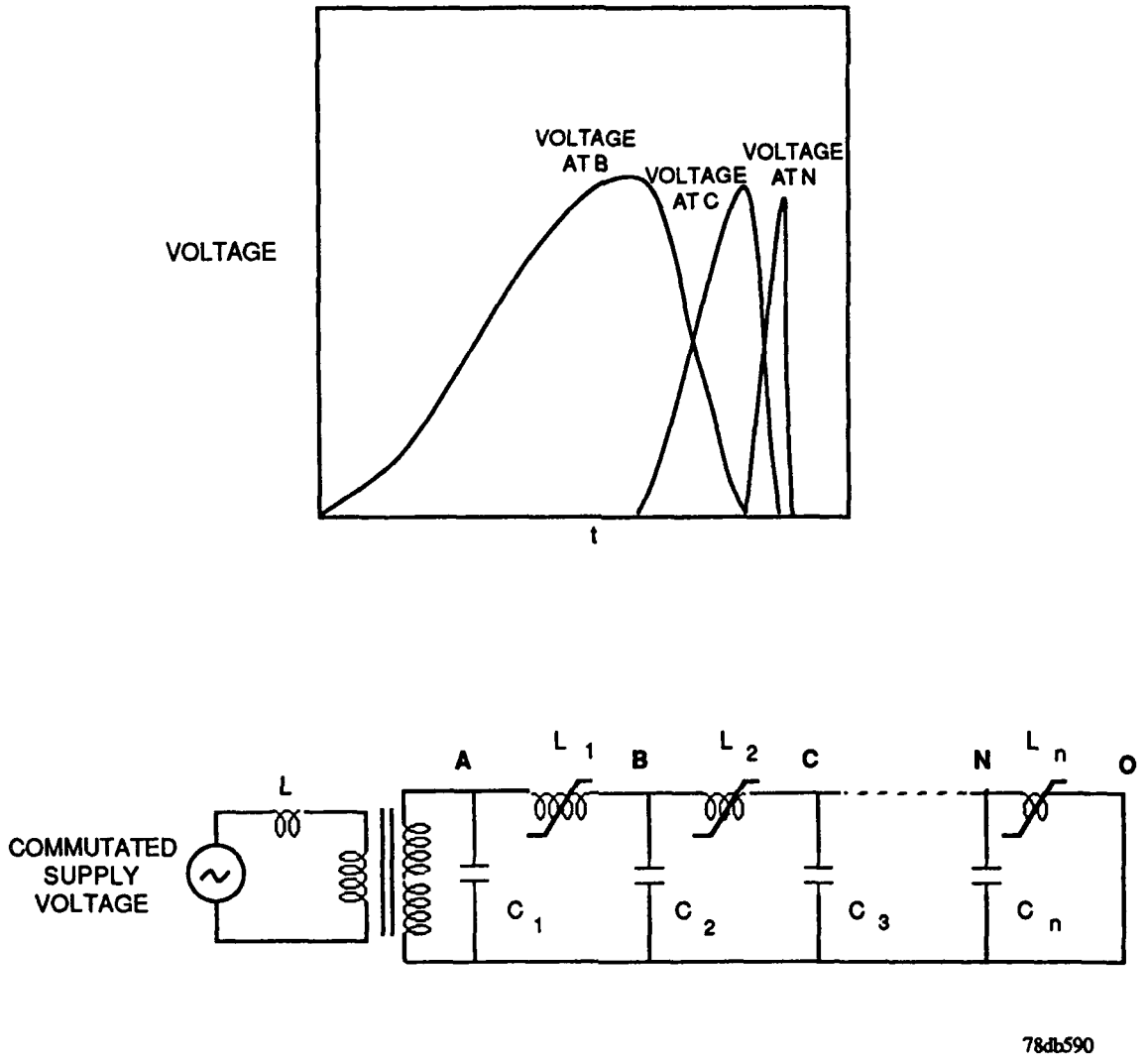

Figure 1.1: Typical magnetic switch operation

device destruction. Circuit designs must be developed which not only avoid this phenomena but store this reflected energy and add it to the energy making up the next pulse. This phenomenon among others has complicated driver designs utilizing SCR commutators but researchers here at Science Research Laboratory (SRL) and at Lawrence Livermore National Laboratory (LLNL) have learned how to handle these problems.

SRL is presently engaged in designing and fabricating advanced SCR-commutated, nonlinear magnetic pulse compressors to be used as induction linac drivers for the SDIO Ground Based Free Electron Laser Program. These drivers employ many new concepts in nonlinear magnetic pulse compressor design and are carefully engineered to be resistant to damage under fault mode conditions which may occur while driving a free electron laser load. An example of such a driver is the Solid state NOnlinear Magnetic Accelerator Driver (SNOMAD-I). This 15 joule per pulse nonlinear magnetic driver (Fig. 2a) was designed for initial operation at 4 kHz, compressing the 30 μsec output of an SCR commutator into a 15 nsec duration pulse (Fig. 2b). A new concept in saturable inductor design makes it possible to achieve this compression efficiently.

The reliability and maintenance associated with thyratron-commutated drivers can be a major cost factor in the operation of the proposed WSMR/GBFEL. This research is directed toward the development of a new, all-solid-state nonlinear magnetic pulse compressor which eliminates the thyratron commutator circuit and replaces it with an SCR commutator. The objective of this new design is to develop a driver for free electron laser amplifiers which can operate without maintenance for 10^{11} shots. This lifetime corresponds to an MTBF of approximately 5000 hrs for the driver and would reduce significantly accelerator operating costs.

1.1 Pulsed Free Electron Laser Driver

The use of solid state devices in place of thyratrons and spark gaps is the key to developing a reliable pulsed power system. The nonlinear magnetic circuits which provide the necessary temporal compression are inherently reliable as they contain no active elements. Both high pressure (spark gaps) and low pressure (thyratrons) gas discharge devices have a finite lifetime. Electrode erosion with subsequent gas contamination and insulator degradation will eventually

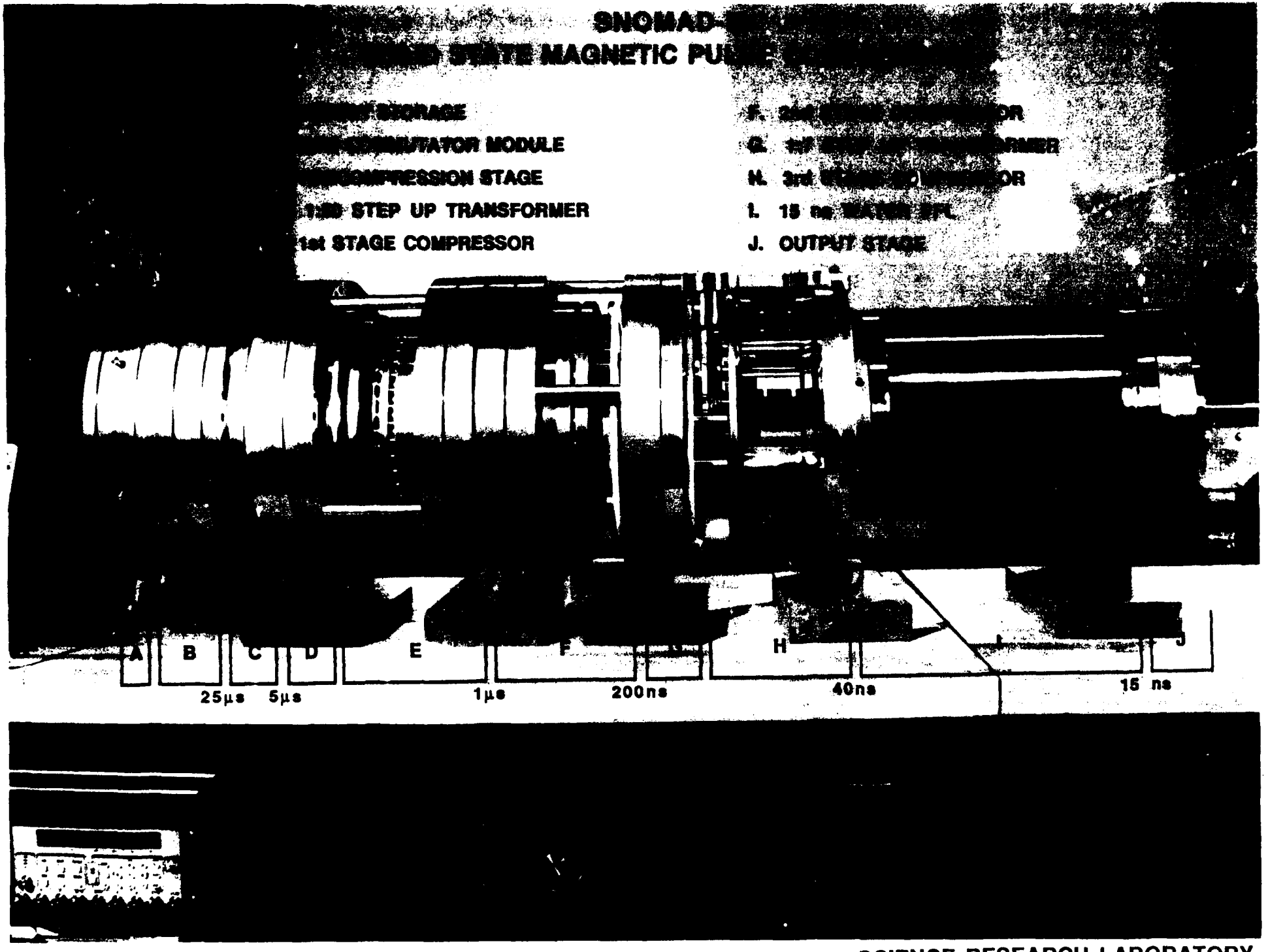

Figure 1.2a

SCIENCE RESEARCH LABORATORY

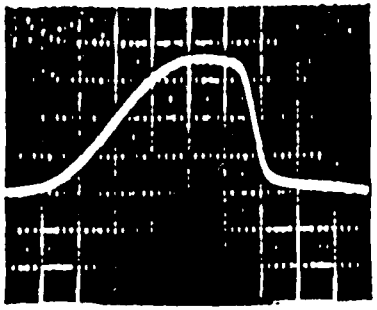

SNOMAD-I INPUT
5 µsec/D 100 V/D

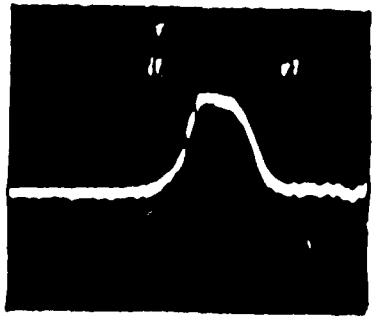

SNOMAD-I OUTPUT
10 Nsec/D 20 kV/D

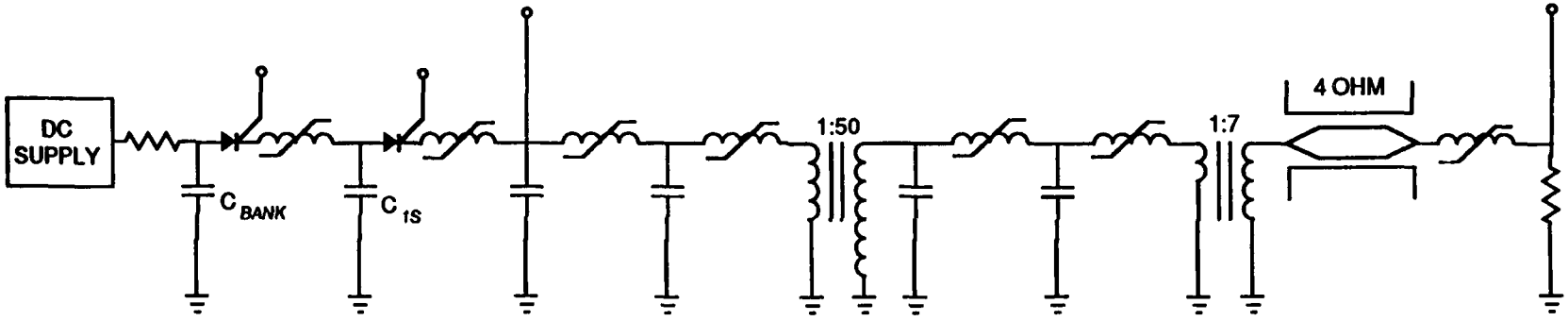

Figure 1.2b: SNOMAD-I test results

degrade the performance of these devices. SCRs, like nonlinear magnetic pulse compressors, do not rely on plasma formation or material displacement to function. An SCR operating within its ratings will last essentially forever. Solid state devices were originally developed by Bell Laboratories for space based applications where maintenance was not possible. Solid state switches, however, will only operate outside their ratings once. They are not very forgiving in this respect, for exceeding the maximum voltage, rms current or dI/dt ratings even instantaneously will result in irreversible damage.

Engineers designing long life pulsed power systems are rapidly moving away from spark gap- and thyratron-based technology and are beginning to employ SCR-commutated nonlinear magnetic pulse compressors. While SCRs functioning alone are not capable of supplying the peak power for these missions, the average power handling capabilities of SCRs far exceed the capabilities of either spark gaps or thyratrons for equivalent device sizes and weights. Combining the voltage hold-off with the average current handling capability has yielded commercially-available SCR devices functioning at a high duty factor that are capable of average power densities exceeding 3 MW/kg and 20 MW/liter.

Through the technology of nonlinear magnetic compressors it is now possible to use the impressive average power handling capabilities of SCRs and still achieve the peak power performance required for free electron laser applications. Nonlinear Magnetic Pulse Compressors sometimes called "Magnetic Switches" take advantage of the large change in permeability of a ferro (ferri) magnetic material as it saturates. It is possible to achieve large factors ($>10^3$) of temporal pulse compression and thereby obtain the required power gain by employing saturable materials as inductor cores. Magnetic switches are beginning to appear in a large number of long life, high repetition rate pulsed power systems. Here we are developing these pulse compression devices to drive induction linear accelerators. They are also employed as drivers of copper vapor lasers for the Atomic Vapor Laser Isotope Separation (AVLIS) program. Here large numbers of drivers are required to operate at 5000 pps continuously for time scales measured in years. SRL is assisting in developing advanced, all solid state drivers for both of these programs.

In these efforts, Science Research Laboratory is exploiting recent progress in Silicon Controlled Rectifier (SCR) and saturable core magnetic switch technology to develop all solid state drivers for free electron lasers which have substantially improved performance and meet all of the performance specifications for GBFEL applications. SCRs can be used in conjunction with metglass saturable core magnetic switches to develop all solid state modules. In addition to the substantial SCR size advantage over thyratrons, SCRs do not require filament transformers, bias supplies and considerable other ancillary equipment. The SCR size advantage is predominantly derived from the increased density of conduction electrons in silicon as opposed to the low pressure gas in the thyratron. In addition these all-solid-state SCR-switched drivers can be engineered to operate for greater than 10^{11} shots at up to 95% efficiency to minimize waste heat rejection.

1.2 SNOMAD-I Design Philosophy

The deployment of SCRs as commutators in magnetic pulse compressor circuits must be engineered in such a manner that the device rating can never be exceeded in any conceivable fault mode. Early efforts at replacing thyratrons with SCRs taught us some valuable lessons. Thyratrons work well at 20 kV and SCRs at 1 kV, so the obvious approach was simply to series sufficient SCRs ($\sim$ 20) to operate at 20 kV (Fig. 3a). The authors expended considerable effort trying to accomplish exactly this and while we hesitate to say that it cannot be done reliably, our efforts were not successful. Fault modes would result in reapplication of voltage on the series SCR stack after the main commutation cycles but before all the devices had recovered. The full voltage then appeared across only the recovered devices, exceeding their voltage ratings and causing junction breakdown. Breakover diodes tied back to the gates (Fig. 3b) afforded some protection but could not always turn the device on in time to protect it. Snubbers were placed across the devices (Fig. 3c) to slow the reapplication of voltage but SCRs require several microseconds to fully turn on and this required the dissipation of so much energy during normal operation that the overall efficiency of the system was seriously degraded.

Compact step-up transformers which can be interleaved with the pulse compression stages

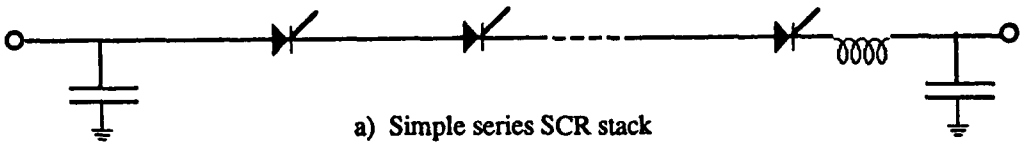

a) Simple series SCR stack

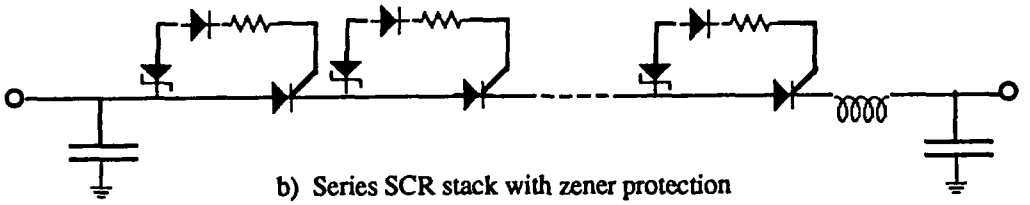

b) Series SCR stack with zener protection

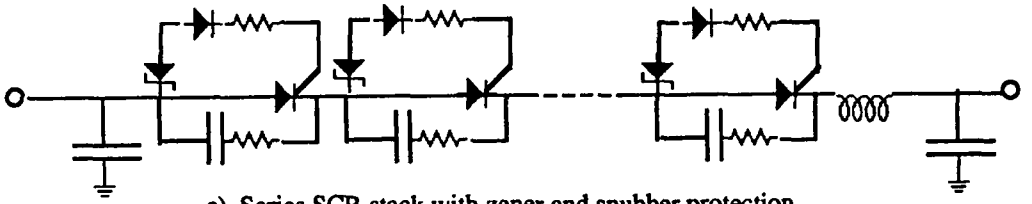

c) Series SCR stack with zener and snubber protection

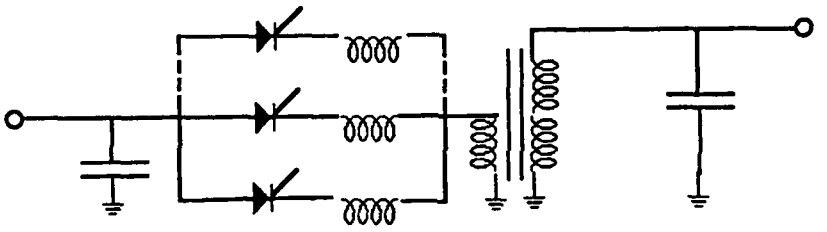

d) Simple parallel SCR commutator

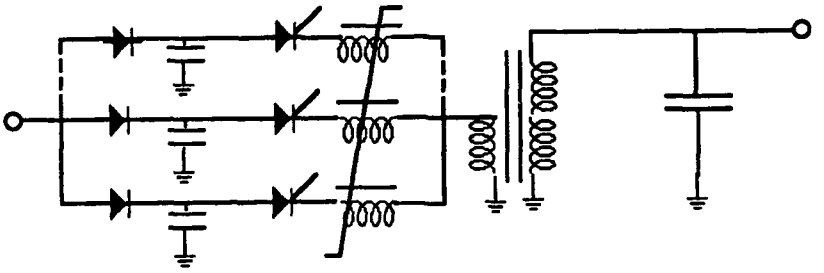

e) Branched SCR commutator

Figure 1.3: SCR commutator circuits

78db590

have been developed at SRL to remove the necessity of operating SCRs in a high voltage stack. Inserting a 1:20 step-up transformer after the SCRs allows them to operate at 1 kV and still deliver 20 kV to the magnetic pulse compressor. This however increases the rms current and dI/dt requirements of the SCR by a factor of 20 and will usually dictate that several devices be used in parallel so as not to exceed the single device rating. Simply tying the SCRs together in parallel (Fig. 3d) will not assure adequate current sharing. The solution to this problem is illustrated in Fig. 3e. Branching the first stage of compression and segmenting the intermediate storage will allow each SCR to be isolated into its own arm of the circuit unable to access the energy of the entire pulse. If only a fraction of the devices fire, they will not find themselves in an overcurrent situation but will simply deliver a reduced energy pulse to the load. No damage will be done and subsequent pulses will be unaffected. Neither the voltage or peak current ratings of the device can ever be exceeded.

The design of efficient high gain pulse compression stages relies on the careful control of the magnetic fields surrounding the core volume. The losses in a compression stage are linearly proportional to the volume of core material used and it can be shown that the core volume requirement for this saturable inductor is given by:

$$\text{volume} = \text{gain}^2 \cdot \text{Pulse Energy} \cdot \left(\frac{\mu_o \cdot \pi^2}{4 \cdot (\Delta B_s \cdot \text{pf})^2} \right) \tag{1.1}$$

where ΔB_s is the available flux swing of the material (with appropriate biasing given by $+B_s - (-B_s) = 2B_s$), gain is defined as the temporal compression factor (τ charge/τ discharge), and pf is the packing factor. The packing factor is defined as

$$\frac{\int_{V_f} H^2 dv}{\int_{all\ space} H^2 dv} \tag{1.2}$$

where V_f is the actual volume occupied by the ferri- (ferro) magnetic core material excluding all interlaminar insulation and voids. Optimization of this packing factor is crucial in magnetic switch design and is accomplished by enclosing the core in a tightly fitting conducting housing. The multiple turns are formed as coaxial transmission lines which pass through this housing.

Circulating currents set up in this housing exclude the magnetic flux and contain it in the desired volumes.

With the saturable material completely enclosed in conducting coaxial housings, the voltage per turn associated with the dB/dt of the core appears across a single narrow gap on the outside diameter of each housing. Connecting the coaxial transmission lines in the inner and outer housings with radial transmission lines across the top and bottom of the core completes the turns. The impedances of these transmission lines are adjusted so that

$$Z_{LINE} \approx \sqrt{\frac{2 \cdot L_{sat}}{C}} \tag{1.3}$$

while simultaneously every effort is made to minimize $L_{sat} \cdot C$ which is proportional to the square of the pulse length. Here L_{sat} and C refer to the saturated inductance of the reactor and the value of the storage capacitance respectively.

In addition to optimizing the core structure, increased SCR protection and efficiency is provided by grading the storage capacitors throughout the chain so that they gradually increase in capacitance in the direction of the output. Grading the capacitors in this manner also increases the efficiency. Core losses introduce a resistive component to the impedance which couples storage capacitors in each stage. Unless each successive capacitor is larger in value than its predecessor, this resistive term will cause positive charge to be left on the preceding capacitor after the discharge cycle is completed.

SECTION 2 - SNOMAD-II ACCELERATOR MODULE

2.0 SNOMAD-II

Science Research Laboratory has designed, fabricated and tested a 1 MeV prototype induction accelerator as part of an ongoing effort to develop compact, high repetition rate accelerators for a variety of applications. This accelerator is powered by the SNOMAD-II pulsed power driver and is the first induction linac to be driven by an all solid state magnetic pulse compression driver. Initial operation of the accelerator commenced in August 1989. These tests included 1 kHz operation of the full accelerator with an electron beam for a durations of several seconds.

A schematic diagram and photograph of the prototype accelerator are shown in Fig. 2.1 and Fig. 2.2 respectively. The accelerator comprises eight induction cells, the SNOMAD-II driver and a thermionic dispenser cathode capable of delivering 600 amps. Each of the accelerator cells is driven at 125 kV for a duration of 50 nsec. The injector is formed by threading a conducting cathode stalk through the first four induction cells, applying up to 600 kV between the cathode and annular anode ring. The design parameters of the prototype accelerator are summarized in Table 2.1.

A schematic diagram and cross-sectional drawing of the SNOMAD-II driver are shown in Fig. 2.3. The electrical and mechanical design share many features with the SNOMAD-IV driver which was constructed as part of this program. The two designs differ in the energy delivered per pulse. SNOMAD-II was designed to drive up to 4 MeV of accelerator cells and therefore it is capable of delivering up to 150 joules per pulse. The SNOMAD-IV compression module is a significantly more compact driver which has been optimized for driving 1MeV of accelerator cells and delivering 50 joules per pulse.

SNOMAD-II utilizes readily available SCRs. Thyratron switches have been completely eliminated permitting significantly higher repetition rate operation and a reduction in cost and size for high average power applications. The SCR commutator arms deliver a 150 joule energy pulse into the first stage energy storage capacitors, charging C_1 to 1 kV in 10 μsec. C_1 is coupled via a low inductance bussing network to a metglas saturable inductor. L_1. L_1 is designed so

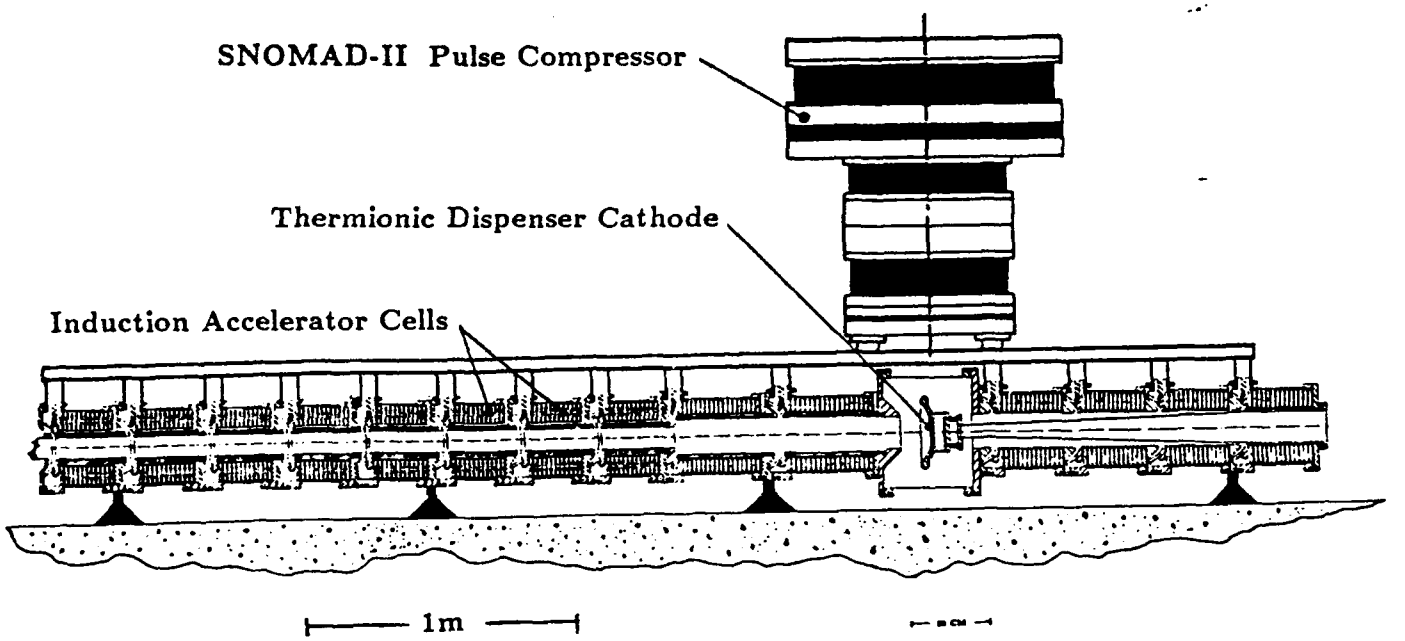

Figure 2.1: Schematic of prototype SRL accelerator with the SNOMAD-II solid state driver.

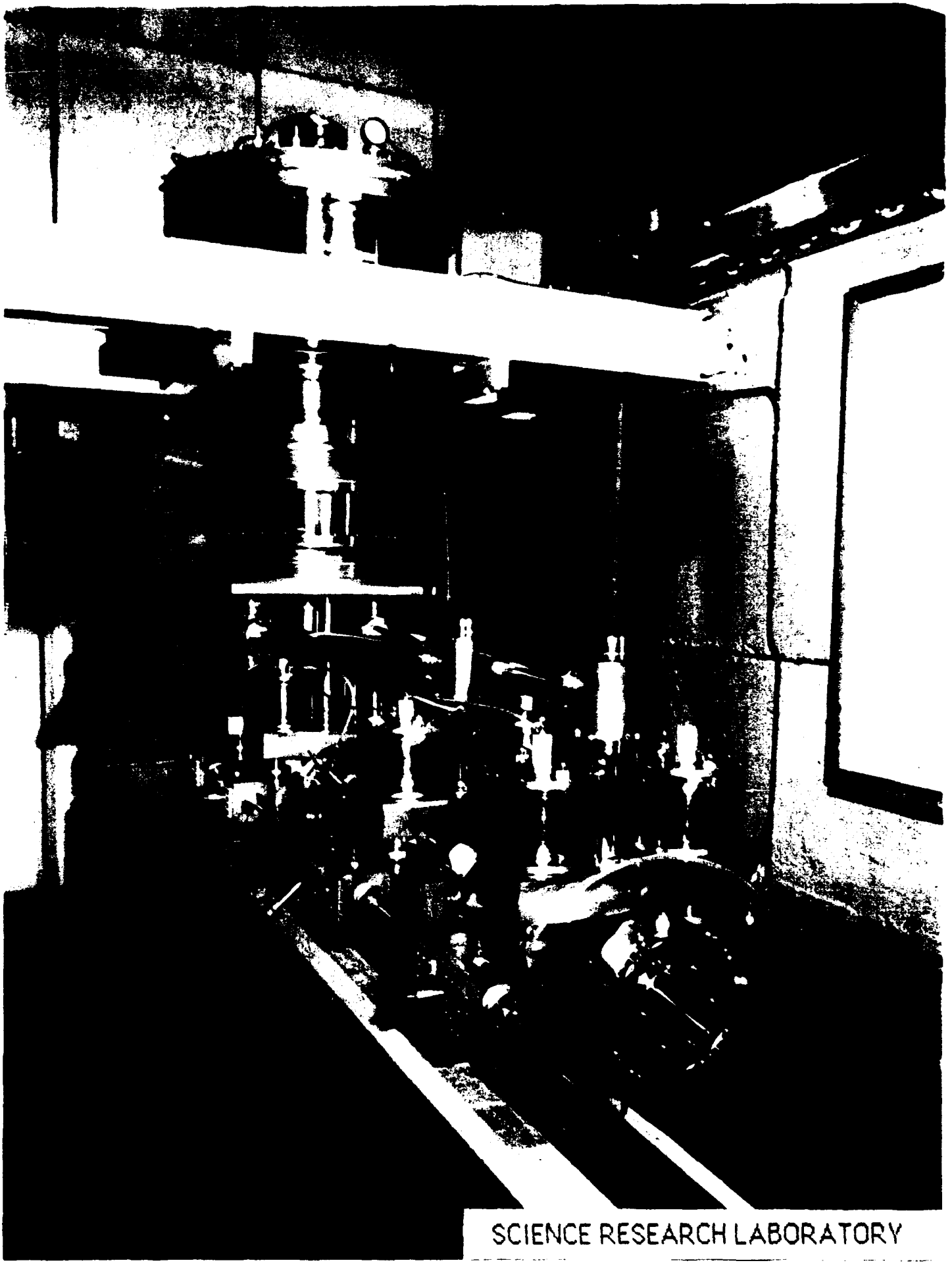

Figure 2.2

Table 2.1: Design Parameters of the SRL Prototype Accelerator

Accelerator Parameters

Beam Energy	1.0 MeV
Beam Current	600 amp
Pulse Length	50 nsec
Pulse Repetition Rate	5 kHz
Single Pulse Energy	30 joules
Voltage per Cell	125 kV
Accelerating Gradient	0.5 MeV/meter
Pipe Radius	6.35 cm
Gap Field Stress	150 kV/cm
Cathode	3.5″ ϕ Dispenser

SNOMAD-II Driver

Single Pulse Energy	150 joules
Commutator Arms	All solid state, SCR switched
Compression stages	Four

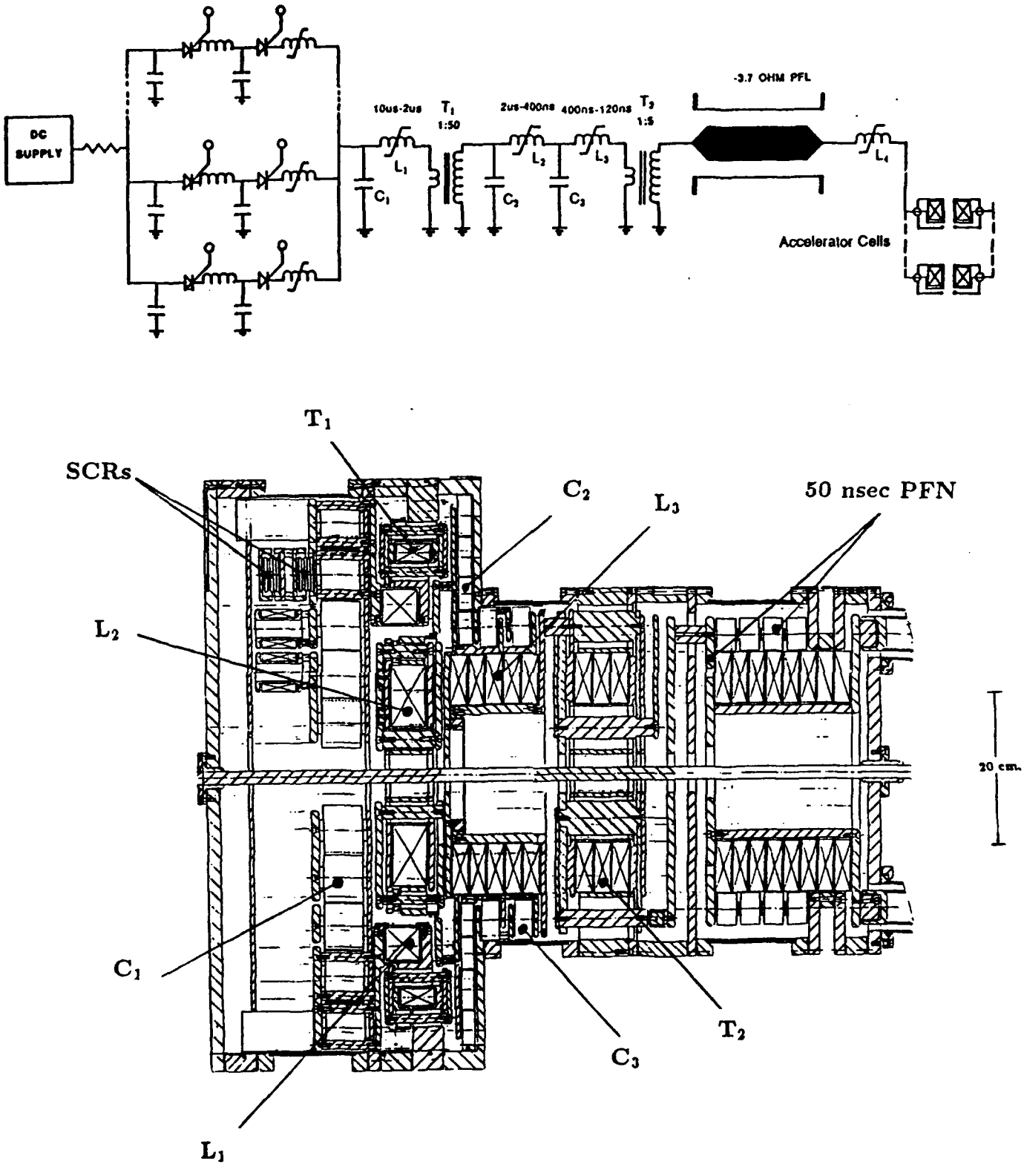

Figure 2.3: Electrical schematic and cross-sectional view of SNOMAD-II SCR commutated pulse compression driver.

that saturation occurs following the termination of the 10 μsec charging of C_1. Once saturated, the energy stored in C_1 is discharged into the primary of a 1:50 step-up pulse transformer, T_1, in 2 μsec thereby achieving a temporal compression of 5. This results in a corresponding increase in the peak power level. The secondary of T_1 charges a bank of strontium titanate capacitors, C_2, to 50,000 volts. T_1 and the second stage compression inductor, L_2, both utilize metglass cores. L_2 has a charging time of 2 μsec and a discharge time of 400 ns.

The third stage compression inductor, L_3, uses ZnNi ferrite as a core material. This stage feeds the primary of a 1:5 step-up transformer which charges the 50 ns pulse forming network (PFN) to 240 kV in 120 ns. The output inductor stage, L_4, is a ZnNi ferrite saturable inductor which delivers the 120 kV pulse to the output transmission line.

A more detailed analyses of the SNOMAD-II operating specifications appears in Table 2.2. Photographs of the various compression stages of SNOMAD-II appear in Figs. 2.4 thru 2.12. In Fig. 2.4 we show an outside view of the fully assembled SNOMAD-II driver. The SCR deck with the SCRs removed showing the bus plates to which the intermediate storage and first stage polypropylene capacitors are mounted in pictured in Fig. 2.5. The 1:50 step-up transformer appears in Fig. 2.6 while the Metglas core 2^{nd} stage compression reactor is displayed in Fig. 2.7. The output of the 2^{nd} stage is attached to the 3^{rd} stage input bus plate shown in Fig. 2.8. In Fig. 2.9 the 3^{rd} stage compression core can be seen mounted above the 1:5 step-up transformer. The windings of this transformer are coaxial transmission lines connected by radial strip lines (Fig. 2.10) and the output charges the 3.7Ω strip line PFN pictured in Fig. 2.11. This entire output section forms a demountable subassembly (Fig. 2.12) for ease of assembly and shipping.

2.1 SNOMAD-II Accelerator Cell Design

The accelerator cells used in the prototype accelerator were designed for accelerating currents of 500 to 1000 A. The cells are ferrite filled and follow the design principles discussed in Appendix H. The ferrite has inner and outer radii of 6.35 cm and 10.15 cm respectively, a length of 28 cm and a shunt impedance of 300 Ω. They were designed to operate with a drive voltage of 125 kV per cell and a pulse length of 50 nsec. A cross-sectional drawing of an accelerator

Table 2.2: SNOMAD-II Performance Specifications

Input Power Requirements:	
Energy/pulse	150 joules
PRF	5 kHz
Power	750 KW
Voltage	600 volt
Current	1250 Amps
Intermediate Storage	
Capacitance	225 μfd
Voltage	1150 volts
Energy	150 joules
Stored charge	2.587×10^{-1} Coulombs
τ discharge	$\leq$ 10 μsec
I peak	40.64×10^{3} Amp
dI/dt	12.8×10^{3} A/μsec
I_T (RMS)	7,250 Amps
dI/dt per device	853 A/μsec (4×R400 West Code)
Commutation losses	$\sim$ 2.27 joules
1^{st} Stage	
Capacitance	225 μfd
Voltage	1145 volts
Energy	147.7 joules
Core Type	.6 Mil × 2605 CO
# Turns	1
Core geometry	1×17.5″ ID × 21.5″ OD × 2″ Wide
$\int V \cdot dt$	$\sim 5.7 \times 10^{-3}$ Vsecs
Lsat	2.06 nh + .5 nh (STRAY) = 2.56 nh
τ discharge	1690 nsecs
Losses	$\sim$ 2.50 joules (1.25 cores, 1.25 caps)
Core volume	4.0×10^{-3} m^3, 16.8kg
1:50 Transformer	
Core Type	2605S3A
# Turns (PRIM)	1
# Turns(sec)	50
Losses	$\leq$ 2.15 joules
Core geometry	1×25.0″ ID × 27.0 ″ OD × 2″ wide

Table 2.2 (Continued)

2nd Stage	
Capacitance	90 nfd
Voltage	56.4 kV
Energy	143 joules
Core type	2605SC METGLASS
Core Geom.	1×5.75″ ID × 12.75″ OD × 2″ w
$\int V \cdot dt$	4 Turns × 28.2 Vmsecs/Turn = 56.4 kV* (2.0μsecs/2)
LSAT	.127 μh + .03 μh stray $\simeq$ .157 μh
τdischarge	264 nsecs
Losses	$\sim$ 2.15 joules
Third Stage	
Capacitance	90 nfd
Voltage	55.9 kV
Energy	141 joules
Core type	CMD-5005 Ferrite
Core Geom.	5×8.0″ ID × 14.0″ OD × 1.0″ w
$\int V \cdot dt$	1 Turns × 11.2 × 10^{-3} Vmsecs/Turn
LSAT	14. nh + 2.5 nh (Stray) $\simeq$ 16.5 nh
τdischarge	$\sim$ 86 nsecs
Losses	$\sim$ 3.5 joules
1:5 Transformer	
Core Type	CMD-5005 Ferrite
# Turns (PRIM)	1
# Turns(sec)	5
Losses	$\lesssim$ 2.5 joules
Core geometry	3×8.0″ ID × 14.0 ″ OD × 1″ wide
Fourth Stage	
Capacitance	3.6 nfd
Voltage	274 kV
Energy	135 joules
Core type	CMD-5005 Ferrite
Core Geom.	8×8.0″ ID × 14.0″ OD × 1.0″ w
$\int V \cdot dt$	1 Turns × 17.9 × 10^{-3} Vsecs/Turn
LSAT	22.4 nh + 2.3 nh (Stray) $\simeq$ 24.7 nh
τdischarge	$\sim$ 50 nsecs (τ_{10-90} =10ns)
Losses	$\sim$ 8 joules

Figure 2.4

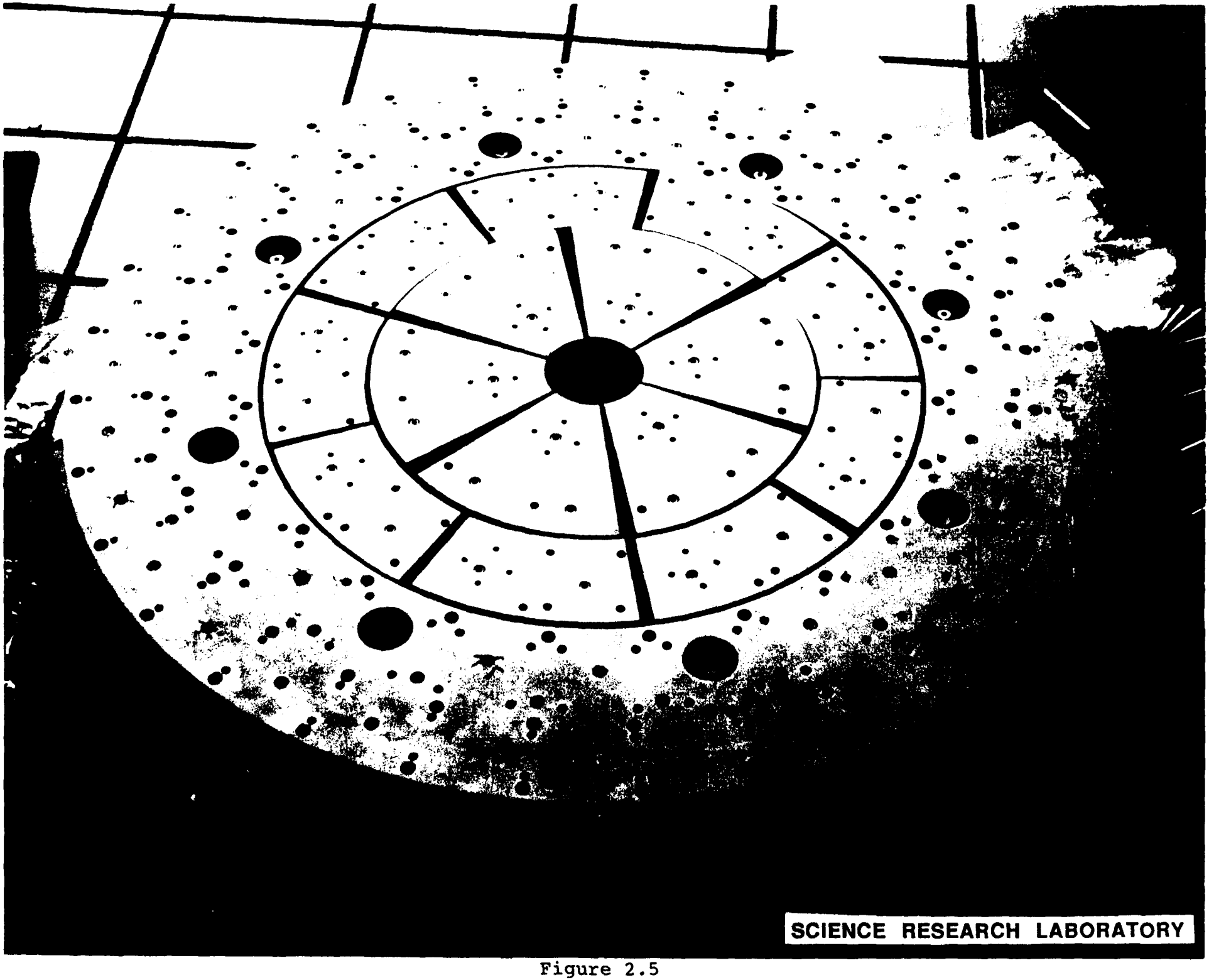

Figure 2.5

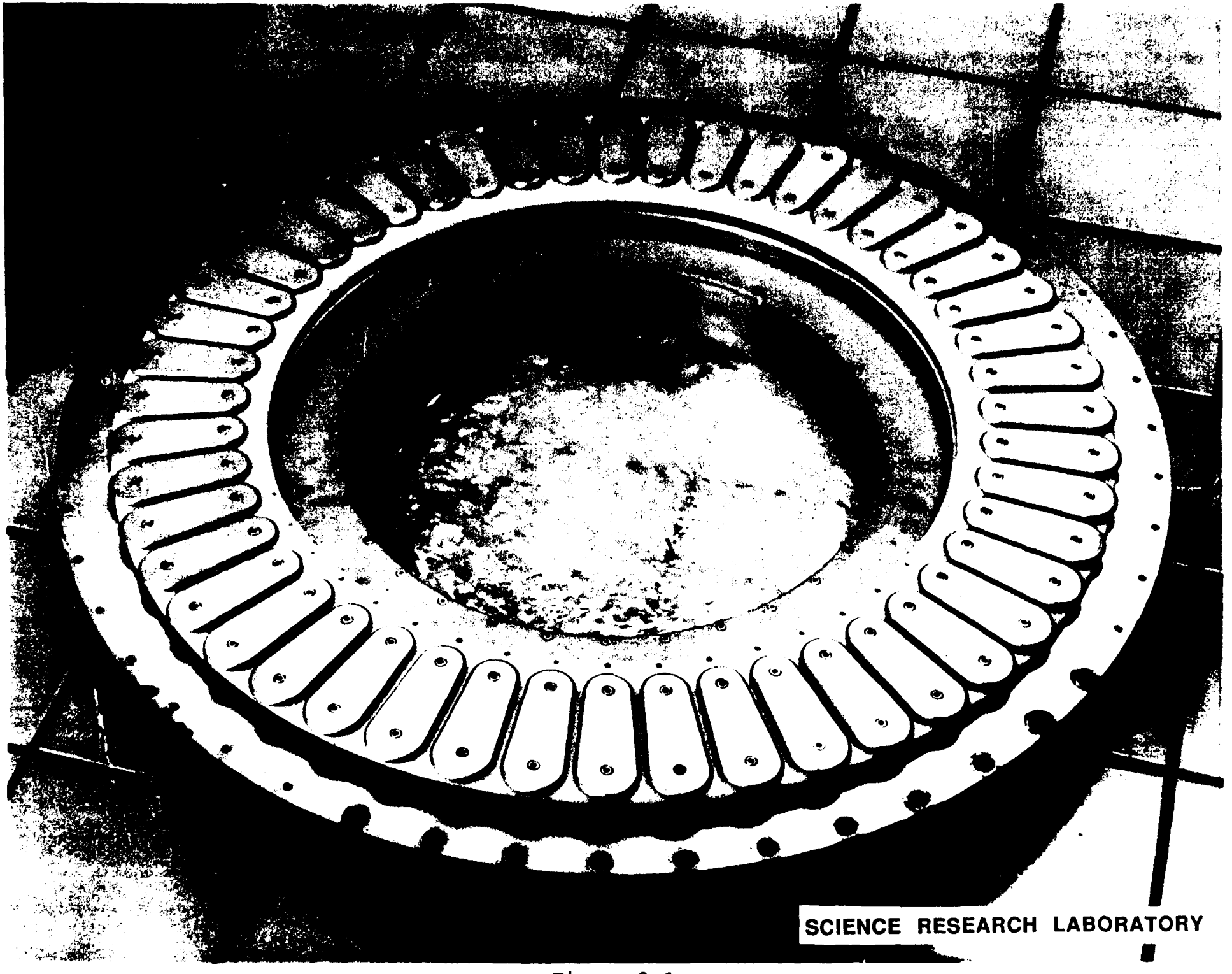

Figure 2.6

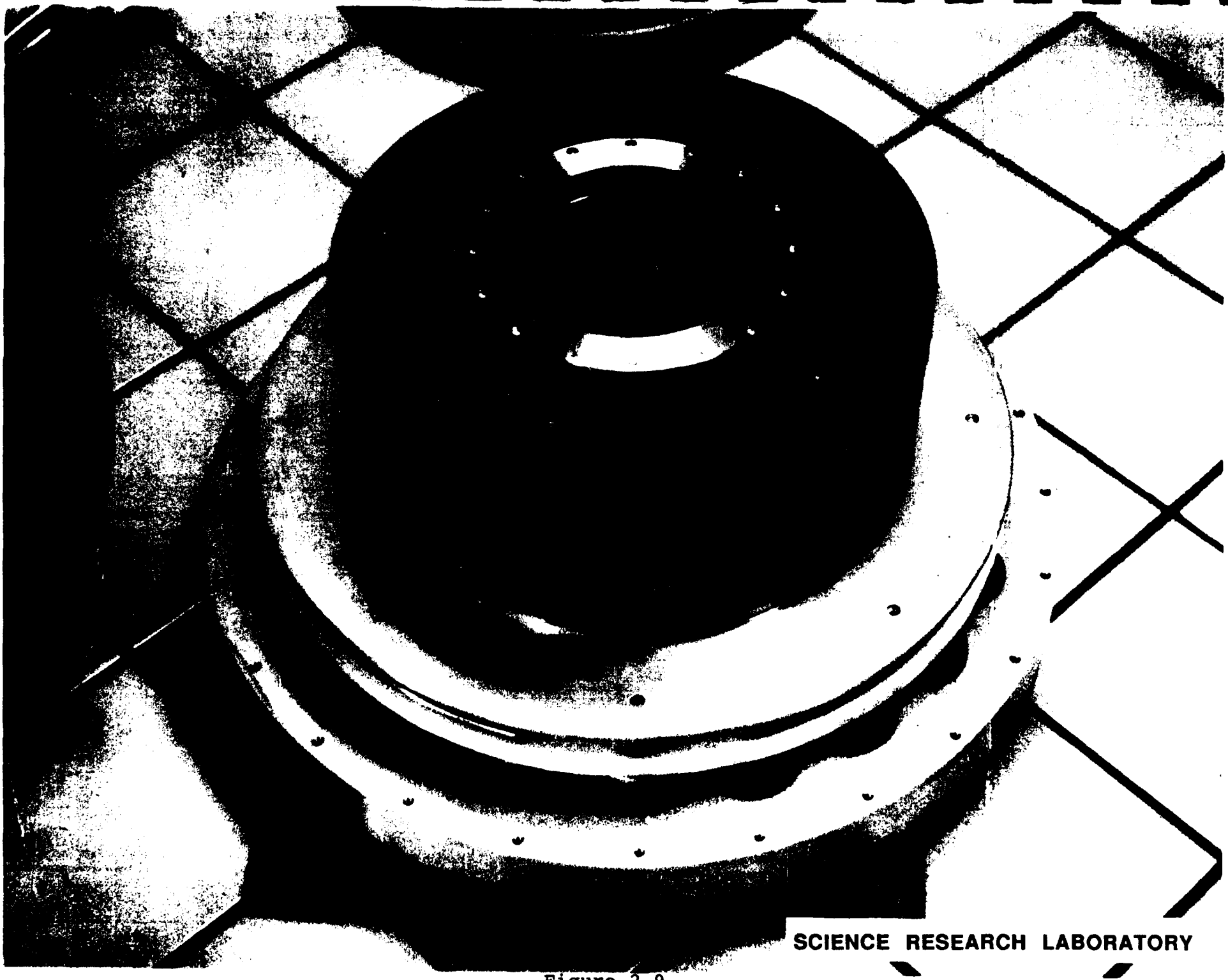

Figure 2.9

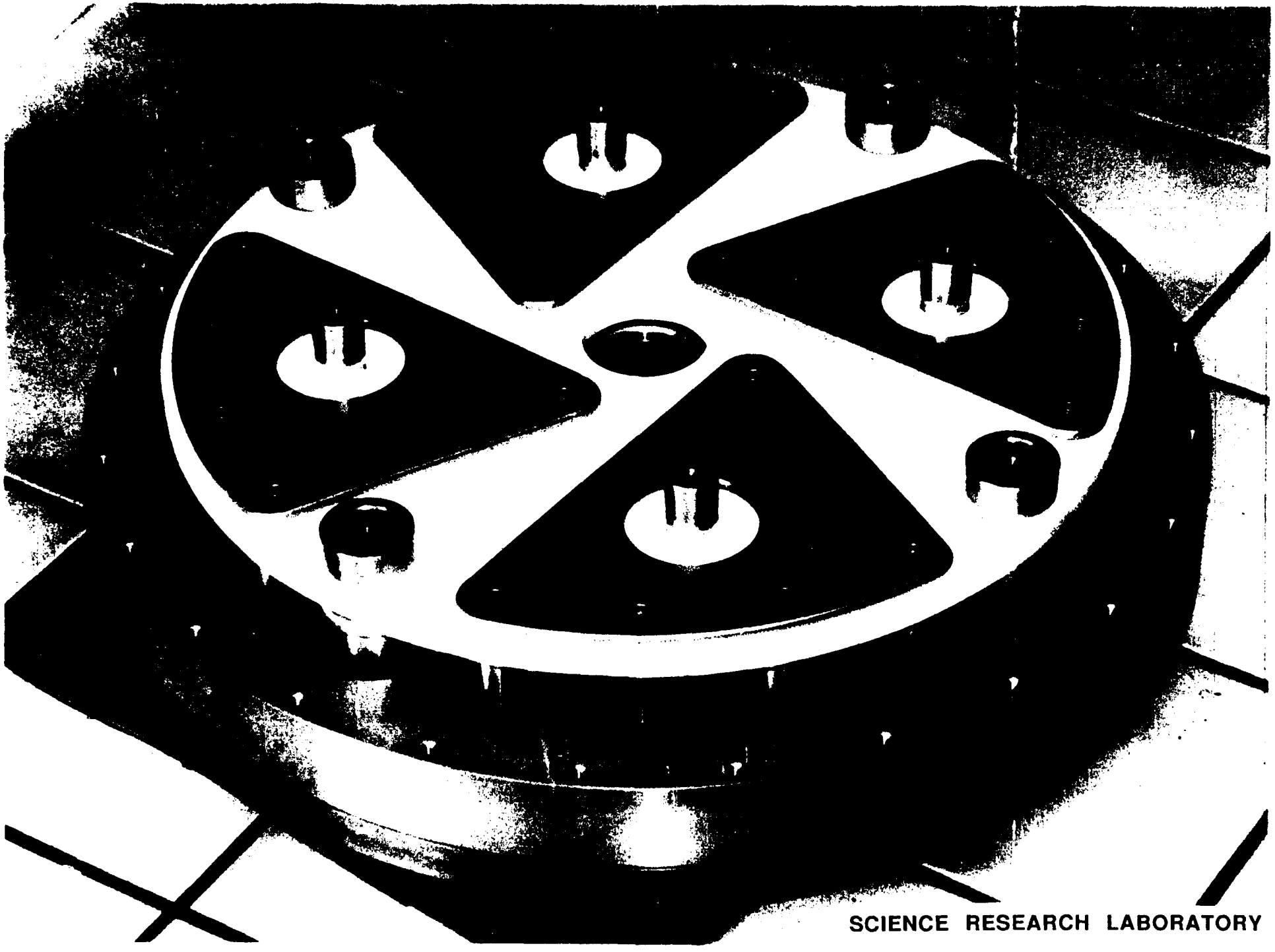

Figure 2.10

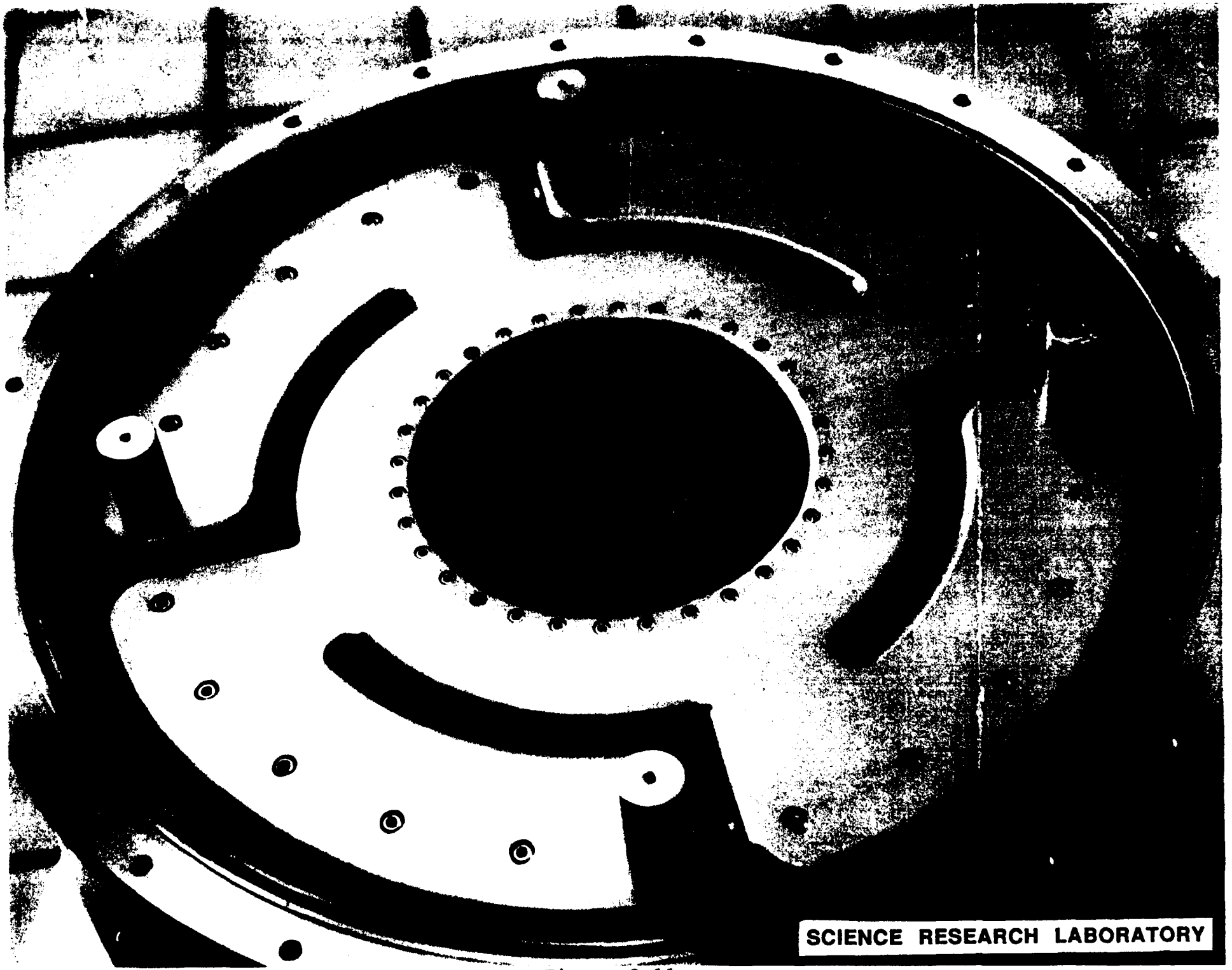

Figure 2.11

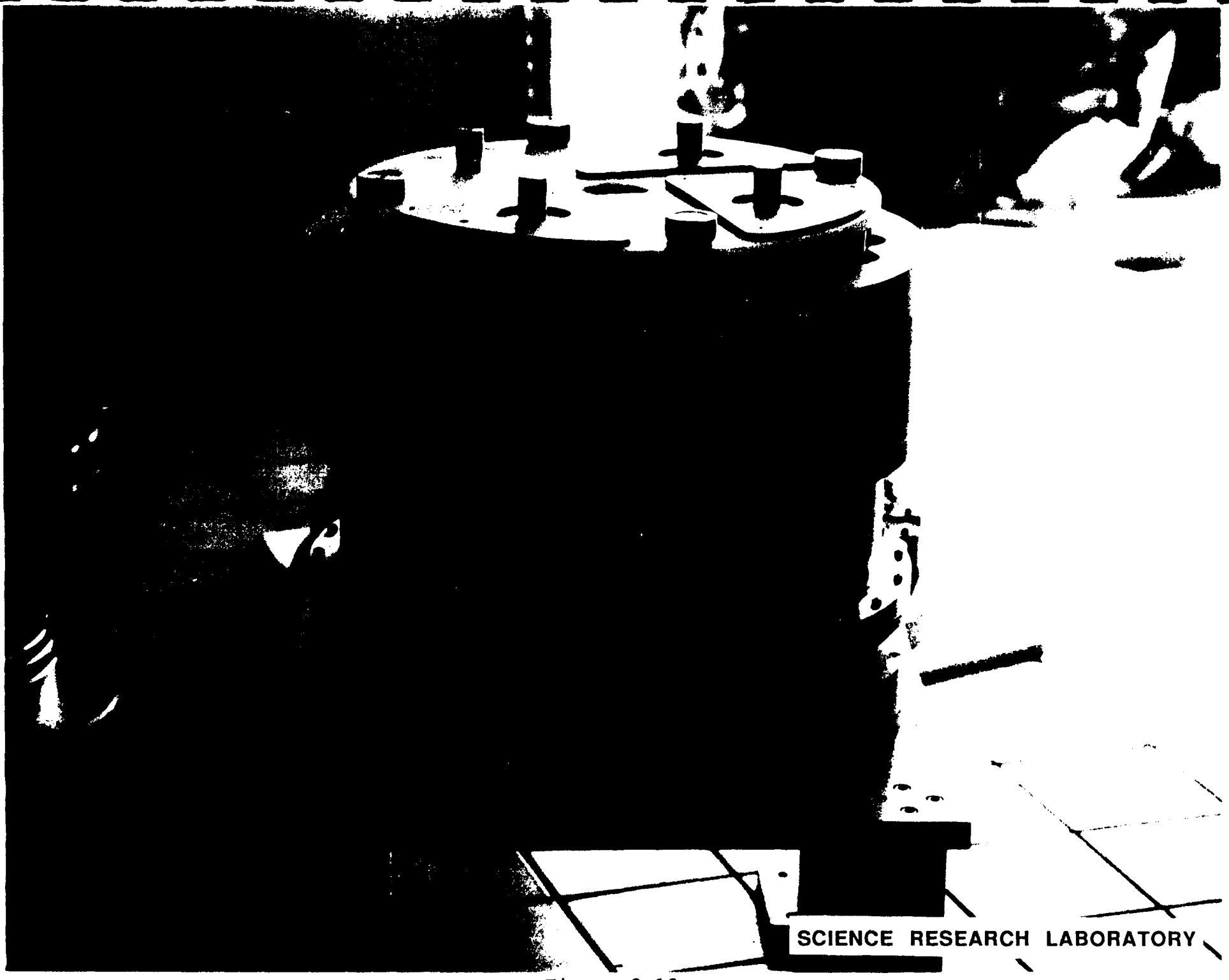

Figure 2.12

cell is shown in Fig. 2.13. A photograph of a two cell assembly is shown in Fig. 2.14.

The cells are blocked in groups of two, each fed by a common bus. Each cell is designed to operate at 125 kV with 1300 amperes drive. The combined impedance is $\sim$ 50 ohms which represents a good match to the driver impedance only if 30 cells are driven. In order to provide a good impedance match with a reduced number of accelerator cells or for operation at reduced electron beam currents, variable resistance copper sulfate loads are mounted on each cell input bus. Copper sulfate dissolved in water is flowed to these loads at a velocity which can be matched to the required power dissipation. The resistance of these loads can readily be varied by adjusting the copper sulfate concentration.

The accelerating gap is 1 cm. wide with a peak enhancement factor of 1.5 corresponding to a peak electric field stress of $\sim$ 187 kV/cm. Considerable effort has been expended to match the strip line impedance presented by the accelerating gap to the radial line impedance extending out into the region of the ferrite. This is done to avoid internal reflections of the electron beam wake field. Once these wake fields reach the ferrite, they are attenuated very rapidly. At the high frequencies ($\geq$300 MHz) associated with the TM_{011} dipole mode, the ferrite exhibits an impedance (Fig. 2.15) very close to that of free space and an attenuation coefficient (Fig. 2.16) close to 4 dB/cm. In summary, the ferrite appears as a total absorber for electromagnetic radiation in the frequency spectrum associated with the Beam Breakup Instability.

The insulator which separates the vacuum from the fluorinert coolant is composed of 99.5% Al_2O_3 ceramic. Great care has been exercised in shaping the radial line so as to compensate for the high permittivity ($\epsilon_r \sim 9$) of this material. Al_2O_3 is chosen because of its low outgassing rate and high dielectric strength as well as its high tracking resistance. The insulator surface presents a weak point for electric field breakdown and must be angled appropriately with respect to the electric field (Fig. 2.17) so as to maximize its tracking resistance.

2.2 The Electron Injector

The design of the electron injector is critical to the operation of the entire accelerator. We have shown that the focusing requirement is a strong function of the beam emittance. Just as

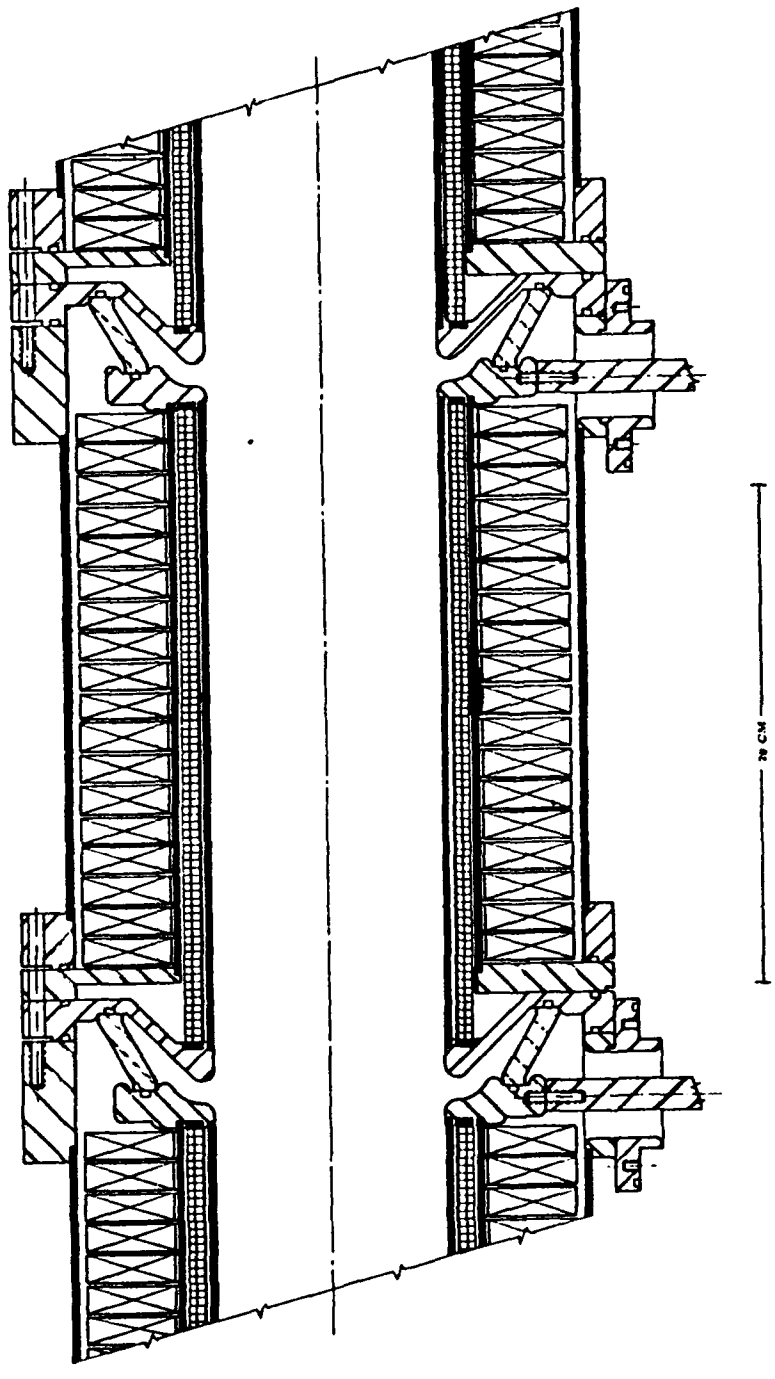

Figure 2.13: Cross sectional drawing of SNOMAD-II induction cell.

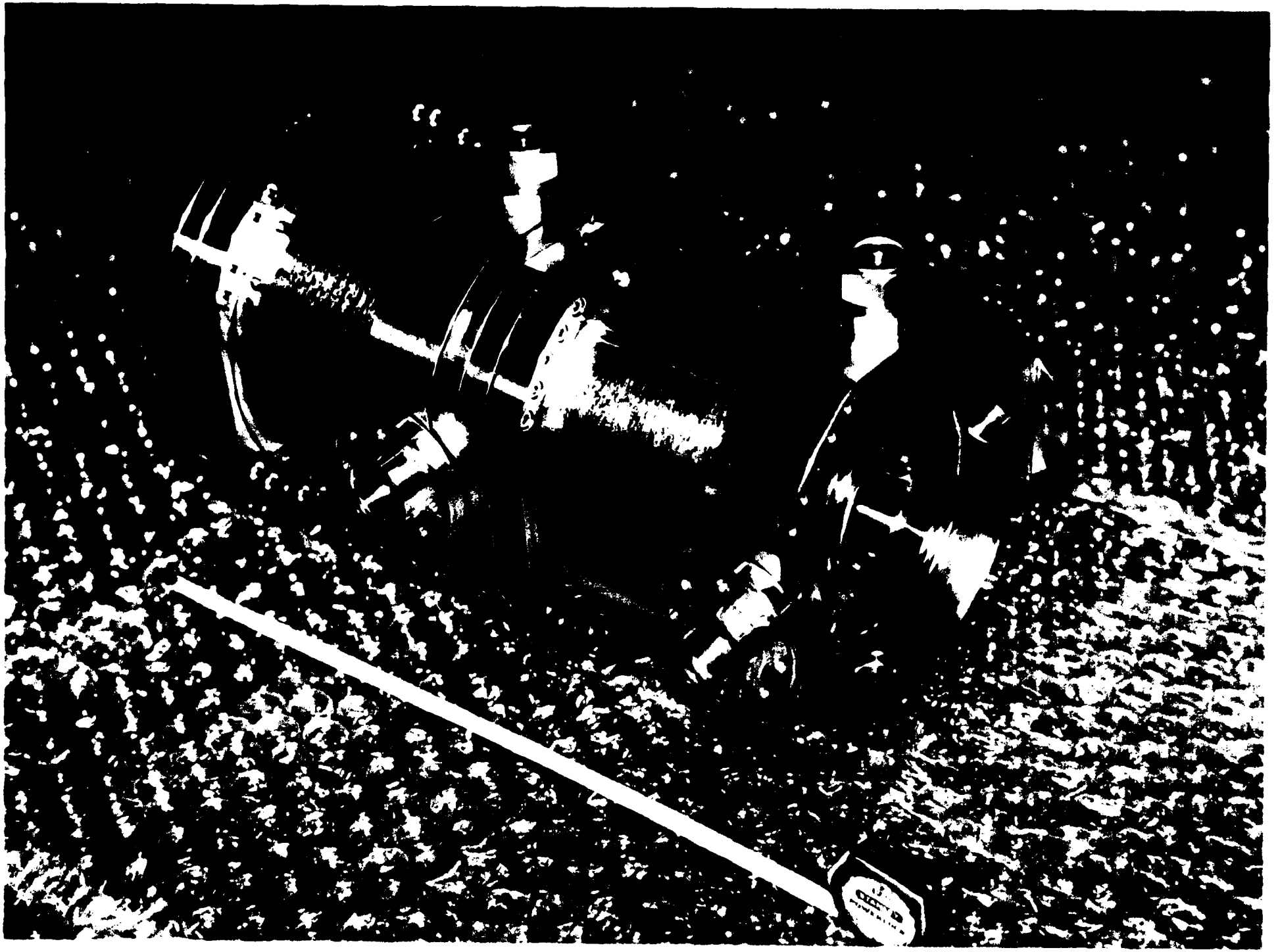

Figure 2.14 SCIENCE RESEARCH LABORATORY

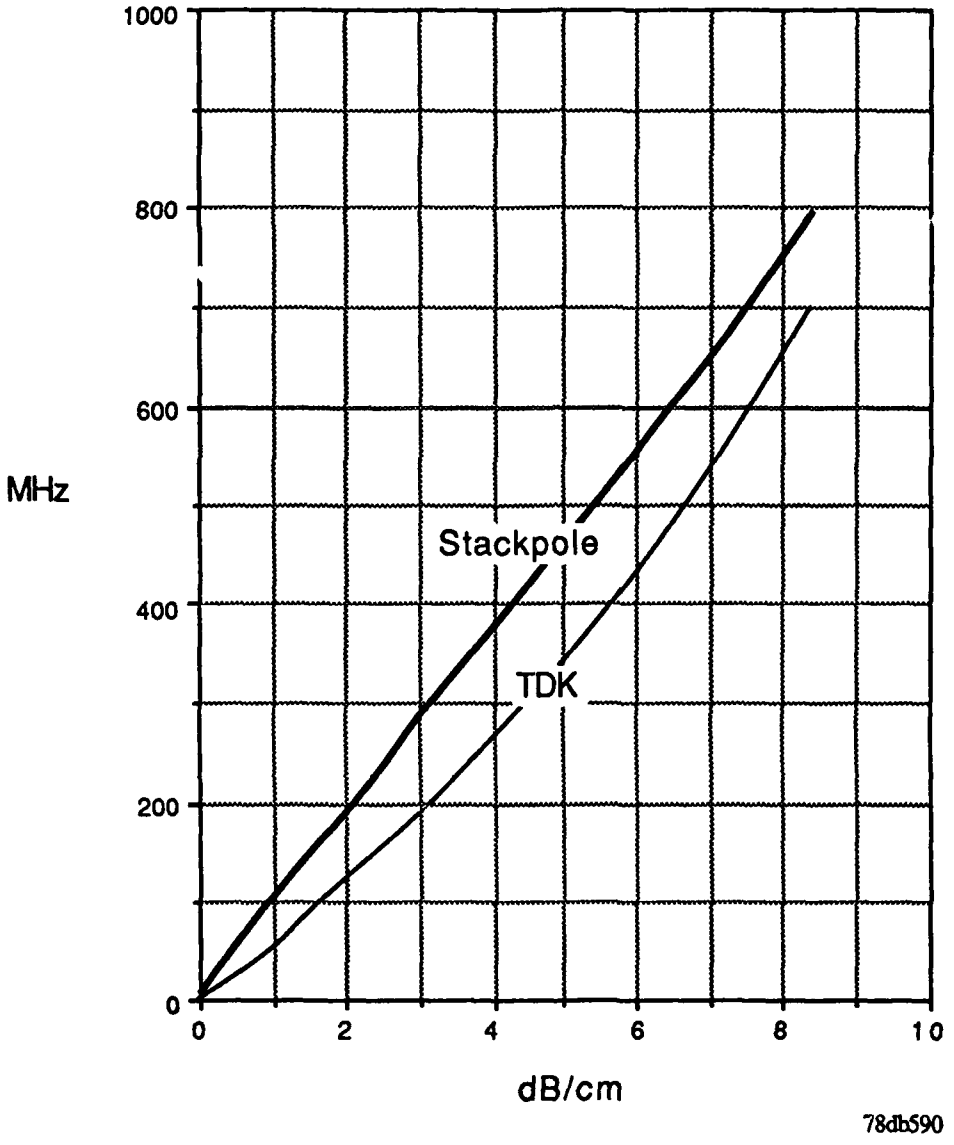

Figure 2.15: RF attenuation in solid ferrite

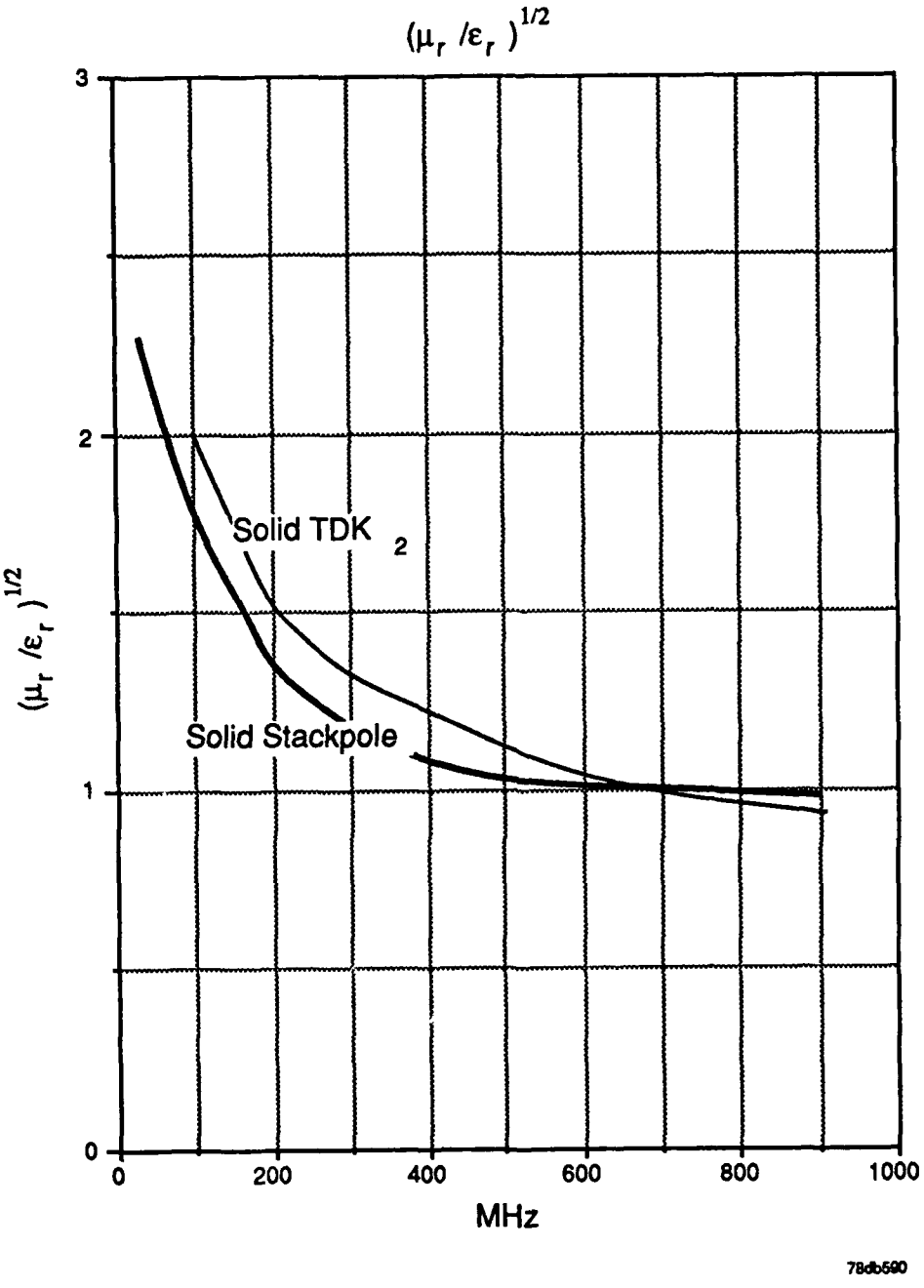
$(\mu_r / \varepsilon_r)^{1/2}$
3
2
1
0
Solid TDK 2
Solid Stackpole
$(\mu_r / \varepsilon_r)^{1/2}$
0
200
400
600
800
1000
MHz
78db590

Figure 2.16

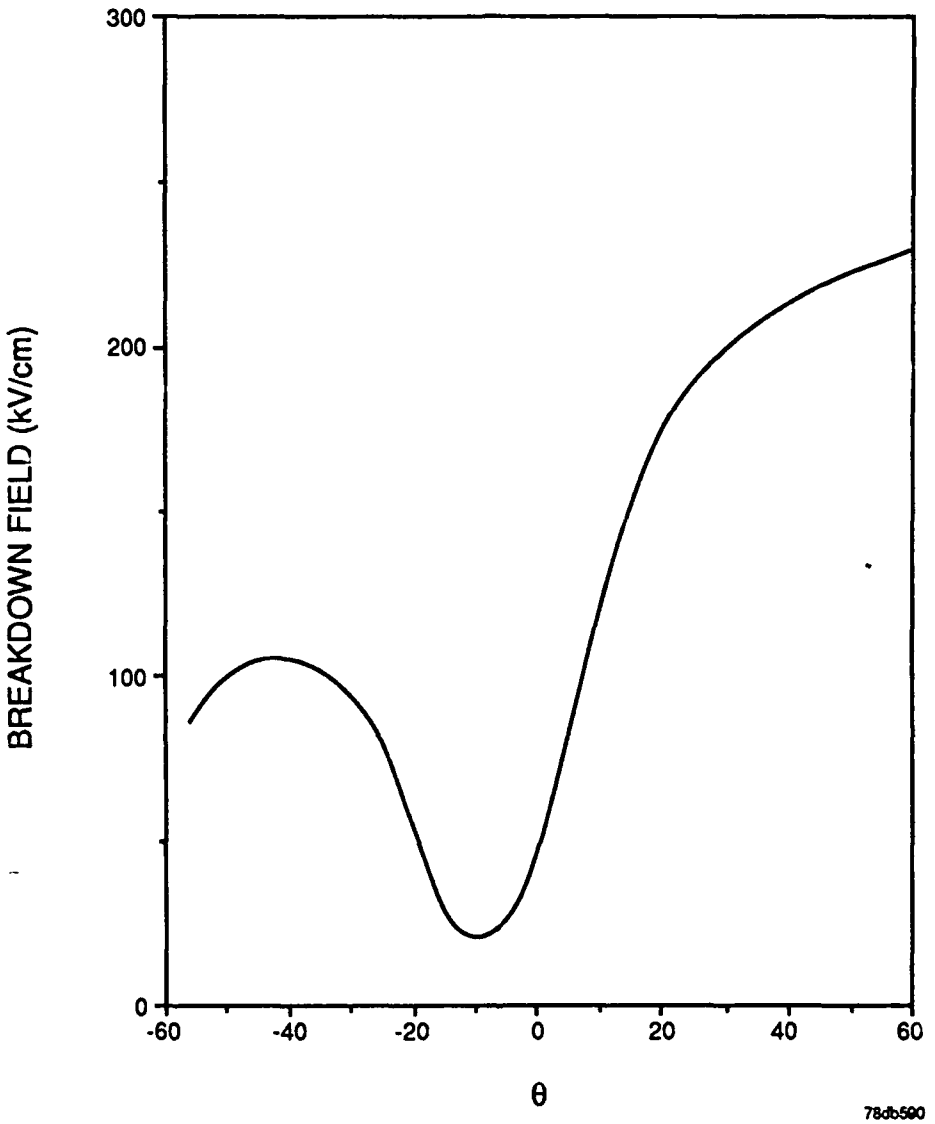

Figure 2.17: Approximate breakdown field as a function of angle for a 50 ns pulse

important as minimizing emittance, the spatial profile must be as close to equilibrium as possible. Beam halos resulting from spurious emission from electrode surfaces must also be eliminated. The wake functions from these non-axially symmetric electrons can severely disturb the main beam envelop.

In order to achieve spatial uniformity while maintaining achromatic operation, area convergence must be minimized. The best performance is achieved when the cathode diameter is kept approximately equal to the anode bore diameter. Therefore in order to minimize the anode stalk diameter while achieving high current operation, the cathode should be chosen to yield as high a current extraction density as possible.

Researchers at Varian have developed a new coating process which forms a very low ($\sim$ 1.7 eV) work function surface. The actual performance data (Fig. 2.18) for a large cathode indicates that extraction current densities in excess of 100 A/cm^2 can be achieved. Injectron, an electron beam injector developed at LLNL, has produced 1.5 kA at 1.5 MeV from a 3.5 inch diameter dispenser cathode.

In order to avoid spurious electron emission while achieving these high extraction densities, the surfaces must be properly polished and greened. As we have shown above, this procedure can yield surfaces capable of sustaining fields in excess of 300 kV/cm, while 200 kV/cm is probably a realistic operating point.

The fields associated with a given extraction density can be simply derived from Poisson's equation. For a planar geometry

$$\nabla^2\phi = -\rho/\epsilon_o$$

which becomes

$$\frac{d^2\phi(z)}{dz^2} = \frac{-\rho}{\epsilon_o} = \frac{J}{v(z)\cdot\epsilon_o}$$

subject to the boundary conditions that

$$\phi(z = d) = V_{anode}$$

$$\phi(o) = 0$$

100 A/cm^2 Dispenser cathode test data (Reproducible for large area)

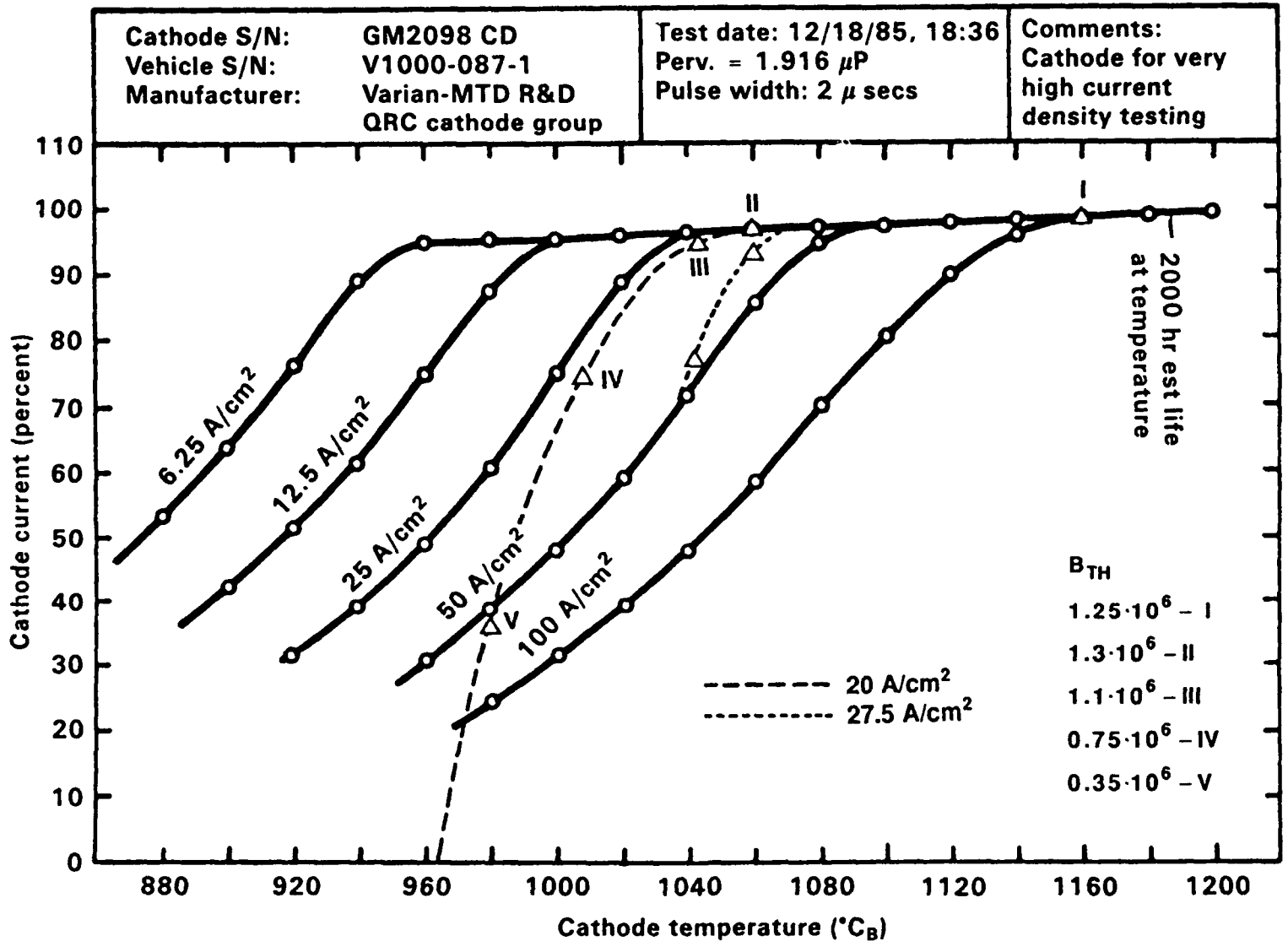

60-C-0686-1043B

Figure 2.18

6/87

$$\frac{d\phi(o)}{dz} = E(o) = 0$$

If the electrons leave the cathode at zero velocity then ignoring the relativistic correction.

$$e\phi(z) = \frac{1}{2}mv^2(z)$$

$$\phi = \frac{V_{anode}}{d^{4/3}}Z^{4/3}$$

and

$$J = \frac{4}{9}\pi\epsilon\left(\frac{2e}{m}\right)^{1/2}\frac{V_{anode}^{3/2}}{d^2} = k\frac{V^{3/2}}{d^2}$$

$$= k\frac{\bar{E}^2}{V^{1/2}}$$

where $\bar{E}$ is the average electric field in the anode cathode gap. This field does not include enhancement factors and therefore a reasonable constraint might be for $\bar{E} \leq 100$ kV/cm. This sets the maximum extraction density to

$$J_{max}(\text{amperes/cm}^2) \leq \frac{2.33 \cdot 10^4}{V^{1/2}}$$

where V is in kilovolts. For a current density of 25 amps/m^2, V must be maintained below 1 MeV.

Space charge sets a minimum voltage at a given current below which the electron beam will no longer propagate down the beam pipe. This sets a lower limit for the injector voltage.

2.3 Space Charge Limited Current

The potential of a beam radius in a pipe of radius b where the average beam energy is given by ϕ_{beam} is approximately given by

$$\phi_{beam} - \phi(r) = \frac{\lambda}{2\pi\epsilon_o}\left[\frac{1}{2}\left(1 - \left(\frac{r}{a}\right)^2 + 2ln\frac{b}{a}\right)\right], r < a$$

$$\phi_{beam} - \phi(r) = \frac{\lambda}{2\pi\epsilon_o}\left[ln\left(\frac{b}{r}\right)\right], a < r < b$$

Here $\lambda = (-\pi a^2 \rho)$ is the beam charge per unit length and the beam current $I(= \lambda \cdot \beta c)$ increases linearly with the charge per length and beam velocity. As λ increases at constant accelerating potential, the electron beam slows due to its increased potential energy. The maximum current which can be propagated in a hollow conducting tube is given approximately as

$$I \leq \frac{Ia}{\beta}\frac{(\gamma^{2/3} - 1)^{3/2}}{(1 + 2ln\frac{b}{a})}$$

For an injector with an anode potential of 0.6 MeV, $I \leq 3$ kA for b/a = 1/e (Fig. 2.19). Attempts to increase the current beyond this level under these conditions will result in the formation of a virtual cathode.

Because the individual accelerator cell voltage is only 125 kV, the 500 kV injector potential can only be achieved by adding the voltage from several cells. This is accomplished by threading reentrant stalks through the cells in place of the electron beam. These conductive stalks make up the secondary winding in these cells. Energy is transferred along the stalk from cell to cell as electromagnetic radiation in the TEM_{00} mode. In a very high current accelerator, this could be continued up to very high voltages but in a 1-2 kA machine it soon becomes impossible to match the impedance of the transmission line formed by the stalk and the beam tube wall to the beam impedance.

2.4 SNOMAD-II Accelerator Tests

Operation of the prototype accelerator began in August 1989. Tests of the SNOMAD-II driver were conducted to verify its performance using the accelerator cells as a load. Initial tests were performed without an electron beam present in the accelerator. Each accelerator cell

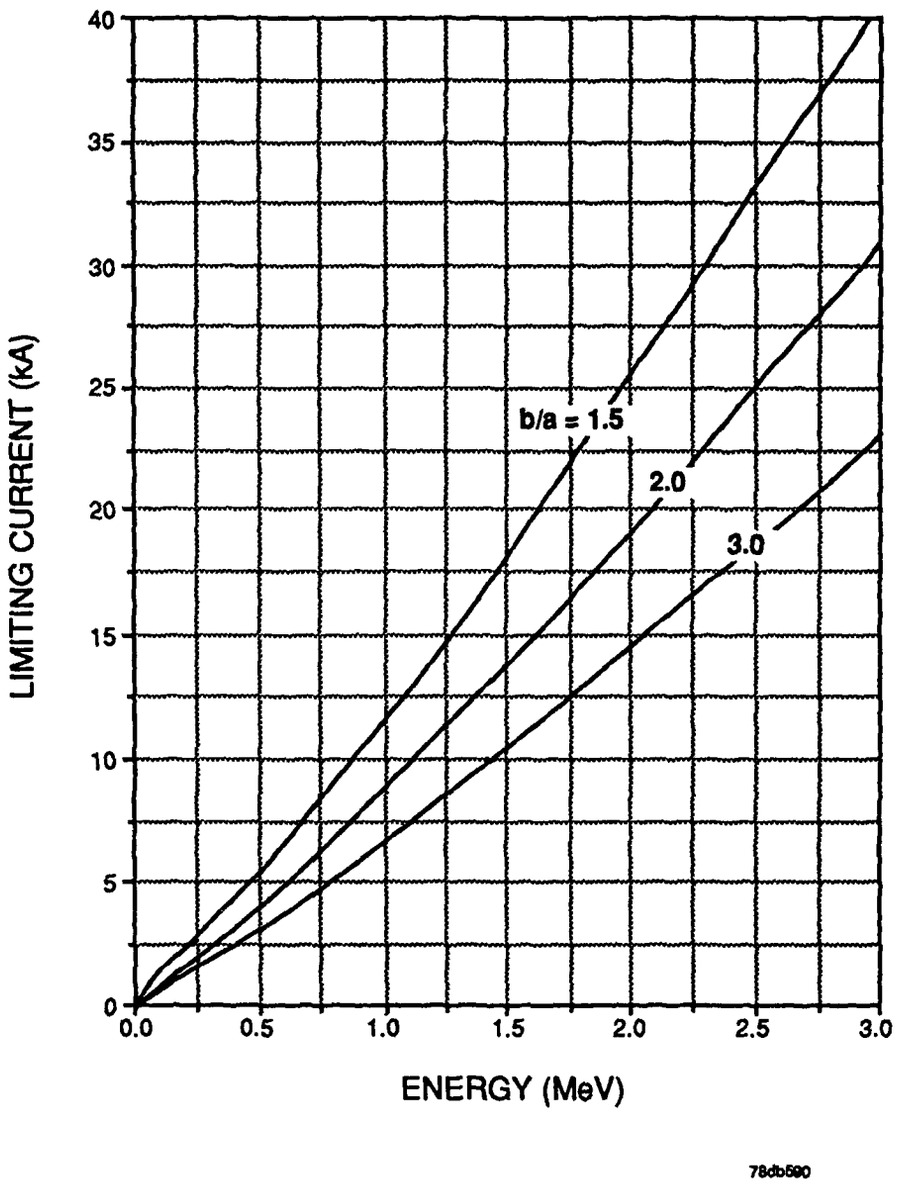

Figure 2.19: Limiting current versus beam energy

was loaded by a water/copper sulfate resistor in parallel with the drive line to simulate the presence of the beam and to aid in matching the impedance of the cell to the driver. Figures 2.20 and 2.21 show the voltage waveforms measured by capacitively coupled voltage monitors located on each of the induction cells. The first four accelerator cells are used to generate the extraction voltage which appears on the cathode. This waveform is shown in Fig. 2.20. The total accelerating voltage produced by eight cells is measured by summing the signals from all of the voltage monitors, Fig. 2.21. The injector waveform exhibits more voltage ripple than the total accelerating voltage. This behavior is common for injector designs and is caused by reflections produced on the cathode stalk. The total voltage exhibits a much smoother waveshape with a flat top of 30 nsec. These data were taken for an accelerating potential of 1 MeV as indicated by the peak of the waveform in Fig. 2.21.

The demonstration of continuous pulse high repetition rate operation was an important objective of this research. These tests were initially conducted with resistively loaded accelerator cells as described above and subsequently the tests were conducted with a high current electron beam produced from a thermionic cathode as described below. The operation of the SNOMAD-II driver was monitored by recording the waveform on the intermediate storage capacitors labeled C_0 in Fig. 2.3. This waveform is displayed with three increasing time bases in Fig. 2.22. In Fig. 2.22a. the intermediate storage capacitor charges to full voltage in a time τ_{ch} = 800 microseconds. The charge time is determined by the value of inductor L_C. The rapid discharge of C_0 at 1 millisecond intervals is produced by triggering the intermediate storage SCRs, thus transferring its charge to the first stage capacitor C_1. Figures 2.22b and 2.22c show the same waveform on progressively longer time scales, demonstrating continuous pulse operation for a duration of 2 seconds. The amplitude droops for approximately 75 milliseconds after the start of the pulse and then recovers. This is caused by the recovery of voltage regulation circuits of the commercial DC power supply which provides prime power to the driver.

The accelerator has not yet been operated at repetition rates higher than 1 kHz or continuous pulse durations longer than two seconds. Limitations currently imposed by the available amount

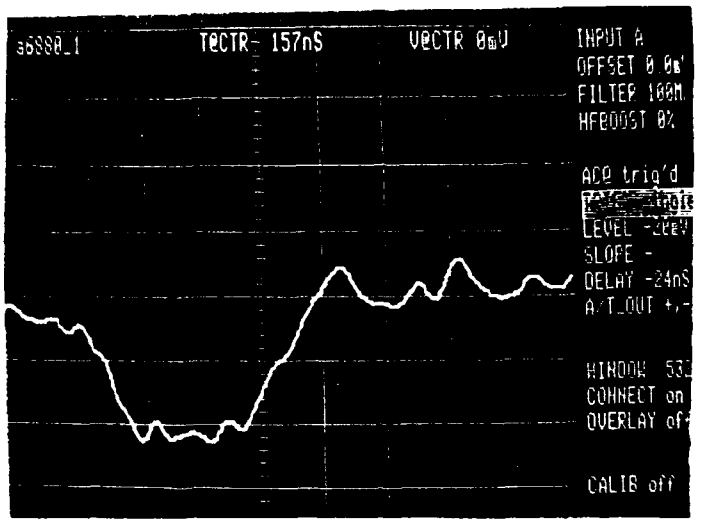

Figure 2.20: Voltage waveform generated by the four cell injector.

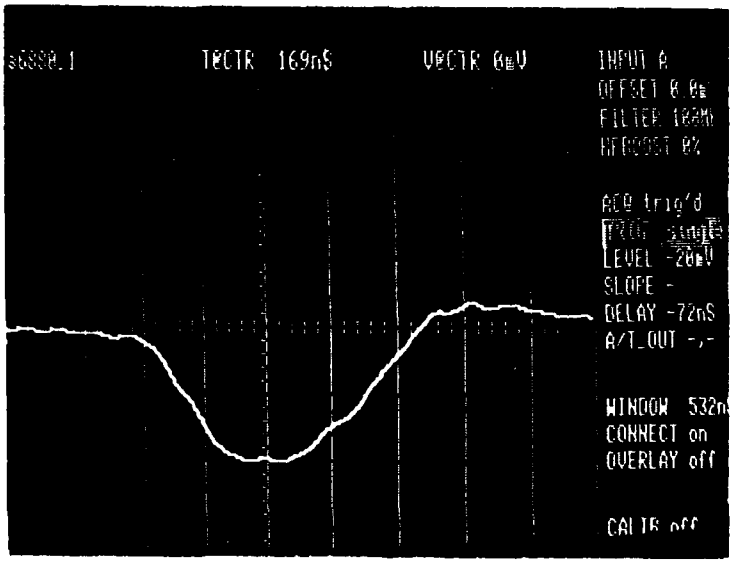

Figure 2.21: Accelerator output voltage. Waveform shows the sum of voltages generated on all eight induction cells.

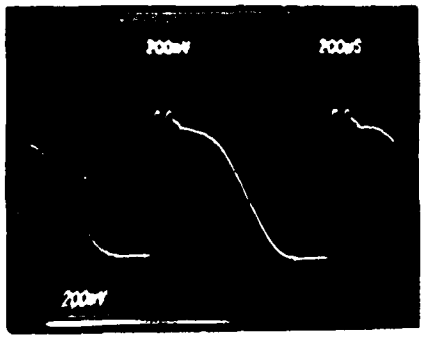

200 microseconds/div

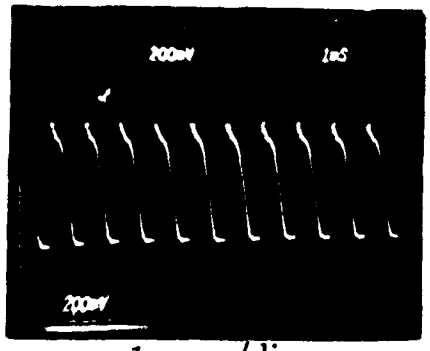

1 msec/div

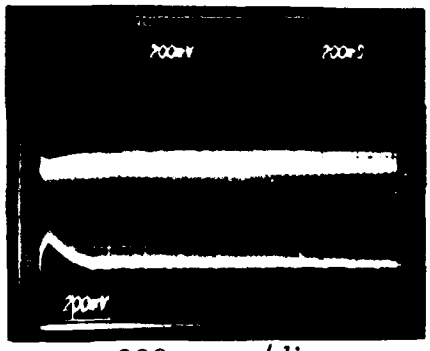

200 msec/div

Figure 2.22 : Demonstration of 1 kHz continuous pulse operation of the SRL prototype induction linear accelerator. Recorded waveform shows voltage on intermediate storage capacitor, C_o for three times scales.

of prime power have restricted operation to 1 kHz. In its present configuration SNOMAD-II is expected to operate reliably at a repetition rate of 5 kHz. This will require the installation of additional DC power and lowering the value of the intermediate storage charging inductor L_C.

A thermionic cathode has recently been installed and initial high repetition rate tests of the accelerator with a high current beam have been performed. The injector has been designed to accept a 3.5 inch diameter dispenser cathode similar in design to the cathode used in the SLAC klystron gun. Power is fed to the cathode heater through the cathode stalk, eliminating any need to electrically isolate the heater power. High repetition rate tests similar to those described above have been performed with the cathode installed. Accelerating voltages were measured by the voltage monitors located on each of the cells and beam current was monitored by a resistive anode beam stop. The waveform displayed in Fig. 2.23 shows the beam current produced by a cathode following 48 hours of conditioning. A peak current of 550 A is achieved. The cathode current exhibits the predicted Child-Langmuir limited behavior rising sharply as the voltage pulse is applied, reaching a plateau and falling rapidly at the end of the voltage pulse. The injector design current was a little over 600 Amps, but a small fraction of the electron beam was intercepted at the Anode bore. This is a standard design philosophy which scrapes the outer edges of the beam removing the electrons with the highest emittance and by default creating a well centered electron beam in the transport tube.

SNOMAD-II INJECTOR 5/1/90

VOLTAGE -

CURRENT -

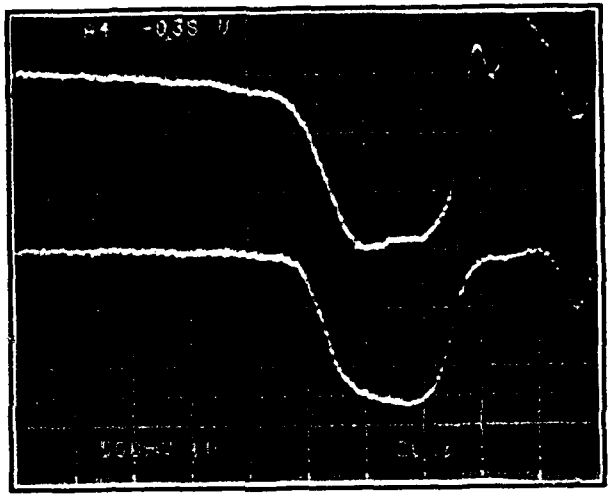

BEAM VOLTAGE	200 kV / cm	20 ns / cm
BEAM CURRENT	200 A / cm	20 ns / cm

Figure 2.23 Linac Injector beam voltage and collectec current waveforms are shown. The waveform scales are 200 kV/div (top trace) and 200 Amps/div (bortom trace). The timescale is 20 ns/div. The current was collected by a Faraday cup mounted 10 inches beyond the anode plane. The cathode temperature was 1100°C.

SECTION 3

3.0 THE SNOMAD-III NONLINEAR MAGNETIC DRIVER

Recently researchers at SRL initiated the design of a higher energy all solid state magnetic pulse compressor. This pulser is designed to deliver 1000 joules/pulse at 6 kHz repetition rate. The input power requirements for this pulser exceeds 6 MW. Even in the most conservative designs, there is always the possibility that a fault mode will develop and initiate an arc which will not recover at this high repetition rate. Unless the driver is interrupted during the interpulse period, 6 MJ per second of energy can be deposited in the fault which will certainly destroy the pulser.

One solution to this problem is to branch the pulse compressor and isolate multiple arms which together supply the total pulse energy. In this mode of operation, if a fault occurs, it will only have access to a small fraction of the total pulse energy. In the case of SNOMAD-III four isolated 250 joule commutation modules drive a single final compression unit (Fig. 3.1). Inside the final compression unit, the four 250 joule arms remain isolated all the way to the output transformer where they are added together and transmitted to the accelerator cells (Fig. 3.2).

Inside the commutation modules, the pulse energy is further branched and isolated into 20 arms per module. This results in each SCR-commutated arm handling only 12.5 joules of pulse energy. Even in a fault mode condition, each SCR handles only the energy required to drive a single isolated 12.5 joule pulser.

The SNOMAD-III accelerator module, combines the commutation modules and compression modules and accelerator in one convenient package. This package is outlined in Fig. 3.3. However, it should be understood that there exists significant technical risk in developing a working, reliable magnetic pulse compressor at 6 MW average power. In order to facilitate cooling and to provide an exit path for shock waves resulting from a possible breakdown, the individual modules are constructed in a ring cage fashion. They are not housed in a tube such as SNOMAD-I or SNOMAD-II: instead, they are immersed within an outer rectangular enclosure similar tp the design of SNOMAD-IV and SNOMAD-V. These enclosures are equipped with

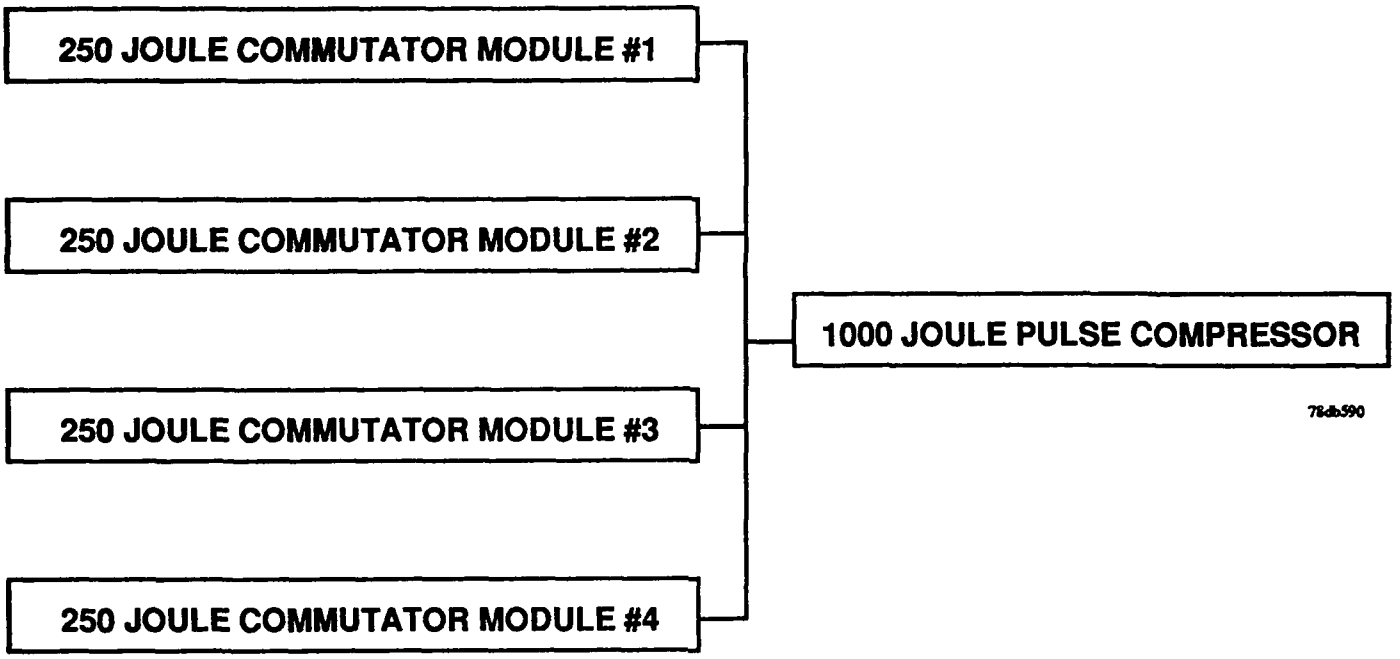

Figure 3.1: Block diagram of SNOMAD-III

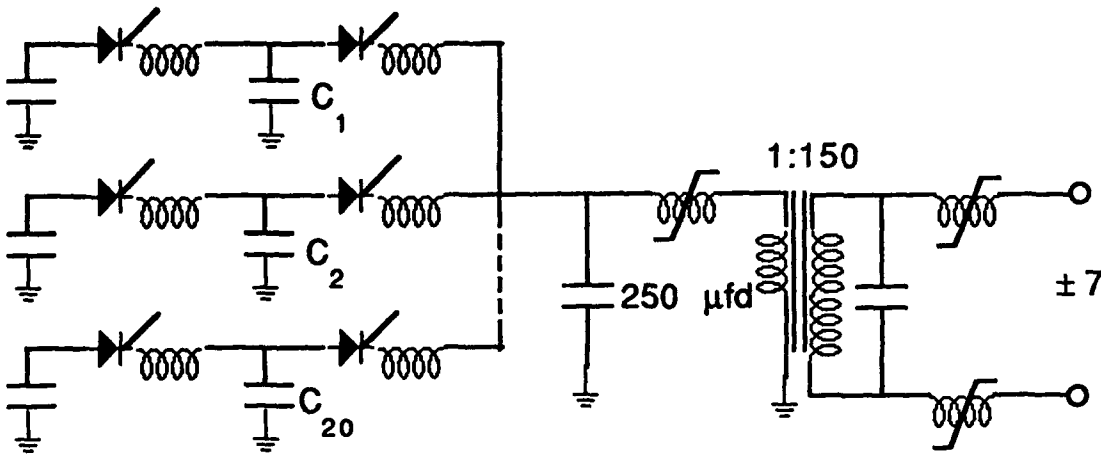

EQUIVALENT CIRCUIT OF COMMUTATOR CIRCUIT

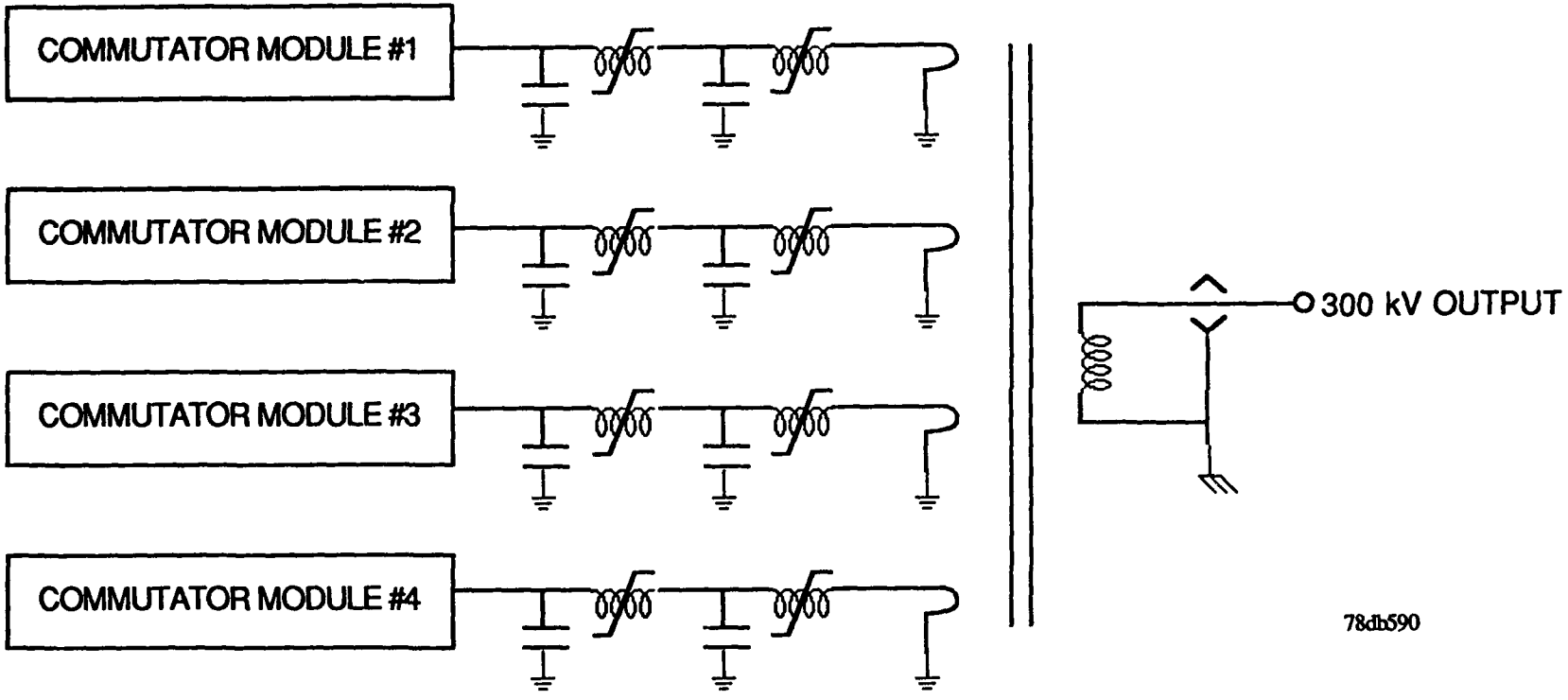

EQUIVALENT CIRCUIT OF SNOMAD III

Figure 3.2

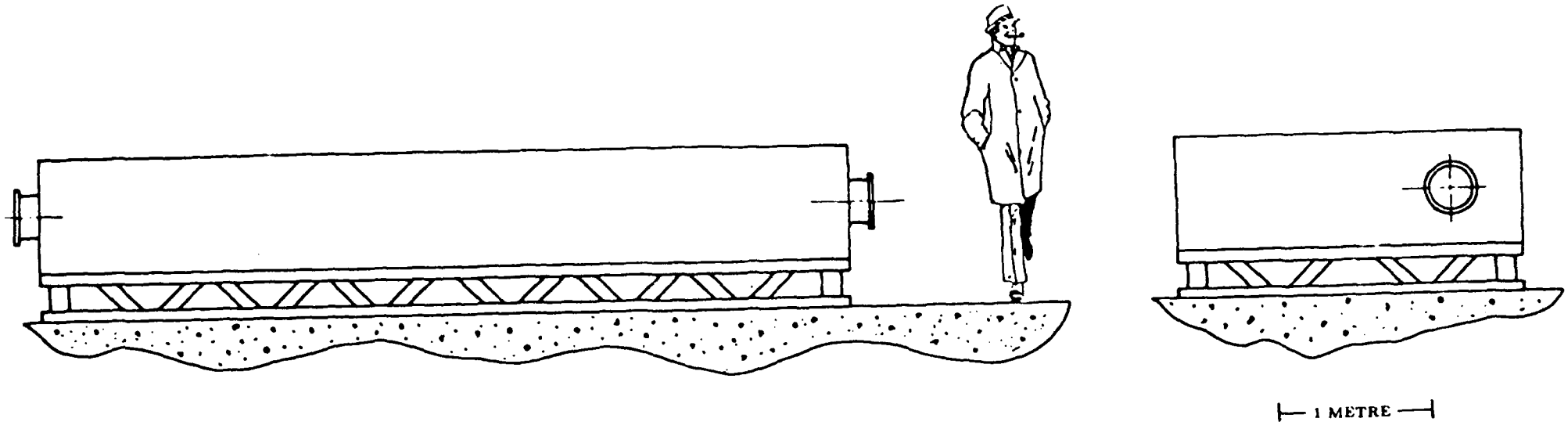

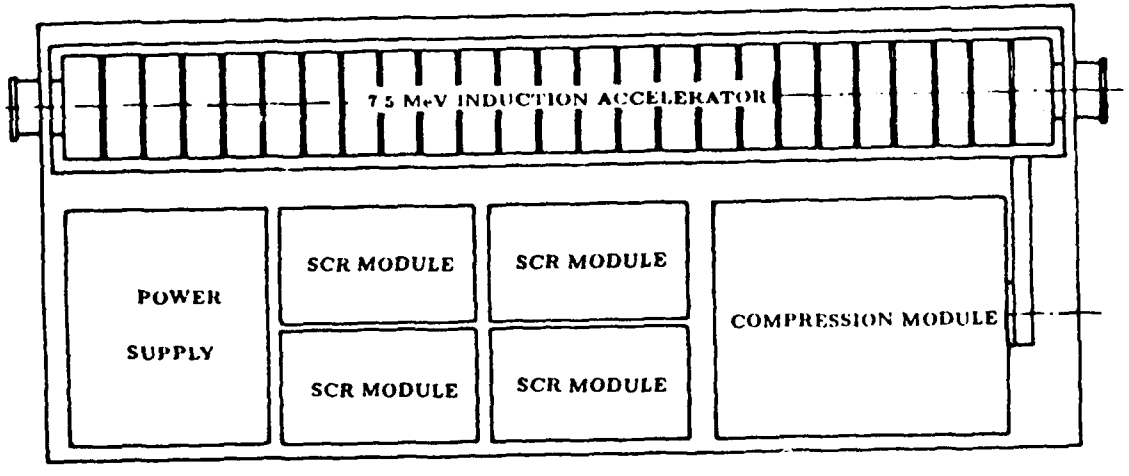

INPUT REQUIREMENTS: 480 VAC, COOLANT WATER

Figure 3.3: SNOMAD-III 7.5 MeV Accelerator Module

heat exchangers in the lids and are filled with freon which serves as both a coolant and dielectric media.

A sketch showing the cross section of the SNOMAD-III Commutator Module appears in Fig. 3.4. Each one of these modules delivers 250 joules to the Compression Module in 438 nanoseconds. Four of these modules are required to deliver the full 1000 Joules to the SNOMAD-III Compression Module pictured in Fig. 3.5. The SNOMAD-III Compression Module compresses the four 250 Joule, 438 nanosecond inputs into a single 1000 Joule, 20-50 nanosecond pulse. The peak output power from the compression module is approximately 20 gigawatts. The output voltage is approximately 400 kV into a matched load. The detailed performance specifications for both the Commutation Modules and the Compression Module is further outlined in Tables 3.1 and 3.2.

The output PFL of the SNOMAD-III Compression Module has been designed so that the output pulse length is variable. The short charge time of 84 nanoseconds assures good output pulse fidelity down to 20 nanoseconds. The pulse length is determined by the patterns cut in the positive input busses to which the capacitors mount. The PFLs are charged at several positions along the length so as to assure uniform charging. The output compression reactors have been carefully designed in order that they appear as a transmission line matched to the impedance of the load. This impedance is also adjustable to match the varying load impedance which would correspond to the differing output pulse lengths.

The SNOMAD-III design has not as yet been constructed and was generated at the request of SDIO to investigate the engineering feasibility of a 1000 Joule module. A complete detailed design was supplied to SDIO for analyses along with a warning that a design such as SNOMAD-IV with much reduced energy per module was much less risky.

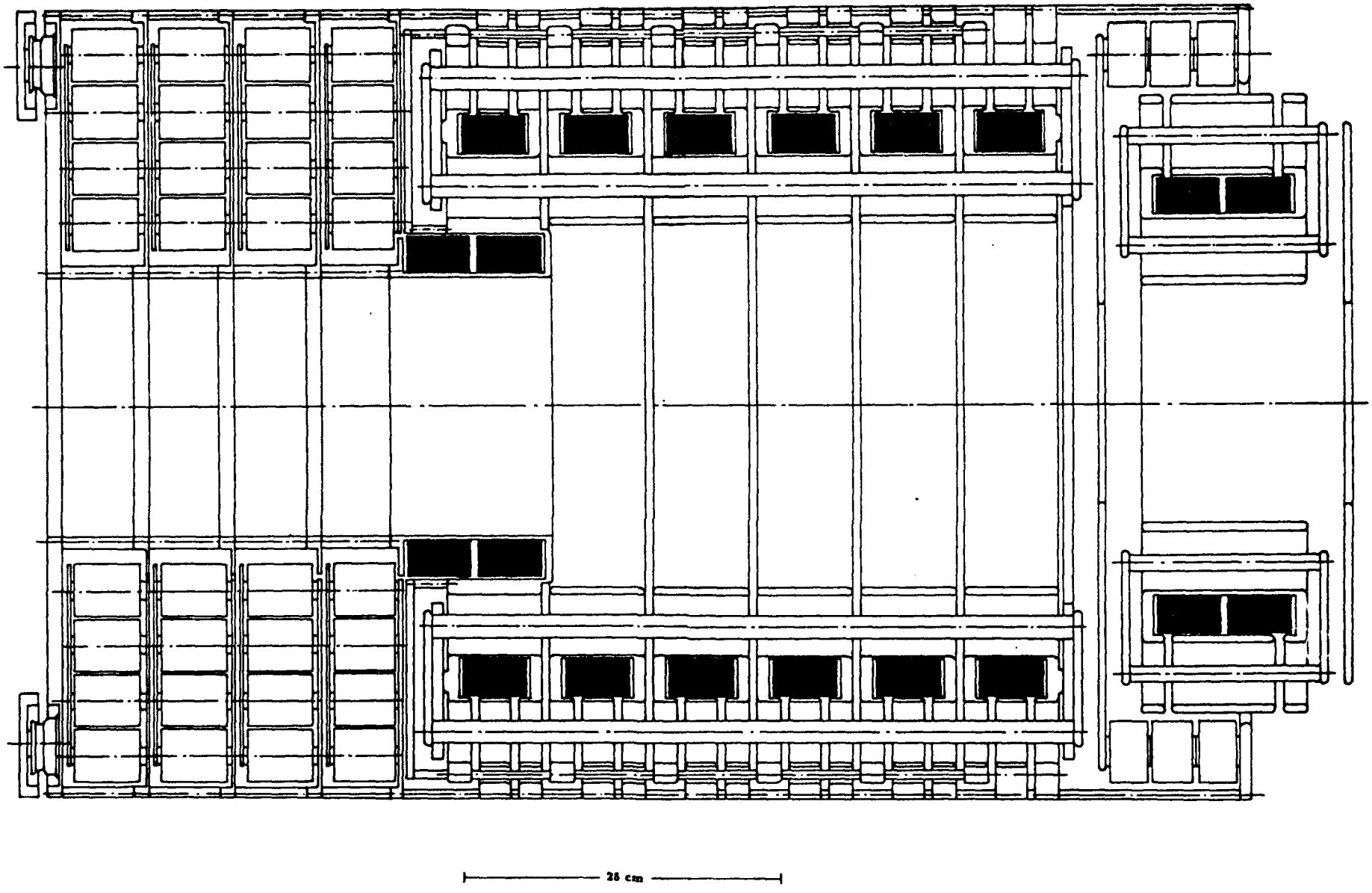

Figure 3.4: SNOMAD-III commutator module

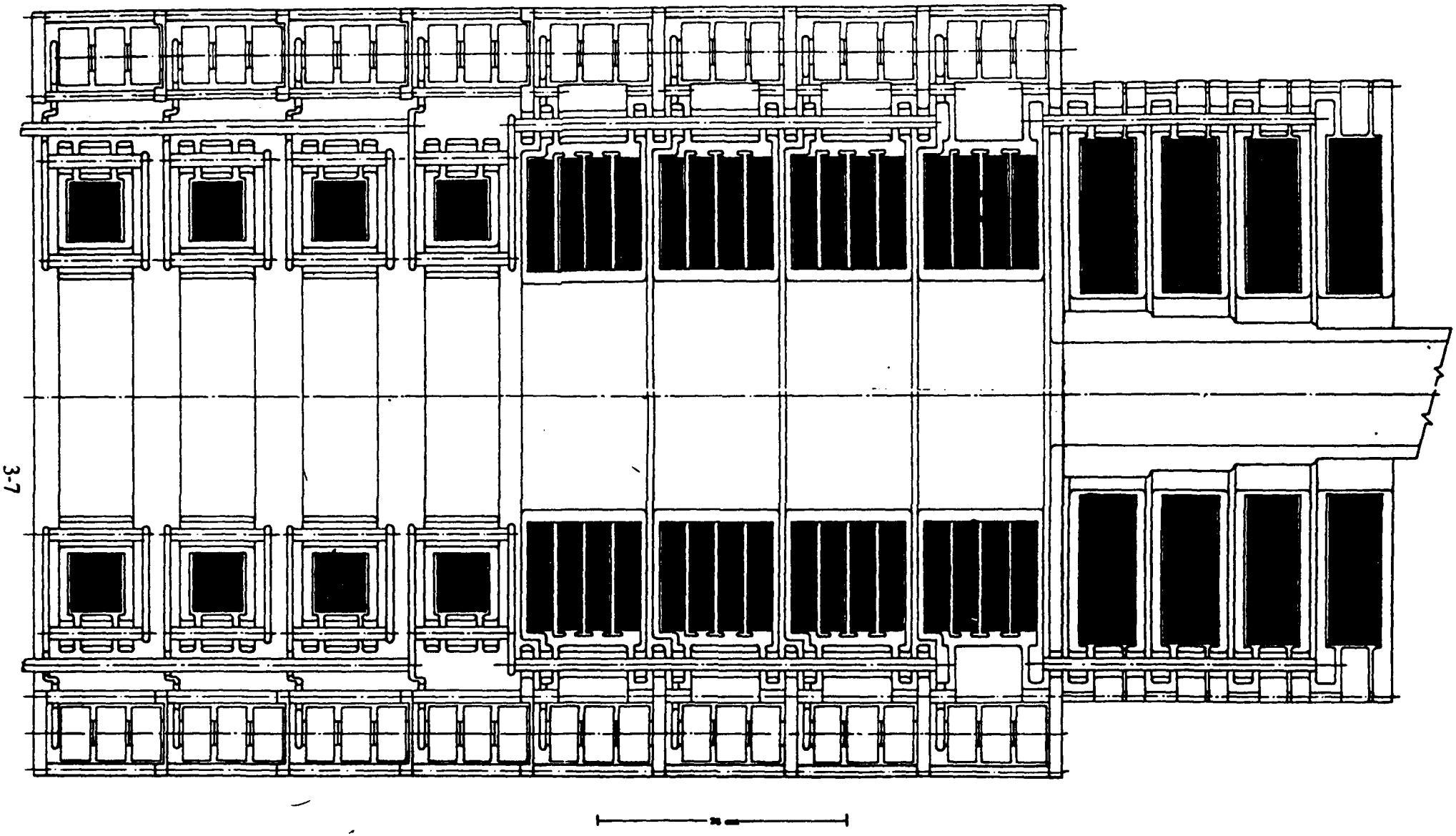

Figure 3.5: SNOMAD-III compression module

Table 3.1: SNOMAD-III Commutator Module

Input Power Requirements:	
Energy/pulse	280 joules
PRF	6 kHz
Power	1.68 MW
Voltage	1500 volt
Current	1,120 Amps
Intermediate Storage	
Capacitance	250 μfd
Voltage	1500 volts
Energy	280 joules
Stored charge	3.75×10^{-1} Coulombs
τ discharge	$\leq$ 10 μsec
I peak	58.904×10^{3} Amp
dI/dt	18.5×10^{3} A/μsec
I_T (RMS)	10.3 KAmps
dI/dt per device	925 A/μsec (20$\times$R305 West Code)
Commutation losses	$\sim$ 5 joules
1st Stage	
Capacitance	250 μfd
Voltage	1,480 volts
Energy	275 joules
Core Type	.6 Mil $\times$ 2605 CO
# Turns	1
Core geometry	2$\times$8.75″ ID $\times$ 11.0″ OD $\times$ 2″ Wide
$\int V \cdot dt$	$\sim 7.5 \times 10^{-3}$ Vsecs
Lsat	4.8 nh + 1.2 nh (STRAY) = 6.0 nh
τ discharge	2,720 nsecs
Losses	$\sim$ 5 joules (2.5 cores, 2.5 caps)
Core volume	2.28×10^{-3} m^3, 11.44 kg
Transformer	
Core Type	2605S3A
# Turns (PRIM)	1/6
# Turns(sec)	25
Losses	$\leq$ 2.5 joules
Core geometry	5$\times$16.0″ ID $\times$ 18.75 ″ OD $\times$ 2″ wide

Table 3.1 (Continued)

2nd Stage		
	Capacitance	11.1 nfd
	Voltage	222 kV
	Energy	272.5 joules
	Core type	2605SC METGLASS
	Core Geom.	2×12.0″ ID × 14.75″ OD × 2″ w
	$\int V \cdot dt$	30 Turns × 10.4 Vmsecs/Turn = 222 kV* (2,800 nsecs/2)
	LSAT	2.6 μh + .9 μh stray $\simeq$ 3.5 μh
	τdischarge	438 nsecs
	Losses	$\sim$ 5 joules

Table 3.2: SNOMAD-III Compression Module

Input Power Requirements:	
Energy/pulse	4×272.5joules=1090
PRF	6 kHz
Power	6.54 MW
Voltage	222kV
1^{st} Stage	
Capacitance	4×11.1nfd
Voltage	222 kV
Energy	1090 joules
Core Type	.6 Mil × 2605 CO
# Turns	4
Core geometry	6×12.75″ ID × 17.5″ OD × 2″ Wide
$\int V \cdot dt$	$\sim 40 \times 10^{-3}$ Vsecs
Lsat	114 nh + 16 nh (STRAY) =130 nh
τ discharge	84 nsecs
Losses	~ 20 joules (10 cores, 10 caps)
Core volume	14×10^{-3} m^3, 70 kg
2^{nd} Stage	
Capacitance	4×11.1nfd
Voltage	219 kV
Energy	1070 joules
Core Type	CMD-5005 Ferrite
# Turns	1
Core geometry	4×10.0″ ID × 19.0″ OD × 1″ Wide
$\int V \cdot dt$	$\sim 8 \times 10^{-3}$ Vsecs
Lsat	13 nh + 7 nh (STRAY) = 20 nh
τ discharge	20-60 nsecs (adj. PFL)
Losses	~ 50 joules (40 cores, 10 caps)
Transformer	
Core Type	2605S3A
# Turns (PRIM)	.25
# Turns(sec)	1
Losses	≤ 20 joules
Core geometry	4×8.0″ ID × 20.0 ″ OD × 2″ wide
Output Voltage	400 kV

SECTION 4

4.0 SNOMAD-IV ACCELERATOR DESIGN

The SNOMAD-IV induction linear accelerator is a self contained 1 MeV accelerator module driven by an all solid state nonlinear magnetic pulse compressor. Twenty induction cells, each driven at 50 kV, produce a total accelerating voltage of 1 MV. A schematic of this accelerator indicating its physical size and layout is shown in Fig. 4.1. Table 4.1 summarizes the performance specifications of SNOMAD-IV. The accelerator module can also be configured as a ten cell (0.5 MeV) electron injector as shown in Fig. 4.2. This injector can be combined with up to ten 1 MeV accelerator modules providing accelerator configurations with beam energies from 0.5 to 10.5 MeV. Above this beam energy, additional consideration must be given to the limitations imposed by the beam break-up instability. A detailed description of the accelerator design considerations is presented below.

The use of solid state devices to replace thyratrons or spark gaps in existing pulse power designs is key to the development of reliable, high average power induction linear accelerators. When combined with the technology of nonlinear magnetic compression circuits, SCR commutated drivers provide operating capabilities at pulse repetition rates and lifetimes greatly exceeding those of thyratron designs. The SNOMAD-IV driver is capable of delivering up to 50 joules per pulse at a rate of up to 20 kHz (cw), to an induction cell load. A circuit diagram of SNOMAD-IV is shown in Fig. 4.3. Commercially available SCRs are utilized in the command resonant charge and intermediate storage power supply. Thyratron switches have been completely eliminated permitting significantly higher repetition rate operation and a reduction in cost and size.

The input is split into multiple arms, each completely isolated from the other, allowing each SCR to perform individually. Isolation between arms is provided by the saturable inductors in series with each SCR. The commutator arms deliver a 55 joule energy pulse into the first stage energy storage capacitors, C_1. C_1 is charged to 1 kV in 2 μsec. The charging time has been chosen so as not to exceed the dI/dt capabilities of commercially available SCRs. Low loss,

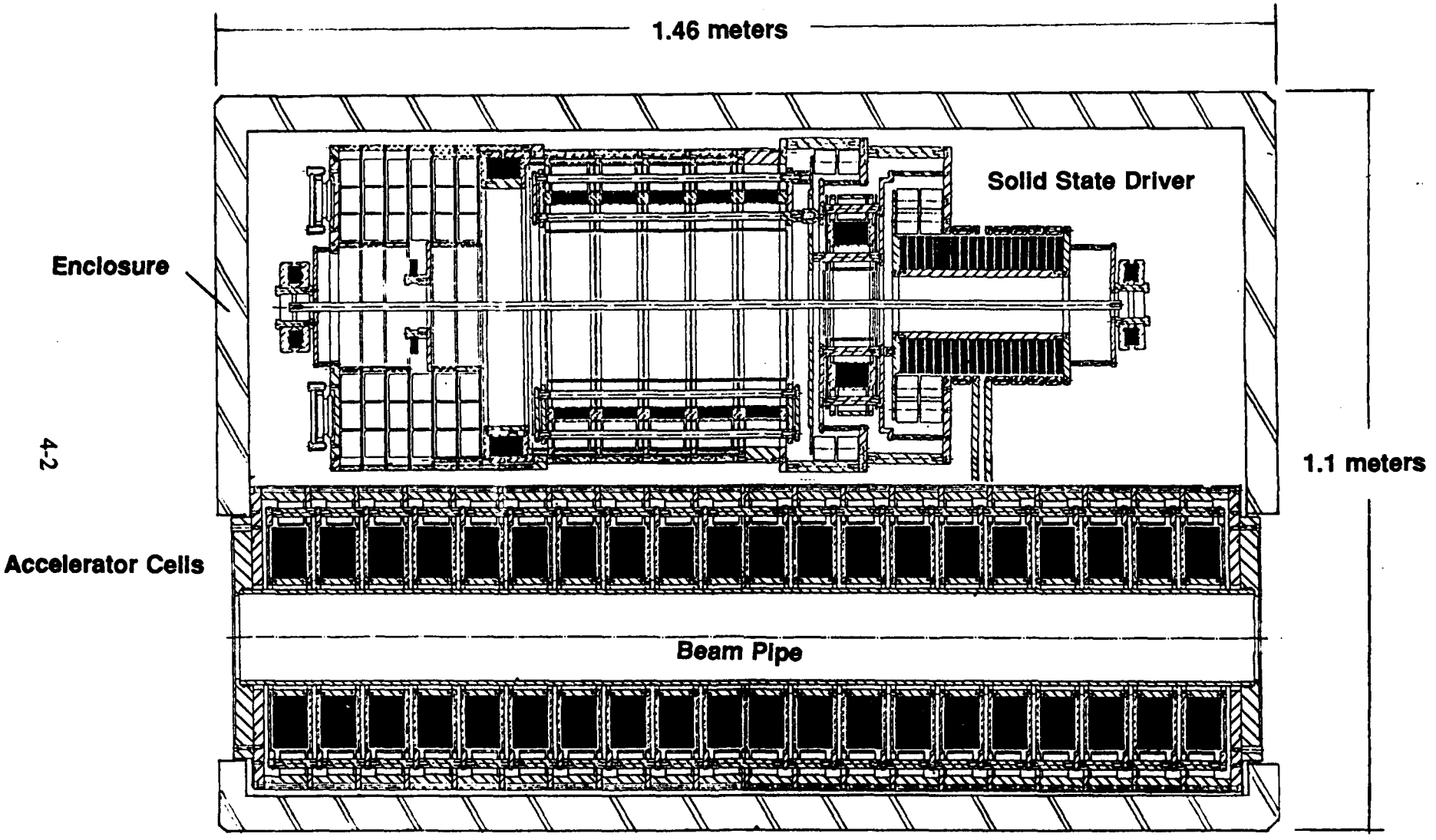

Figure 4.1: SNOMAD-IV 1.0 MeV accelerator module

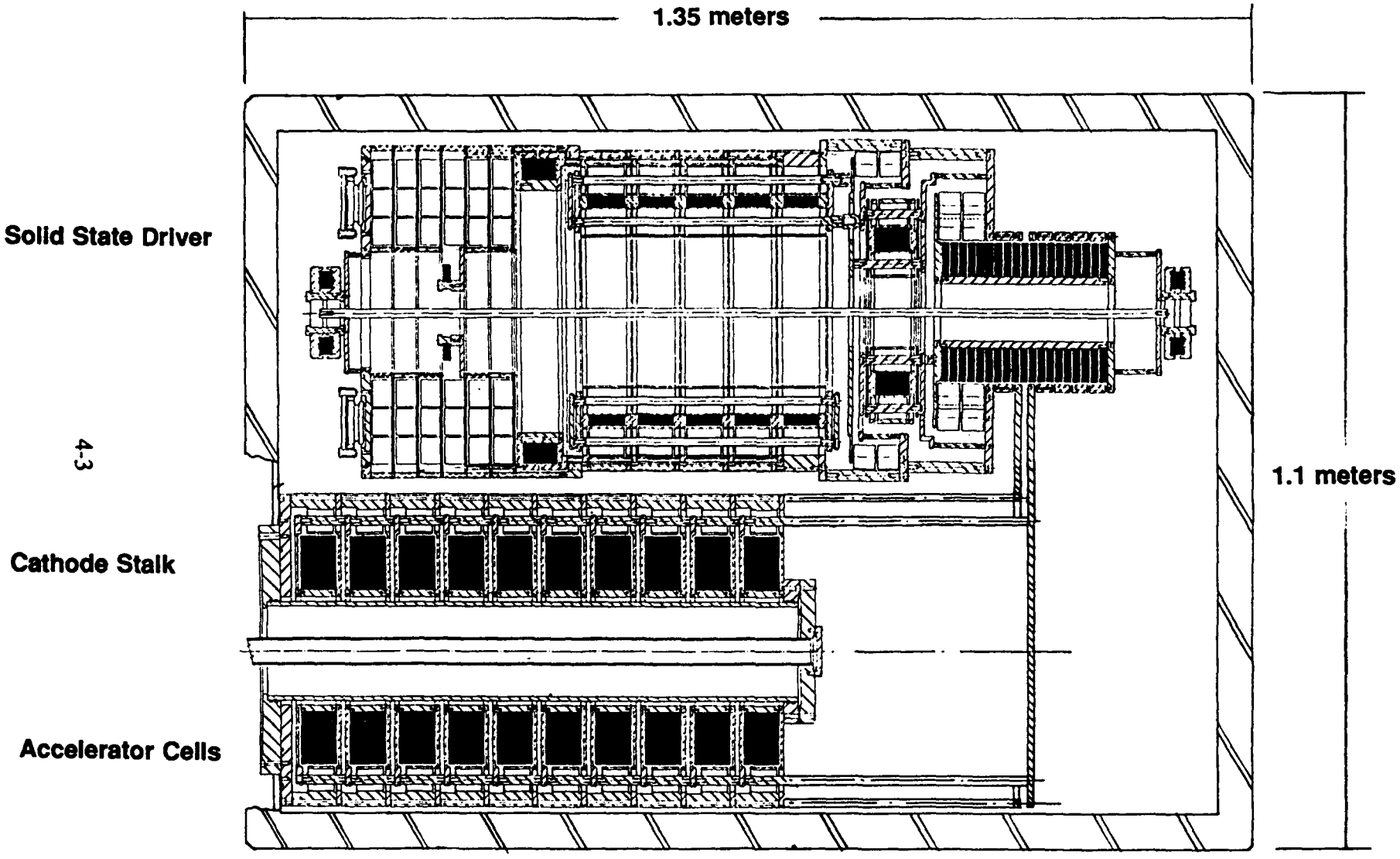

Figure 4.2: SNOMAD-IV 0.5 MeV Electron injector module

Table 4.1: Summary of SNOMAD-IV Accelerator Design Parameters

Beam Energy	1.0 MeV
Beam Current	600 amp
Pulse Length	50 nsec
Pulse Repetition Rate	20 kHz
Single Pulse Energy	30 joules
Voltage per Cell	50 kV
Accelerating Gradient	0.68 MeV/meter
Pipe Radius	12.7 cm
Gap Field Stress	90 kV/cm

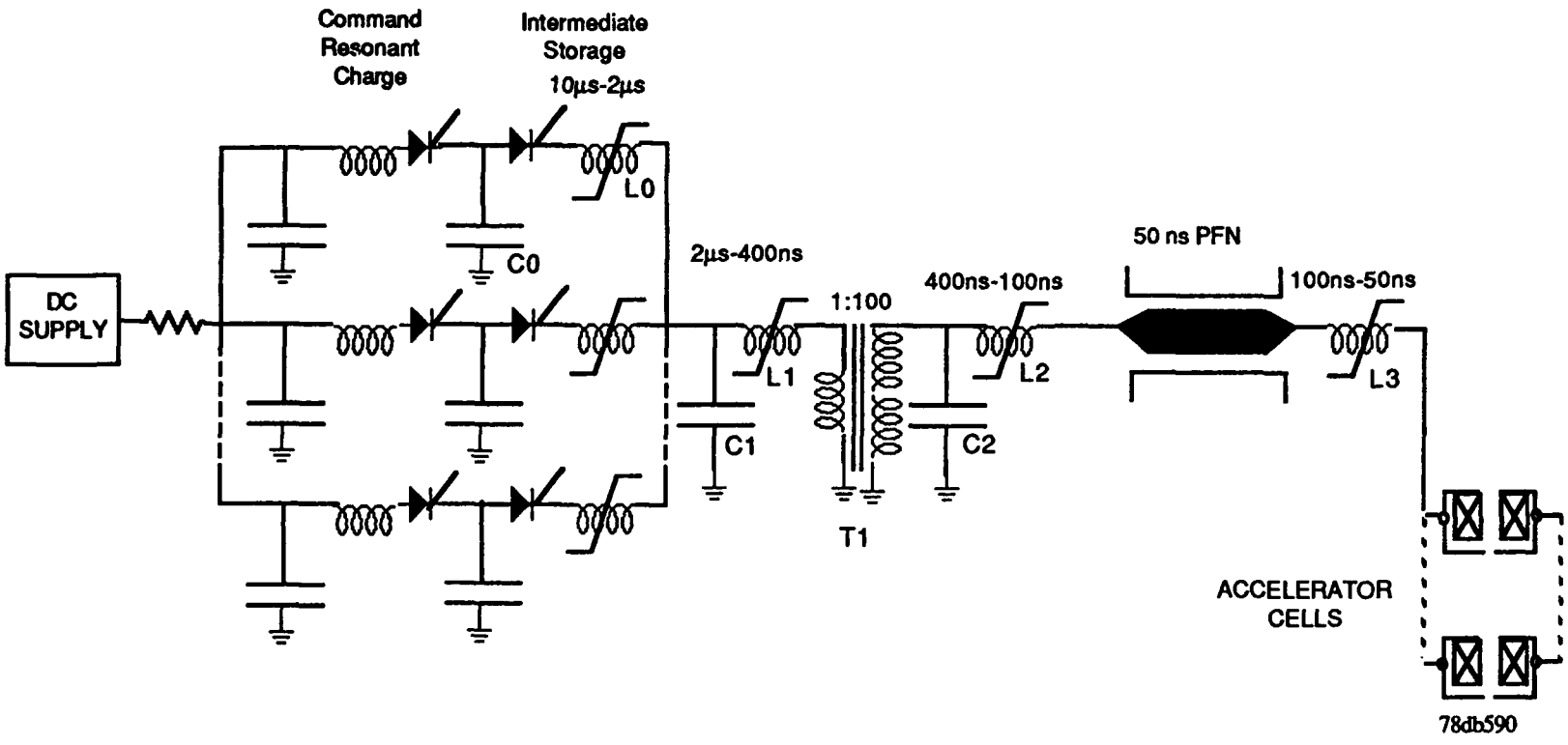

Figure 4.3: Electrical schematic of SNOMAD-IV solid-state driver

aluminized polypropylene capacitors are utilized in the first energy storage stage, C_1. These capacitors are coupled via a low inductance bussing network to a metglass saturable inductor, L_1. L_1 is designed so that saturation occurs following the termination of the 2 μsec charging pulse. Once saturated, the energy stored in C_1 is discharged into the primary of a 1:100 step-up pulse transformer, T_1, in 400 ns thereby achieving a temporal compression of 5. This results in a corresponding increase in the peak power level.

The secondary of T_1 charges a bank of strontium titanate capacitors, C_2, to 100,000 volts. T_1 and the second stage compression inductor, L_2, both utilize metglas cores. Metglas is a silicon-iron alloy, developed by Allied Chemical Co, with a resistivity that is three times higher than most ferro-magnetic materials. L_2 has a charging time of 400 ns and a discharge time of 100 ns. This is the last stage in the compression chain where metglas can be employed. A saturation time of less than one microsecond results in excessive losses due to eddy currents. The second stage inductor, L_2 feeds a 50 ns pulse forming network (PFN) to 100 kV in 100 ns. Input coupling to the PFN is accomplished at its electrical midpoint which allows for charging twice as fast as could be accomplished by coupling to either end. However, if the charging time becomes too short with respect to the output pulse length, remnants of the charging waveform can appear on the output pulse as voltage fluctuations. The output inductor stage, L_3, is a ZnNi ferrite saturable inductor which delivers the 50 kV pulse to the output transmission line. L_3 has been carefully designed to take advantage of the high dielectric constant ($\epsilon_r \approx 12$) of the ferrite. This single turn compression stage operates to some extent as a shock line. Once saturated, the ferrite forms the medium for a transmission line with an impedance close to that of the PFN.

Special care has been taken in the design of SNOMAD-IV to minimize the saturated inductance of the compression reactors L_1, L_2 and the transformer windings of T_1. The ferrite core volume, required to obtain a given temporal compression, τ_c, in a nonlinear magnetic pulse compression stage is proportional to the square of the saturated inductance.

$$\mathcal{V}_{ferrite} = \tau_c^2 E \frac{\mu_o \pi^2}{4 B_{sat}^2 P_f^2}$$

where B_{sat} is the available flux swing of the ferrite, P_f is the packing factor and E is the single

pulse energy. The packing factor is defined as the ratio of the ideal toroidal inductance to the actual device inductance including stray inductance. It is essential to minimize the core volume if efficient operation is to be achieved since the energy lost in the compression reactor scales linearly with the core volume.

The SNOMAD-IV accelerator cell design is shown in Fig. 4.4. This design has been optimized for accelerating beam currents of 1 kA or less with pulse durations of 50 to 100 nsec. Each cell utilizes a metglas core measuring 6.75 inches I.D. by 12.75 inches O.D. by 2.0 inches in length. The cells are fed by a common bus which supplies 50 kV of drive from the SNOMAD-IV driver. Several innovative features have been incorporated into the mechanical design of the accelerator cell assembly to simplify the construction and lower its cost. In the injector accelerator cells, a quartz tube separates the evacuated beam pipe from the freon or oil filled accelerator gap and core region of the cell. In conventional accelerator cell designs, the gap and core winding are placed in the high vacuum region shared by the beam. This requires that these materials have ultra-high vacuum compatibility and that the electric field strengths be maintained below the vacuum break-down limit. Isolating these materials from the vacuum permits less expensive materials to be utilized and allows an insulating dielectric liquid to fill the high field gap region. The induction cells used in the 1 MeV accelerating modules will use more conventional ceramic alumina rings to provide the vacuum interface in the accelerator gap region (e.g. Fig. 1.4).

An induction cell is a high impedance transmission line transformer filled with ferrimagnetic or ferromagnetic materials with the electron beam forming the single turn secondary winding. The e-beam gains energy equal to the drive voltage as it passes through each cell and appears as a resistive load in parallel with the accelerator cell impedance.

If the accelerator is to be efficient, the losses in the accelerator core must be negligible in comparison to the energy coupled into the electron beam. This requires that the characteristic impedance of the transmission line, Z_{line}, which forms the cell must be large compared to the impedance of the beam, $Z_{beam} = V_{line}/I_{beam}$. Typically, vacuum filled accelerator cell has a characteristic line impedance, Z_{line}, of less than 100 ohms.

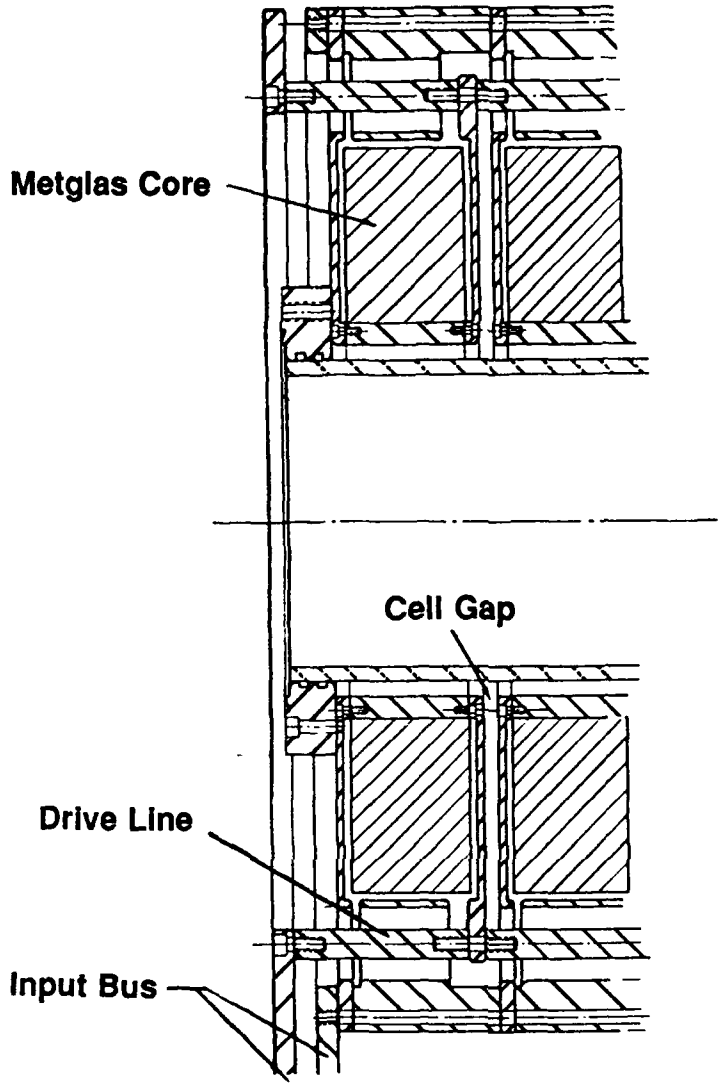

Figure 4.4: SNOMAD-IV accelerator cell

The impedance of an accelerator cell can be increased significantly by one of two methods: by filling the cell with a high permeability, low permittivity material, $(\mu_r/\epsilon_r)^{1/2} > 1$ or operating the cell as a resonant transmission line. The disadvantage of resonant structures is that the cavity is never resonant with a single mode. Wake fields produced by the electron beam can feed energy into spatially antisymmetric modes which can steer the beam electrons off axis. This sets an upper limit to the total charge which can be accelerated during an rf cavity decay time.

An induction cell is a non-resonant transmission line and, if properly designed, stores neither the drive fields nor the beam wake fields. This dramatically increases the practical operating e-beam current of the induction cell over that of the rf resonant cavity. However, it also constrains the minimum efficient operating current. Induction linacs which provide short pulses ($\leq$ 50 ns), are usually filled with ferrimagnetic material (ferrite) to increase the impedance of the cell; for long pulses (50 nsec $\leq \tau_p \leq$ 1 μsec) ferromagnetic materials such as Si-Fe, metglas, or superpermalloy are employed. Most high frequency ferrites have dielectric constants of order $\epsilon_r \simeq 10$ and permeabilities of order $\mu_r \simeq 1000$. With ferrite as a medium, the characteristic transmission line impedance is increased over the vacuum value by a factor of $(\mu_r/\epsilon_r)^{1/2} = 10$, yielding an effective shunt impedance as high as several hundred ohms. The use of ferrite also shortens the required physical length of the transmission line since the group velocity, $v_g = c/(\mu_r\epsilon_r)^{1/2}$, in a ferrite filled transmission line is decreased by 100 fold.

The design of an induction accelerator cell is governed by the basic operating principles discussed above. Referring to Fig. 1.4, the length (h) of the ferrite loaded transmission line is determined by the pulse length and the electrical characteristics of the ferrite.

$$2h \geq \tau_p \frac{c}{\sqrt{\epsilon_r \mu_r}} \approx \frac{\tau_p c}{100} \qquad (1)$$

In practice, the best performance is achieved by setting $h = \tau_p$ c/100, thereby setting the line length equal to a single transit time rather than a round trip time. The reason is that ferrite properties are field dependent and the minimum ferrite volume is achieved by designing for a single transit time. However, the additional size and cost of achieving this improvement in

performance may not be required. Making h longer than a transit time has no benefit since the additional ferrite will not be used during the pulse.

The radial dimensions of the of the ferrite $(r_o - r_i) = \Delta R$ is set by the drive voltage and the maximum flux swing available in the ferrite. The ferrite must not be permitted to saturate as the wave generated by the drive pulse is transmitted down the line. The magnetic flux density, **B**, in the ferrite is related to the drive voltage, V_{cell}, and cross sectional area of the ferrite, A, by the following relationship

$$V_{cell} = \oint \mathbf{E} \cdot dl = -\frac{d}{dt} \int_A \mathbf{B} \cdot d\mathbf{A}$$

$|\ \mathbf{B}\ |$ must be maintained below the saturation flux density, B_{sat}, of the ferrite. Thus, the minimum size of the ferrite which fills the accelerator cell must then satisfy the relationship

$$V_{cell} < B_{sat}\, v_g\, r_i \ln\left(\frac{r_0}{r_i}\right) \tag{2}$$

Typically, $B_{sat} \simeq 0.6$ Wb/m^2.

The beam pipe radius, R_{pipe}, is determined by three competing requirements: reducing growth of the beam break-up instability; designing for high shunt impedance; and designing for minimum cost and weight of the accelerator cell.

The beam break-up (BBU) instability arises from the excitation of azimuthally asymmetric cavity modes in the accelerator cell. These modes are characterized by asymmetric longitudinal electric fields and transverse magnetic field on axis which cause sweeping of the electron beam tail. This instability sets the minimum pipe radius and is therefore critical in determining the cost of the accelerator cells. The radial displacement of the beam, ξ, resulting from the beam break up instability depends on the pipe radius, R_{pipe}, gap width, w, total accelerating voltage, V_{acc}, beam current, I_{beam}, gap electric field, E_g, and focusing magnetic field, B.

$$\xi \propto exp(I_{beam} w \Psi V_{acc} / B E_g R_{pipe}^2)$$

The quantity Ψ depends on the beam interaction with the TM_{1n0} beam break-up modes of the accelerator cell. The beam interaction with the cell must be minimized by reducing the beam

coupling to the cell and lowering the Q of the cavity. This is accomplished by insuring that the beam induced fields are coupled out of the cell via the accelerator gap and damped in the ferrite. If a ceramic interface is used its angle is also chosen so that all TM modes excited by the beam will pass through the ceramic into the ferrite. To preserve beam quality and insure good transmission of the beam through the accelerator, an overall amplification of beam displacement due to BBU of less than five must be maintained.[4]

In theory it should be possible to offset the effects of a small beam pipe diameter by arbitrarily increasing the focusing magnetic field. In practice, however, as the focusing field is increased to suppress beam break-up, the number of betatron wavelengths in the accelerator increases. This leads to cork screwing and increased beam break-up excitation. Tuning becomes more complicated as the radial position of the beam becomes a rapidly oscillating function of time.

The operating current, total accelerator voltage, and pulse length of an induction linac are usually restricted by the requirements of the microwave generation device. However, the accelerator cell gap voltage remains an unspecified parameter. The accelerator gradient is linearly proportional to the gap voltage and, therefore, designing for a high gap voltage yields the shortest accelerator. However, the accelerator weight and cost increases rapidly with increasing acceleration gradient. The coupling coefficient (defined as the fraction of electrical pulse energy deposited in the beam) is independent of the gradient and therefore the only penalty paid for reducing the accelerating gradient is an increase in overall length of the accelerator. Additionally, for constant BBU growth the accelerator weight and cost increase exponentially with $I_{beam}^{1/2}$. These design considerations are discussed in detail below.

The coupling coefficient, K, for an induction accelerator cell is found by computing the shunt impedance, $Z_{shunt} = Z_{line}$, of the ferrite filled transmission line and the load imposed by the e-beam, Z_{beam},

$$K = \frac{Z_{shunt}}{Z_{beam} + Z_{shunt}}$$

where

$$Z_{shunt} = \frac{1}{2\pi}\sqrt{\frac{\mu}{\epsilon}}\ln\left(\frac{r_o}{r_i}\right)$$

$$Z_{beam} = \frac{V_{cell}}{I_{beam}}$$

Under the assumption that the cell gap voltage is related to the minimum ferrite radius by Eq. (2), the shunt impedance and coupling coefficient can be written,

$$Z_{shunt} = \frac{1}{2\pi}\mu\frac{V_{cell}}{B_{sat}r_i}$$

$$K = \frac{1}{1 + \frac{2\pi B_{sat} r_i}{\mu I_{beam}}}$$

A plot of K versus ferrite core inner radius, r_i, for several beam currents from 1 kA to 5 kA is shown in Fig. 4.5. The coupling coefficient increases with increasing beam current and decreasing inner radius.

The total cost and weight of the accelerating structure is linearly proportional to the volume of the ferrite core, $\mathcal{V}_{ferrite}$

$$\mathcal{V}_{ferrite} = \frac{V_{acc}}{V_{cell}} h\,\pi(r_o^2 - r_i^2) \tag{3}$$

Using Eq. 2 to solve for r_o in terms of V_{cell} and B_{sat} and substituting into Eq. 3 yields

$$\mathcal{V}_{ferrite} = \frac{V_{acc}}{V_{cell}} v_g \tau_p \pi r_i^2 \left(\exp\left(\frac{2V_{cell}}{B_{sat} v_g r_i}\right) - 1\right) \tag{4}$$

The ferrite core volume required per MeV of acceleration is plotted as a function of accelerator cell gap voltage for several accelerator cell inner radii, r_i. For large values of the exponential argument in Eq. 4, the ferrite core volume increases exponentially with gap voltage. For a specified gap voltage, there exists an inner radius, r_i, which yields the smallest ferrite core volume according to Fig. 4.6. Likewise, we can see that the minimum ferrite core volume required is achieved by operating with the lowest possible gap voltage. Other constraints (i.e. restricting the overall length of the accelerator) may restrict the gap voltage to be larger than some minimum value. Figures 4.5 and 4.6 show that designing for the smallest inner core radius

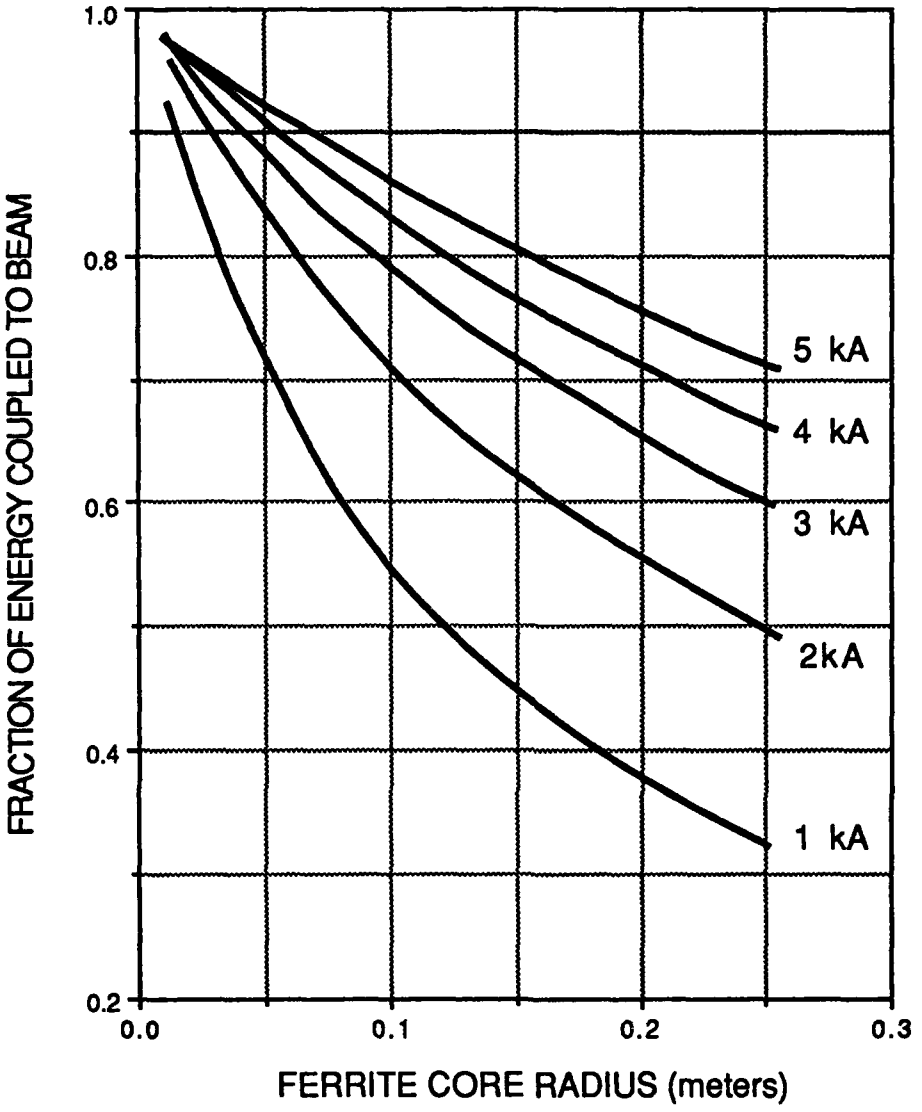

Figure 4.5: Coupling coefficent, K, versus ferrite core inner radius for beam currents from 1 to 5 kA. Ferrite parameters: $\mu_r = 400$, $\varepsilon_r = 12$.

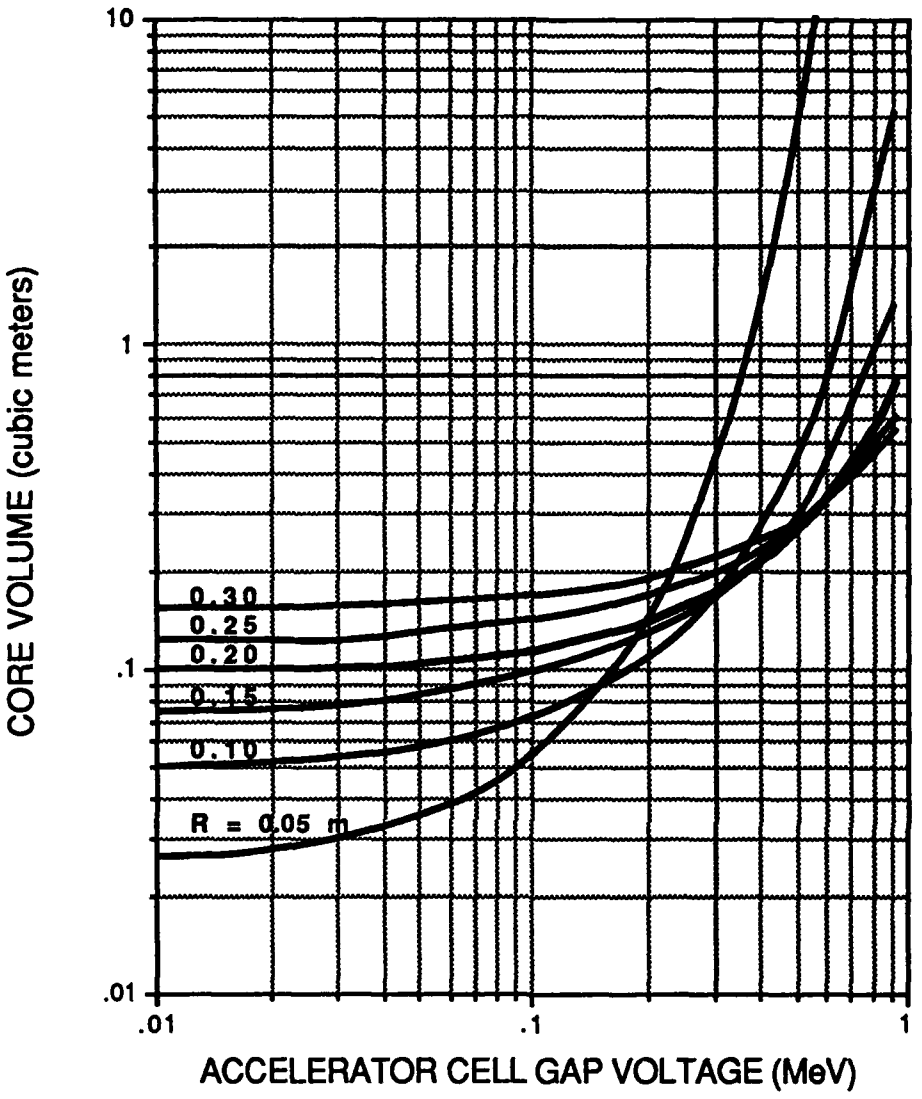

78db590

Figure 4.6: Required ferrite core volume, $v_{ferrite}$, versus accelerating gap voltages for r_i = 0.05, 0.10, 0.15, 0.20, 0.25, 0.30 meters. Ferrite parameters: $\mu_r = 400$, $\varepsilon_r = 12$, $\tau_p = 50$ nsec.

and lowest gap field will always yield the most economical design. However, arbitrarily reducing these parameters at fixed beam current will result in the onset of the beam break-up instability.

4.1 Cost Optimization of the SNOMAD-IV Design

The principle impetus behind the SNOMAD-IV design is cost optimization of the induction accelerator. The goal is to achieve this without any degradation in operating performance. We feel we have realized this in the SNOMAD-IV accelerator module.

The induction linac is modular in construction, as shown in Fig. 4.7. A series of several identical accelerator cells are driven in parallel by a pulsed power drive module which provides short duration high voltage pulses to each of the accelerator cells at a high repetition rate. The pulsed power drive modules comprise a command resonant charge power supply, intermediate storage power supply, and nonlinear magnetic pulse compression modules.

Barletta[1] and Birx[2] have examined the costs of each of these subsystems in terms of several accelerator design and performance parameters: voltage flux swing of the accelerator cells, accelerating gap field stress in the accelerator cells, micropulse energy, average power, accelerator gradient, and inner and outer radii of the accelerator cell. Minimum cost is achieved when the micropulse energy, is made as small as possible and the physical size of the accelerator cells is minimized. Since the average beam power is directly related to the micropulse energy by the repetition rate, $P_{avg} = fE_{pulse}$, the lowest cost design is achieved in a when the repetition rate is maximized thus, minimizing the single pulse energy. This design philosophy is especially cost effective when utilizing SCR commutated pulse compression power supply modules. The fabrication cost of such a module is almost independent of repetition rate (average power). Generally, the cost of fabricating a low repetition rate pulse compression circuit utilizing SCRs is greater than an equivalent thyratron design since the lower working voltage of the SCR requires additional compression stages. However, for high repetition rate applications, multiple thyratron arms are required, offsetting any initial savings. This is illustrated in Fig. 4.8. The estimated costs, normalized to peak power, (k$/MeV-kiloamp) of three driver designs versus repetition rate are shown. Two of the drivers, the SNOMAD-I and SNOMAD-II, are SRL solid state

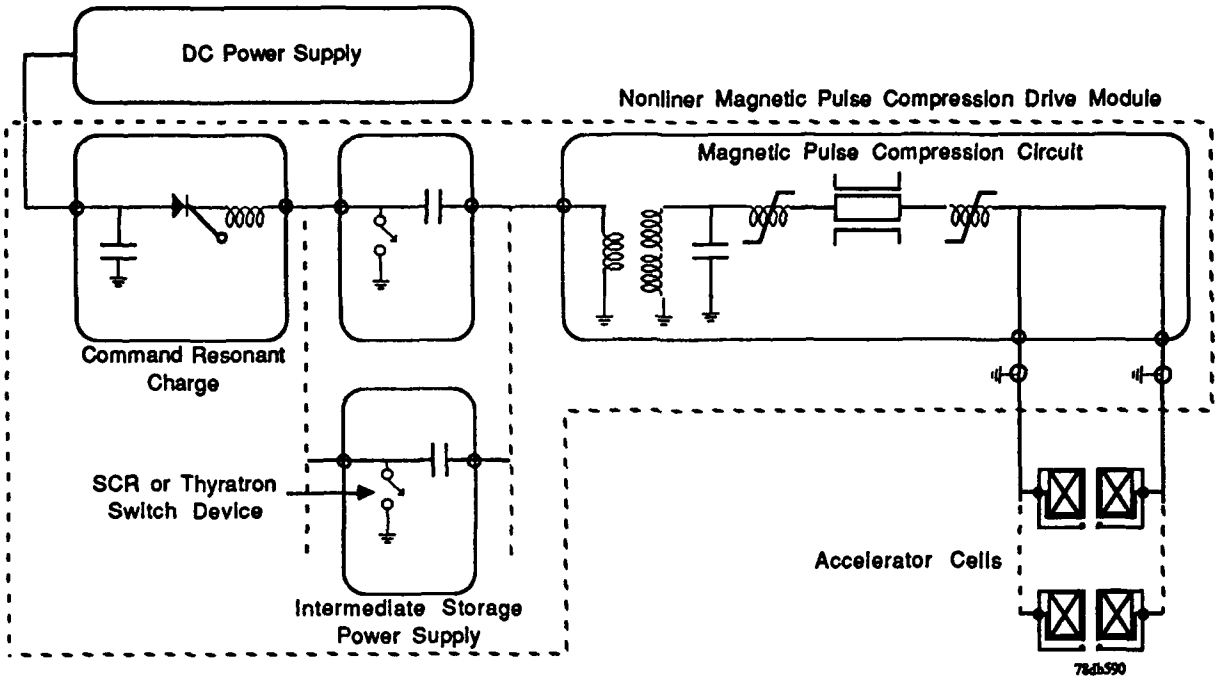

Figure 4.7: Schematic of an induction linac showing pulse power components and induction cells.

designs. The MAG-I-D, a Lawrence Livermore National Laboratory design, currently in use on the ETA-II accelerator utilizes a thyratron intermediate storage power supply. The normalized costs of the SNOMAD-I and SNOMAD-II drivers are lower than the MAG-I-D for repetition rates greater than 4 kHz and 2.5 kHz respectively. The SNOMAD-I and SNOMAD-II designs have maximum operating repetition frequencies of 100 kHz and 20 kHz respectively.

The costs for these drivers, normalized to average power (k$ /MW), are illustrated in Fig. 4.9. The cost per megawatt of average power is plotted as a function of repetition rate up to their maximum operating frequency for each of the three drivers. The maximum repetition rate is set by one of three design limitations: cooling of the ferrite, reset time of the ferrite, or recovery time of the SCRs or thyratrons. When compared at their respective maximum operating repetition frequencies, the SNOMAD-I represents a 14 fold reduction in cost per megawatt compared to the MAG-I-D, and the SNOMAD-II represents a 4.5 fold reduction in cost.

The induction accelerator cells often constitute greater than 50% of the total cost of the linac. A cross sectional drawing of an induction accelerator cell is shown in Fig. 4.10. The cost of the accelerator cell is dictated by the cost of the ferrite plus the cost of the cell block housing. Costs increase proportionally with the volume of ferrite and the volume of the cell block housing. Three competing requirements determine the inner and outer radii of the accelerator cells: reducing the growth of the beam break-up instability, maximizing the shunt impedance of the ferrite filled accelerator cell, and satisfying the required magnetic flux swing for the drive voltage and pulse length. These requirements are discussed in detail in Section 2.1. Although the peak operating current may be dictated by the requirements of the microwave generation device, a substantial cost savings in accelerator fabrication can be realized by designing for peak currents of 0.5-1.0 kamps as compared with 1.0-4.0 kamps for the ETA II accelerator. The advent of very high repetition rate pulse compression accelerator drivers permits operation at these reduced peak current levels without a reduction in delivered beam power.

A detailed cost analysis of the components and subassemblies which comprise the SNOMAD-IV accelerator is provided below. These costs are based on actual fabrication costs of the

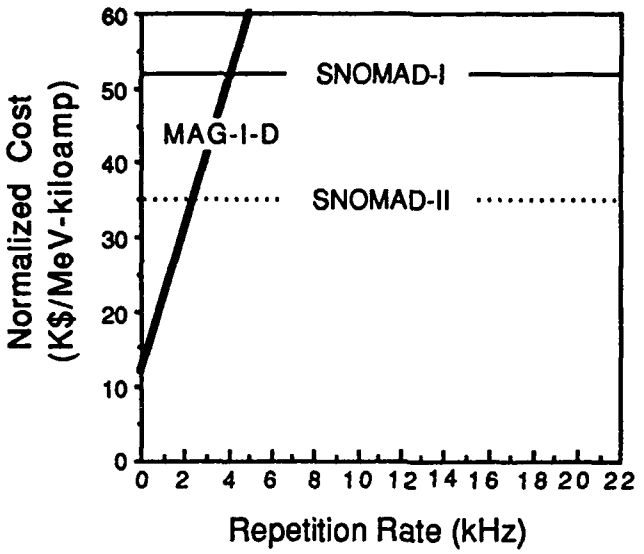

Figure 4.8: Cost of SCR (SNOMAD-I, II) and thyratron (MAG-I-D) pulse power systems normalized to peak e-beam power.

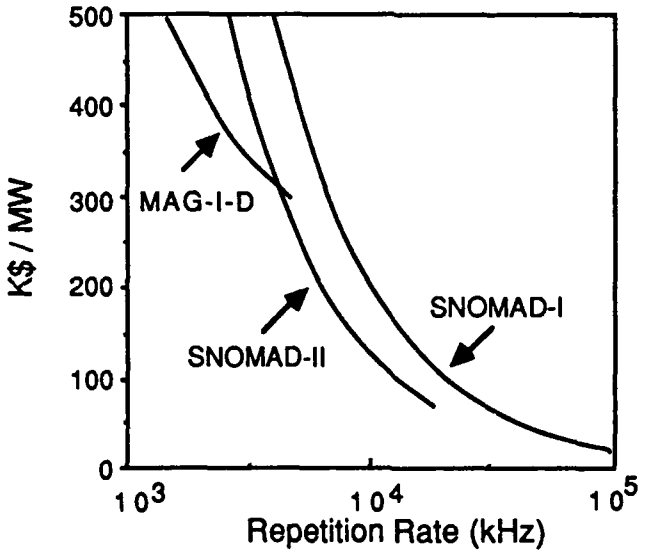

Figure 4.9: Cost of SCR (SNOMAD-I, II) and thyratron (MAG-I-D) pulse power systems normalized to average power.

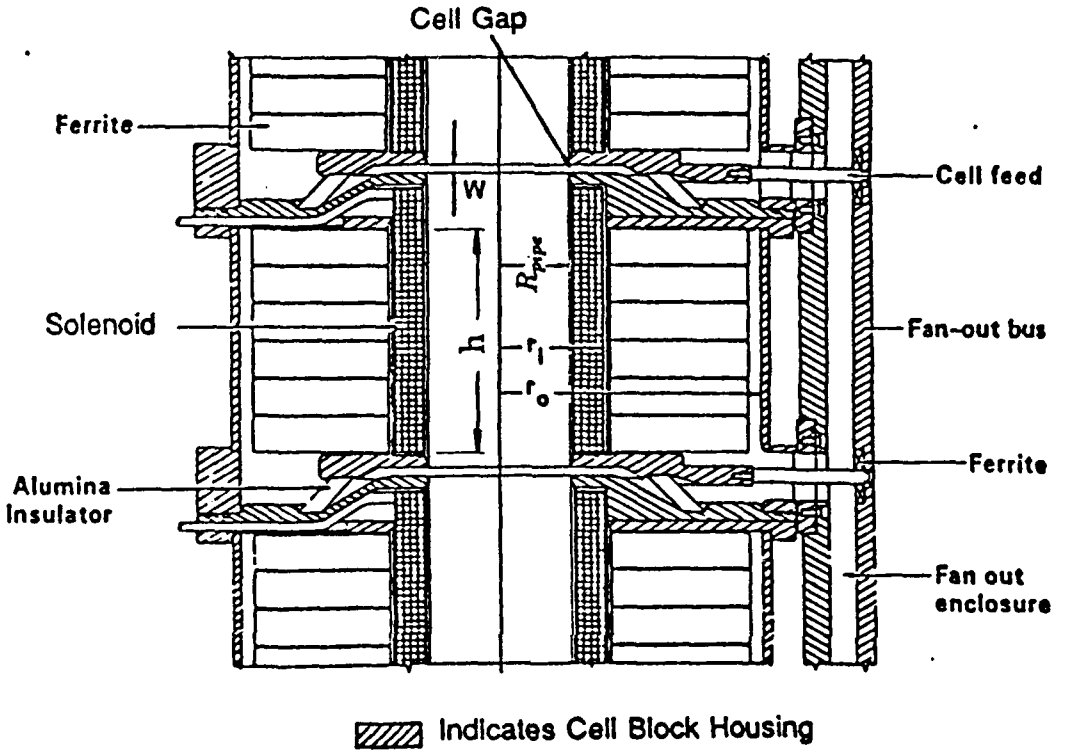

Figure 4.10: Cross sectional drawing of induction accelerator cell

SNOMAD-IV accelerator module.All components are commercially available or can be fabricated using standard CNC machine tools. The cost of supplying the prime power to the SNOMAD-IV driver is not included. Prime power in the form of 1.1 MW @ 500 volts DC is required to operate at full output.

SNOMAD-IV Fabrication And Assembly Costs

Mechanical Parts Fabrication	
SNOMAD-IV Driver	$39,010.
SNOMAD-IV Acc. Cells	$31,650.
Enclosure	$13,105.
Misc.	$11,130.
Bias Power Supply	$8,500.
Timing system	$6,577.
Metglas	$1,500.
Ferrite	$4,320.
Capacitors	$10,080.
SCRs	$2,560.
Vacuum System	$14,600.
Cathode	$4,100.
Assembly	$5,000.
Total	$152,132.

The self contained accelerator module is comprised of an all solid state nonlinear magnetic pulse compression driver, twenty accelerator cells, vacuum system and enclosure. The SNOMAD-IV accelerator will be designed to operate at a continuous pulse repetition rate of up to 20 kHz, for several seconds, e-beam energy of 1 MeV, e-beam current of 600 A, and pulse duration of 50 nsec. Following completion of the construction and testing phase of the program, the accelerator will be installed at the MIT Plasma Fusion Center where it will be available to support spin-off technologies such as ECH RF source development. This provides feedback as

to just how user-friendly the SNOMAD-IV design is and allows SRL to modify the design in order to optimize its performance in an actual operating environment. This is essential if SDIO were to deploy large numbers of these modules in an accelerator somewhere in the middle of the desert with a nonspecialized operating crew.

An assembly drawing of the SNOMAD-IV driver is shown in Fig. 4.11 and Fig. 4.12. and an electrical schematic is shown in Fig. 4.13. Five hundred volt DC power enters through the eight command resonant charge SCRs which are mounted on the left deck of the driver assembly. Eight Intermediate storage SCRs are mounted in reverse polarity from the same deck. The number of SCRs has been chosen so that the dI/dt rating of each device is not exceeded. The saturable inductors, labeled L_0, isolate the branches of the intermediate storage power supply. These are all wound from a common toroidal core which is mounted on the first compression stage capacitor bank, C_1. The first stage saturable inductor, L_1, is single turn design which will utilize a 0.6 mil toroidal metglas core. The discharge of C_1 through L_1 and T_1 to C_2 results in a 5 to 1 temporal compression with a voltage gain of 100. The 1:100 step-up transformer will be wound on four metglas toroidal cores. The design achieves a large step-up ratio with a twenty five turn secondary and fractional, one quarter turn, primary made possible by the use of four transformer cores.

In the second compression stage, high voltage strontium titanate ceramic capacitors, C_2, will be used. Unlike barium titanate, strontium titanate does not suffer from piezoelectric mechanical failure under high repetition rate operation. The second stage saturable inductor, L_2, will be a ten turn toroidal inductor wound on a 6.75 inch I.D. X 9.65 inch O.D. X 2 inch wide core. L_2 discharges C_2 into a pulse forming network with a electrical length of 25 nsec. The PFN is a hybrid design consisting of lumped capacitors and distributed inductance. This permits the design to be significantly more compact than either a water filled transmission line or a lumped PFN and allows the electrical length to be varied by the addition of capacitive elements. The output saturable inductor, L_3, serves as a passive high speed switch to discharge the PFN into the accelerator cell load. L_3 will be constructed using nineteen toroidal ferrite pancakes. A

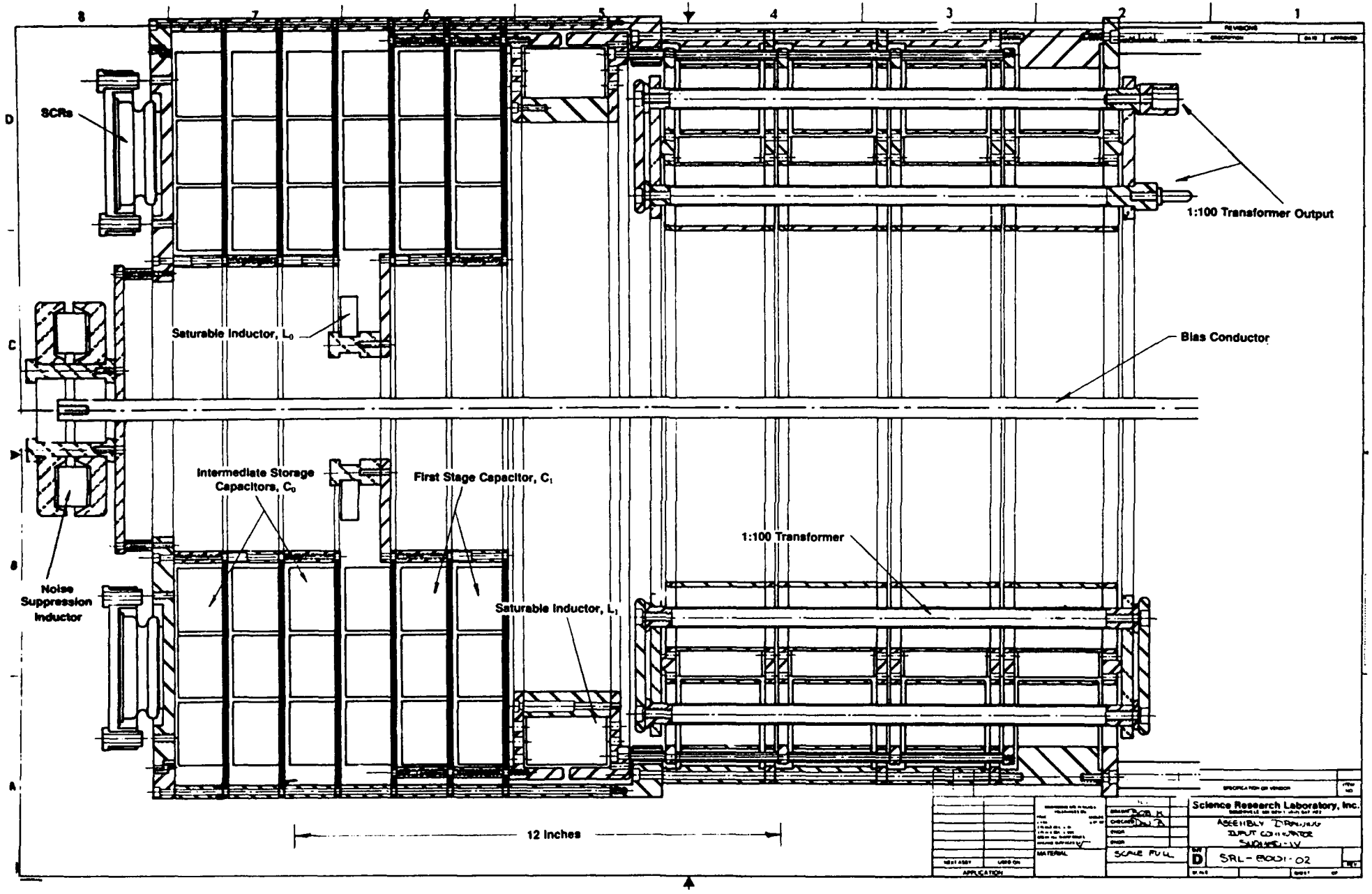

Figure 4.11: Assembly drawing SNOMAD-IV input commutator arms, first compression stage and step-up transformer.

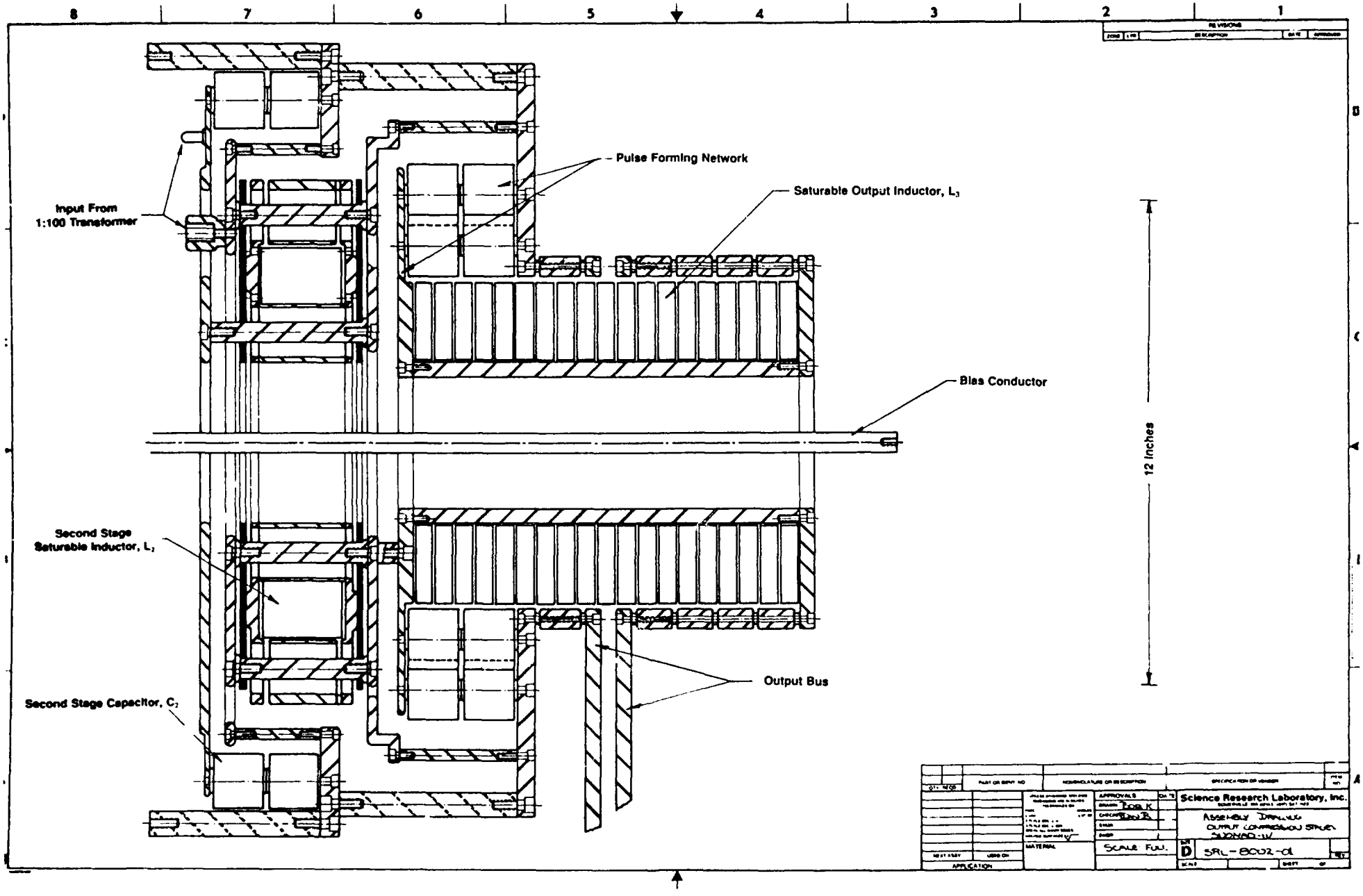

Figure 4.12: Assembly drawing of SNOMAD-IV second compression stage, PFN and output stage.

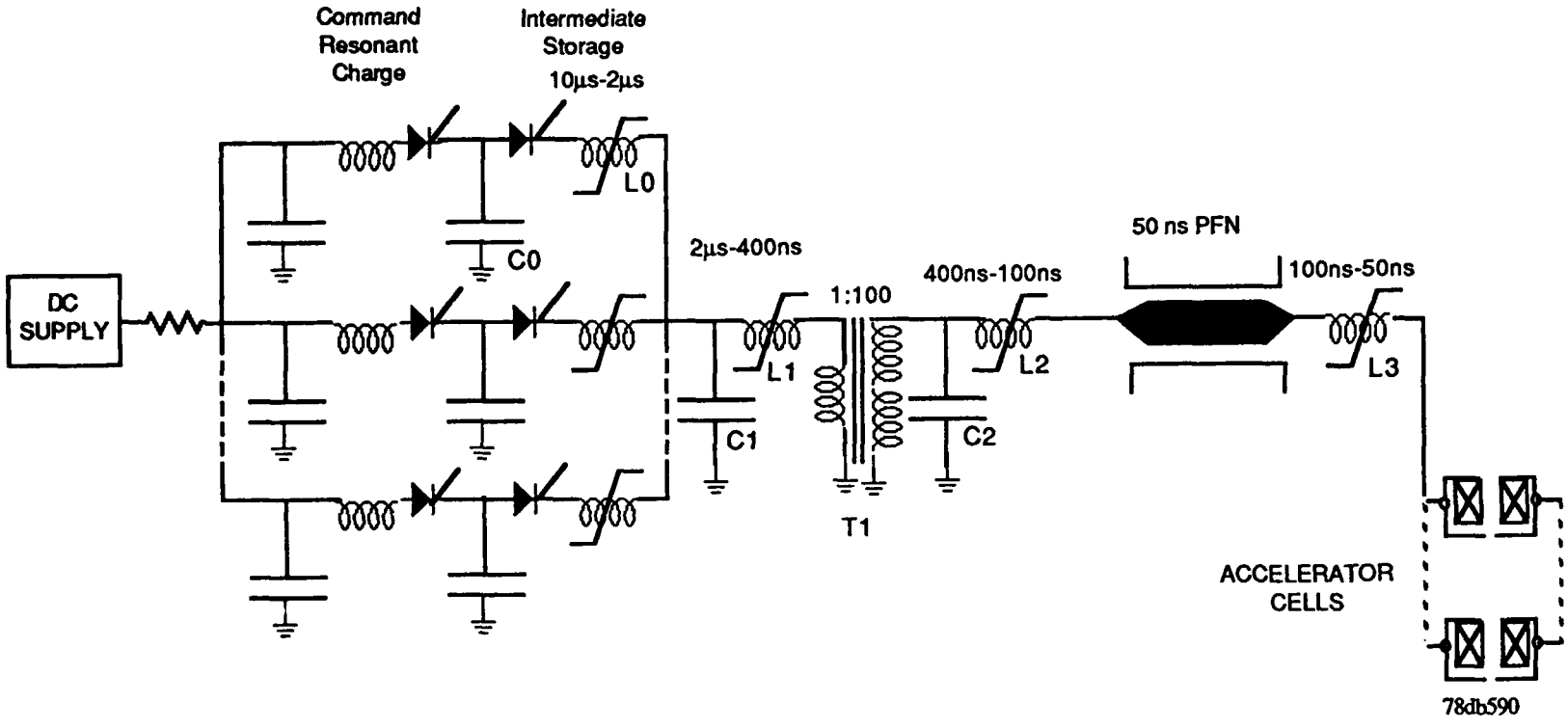

Figure 4.13: Electrical schematic of SNOMAD-IV solid-state driver

zinc-nickel ferrite has been selected for the output stage to minimize losses and provide fast switching.

A bias conductor, placed on the axis of the driver, will be used for biasing the metglas and ferrite inductor cores into saturation and to provide the reset current between pulses. Both ends of the bias conductor will be terminated with a powdered iron core noise suppression inductor. This prevents electrical noise, generated inside the driver, from being transmitted out along the bias conductor. The assembled driver will be 20 inches in diameter and an overall length of 44 inches. Table 4.2 summarizes the design specifications of the SNOMAD-IV driver.

The SNOMAD-IV driver is capable of powering a 1.0 MeV accelerator cell assembly or a 0.5 MeV injector assembly as described above. Both will utilize metglas core induction cells. An assembly drawing of the injector showing the induction cells, drive line, cathode stalk and input bus from the driver is shown in Fig. 4.14. For obvious reasons the first SNOMAD-IV module has been configured as an injector. Some consideration was given to using the SNOMAD-II accelerator as the injector for the first tests and configuring the initial SNOMAD-IV modules as a 1.0 MeV accelerator. This has not been ruled out in the future as the existing SNOMAD-IV module can be so modified. It was deemed more advantageous for the first tests to minimize the interference with the SNOMAD-II operating schedule. The SNOMAD-II accelerator is being used by MIT for a wide array of experiments and it was felt inconsiderate to unnecessarily interrupt their planned schedule.

Ten induction cells make up the SNOMAD-IV injector. Each cell uses a metglas core measuring 6.75 inches I.D. X 12.75 inches O.D. X 2 inches wide. The choice of metglas over ferrite was chosen as a core material for several compelling reasons. The saturation flux density of metglas is a factor of five times higher than nickel-zinc ferrites, allowing a significantly more compact design. In addition, a significant cost savings is realized by using metglas and large toroidal cores are more easily fabricated than ferrite cores. The primary disadvantage of a metglas filled induction cell design are limitations imposed by its electrical pulse performance characteristics. A metglas filled cell exhibits characteristics which are inductive rather than

Table 4.2: SNOMAD-IV Driver Design Specifications

Input Power Requirements:	
Energy/Pulse:	55 Joules
PRF:	20 kHz
Power:	1.1 MW
Voltage:	500 Volts
Current:	2200 Amps
Intermediate Storage:	
Capacitance:	110 μfd
Voltage:	1000 Volts
Energy:	55 Joules
Stored Charge:	0.11 Coulombs
τ Discharge:	≤ 7.0 μsec
I Peak:	16.8×10^3 Amps
dI/dt:	7.55×10^3 A/μsec
I_T (RMS):	2081 Amps
dI/dt per device:	943 A/μsec
Commutation Losses:	1.5 Joules
1st Stage:	
Capacitance:	110 μfd
Voltage:	980 Volts
Energy:	52.8 Joules
Core Type:	0.6 Mil 2605 CO Metglas
Number of Turns:	1
Core Geometry:	1 x 15.5" ID x 18" OD x 2" Wide
∫V•dt:	4×10^{-3} Vsecs
Lsat:	1.988 nH
τ Discharge:	857 nsec
Losses:	~ 0.975 Joules
Transformer:	
Core Type:	2605S3A Metglas
Number of Turns (Prim.):	1/4
Number of Turns (Sec.):	25
Losses:	≤ 0.5 Joules
Peak Stress:	68.25 kV/cm
Core Geometry	5 x 12" ID x 13.5" OD x 2" Wide
2nd Stage:	
Capacitance:	11.3 nfd
Voltage:	95.25 kV
Energy:	51.3 Joules
Core Type:	2605 SC Metglas
Core Geometry:	6.75" ID x 9.65" OD x 2" Wide
∫V•dt:	2.85×10^{-2} Vsecs
Lsat:	0.474 μH
τ Discharge:	138 nsec
Losses:	1.05 Joules
Output Stage:	
Capacitance:	11.8 nfd
Voltage:	92.31 kV
Energy:	50.25 Joules
Core Type:	CMD55005 Ferrite
Core Geometry:	18 x 4" ID x 8" OD x 0.5" Wide
∫V•dt:	6.9×10^{-3} Vsecs
Lsat:	31.2 nH
τ Discharge:	75 nsec
Losses:	2 Joules

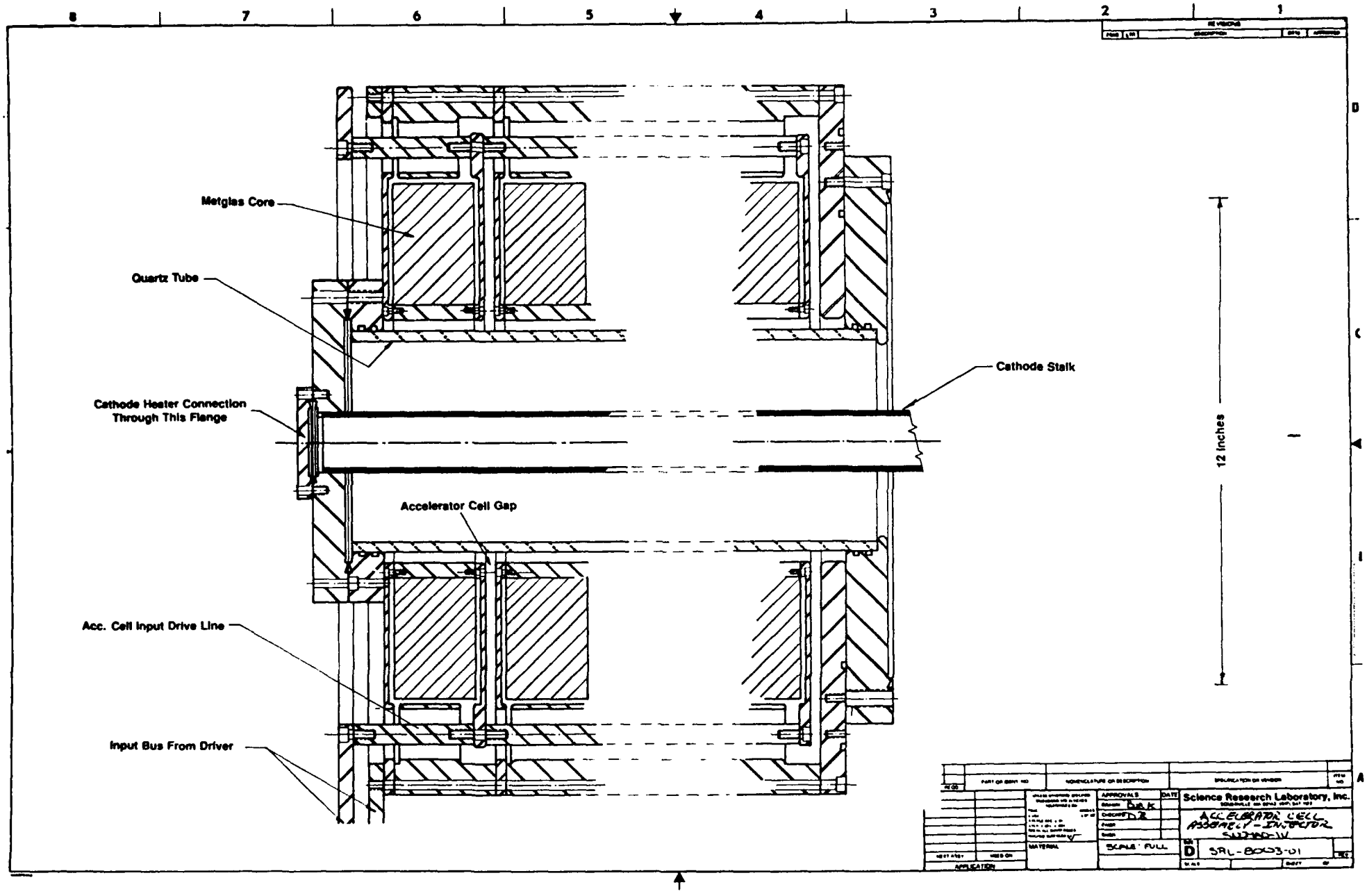

Figure 4.14: Drawing of SNOMAD-IV 0.5 MeV injector accelerator cell assembly.

transmission like. As a result, the electrical impedance of the cell decreases as a function of pulse duration. In contrast, the ferrite filled cell presents a constant impedance for the duration of the pulse. This difference can manifests itself by producing an inductive voltage droop during the pulse. However, by using a sufficiently large core volume this effect can be minimized to meet any specified level of performance. We believe that the choice of metglas is prudent in achieving the goals of this program: low cost and compact design.

The injector assembly, shown in Fig. 4.14, and the 1 MeV module assembly differ in design in two significant ways. The injector utilizes a quartz tube as the vacuum interface. This design eliminates many sealing joints and simplifies the construction, cooling and insulation of the accelerator cells. The simplified design is made possible because there is no electron beam present in the injector cells. Electron beam propagation in the accelerator cells require that the walls be of a conducting material to prevent charge accumulation which results from lost beam electrons. Therefore, the accelerator modules will employ o-ring sealed ceramic insulators in each of the accelerator gap, similar in design to those shown in Fig. 4.10. In addition, each induction cell used in the accelerator module will be fitted with a solenoidal focusing magnet which is required for the propagation of high current e-beam propagation.

The injector module is fitted with a cathode assembly and vacuum pump housing as shown in Fig. 4.15. A 3.5 inch diameter dispenser cathode is mounted at the end of the cathode stalk and will supply up to 600 amps of electron beam current. The cathode, cathode shroud and anode ring geometry establish the charged particle extraction optics. The radius of curvature of the cathode surface determines the degree of convergence of the extracted beam. The design of the extraction optics is often dictated by the requirements of matching the beam transport characteristics to the beam pipe of the FEL or CARM. Therefore, a final design of the cathode and its associated injector components is not feasible without a detailed knowledge of the beam matching requirements of the radiation source.

The SNOMAD-IV driver and accelerator cell assembly is housed in a rectangular aluminum enclosure which supplies cooling and electrical shielding to both units. All high voltage bus

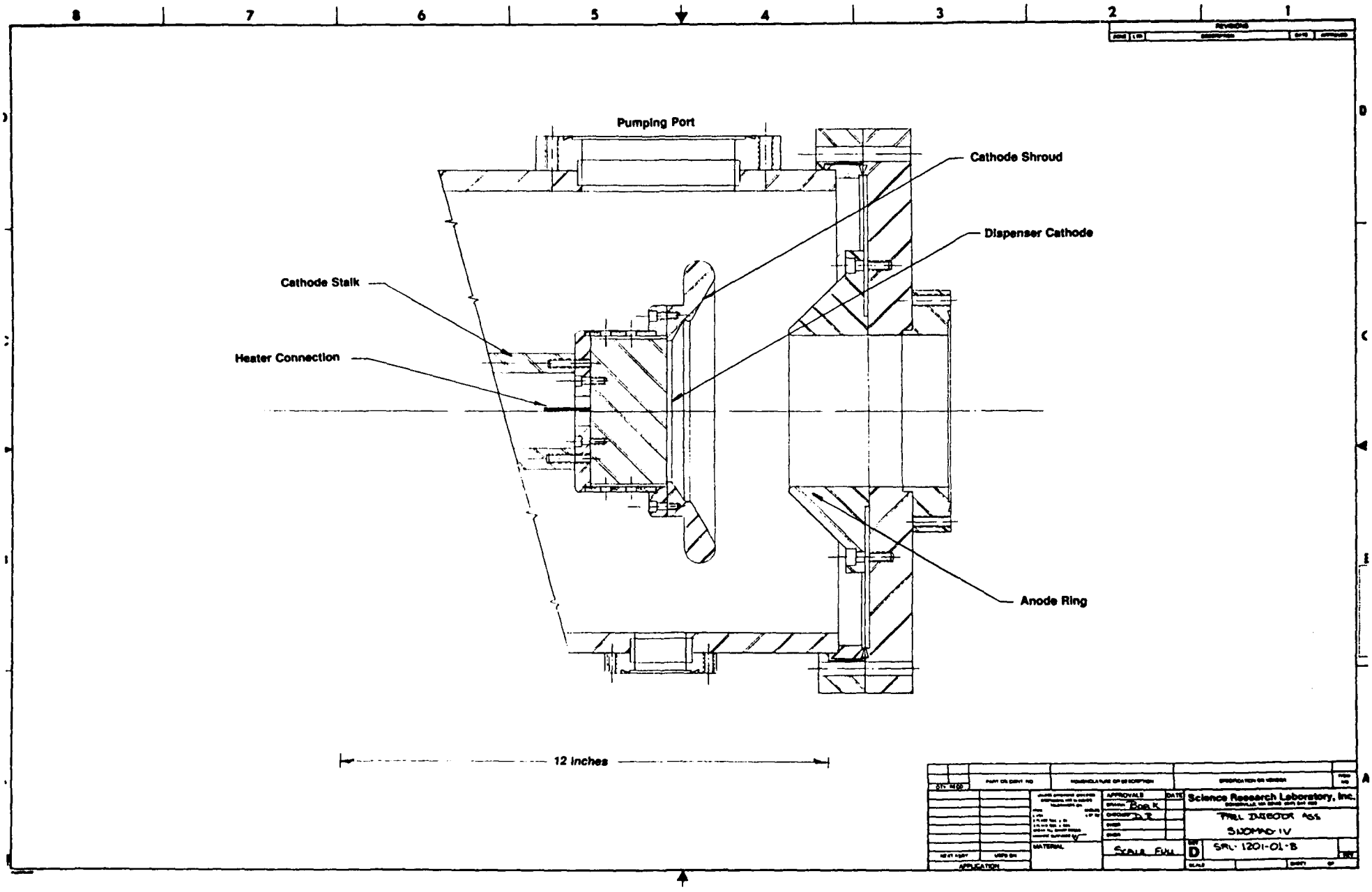

Figure 4.15: Preliminary assembly drawing of cathode extraction optics and vacuum pumping port.

connections between the driver and induction cells are made within enclosure forming a self contained 1 MeV accelerator module. External connections to the module will include: 500 volt DC prime power, low voltage timing signals, and entrance and exit ports for the beam.

Several concepts have been investigated for providing cooling and electrical insulation for the driver and accelerator components within the enclosure. A freon vapor environment is sufficient to provide the necessary peak electric field break-down strength of 70 kV/cm, and will permit the accelerator to operate at a repetition rate of 20 kHz for several seconds or an average repetition rate of up to 1 kHz for an indefinite period of time. Heat removal is accomplished by transferring heat to the aluminum tank without additional heat exchangers or coolers. Filling the tank with liquefied freon or transformer oil will permit the accelerator to operate at an average repetition rate of 5 kHz for an indefinite period. In this mode of operation, the aluminum tank can not dissipate sufficient heat and must be assisted by a water cooled heat exchanger mounted within the tank. Assembly drawings of the enclosure are shown in Figs. 4.16 and 4.17.

Following completion of all necessary testing at SRL of the SNOMAD-IV 1 MeV accelerator module, the device will be installed in a laboratory at the MIT Plasma Fusion Center which is equipped to provide power, radiation shielding and computerized control. Under the supervision of Dr. Richard Temkin, the accelerator will be made available to research members of the Fusion Center for developing and testing high power millimeter wave sources. SRL will assist in training MIT personnel in the operation and maintenance of the accelerator. The goal of this task will be to gain field experience in operating and maintaining a production prototype of the accelerator module. Information and experience gathered in this effort will be used to improve upon subsequent accelerator designs.

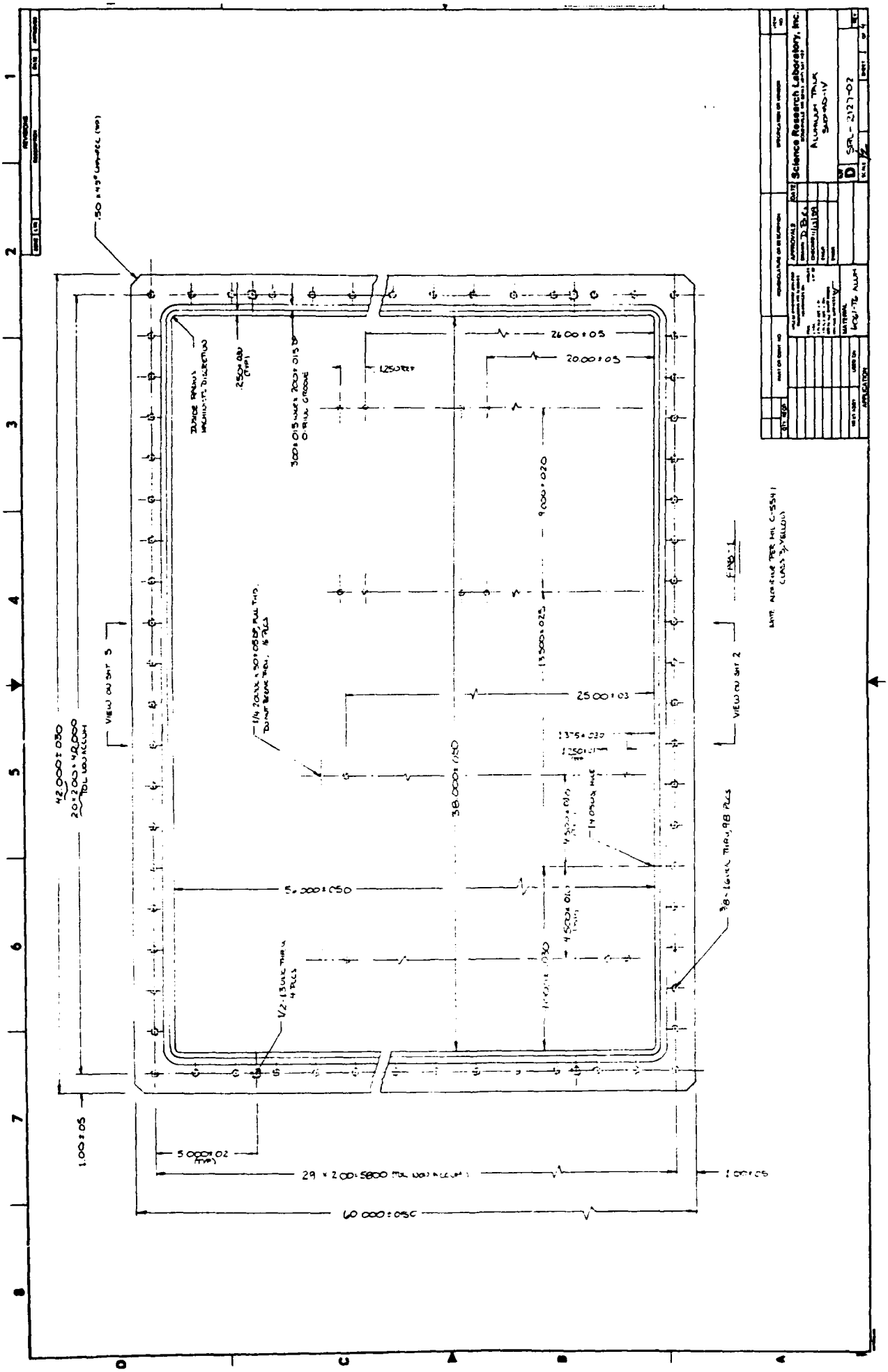

Figure 4.16: SNOMAD-IV enclosure, plan view.

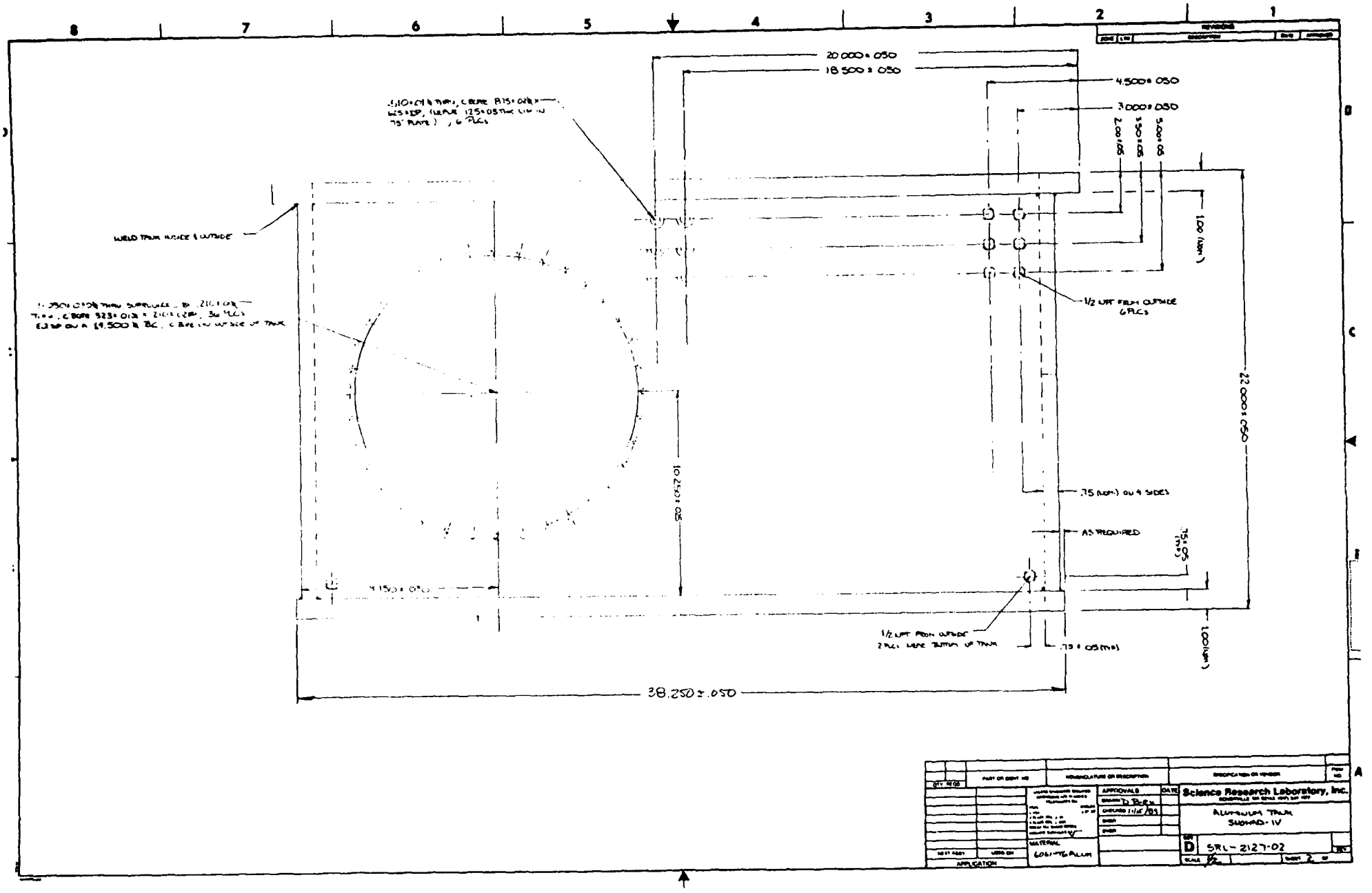

Figure 4.17: SNOMAD-IV Enclosure, elevation

SECTION 5

5.0 SNOMAD-V ACCELERATOR DESIGN

The SNOMAD-V induction linear accelerator is a self contained 1 MeV accelerator module driven by an all solid state nonlinear magnetic pulse compressor. Ten induction cells, each driven at 100 kV, produce a total accelerating voltage of 1 MeV. A schematic of this accelerator indicating its physical size and layout is shown in Fig. 5.1. Table 5.1 summarizes the performance specifications of SNOMAD-V. A photograph of the SNOMAD-V driver appears in Fig. 5.2.

The principle impetus behind the SNOMAD-V design is gradient optimization of the induction accelerator. The goal is to achieve gradients approaching 3 MeV/meter.

The induction linac is modular in construction, as shown in Fig. 5.1. A series of several identical accelerator cells are driven in parallel by a pulsed power drive module which provides short duration high voltage pulses to each of the accelerator cells at a high repetition rate. The pulsed power drive modules comprise a command resonant charge power supply, intermediate storage power supply, and nonlinear magnetic pulse compression modules.

The output pulse length of the SNOMAD-V pulse compressor can be varied by changing the output PFL impedance from a minimum of 5 nanoseconds to a maximum of 15 nanoseconds. The SNOMAD-V pulse compressor will not only be used to drive the 1 MeV high gradient test module but will serve as a tool for experimentally determining the temporally dependant properties of the ferrite accelerator cores. Much has already been learned from the initial experiments.

5.1 Design Philosophy Behind SNOMAD-V

The size and weight of induction accelerators varies faster than linearly with the duration of the drive pulse even in conventional designs. In the alternate design architectures discussed in Appendix H the scaling is proportional to pulse duration squared. The scaling of conventional induction accelerators with pulse length is discussed in detail in Section 3 of the main report. This scaling can best be understood by considering the induction cell as a ferrite loaded transmission line whose length is determined by the speed of light in the ferrite multiplied by the pulse length. The length of this transmission line therefore scales linearly with the pulse length. The

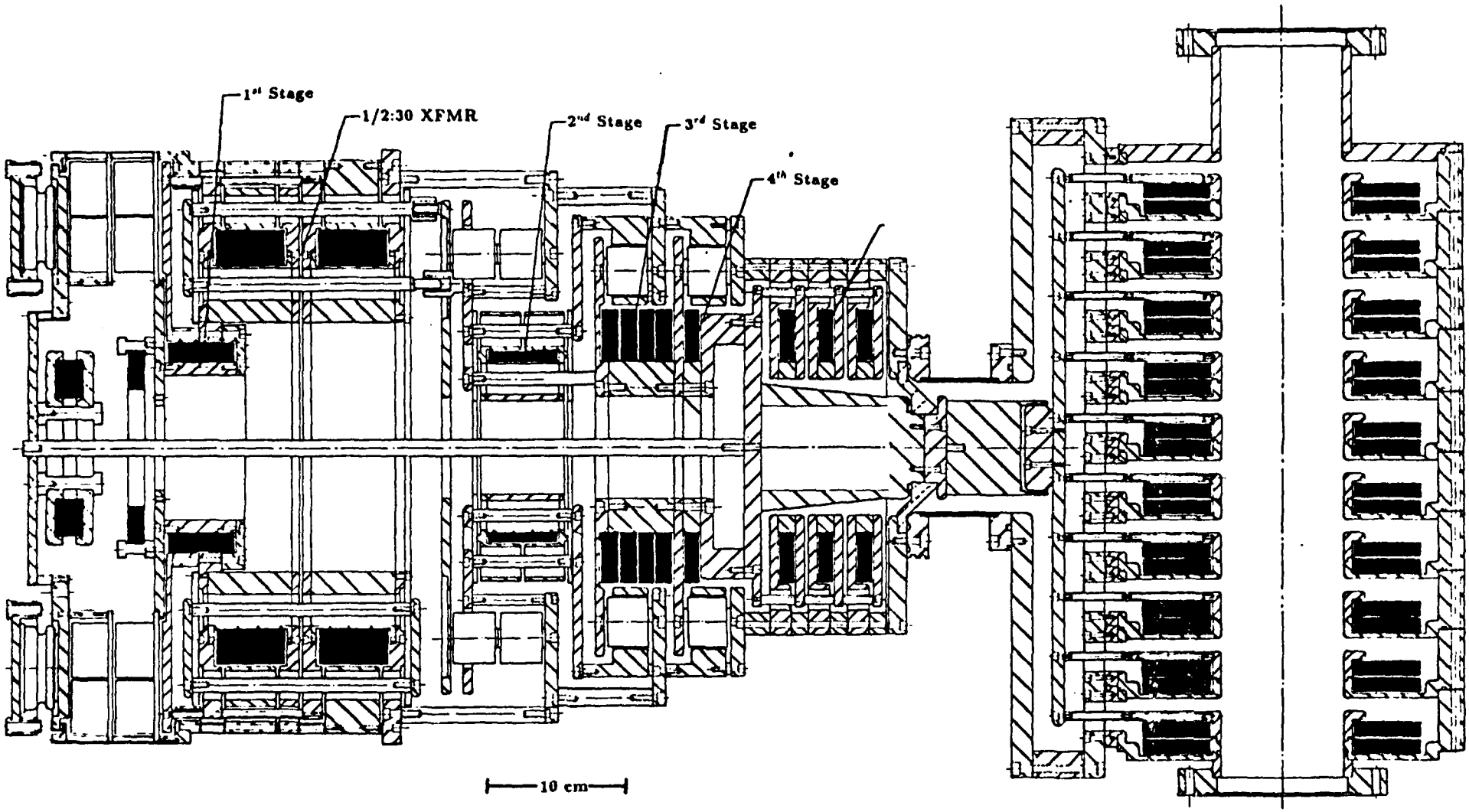

Figure 5.1: SNOMAD-V Nonlinear Magnetic Compressor and 1 MeV High Gradient Accelerator Section

Table 5.1: SNOMAD-V Preliminary Specifications

Input Power Requirements:	
Energy/pulse	5.27 joules
PRF	5 kHz
Power	26.4 KW
Voltage	465 volt
Current	56.6 Amps
Intermediate Storage	
Capacitance	12.3 μfd
Voltage	930 volts
Energy	5.27 joules
Stored charge	1.144×10^{-2} Coulombs
τ discharge	$\leq$ 5 μsec
I peak	3.594×10^{3} Amp
dI/dt	2.258×10^{3} A/μsec
I_T (RMS)	430 Amps
dI/dt per device	564 A/μsec (4×R400 West Code)
Commutation losses	$\sim$ .27 joules
1^{st} Stage	
Capacitance	12.5 μfd
Voltage	894 volts
Energy	5.0 joules
Core Type	.6 Mil × 2605 CO
# Turns	1
Core geometry	1×5.75″ ID × 7.0″ OD × 2″ Wide
$\int V \cdot dt$	$\sim 2.4 \times 10^{-3}$ Vsecs
Lsat	1.97 nh + 2 nh (STRAY) = 3.97 nh
τ discharge	494 nsecs
Losses	$\sim$ .20 joules (.10 cores, .10 caps)
Core volume	4.1×10^{-4} m^3, 2.46 kg
Transformer	
Core Type	2605S3A
# Turns (PRIM)	.50
# Turns(sec)	30
Losses	$\leq$ .15 joules
Peak stress	53 kV/cm at 50.5/2 kV (.375″ dia. Rod in .875 ″ dia. hole)
Core geometry	2×10.5″ ID × 12.875 ″ OD × 2″ wide

Table 5.1 (Continued)

2^{nd} Stage

Capacitance	3.64 nfd
Voltage	50.546 kV
Energy	4.65 joules
Core type	2605SC METGLASS
Core Geom.	1×4.25″ ID × 5.75″ OD × 2″ w ($.371\times10^{-3}M^2$)
$\int V \cdot dt$	6 Turns × 2.48 Vsecs/Turn = 50.546 kV* (.589 Vsecs/2)
LSAT	.112 μh + .06 μh stray $\simeq$ .172 μh
τdischarge	55 nsecs
Losses	$\sim$ .15 joules

Third Stage

Capacitance	3.92 nfd
Voltage	47.9 kV
Energy	4.5 joules
Core type	CMD-5005 Ferrite
Core Geom.	4×5.0″ ID × 8″ OD × .5″ w
$\int V \cdot dt$	1 Turns × 1.257×10^{-3} Vsecs/Turn
LSAT	4.7 nh + 1.3 nh (Stray) $\simeq$ 6 nh
τdischarge	$\sim$ 10.7 nsecs
Losses	$\sim$ .4 joules

Fourth Stage

Capacitance	4 nfd
Voltage	45.27 kV
Energy	4.1 joules
Core type	CMD-5005 Ferrite
Core Geom.	1×5.0″ ID × 8″ OD × .5″ w
$\int V \cdot dt$	1 Turns × $.314 \times 10^{-3}$ Vsecs/Turn
LSAT	1.17 nh + .3 nh (Stray) $\simeq$ 1.47 nh
τdischarge	$\sim$ 5.4 nsecs
Losses	$\sim$ .4 joules

1:4 Transformer

Core Type	CMD-5005
# Turns (PRIM)	.25
# Turns(sec)	1
Losses	$\leq$ .4 joules
Core geometry	4×5″ ID × 8 ″ OD × .5″ wide

diameter of the ferrite cores is determined primarily by considerations involved in minimizing Beam Breakup Instabilities. The growth rate of these instabilities depends exponentially on the inverse square of the beam pipe diameter. The ferrite must surround the beam pipe in a conventional induction accelerator. The growth rate of the beam breakup instability also depends exponentially on the inverse of the focusing field strength. In theory one could arbitrarily reduce the diameter of the beam pipe and maintain a constant Beam Breakup Instability growth rate by increasing the magnetic focusing field strength at a rate corresponding to the square of the beam pipe diameter change. Unfortunately it is also very important to minimize the number of Betatron wavelengths in the accelerator transport.

The number of Betatron wavelengths along the length of the accelerator depends linearly on the focusing field strength and the length of the accelerator. As the number of wavelengths increases, small energy variations lead to phase differences in the particle orbits. Particles injected off axis will spiral around the magnetic field center line with wavelengths that depend on their energy. After many orbits the particles angular position becomes a strong function of its energy and small energy variations over the duration of the electron beam pulse begin to appear as a cork screwing electron beam to a stationary observer. The Beam Breakup Instability is actually a transverse klystron instability created when the dipole modes in the accelerating cavities are excited. These dipole modes are driven by time dependent variations in the particles position with respect to the center line. A cork screwing electron beam is an excellent drive source for this instability. Because of this phenomena the maximum useable focusing field varies linearly with the overall accelerator length. If we can increase the overall accelerator gradient it also becomes possible to increase the strength of the focusing field by the same factor.

In other words, increasing the overall accelerator gradient allowed us to increase the focusing field strength and still hold the number of particle orbits constant. By increasing the focusing strength we can decrease the beam pipe diameter and still maintain the same Beam Breakup Instability growth rate. In order to maintain a constant instability growth rate we can decrease the beam pipe diameter as the square root of the focusing field strength, and we can increase the

focusing field strength as the overall accelerator gradient increases. Therefore the inner diameter of the ferrite cores can be decreased in inverse proportion to the increase in the overall gradient. Since the weight of the ferrite scales inversely with length and faster than the inverse of the inner diameter. The scaling of ferrite volume with beam pipe diameter is discussed further in Appendix H, but even with our cursory analyses above it becomes obvious that the ferrite weight and volume will scale inversely at least as fast as the overall gradient to the three halves power. Since the overall gradient is inversely proportional to the pulse length we can derive the approximate expression

$$\text{Core Volume} \propto \text{Pulse Length}^{>3/2}$$

The cost, size and weight of an induction accelerator scale faster with pulse length than any other parameter. Pulse length is the driving term in the accelerator design and is often ignored. In the early development of induction accelerators, pulse lengths were as long as 300-400 nanoseconds and the Astron accelerator developing an energy of only 3-4 MeV approached the dimensions of the 50 MeV ATA accelerator operating with a 75 nanoseconds. The ATA accelerator was designed to experimentally investigate the propagation of charge particle beams through the atmosphere. The physics associated with this phenomena determined the pulse length at which the ATA accelerator had to be designed to. In more recent induction accelerator designs this 75 nanosecond pulse duration has been maintained most probably out of tradition. In applications such as driving FEL amplifiers the minimum pulse length required is at most 1 nanosecond and the choice of a 75 nanosecond duration beam pulse is not mandated but has historically been chosen.

If the final application of the induction accelerator is to drive an FEL amplifier than it would appear that the optimum pulse length should be on the order of 1 nanosecond. The same average beam power could be achieved by simply increasing the repetition rate. After all, an induction accelerator operating at 1 nanosecond pulse length should be more the 500 times less bulky than a similar device operating at 75 nanosecond pulse lengths. The expense of such an accelerator would be reduced by a corresponding amount. Unfortunately not everything scales in a friendly

direction with reduced pulse length. The nonlinear magnetic pulse compressors are less efficient at shorter pulse lengths and the ferrite core material becomes more lossy. The overall efficiency drops as the pulse length is reduced. At a given average output beam power, the acceleration process is less efficient and more power is dissipated in a smaller volume. As the pulse length goes to zero so does the efficiency, but is the 75 nanosecond pulse duration set by charged particle atmospheric propagation physics also somehow magically the optimum pulse length for driving FELs. The answer to this question can only be determined by evaluating the relative merits of increasing efficiency versus drastically increasing accelerator size and cost.

The goal of the SNOMAD-V development program is to explore this parameter. As part of this development effort the effects of pulse length on efficiency is being carefully studied. The initial results from these studies are presented in Appendices A-C. SNOMAD-V designed to operate at pulse durations in the range between 5 and 10 nanoseconds will be used to obtain more data about the temporal dependency of efficiency. The SNOMAD-V research program is designed to optimize the induction accelerator for driving FEL amplifiers. Included in this research program will be the development of a complete database on how the efficiency of the various components used in an induction accelerator vary with pulse length. This will enable future induction accelerator designers to determine the exact cost in terms of size and weight of increasing pulse length to achieve higher efficiencies.

SECTION 6

6.0 CONCLUSION

In the preceding report and in the appendices which follow we have tried to acquaint the reader with the advanced design features incorporated in the SNOMAD accelerator line. In the way of a brief review, the SNOMAD-I modulator served as a proof-of-principle experiment and as a testbed for future all-solid-state accelerator driver design. SNOMAD-I was the first of the SCR commutated induction accelerator drivers and proved the feasibility of building an all-solid-state induction accelerator driver. After generating a database for the SNOMAD-II design, under an agreement between SDIO, ONR, and the DoE, SNOMAD-I was shipped to the DoE/LLNL on long term loan. There SNOMAD-I was used to drive a copper vapor laser. In this role SNOMAD-I proved that the application of this advanced modulator technology to the problem of driving copper vapor lasers used in Uranium enrichment would result in a significant improvement in efficiency and reliability over the existing thyratron based modulators. These tests spawned a whole series of laser modulators designed by SRL for the DoE and in production at LLNL.

SNOMAD-II built on the SNOMAD-I results and was designed as a complete accelerator module rather than simply a modulator. The SNOMAD-II accelerator module as it exists today is a self contained 1 MeV module being operated on a regular basis by scientists at the MIT Plasma Fusion Center. SNOMAD-II was loaned to MIT under a separate SDIO/ONR/DoE agreement similar to the one mentioned above. SNOMAD-II is currently being used as a testbed for advanced ECH RF heating sources which are to be applied to plasma heating in Tokomaks.

SNOMAD-III was designed at the request of SDIO solely for the purposes of proving that a 1000 Joules modulator design was feasible based on these principles. The SNOMAD-III design was detailed and analyzed but has not as yet been fabricated.

The SNOMAD-IV accelerator is a 1 MeV accelerator module designed to serve as a cost optimized production prototype. SNOMAD-IV is a complete fully enclosed 1 MeV accelerator section and has been fabricated for a materials cost of only $150,000.00. This represents a cost

of on $0.15 per volt and $0.14 per watt. SNOMAD-IV is also serving a technology spin-off role at the MIT Plasma Fusion Center, demonstrating that this new induction accelerator technology can function reliably in a turn-key role where a Phd. is not required to operate it.

SNOMAD-V is the most recent development in the SNOMAD accelerator driver line. SNOMAD-V is an experimental 1 MeV accelerator, designed to prove that gradients in excess of 3 MeV/meter can be achieved using an induction accelerator. SNOMAD-V also serves as a tool in the development of advanced induction accelerator architectures. With its extremely short 5 nanosecond duration output pulses, SNOMAD-V can explore a realm of induction accelerator technology which has not yet been investigated. The unique features of this new technology may lead one day to induction accelerator designs, light enough, compact enough, and reliable enough to function in the space environment.

7.0 REFERENCES

1) R.E. Klinkowstein, D. Birx, A Low Cost Induction Linac for High Power Electron Cyclotron Heating Millimeter Wave Sources, Bul. Am. Phys. Soc., 34, 1987 (1989).

2) W. Barletta, Lawrence Livermore National Laboratory, Livermore, CA, UCRL-95909, 1987.

3) D. Birx, S. Hawkins, S. Poor, L. Reginato, M. Smith, Lawrence Livermore National Laboratory, Livermore, CA UCRL-92828, 1985.

4) D. Birx, G. Caporaso, L. Reginato, Lawrence Livermore National Laboratory, Livermore, CA, UCID-20786, 1986.

APPENDIX A

1.0 FERRITE AND NONLINEAR MAGNETIC PULSE COMPRESSORS

Ferrites play two key roles in the SNOMAD accelerator designs. They are employed in the final compression stage of the nonlinear magnetic pulse compressor and they are used in the accelerator cells. Before identifying an optimum ferrite composition, it is necessary to determine the desired electromagnetic properties of the ferrite materials. In this section we will examine ferrite core requirements of Nonlinear Magnetic Pulse Compressors.

Nonlinear magnetic pulser compressors are themselves resonant circuits. The basic principle underlying nonlinear magnetic driver operation involves using a saturable core which is an inductor in a resonant circuit. The circuit is designed to allow the core of the next stage to saturate before a significant fraction of the energy stored in the capacitors of the previous stage is transferred. This nonlinear saturation phenomenon shifts the resonant frequency of this resonant circuit by the square root of the permeability shift as the core saturates. These stages are typically cascaded (Fig. A.1) and energy is coupled faster and faster from one stage to the next. These circuits are efficient at transferring power in both directions since they act not only to upshift the frequency in the forward direction thereby providing temporal compression, but also downshift the frequency of a voltage pulse as it cascades back up the chain in the reverse direction. The energy which reflects from the mismatched load can propagate back up the chain to the SCR commutator. This reflected energy is stored and added to the next pulse energy via the energy recovery circuit.

The design of efficient high gain pulse compression stages relies on the careful control of the magnetic fields surrounding the core volume. The losses in a compression stage are linearly proportional to the volume of core material used and it can be shown that the core volume requirement for this saturable inductor is given by:

$$\text{volume} = \text{gain}^2 \cdot \text{Pulse Energy} \cdot \left(\frac{\mu_o \cdot \pi^2}{4 \cdot (\Delta B_s \cdot \text{pf})^2} \right) \qquad (A.1)$$

where ΔB_s is the available flux swing of the material (with appropriate biasing given by $+B_s - (-B_s) = 2B_s$), gain is defined as the temporal compression factor (τ charge/τ discharge), and

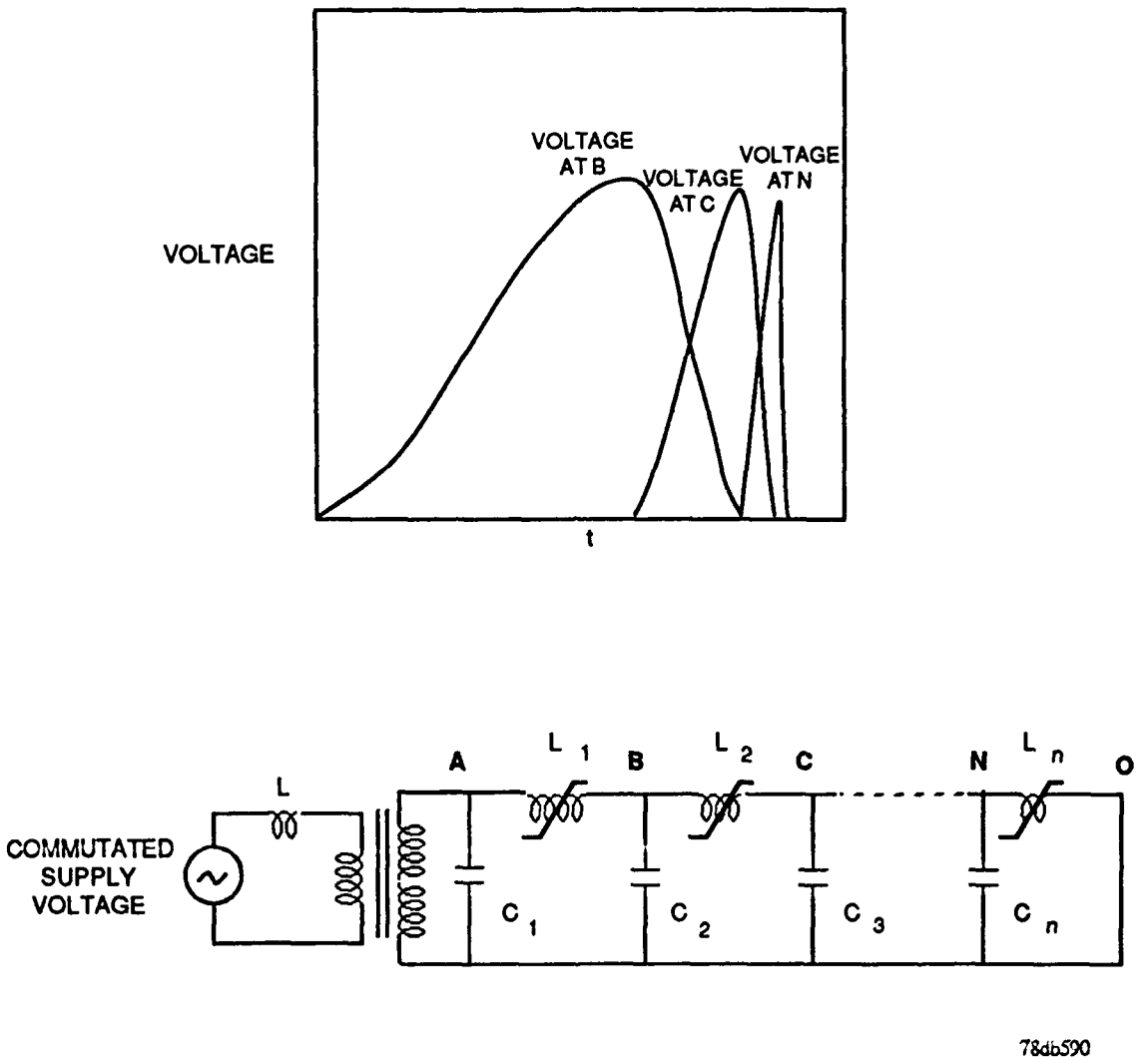

Figure A.1: Typical magnetic switch operation

pf is the packing factor. The packing factor is defined as

$$\frac{\int_{V_f} H^2 dv}{\int_{all\ space} H^2 dv} \qquad (A.2)$$

where V_f is the actual volume occupied by the ferri- (ferro) magnetic core material excluding all interlaminar insulation and voids. Optimization of this packing factor is crucial in magnetic switch design and is accomplished by enclosing the core in a tightly fitting conducting housing. The multiple turns are formed as coaxial transmission lines which pass through this housing. Circulating currents set up in this housing exclude the magnetic flux and contain it in the desired volumes.

It is obvious that because the core volume requirement scales with the inverse square of the ΔB_s and losses will vary linearly with the core volume, that losses per unit volume must be normalized by $(1/\Delta B_s)^2$ before a relevant comparison among different materials can be made. In other words using a material with twice the losses per unit volume but twice the ΔB_s will decrease the losses by a factor of two since only one fourth the volume is required.

APPENDIX B

1.0 NONLINEAR MAGNETIC MATERIAL SELECTION

It is important to understand when it is advantageous to use ferrite rather than metglass tapes. In this section we will compare the attributes of ferrites with those of metglass tapes. The first stage compression reactor step-up transformer and (sometimes) the second stage compression reactor are designed around metglass cores. This is the last stage in the compression chain where metglass can be employed if operation at greater than 5 kHz CW repetition rate is to be possible. Metglass is composed of a mixture of silicon and iron which is mixed while liquefied and then rapidly quenched so that it remains amorphous. The resistivity of this alloy is three times that of most ferro-magnetic materials. However, at saturation times much less than 10^{-6} seconds, the losses begin to scale inversely with the saturation time as eddy currents become the dominant loss mechanism (see Fig. B.1).

Further increases in performance can be achieved through basic material improvements. The proposed drivers will predominately employ 2605 CO, SC and S3A metglass as a saturable core material. These mixtures of silicon and steel possess the magnetic properties of steel (i.e. $\Delta B \sim$ 36 kg, $H_c \sim 0.05$ Oe, $\mu_r \approx 10{,}000$) but afford much higher resistivities ($\rho \sim 130\ \mu\Omega$-cm) because of its glass-containing atomic structure. Unfortunately it has a rough surface texture resulting in inherent packing factors of only 0.75 and the addition of interlaminar insulation further reduces this to ~ 0.5 in a wound core. Interlaminar insulation can be avoided if the material can be vapor deposited with a very thin layer of MgO or SiO_2. The inherent 0.75 packing factor associated with roughness can be improved upon by hot rolling the metglass. These techniques are aimed at the objective of achieving an overall packing factor of 0.8.

Even with a packing factor of only 0.5 (compared to almost unity with ferrite), when the inherent $\Delta B_s \leq 3.3$ Tesla of metglass is compared to $\Delta B_s \leq 0.65$ Tesla of $Zn_{.60}\ Ni_{.40}$ ferrite (core volume depends inversely on ΔB_s^2), metglass is preferred when eddy current losses are not a problem. As the saturation times get shorter and eddy current losses increase, removing the waste heat from the interlaminar core structure becomes very difficult. Manganese zinc

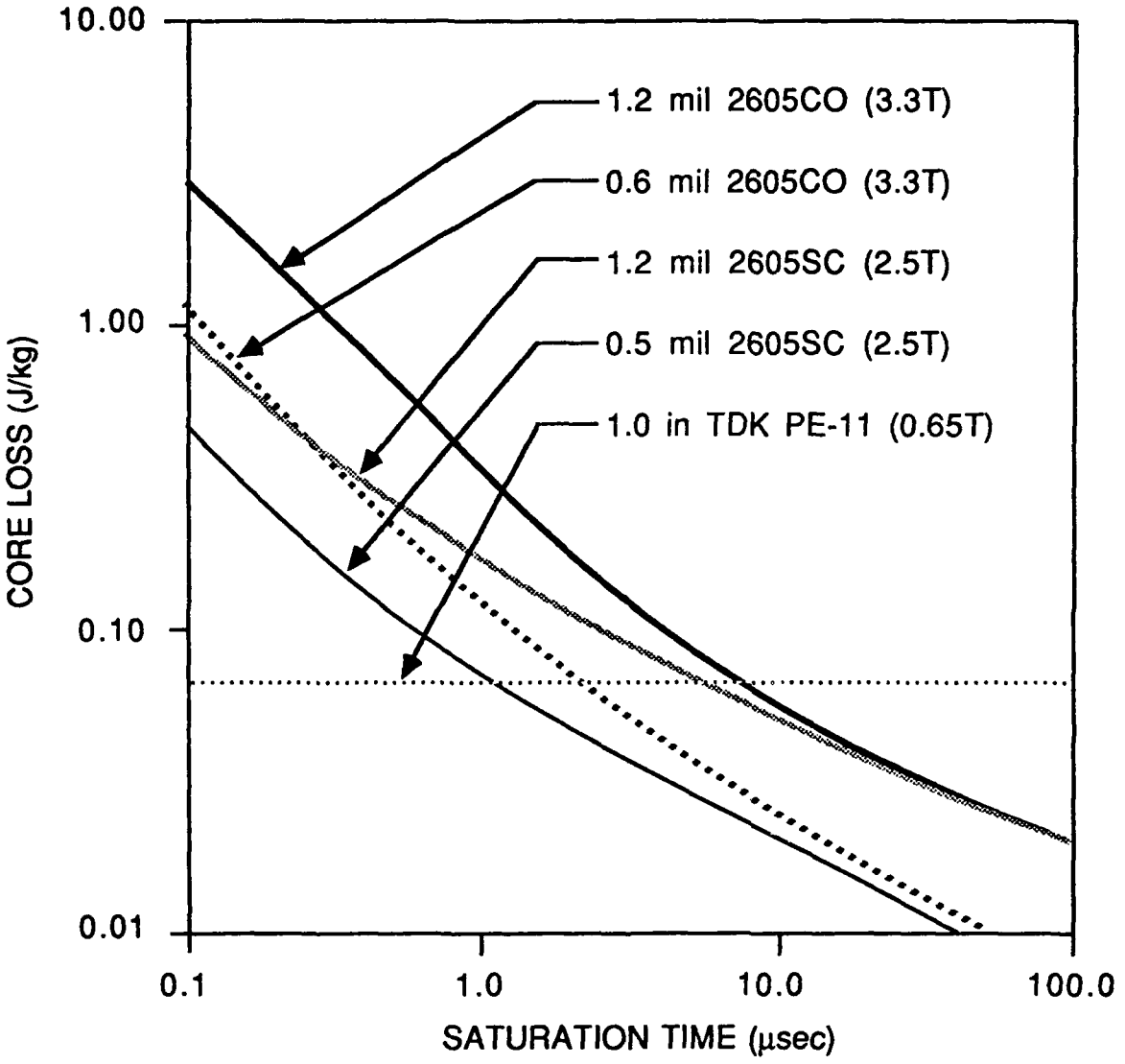

Figure B.1: Estimated core loss versus saturation time in metglass tapes

78db590

ferrites would seem a logical choice to span the gap between metglass and $Zn_{.60}$ $Ni_{.40}$ ferrite, but geometric resonances encountered in the large cores required at this pulse energy eliminate it from consideration. Other iron alloys such as superpermalloy have been considered but suffer from the same heat removal problems as metglass. The higher conductivity of these alloys requires them to be thinner and this results in a greater expense and a lower net packing factor. It is hoped that advances in coating technology will improve the situation in the future.

The time dependent losses in ferro-magnetic ribbons are typically explained in terms of a saturation wave which encircles the tape and proceeds toward the center at a rate which is linearly dependent on the applied voltage. Ignoring the fact that domain wall locations are initially pinned to impurity sites, the H-field required to change the state of magnetization of a tape is given by

$$H_a = H_c + \left(\frac{d^2}{4\rho}\right)\left(\frac{\Delta B}{2B_s}\right)\left(\frac{dB}{dt}\right)$$

where B_s is the saturation induction, H_c is the DC anisotropy coercive field, d is the sample thickness and ρ is the resistivity. The energy density deposited in the tape during saturation is given by

$$E_L = H_c\Delta B + \left(\frac{d^2}{8\rho}\right)\left(\frac{\Delta B^2}{2B_s}\right)\left(\frac{dB}{dt}\right)$$

This theory assumes the material is completely isotropic and possesses no preferred domain geometry. This is certainly not true and experimental measurements of time dependent losses conducted by Dr. Carl Smith at Allied Chemical Research Laboratories indicate a much more complicated behavior. This data, summarized in Fig. B.1, is further documented by graphs prepared by Dr. Carl Smith which appear in Fig. B.2.

The chart of losses versus saturation time in Fig. B.1 shows clearly that once normalized by $(1/\Delta B_s)^2$, metglass is the optimum material down to 100 nsec. saturation times and then ferrite takes over.

In the past ferrite was sometimes used where metglass was the best material choice. The cause of this apparent inconsistency was centered in the fact that techniques for adequately cooling tape wound cores had not been developed. This is no longer true and metglass is the

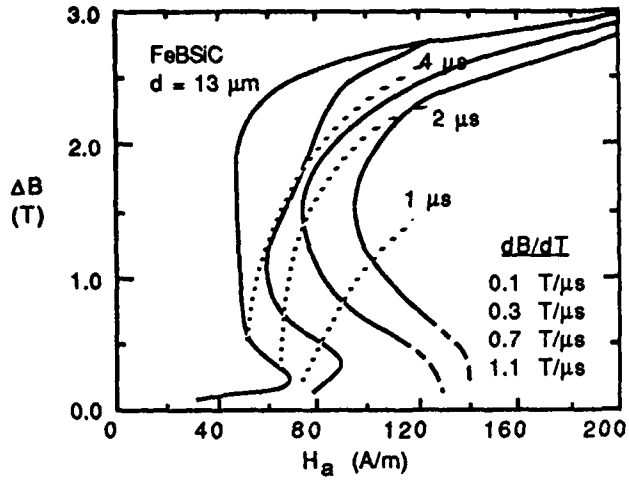

Dynamic magnetization and pulse permeability curves for 13 μm FeBSiC ribbon. Dashed extrapolations are for before the first digitized point.

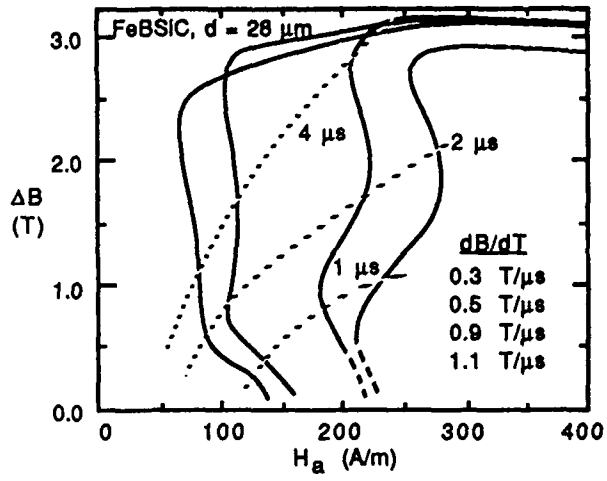

Dynamic magnetization and pulse permeability curves for 28 μm FeBSiC ribbon.

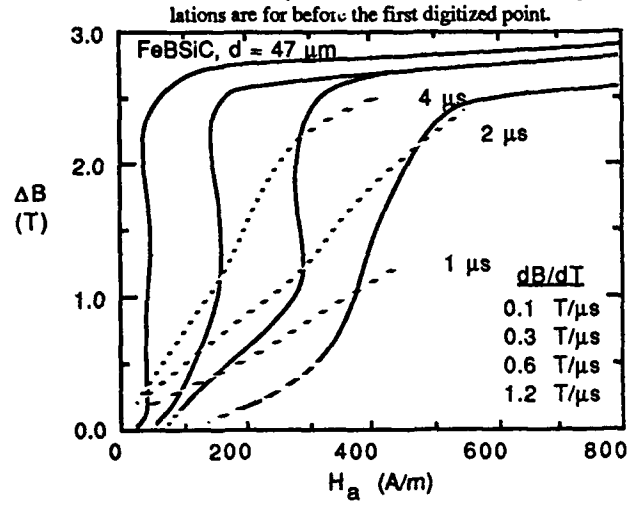

Dynamic magnetization and pulse permeability curves for 47 μm FeBSiC ribbon.

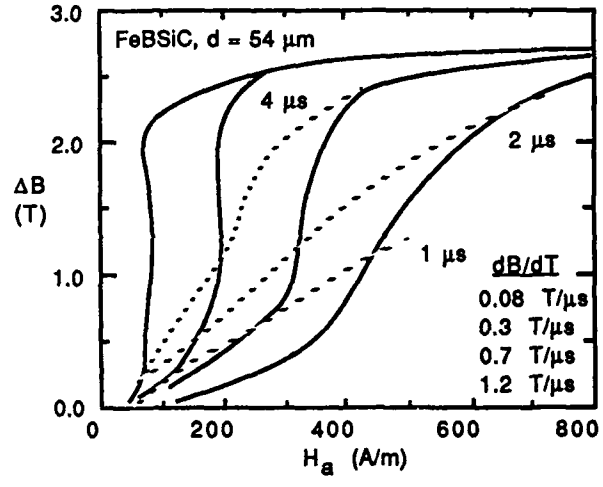

Dynamic magnetization and pulse permeability curves for 54 μm FeBSiC ribbon.

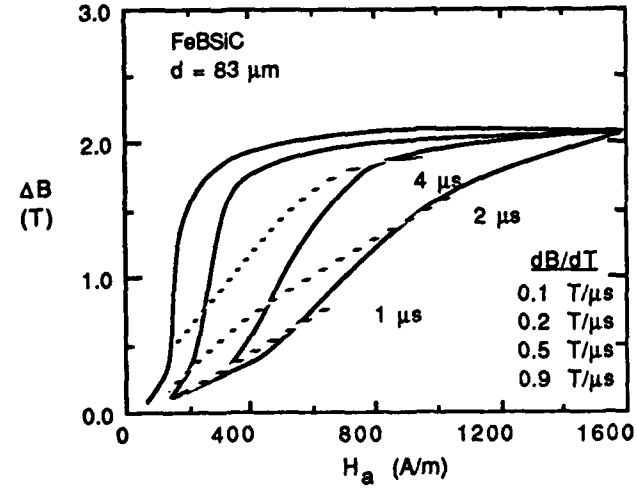

Dynamic magnetization and pulse permeability curves for 83 μm FeBSiC ribbon.

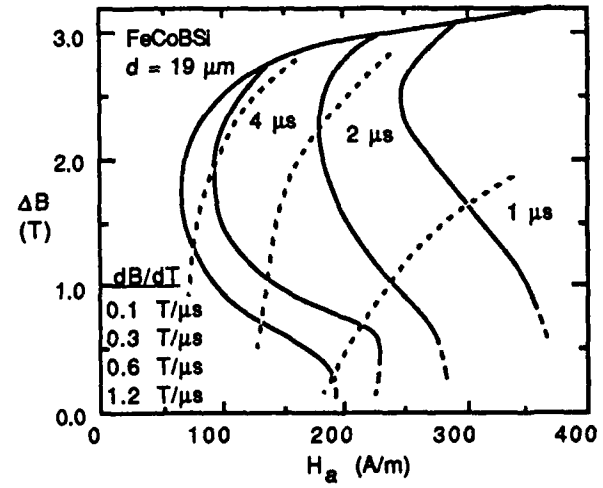

Dynamic magnetization and pulse permeability curves for 19 μm FeCoBSi ribbon.

78db590

Figure B.2: Time dependent ferrite loss measurements

optimum material choice for nonlinear magnetic compressor cores operating with $\geq$ 100 nsec saturation times.

1.1 Ferromagnetic Resonance

The concept of ferromagnetic resonance can best be understood by simple analogy to the processional motion of a spinning top. The spinning electron may be treated as an electrically-charged spinning mass. The magnetic forces acting on the spinning electron are similar to the gravitational forces acting on a spinning top. These magnetic forces acting on the electron in a ferromagnetic material are derived from two primary sources. These two components consist of the internal magnetic fields generated by the many individual magnetic dipoles which make up the domains and secondly the external forces which when applied perturb the alignment of these dipoles. When the external fields are applied perpendicular to the internal fields they exert a thrust or torque on the spinning electrons.

In the case of a spinning top (Fig. B.3) application of a force perpendicular to the axis of spin will initiate procession. The procession frequency ω_0 depends on the angular momentum of the top and the gravitational force Mg acting on the center of mass of the top. The gravitational torque is

$$T = MgL\sin\theta$$

where θ is the angle of inclination and L is the distance from the pivot point to the center of mass. The angular momentum vector will maintain a constant angle θ with the vertical and the top will precess about the vertical axis with an angular velocity

$$\frac{d\phi}{dt} = \omega_0 = \frac{T}{p\sin\theta}$$

The spinning electron can be treated as a spinning top where the forces of gravity are replaced by the magnetic forces. In the case of a spinning electron the angular momentum and magnetic moment are parallel vectors with absolute values of p and μ_e. The gyromagnetic ratio is defined as

$$\gamma = -\mu_e/p = ge/2mc$$

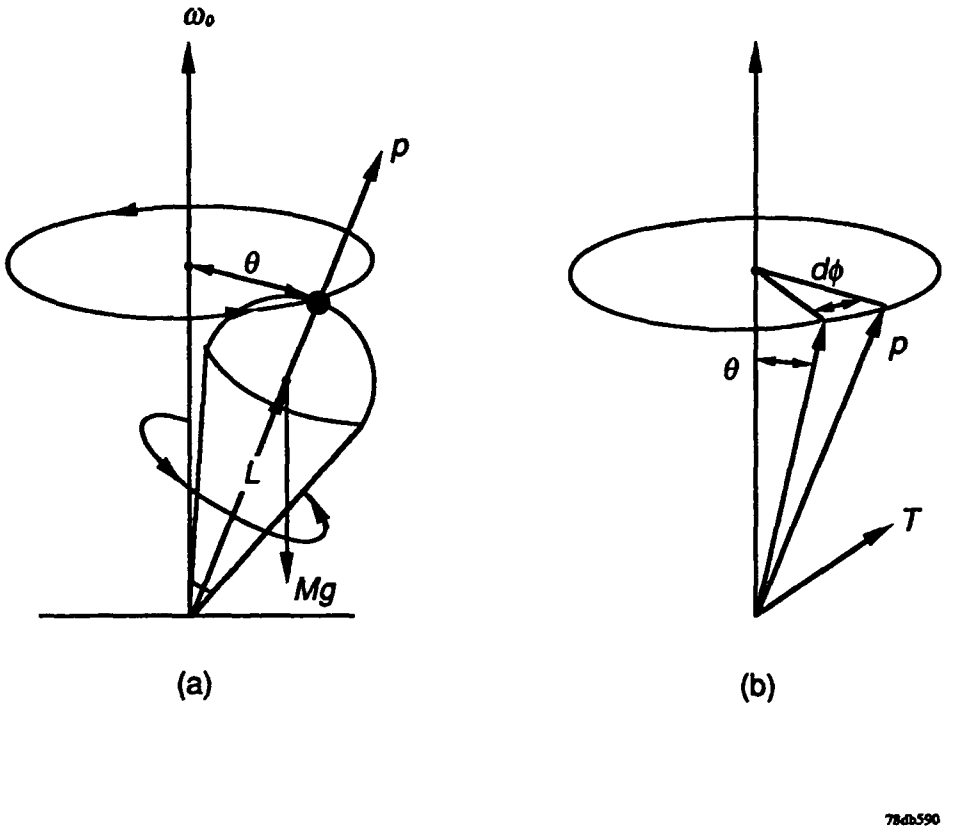

Figure B.3: Processional motion of a spinning symmetrical top in a gravitational field. The precession of the rigid body at frequency ω_0 is shown schematically in (a), and the angular momentum and torque vectors are shown in (b).

where e is the electronic charge, m the electron mass, c the velocity of light and g is the Lande g-factor and is approximately equal to 2. The torque on the electron from a constant magnetic field is simply

$$T = \mu_e H \sin(\theta)$$

By comparison with the above result for a spinning top, it is obvious that the processional frequency is simply given as

$$\omega_0 = \gamma H$$

Here the magnetic field H is the actual magnetic field seen by the electron and represents the vector sum of both the internal and applied external fields.

In the case of microwave circulators, a very large external field is applied which dominates the internal fields. In this case the resonance line width is very narrow and occurs at a frequency of thousands of megahertz. In the cases where the internal field dominates, the resonance occurs at much lower frequencies and the linewidth is quite broad as the internal domain structure is by definition nonisotropic and is randomly oriented with respect to the applied field. The internal field arises from the alignment of individual spinning electrons into domains and is given by

$$H_{int} = M_{sat}/\mu - 1$$

If the alignment is truly random, then a simple vector sum will result in an average field given as

$$H_{int} = 2/3 M_{sat}/\mu - 1$$

Therefore, as related above, the resonant frequency in the absence of an externally applied field is given by:

$$\nu_{res} = \frac{\gamma \cdot M_{sat}}{3 \cdot \pi \cdot (\mu_i - 1)}$$

where:

γ = gyromagnetic ratio ($\sim 0.22 \times 10^6$)

M_{sat} = Saturation magnetization ($2.5 \rightarrow 3.5 \times 10^5$ A/M)

μ_i = Initial permeability as $\nu \rightarrow 0$.

It is now obvious that the resonant frequency of a material can be easily shifted through a variety of measures. Application of an external bias field parallel to the applied time dependent field will increase the resonant frequency. Annealing a toroidal ferrite in the presence of a strong toroidal field can increase the ferromagnetic resonant frequency by a factor of 1.5. Reduction of the permeability will also increase the resonant frequency. This can be accomplished through the introduction of an air gap in the toroid or through a change in composition.

In zinc-nickel ferrites, the initial permeability and therefore the ferrimagnetic resonant frequency can be varied simply by reducing the zinc content and replacing it with additional nickel. An example of this behavior is shown in a plot of the real part of the initial permeability versus frequency for ferrites of various compositions (Fig. B.4). These ferrites are manufactured by Ceramic Magnetics Corporation and the compositions $(Zn_{45}\ Ni_{55})$, $(Zn_{30}\ Ni_{70})$, $(Zn_{15} \cdot Ni_{85})$, $(Ni_{1.0}) \cdot Fe_2O_4$ correspond to C2025, C2050, C2075, N40 respectively. Also available from this manufacturer are the compositions $(Zn_{54}\ Ni_{46})$, $(Zn_{60}\ Ni_{40})$, $(Zn_{65}\ Ni_{35}) \cdot Fe_2O_4$ corresponding to C2010, CN20, and CMD5005 respectively.

It is also critical to note that as the initial permeability drops, the Curie temperature increases. This can be understood by realizing that as the permeability drops, the energy required to change magnetic states increases and therefore the random thermal energy required to disrupt the state also increases.

The frequency dependence of ferrite losses has best been modeled by Landau and Lifshitz. They have proposed that the losses be modeled as

$$\frac{d\vec{M}}{dt} = \gamma(\vec{M} \times \vec{H}) - \lambda(\frac{\vec{M} \times (\vec{M} \times \vec{H})}{M_0^2} - \vec{H})$$

In this equation, γ is the gyromagnetic ratio and λ is the relaxation frequency. This model describes the motion of a spinning top in a viscous medium. The term multiplied by γ represents the DC anisotropy and the term multiplied by λ is the viscous damping. The first term represents the precessional motion of the magnetization. This motion as in the case of a spinning top is

C2025, C2050, C2075, N40 High Frequency Nickel-Zinc Ferrites

This group of materials was specifically engineered to give high flexibility in accommodating requirements to 400 MHz. Our engineering department will work with you on your particular needs to determine which if these ferrites is best for you.

Typical Magnetic Characteristics

	C2025	C2050	C2075	N40
INITIAL PERMEABILITY, <1 MHz	175	100	35	15
MAXIMUM PERMEABILITY	1100	390	150	50
MAXIMUM FLUX DENSITY, 'gaus	3500	3400	2700	1600
REMANENT FLUX DENSITY, 'gaus	2600	2400	1800	700
COERCIVE FORCE, 'cerstad	1.5	3.0	7.0	7.5
CURIE TEMPERATURE, °C	270	340	420	510
dc VOLUME RESISTIVITY, ohm-cm '@ 40 cerstad applied field strength	10^6	10^7	10^8	10^{10}

Initial Permeability Versus Frequency

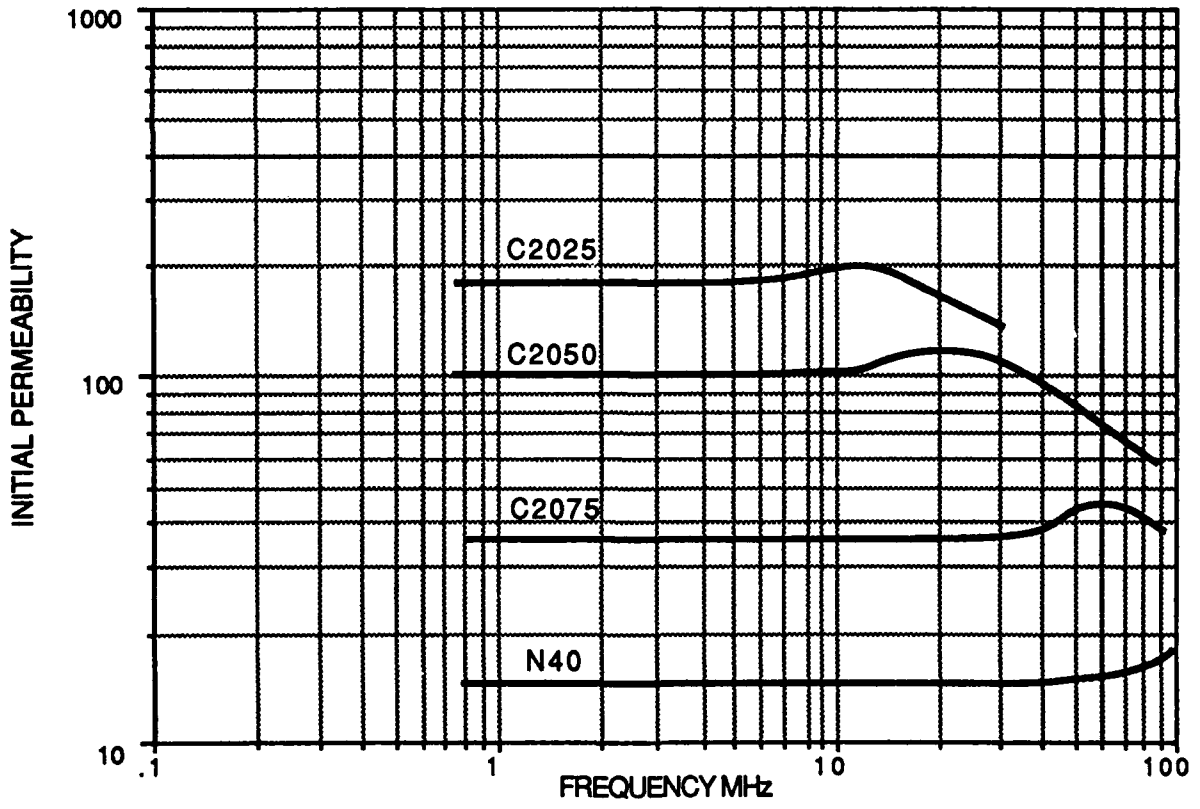

Figure B.4: High frequency nickel-zinc ferrite permeability

78db590

perpendicular to the direction of both $\vec{H}$ and $\vec{M}$. The second term signifies a damping force acting on the precessional motion. In the case where the second term dominates, this equation can be rewritten as

$$\frac{dM}{dt} \approx \lambda H(1 - \frac{M^2}{M_0^2})$$

The value for λ can be derived from the frequency dependence of the initial permeability. For large displacements around the demagnetized state let us assume

$$(1 - \frac{M^2}{M_0^2}) \approx 1/2$$

We will also assume the motion is oscillatory in which case

$$\frac{dM}{dt} = i\omega M \approx \frac{\lambda H}{2}$$

and since

$$\mu_r = 1 + \frac{4\pi M}{H}$$

$$\frac{\omega(\mu_r - 1)}{4\pi} = \frac{\nu}{2}(\mu_r - 1) \approx \frac{\lambda}{2}$$

In other words λ is the frequency at which $(\mu_r - 1)$ approaches unity. It might be expected that because the crystal structures are identical, the value of λ would be similar between various ZnNi ferrite compositions. Indeed examination of Fig. B.5 allows one to draw the conclusion that λ is almost identical between the various compositions and is equal to $\sim 10^{10}$ Hz.

1.2 Dielectric Properties

Ferrites are semiconductors with resistivities ranging from 10 Ω-cm to 10^8Ω-cm at room temperature. The relative dielectric permittivity ranges from 10 to as high as 100,000. The dielectric permittivity along with its frequency dependence are extremely important parameters in electromagnetic shock line design as the ferrite forms the transmission line medium.

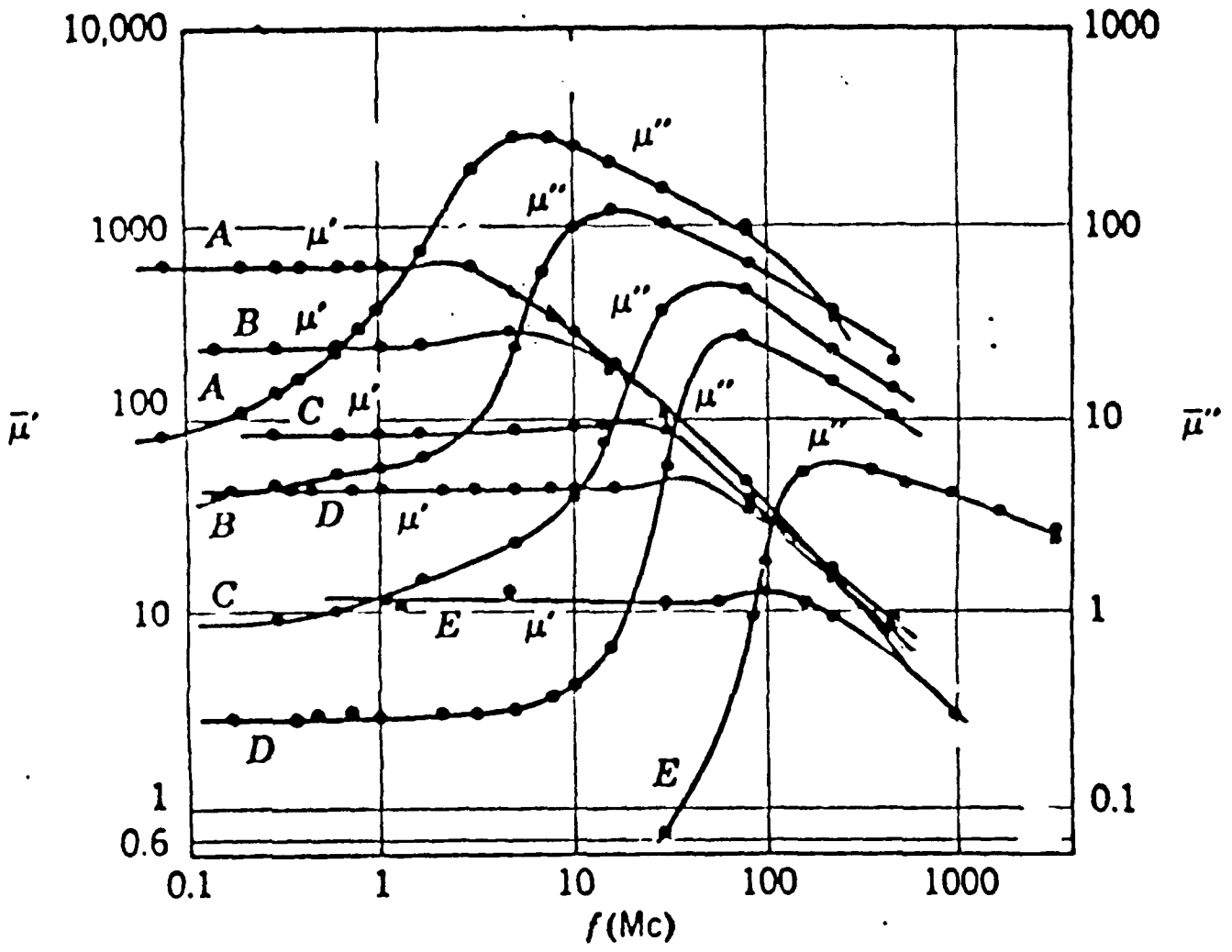

Figure B.5: Frequency dependence of real and imaginary parts of the initial permeability for polycrystalline NiZn ferrite (compositional ratio Ni O:ZnO = 17.5:33.2 (A), 24.9:24.9 (B), 31.7:16.5 (C), 39.0:9.4 (D), 48.2:0.7 (E), remaining part, Fe_2O_3) (Gorter).

Ferrite is a polycrystalline material consisting of semiconducting grains surrounded by thin boundaries with much higher resistivity. The grain boundaries are typically composed of insoluble materials which diffuse into the grain boundaries during sintering. They are typically nonmagnetic and are occasionally added intentionally. Calcium Oxide and Silicon Dioxide are examples of materials which are sometimes added by the manufacturer to increase the low frequency resistivity. One example of such a material is Ceramic Magnetics MN8CX. This ferrite is a manganese-zinc ferrite with an artificially high DC resistivity of 10,000 Ω-cm. As we will see below, such additions are of little practical significance at high frequencies at which the large capacitance of these grain boundaries shunts the high resistivity, exposing the inherent resistivity of the crystallites.

If we define α as the ratio of the boundary layer thickness to thickness of the average crystallite, then we can predict the dielectric behavior of the ferrite based on the experimentally determined conditions that $\alpha \ll 1$, $\epsilon_{crystallite} \approx \epsilon_{boundary}$, and $\alpha\rho_{boundary} \gg \rho_{crystallite}$. Therefore at low frequencies the impedance of the crystallite is negligible compared with the impedance of the boundary layers and the resistivity is approximately given as $\alpha\rho_{boundary}$ and the permittivity approaches $\epsilon_{boundary}/\alpha$.

At high frequencies the boundary layer capacitance is short-circuited by the high boundary layer capacitance and the dielectric permittivity and resistivity approach that of the crystallites. The relaxation frequency is defined as $1/2\pi\tau$ where τ is the characteristic decay time of the junction capacitance. The relaxation frequency is given by

$$f_r = \frac{1}{2\pi\epsilon_0} \frac{\frac{1}{\rho_{crystallite}} + \frac{1}{\rho_{boundary}}}{\epsilon_{crystallite} + \epsilon_{boundary}/\alpha}$$

Experimentally-measured curves of both permittivity and resistivity as a function of frequency for two different zinc-nickel compositions are presented in Fig. B.6. These compositions labeled B1 and 4B1 are produced by Phillips and correspond to $(Zn_{60}\ Ni_{40})$ and $(Zn_{50}\ Ni_{50}) \cdot Fe_2O_4$ respectively.

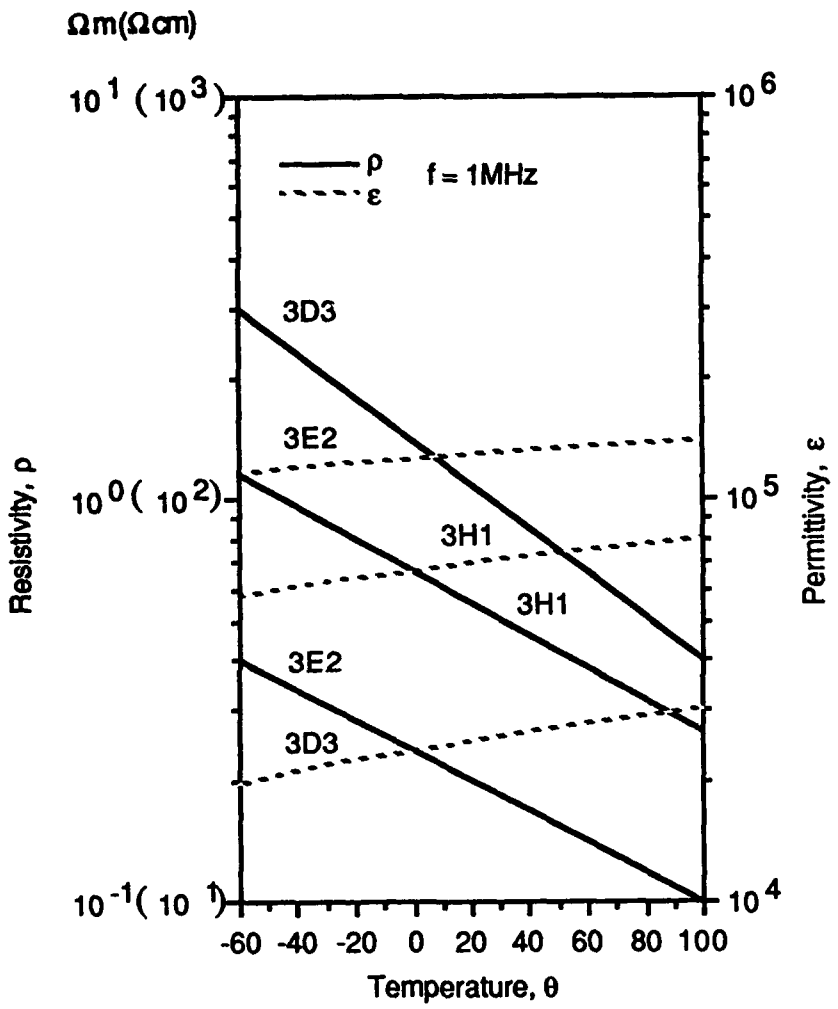

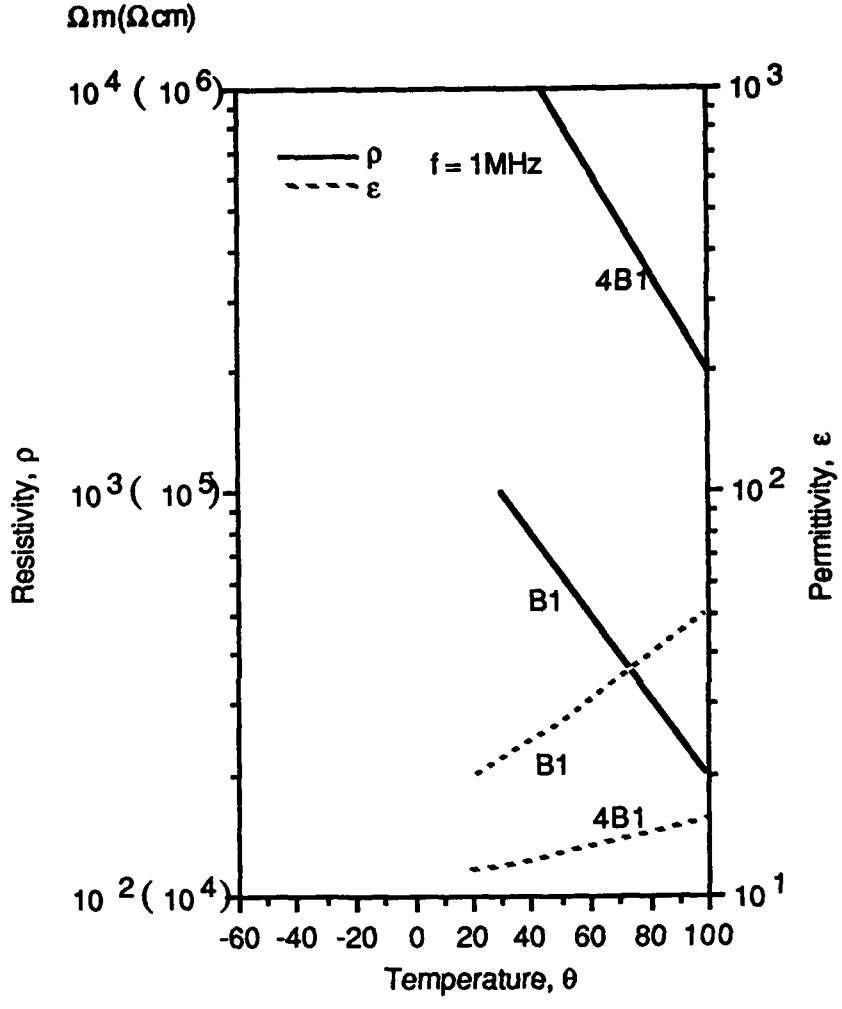

	Code No.	Manufr.	Class
MnZn ferrite	3H1	4	I
	3D3	4, 19	II
	3D2	4	III

	Code No.	Manufr.	Class
NiZn ferrite	B1	4	VI
	4B1	4	VII

Figure B.6: Resistivity of various ferrites as a function of temperature

78db590

The eddy current power loss density is simply given as

$$P = \frac{(\omega B_0 d)^2}{\rho\beta}$$

where ρ is the resistivity, d is the characteristic dimension and β is the geometric factor. For a toroid, d is the width of the toroid and $\beta = 24$. For a sphere, d is the diameter and $\beta = 80$. The eddy current losses can also be characterized as a contribution to the loss angle given as

$$\tan(\delta_r) = \frac{\omega\mu\mu_0 d^2}{2\rho\beta}$$

The resistivity and permittivity are also temperature dependent. This effect is documented by the measurements presented in Fig. B.7 of the same two compositions. These measurements were taken at 1 MHz but the slopes of the curves are similar at differing frequencies.

The curves indicate that for Zn-Ni compositions, the resistivity never will drop below 10^4 Ω-cm. This resistivity is 10^8 times higher than the resistivity of metglass. The eddy current losses in a 1 inch thick Zn-Ni toroid are equivalent to the losses in a 0.1 mil metglass tape for the same flux excursion. In Mn-Zn ferrites, the eddy current losses cannot be neglected as they approach 10 Ω-cm in the frequency range we are interested in. This means that a 1 inch thick Mn-Zn ferrite toroid will exhibit eddy current losses equivalent to 3 mil thick metglass tape undergoing the same flux excursion. In addition the Mn-Zn ferrites exhibit a large dielectric constant. Electromagnetic radiation propagates through the material at only a few centimeters per microsecond. This allows fairly small structures to be resonant in the frequency ranges of interest. If the entire ferrite toroid forms a single resonant structure, the loss tangent approaches unity.

1.3 Ferrite Sample Measurements

Sample ferrites were tested which spanned the range of applicable compositions. These ferrites were manufactured by Ceramic Magnetics Corporation and the compositions purchased - $(Zn_{65}\ Ni_{35})$, $(Zn_{60}\ Ni_{40})$, $(Zn_{54}\ Ni_{46})$, $(Zn_{45}\ Ni_{55})$, $(Zn_{30}\ Ni_{70})$, $(Zn_{15} \cdot Ni_{85})$, $(Ni_{1.0}) \cdot Fe_2O_4$ - correspond to CMD-5005, CN20, C2010, C2025, C2050, C2075, N40 respectively. Preliminary evaluation eliminated both C2075 and N40 from consideration.

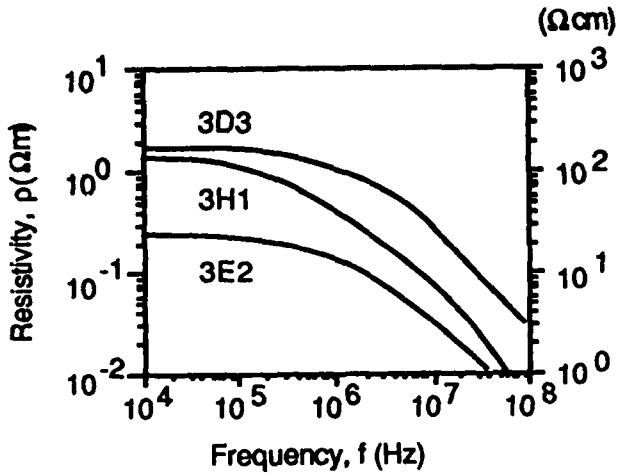

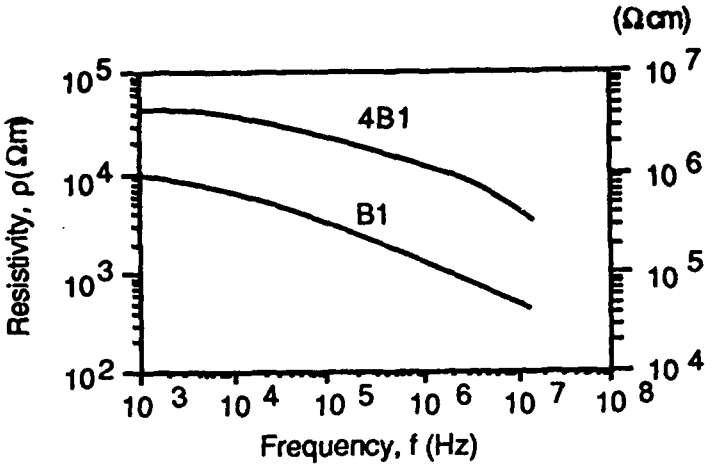

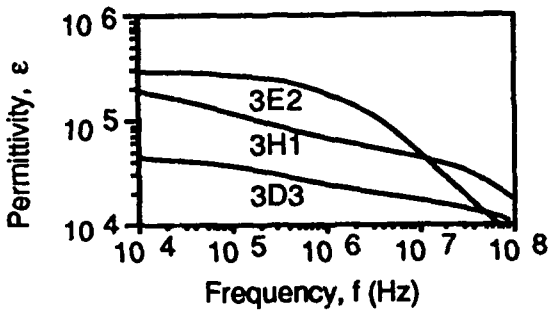

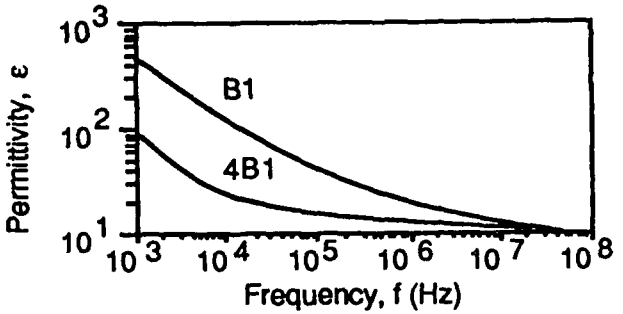

	Code No.	Manufr.	Class
MnZn ferrite	3H1	4	I
	3D3	4, 19	II
	3D2	4	III

	Code No.	Manufr.	Class
NiZn ferrite	B1	4	VI
	4B1	4	VII

Figure B.7: Resistivity and permeability of various ferrites as a function of frequency

78db590

A simplified schematic of the test stand used to evaluate these samples is presented in Fig. B.8. Samples were reset slowly and then rapidly cycled from $-B_r$ to $B-s$. Minor loops were not measured as they are not of interest in the applications we are considering where all of the available flux excursion in the ferrite is typically required. The saturation time-scales which could be measured range from 50ns to 500ns. At saturation times longer than 500ns, metal tape wound cores will outperform any available ferrite. At saturation times shorter than 50ns the test stand did not have sufficient drive power. The experimental results are presented in Figs. B.9-B.12.

The energy dissipated in the ferrite as the flux swings from $-B_r$ to B_s is plotted as a function of saturation time in Fig. B.13. The units are Joules/Meter^3 versus saturation time in nanoseconds.

If the ferrite is employed as a saturable reactor in a nonlinear magnetic compressor, then the volume of core required is linearly dependent on the square of the available flux swing. Simply because a candidate material exhibits a lower loss per unit volume does not mean it is the best choice as the core material. The best technique to identify the optimum core material in a saturable reactor is to plot energy loss per meter^3 per Tesla^2. This plot appears in Fig. B.14.

In high repetition rate applications, temperature rise can be an issue. As the temperature rises, the available flux swing is reduced until at the Curie temperature the available ΔB goes to zero. The higher the Curie temperature for a given composition, the more power can be dissipated in a given size sample with a specified surface temperature. In a case where the ferrite surface is anchored to a temperature of 50°C, the plot in Fig. B.15 gives an indication of the maximum repetition rate at which a given composition can be operated. Here the energy loss per cycle is divided by the maximum allowable temperature rise. The lower a curve lies on this plot, the higher the usable repetition rate.

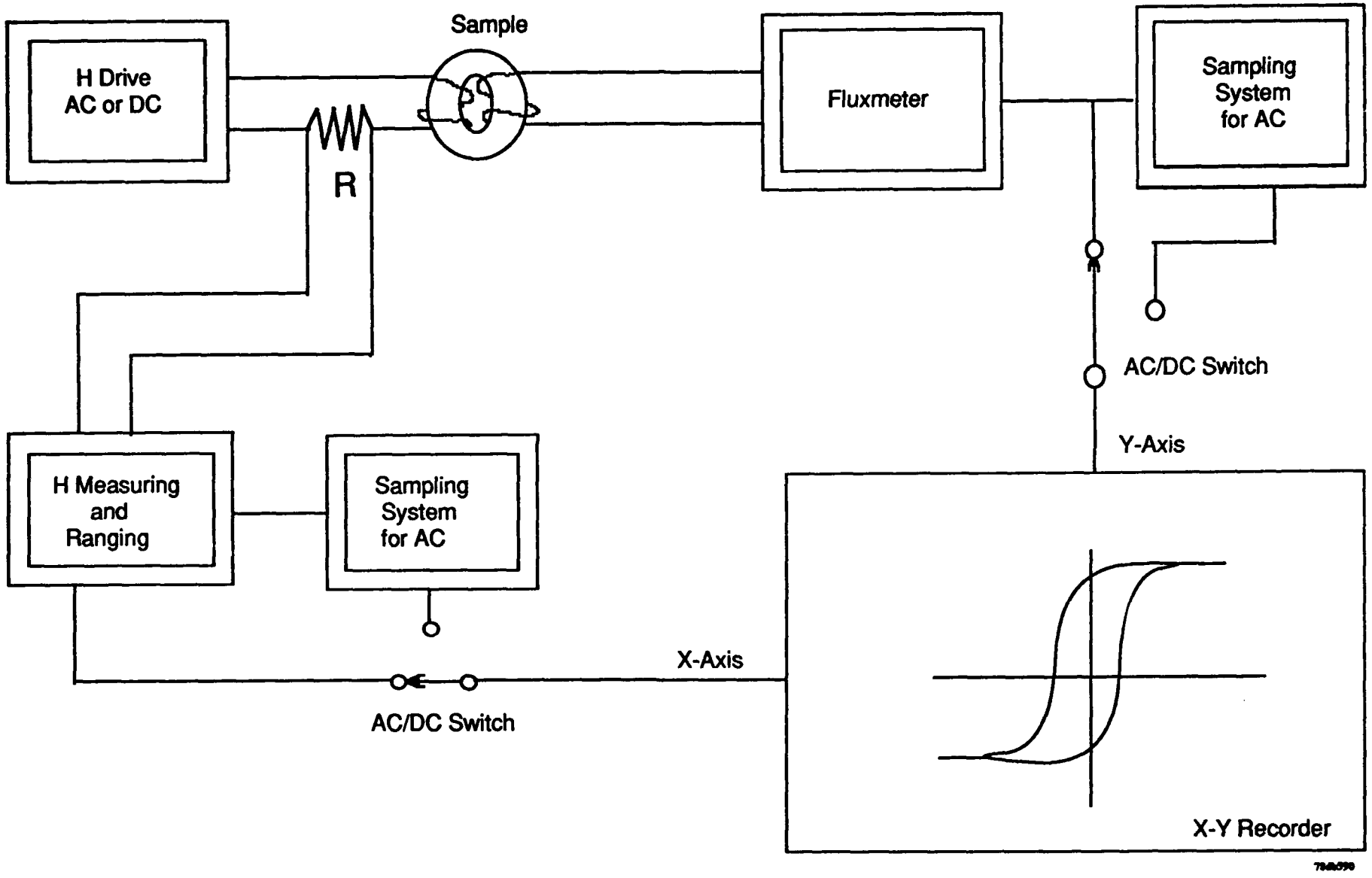

Figure B.8: B-H loop measurements

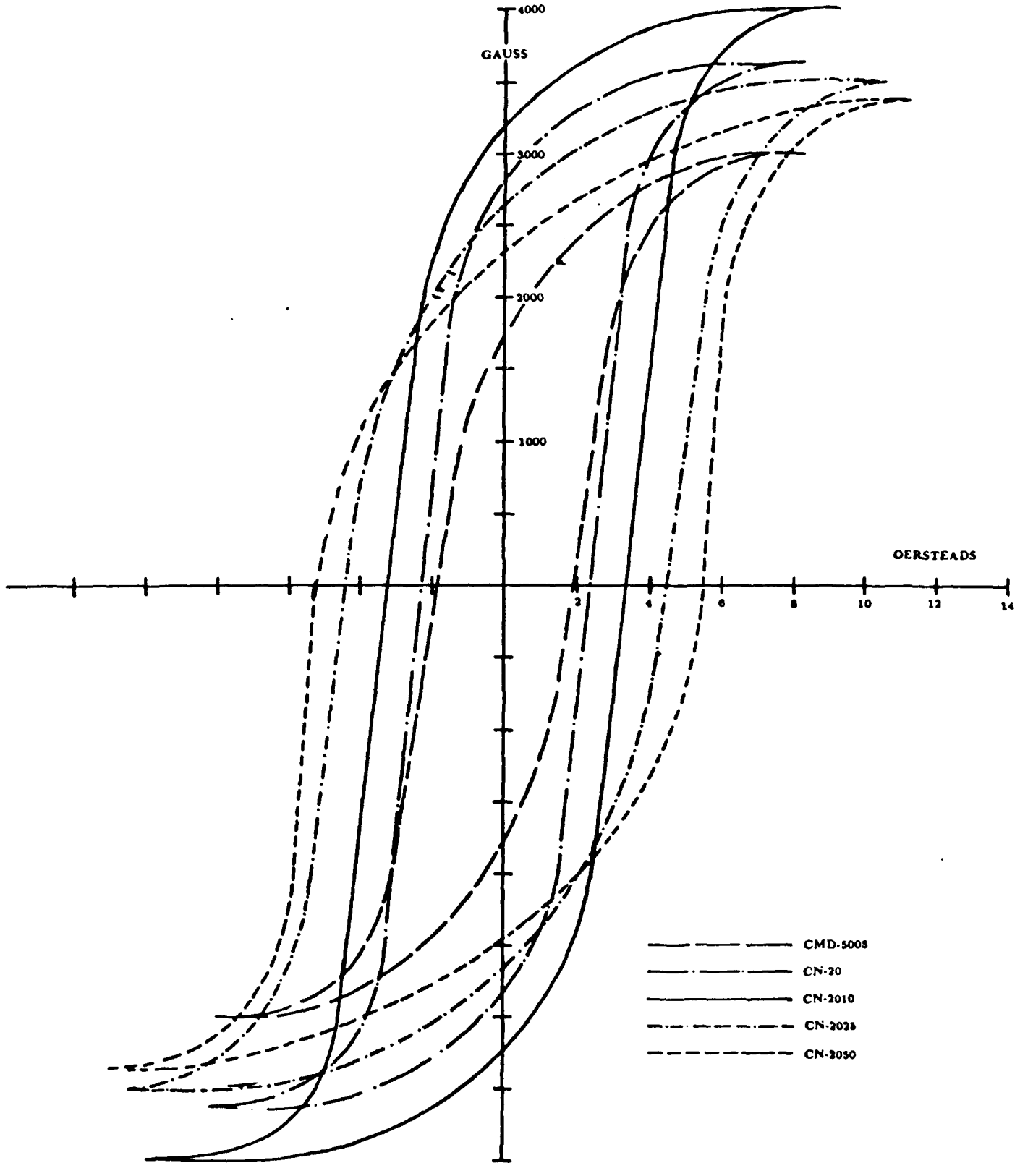

Figure B.9: Hysteresis curves measured at τ_{sat} = 500 ns

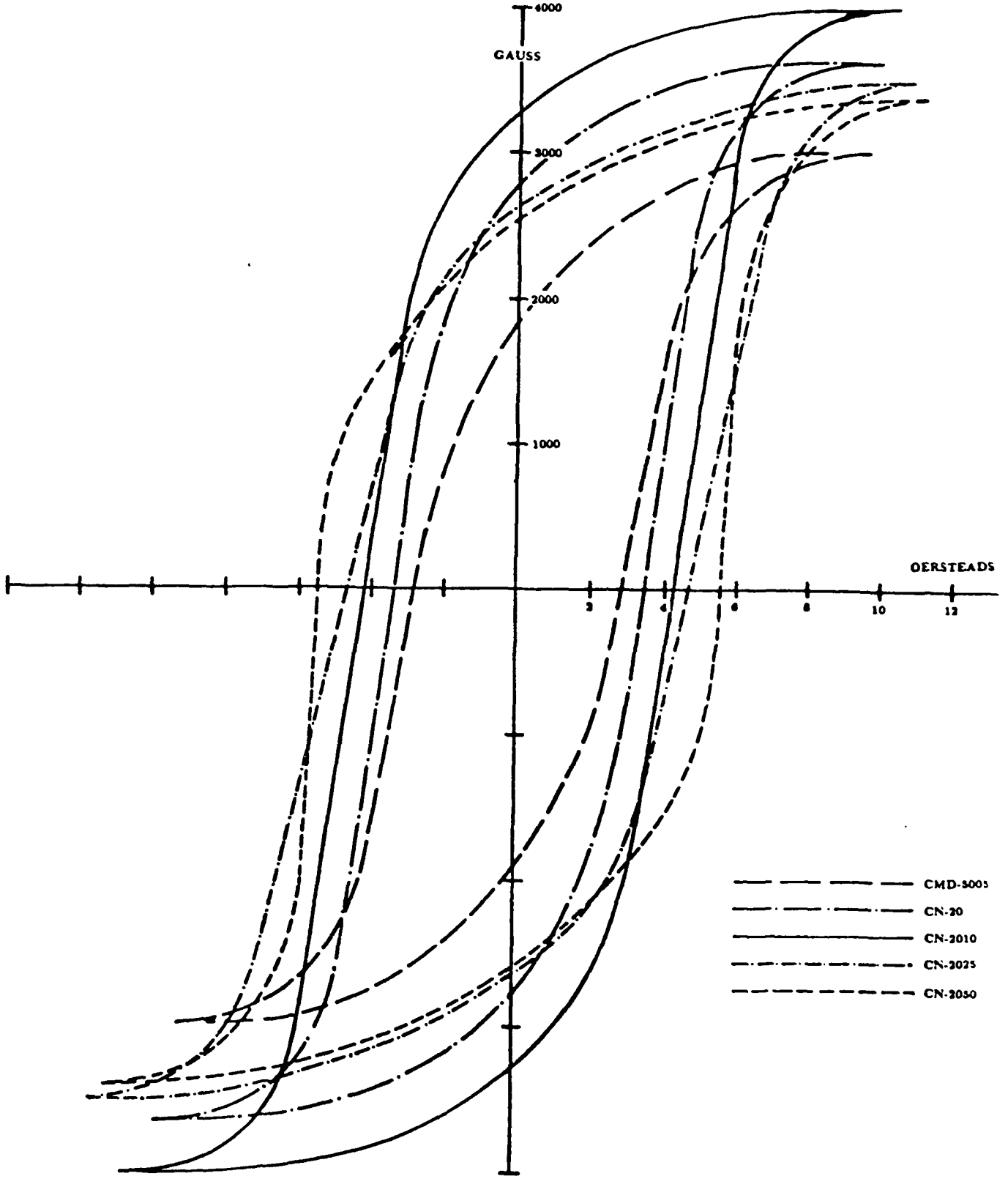

Figure B.10: Hysteresis curves measured at τ_{sat} = 250 ns

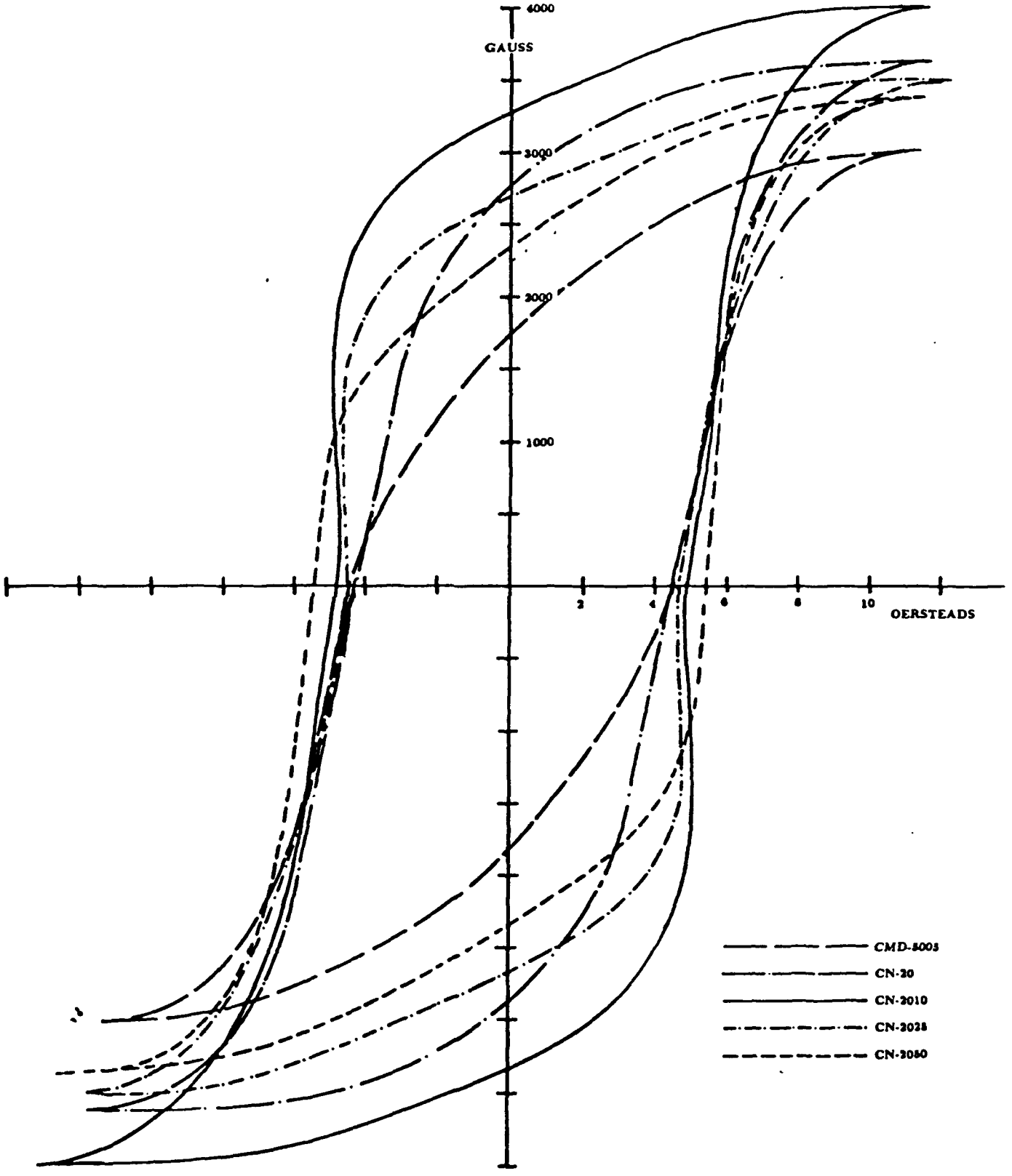

Figure B.11: Hysteresis curves measured at τ_{sat} = 100 ns

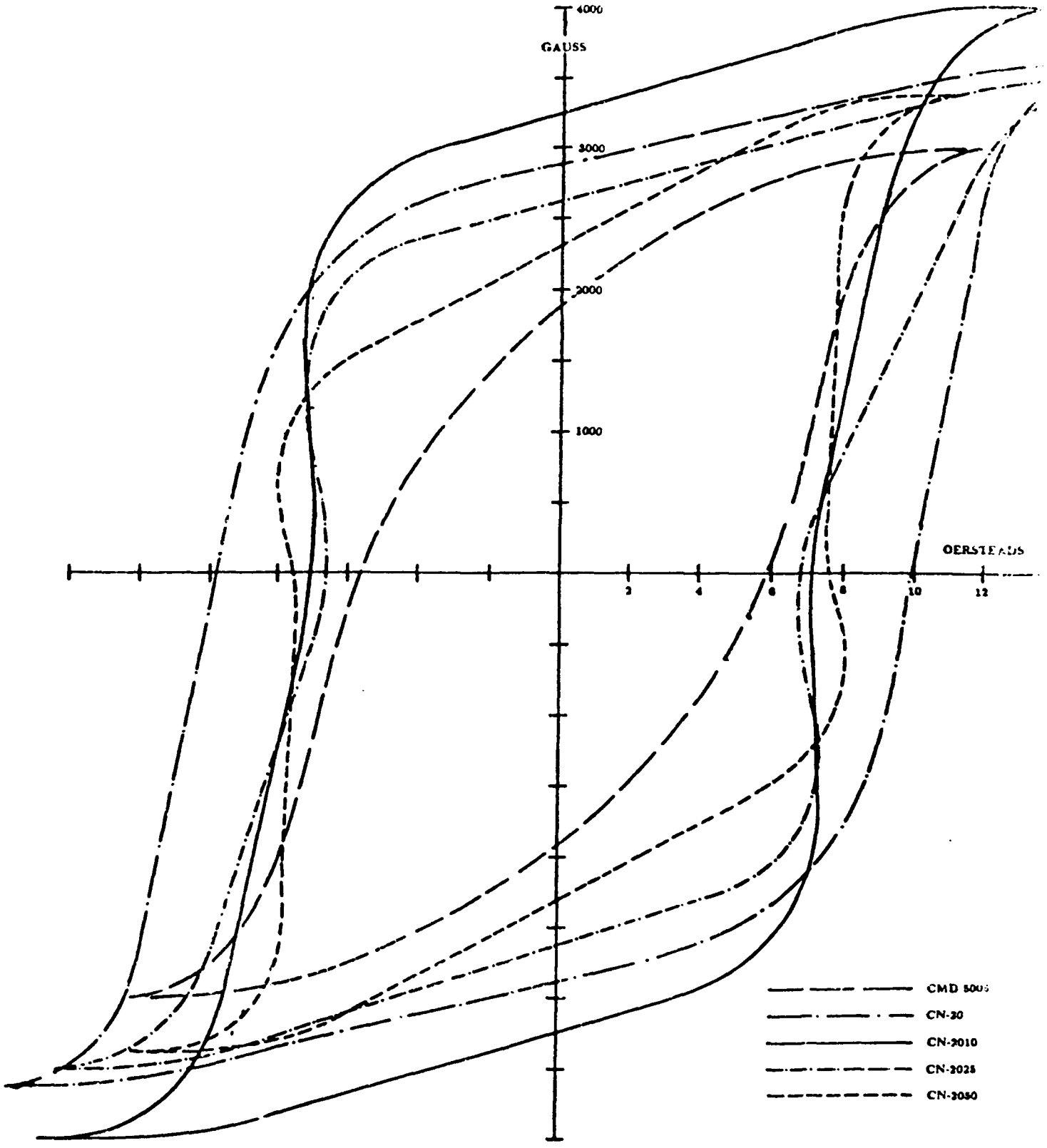

Figure B.12: Hysteresis curves measured at τ_{sat} = 50 ns

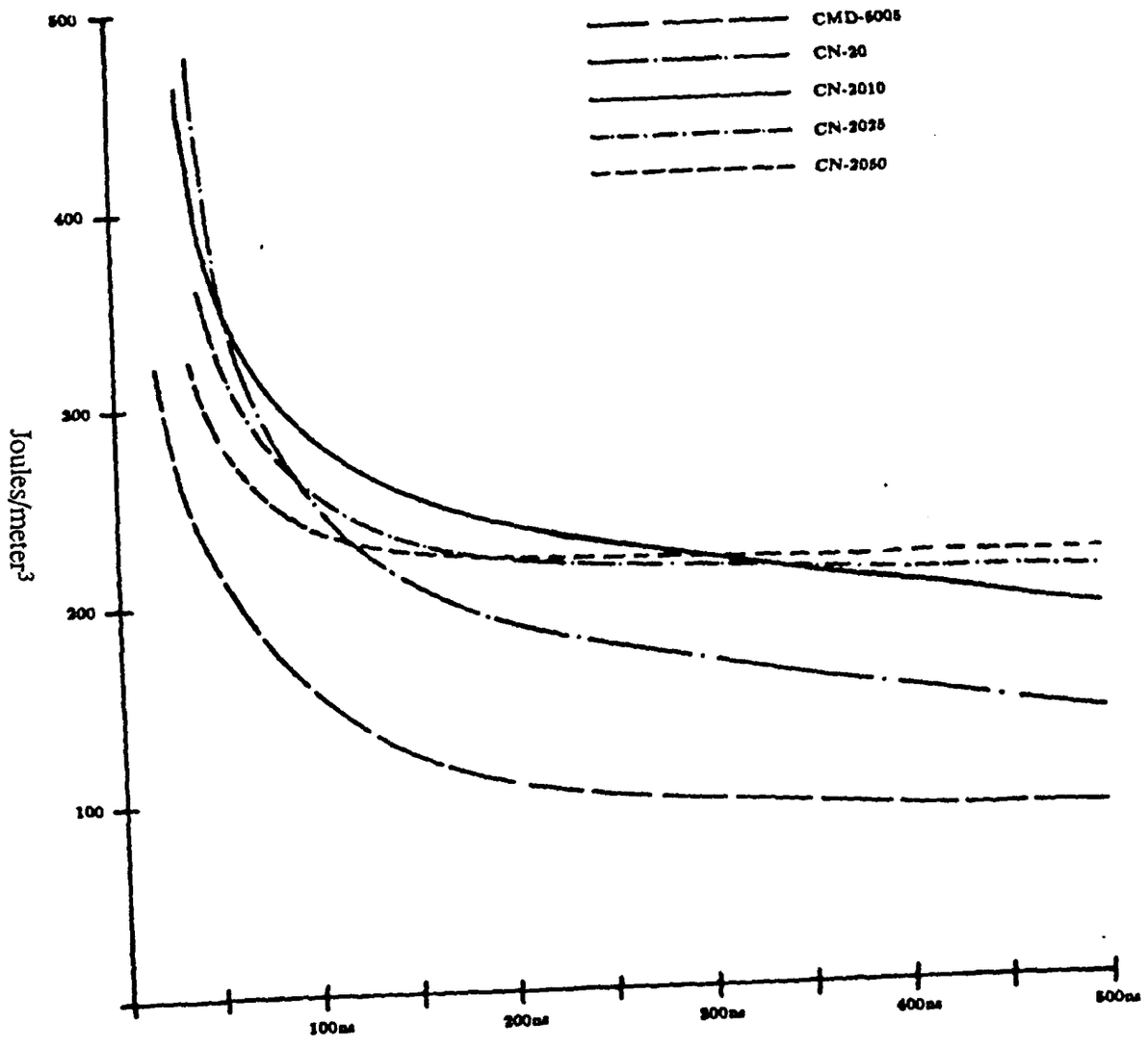

Figure B.13: Energy dissipated in ferrite materials as a function of saturation time.

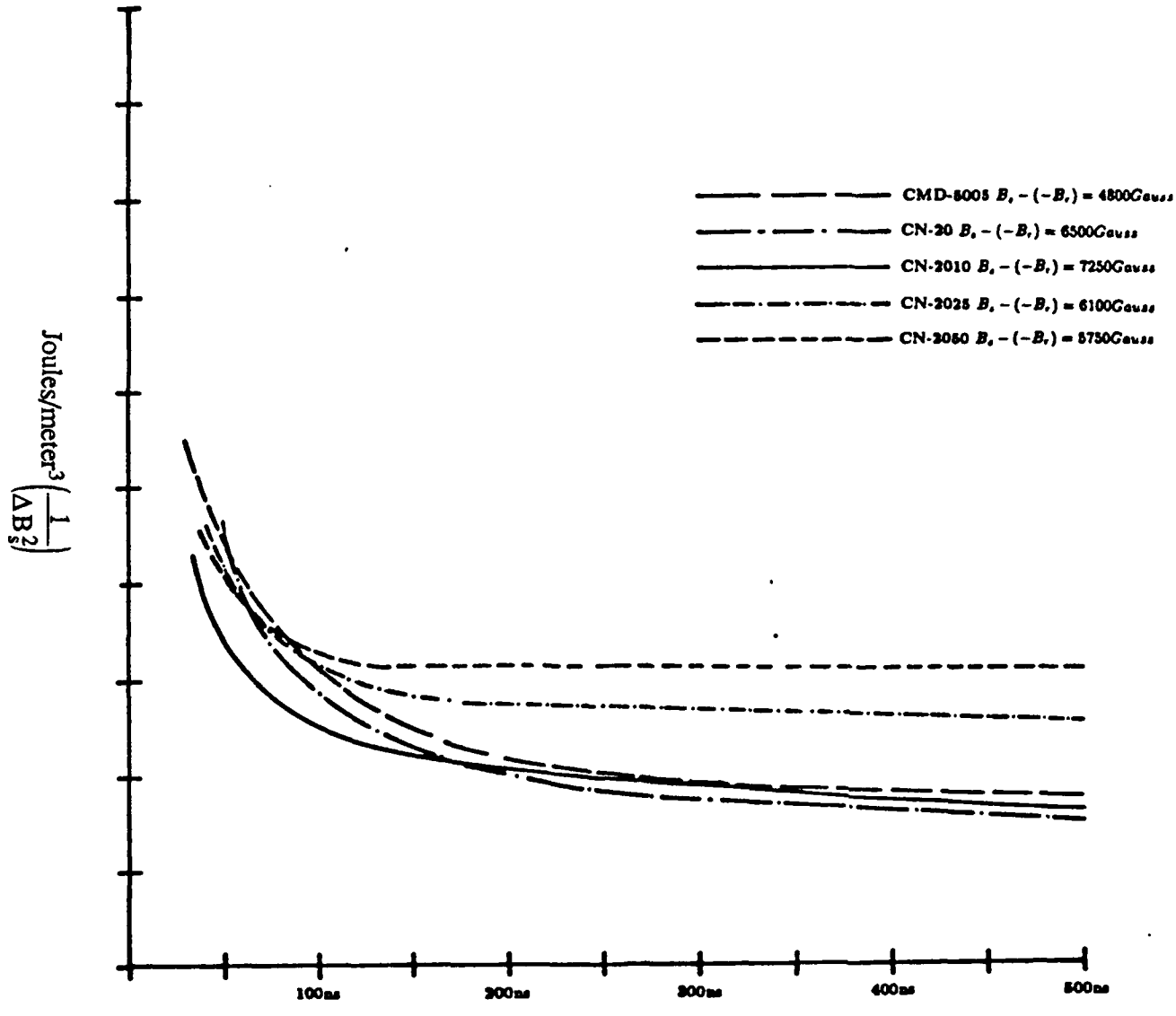

Figure B.14: Normalized energy dissipated in various ferrite materials as a function of saturation time.

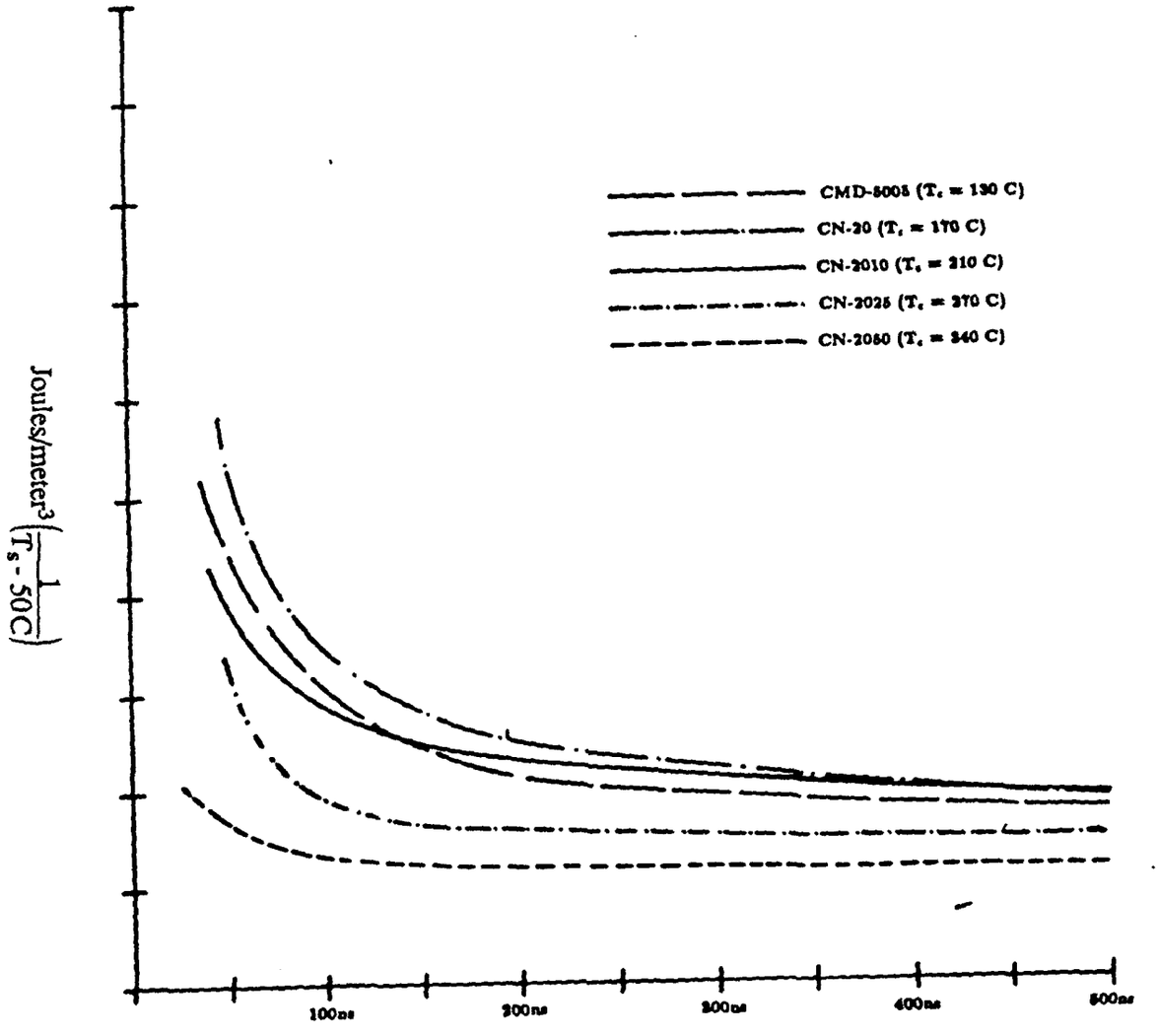

Figure B.15: Data for maximum temperature rise allowable in various ferrite materials.

APPENDIX C

1.0 COOLING OF FERRITE CORES

Improvements in the performance envelope can also be achieved through enhanced ferrite cooling. Coolant rates depend not only on the thermal conductivity and geometric dimensions of the ferrite core but also on the shape of coolant channels and the coolant flow dynamics. Efforts are made to avoid long, wide cooling channels which promote laminar flow and reduce the heat transfer coefficients. Short narrow channels are optimum and must be broken up at regular intervals to promote turbulence. A coolant liquid with an appropriately selected boiling point and enthalpy is also important as subcooled nucleation can play a critical role in increasing turbulence at the surface.

The heat transfer coefficient of a surface is a strong function of both the geometry and the surface texture. Every effort is made to break up laminar flow profiles and promote turbulence. This is accomplished without causing deterioration of the electrical properties of the ferrite. With an azimuthal magnetic field, radial grooving must be avoided but slotting along a radius can be extremely effective in promoting cooling. By machining slots into the ferrite comprising the multiple coaxial segments, the resistance to fracturing due to differential thermal expansion can also be avoided. Staggering these slots from one toroid to the next will break up the laminar flow patterns and promote turbulence.

The ferrite must be maintained at a temperature well below its Curie point. Energy is dissipated in the core material of a rate of $\sim$ 300 joules/m^3 per pulse. Waste heat removal is expedited by segmenting the core into thin split-washer-like toroids. The ferrite is immersed in freon and is cooled by the enthalpy of vaporization. In the case of the design discussed, the ferrite is not allowed to saturate and the average energy deposition is only 150 joules/m^3 per pulse. The core volume of 3.7 liters results in $\sim$ 0.5 joules per pulse per cell waste heat generation. Assuming f-11 Freon is used as a coolant (enthalpy of boiling = 180 joules/gram, vapor density = 0.005 grams/cm^3) the boiling rate would be $\sim$ 0.5 cm^3/Hz. Bubbles generated through this process and are collected on a cooled plate where heat exchangers recondense the

vapor back into the liquid phase. This method of cooling eliminates flowing liquids with the exception of room temperature coolant water to supply the heat exchangers. In the event that space or air basing is desired, a recirculating refrigerant might replace the water in the heat exchanger.

The maximum repetition rate at which a ferrite can be operated is determined by its Curie temperature and cooling rate. The cooling rate will depend on the temperature of the coolant, the temperature drop at the surface, and the temperature drop from the interior to the surface of the ferrite. The largest temperature drop for most geometries of interest is between the surface and the interior of the ferrite. The rate of heat transfer perpendicular to a lamina of area A, thickness δx, and thermal conductivity λ, when the temperature difference is $\delta\theta$, is given by $\lambda A\delta\theta/\delta x$ or

$$P_{cond} = \frac{\lambda\delta\theta}{\delta x} \text{w/cm}^2$$

Where P_{cond} is the rate of heat transferred by conduction. For a slab of thickness, d, the temperature difference between the center and the surface is given by

$$\Delta\theta = \frac{\text{Powerdissipated/UnitVolume}}{8\lambda} \cdot d^2.$$

The dimensions are in units of centimeters and degrees Celsius. For zinc-nickel ferrites $\lambda = 4 \cdot 10^{-2}$ w/cm^2.

APPENDIX D

1.0 COOLANT LIQUID SELECTION

The selection of an optimum coolant liquid is critical to the operation of the nonlinear magnetic pulse compressor. The coolant liquid serves both as an insulating and energy storage medium as well as the heat removal medium. The ability of a liquid to remove heat is dependent on many of the liquid properties. Of primary importance is the compatibility of the liquid with the operating environment. The coolant liquid must be non-corrosive, non-conductive, preferably non-flammable and capable of sustaining the electric field stresses which appear in the driver. In addition to these constraints it is preferred that the liquid remove heat by enthalpy of evaporation so that no active flow mechanism is required and waste heat can be removed by the process of heat piping. This requires that the boiling point of the liquid at reasonable operating pressures lie within the desired operating temperature envelopes. For one or more of the above considerations, the best liquids for heat removal (water, mercury, and alcohol) are eliminated.

If a candidate liquid satisfies the above criteria, then a relative figure of merit can be established by comparing the heat capacity, enthalpy of vaporization, thermal conductivity, inverse viscosity and dielectric strength. Referring to Table D.1, the critical properties for several candidate coolant liquids are summarized. The properties of water, mercury, and methanol are included for comparison. In order of performance, the author would list the candidates as Freon 11, Freon 113, Fluorinert FC-72 and Fluorinert FC-77. Fluorinert FC-72 is the perfluorinated sister to Freon 113 while Fluorinert FC-87 (which no longer appears in the 3M catalog) is the perfluorinated sister to Freon 11. In comparing Freon to Fluorinert it appears that Fluorinert has a dielectric strength almost 1.3 times higher than Freon but that Freon with its lower viscosity and higher enthalpy can remove heat about twice as fast. Fluorinert does have the advantage that it is considerably more chemically stable and non-hygroscopic. It is much less prone to decompose into an organic acid and to contamination by other organic compounds and will not remove the plasticizers from PVC.

Table D.1: Properties of Coolants

Measurements at 27°C

Fluid	Conductivity (W/cm -°K)	Mass Density (kg - m^3)	Specific Heat (J/kg - °K)	Viscosity (m^2/sec)	Dielectric Enthalph (kJ/kg)	Strength (kV/cm)	ε_r	Boiling Point (°C)
Freon 11	0.088	1472	0.888	2.82×10^{-7}	179.2	93		24
Freon 12	0.067	1305	980	1.95×10^{-7}	136.9	72		-29
$C_2Cl_3F_3$ Freon TF 113	0.067	1579	912	4.5×10^{-7}	169	117	1.849	45.8
Methanol	0.2022	785	2534	7×10^{-7}	1179		32.63	65
Water	0.6084	996.6	4177	8.26×10^{-7}	2438		81	100
Mercury	8.34	13,611	139.1	1.2×10^{-7}	302	N/A	∞	356
Fluorinert FC-77	0.064	1730	1044	13.032×10^{-7}	90.29	157		
Fluorinert FC-72	0.057	1680	1044	6.16×10^{-7}	94.8	150	1.76	56

APPENDIX E

1.0 THE SNOMAD DRIVER SCR TRIGGER SYSTEM

The performance of the main commutator SCRs influences the design of the entire SNOMAD modulator. In order for SCRs to function properly they must be provided with adequate trigger signals at the proper times. Indeed SCRs will fail if improperly triggered and experience has proven that any SCR failure in a SNOMAD modulator can always be directly linked to a failure in the SCR trigger circuit. This understanding has resulted in an almost complete elimination of SCR failures. Providing proper SCR triggers at the correct times is the responsibility of the SCR Driver in conjunction with the TRIGGER-I Snubber board.

We will begin our discussion of the SCR trigger system with a description of the TRIGGER-I snubber board. A detailed schematic of this circuit can be found in Fig. E.1. A printed circuit board containing this circuit is mounted to the lid of each SCR in the SNOMAD modulator. This snubber board assures that under almost all conditions the SCRs will receive sufficient trigger signal to turn on the entire junction. A partial trigger will only turn on some fraction of the junction resulting in almost certain device failure if the area turned on is smaller than required for the dI/dt to which the device is subjected.

The TRIGGER-I snubber board contains a trigger transformer which receives its input from two sources. The primary trigger source is the SCR Driver and this drives a 30 turn winding of the trigger transformer through a 100 Ω current limiting resistor. The SCR Driver also supplies a reverse bias to reset the transformer in between trigger pulses. A second winding on the trigger transformer is fed from energy stored in the .1 μfd. snubber capacitor. This winding performs a regenerative function in that as the SCR begins to conduct, energy is fed into the gate via the auxiliary 60 turn winding. The more the SCR conducts, the more energy is fed into the gate until the SCR is fully turned on. The voltage appearing on this auxiliary winding also induces a voltage on the 30 turn winding used by the primary trigger source. This signal is transmitted to all of the main commutation SCRs, so as one SCR turns on all of the other SCRs are guaranteed to be turned on to share the load.

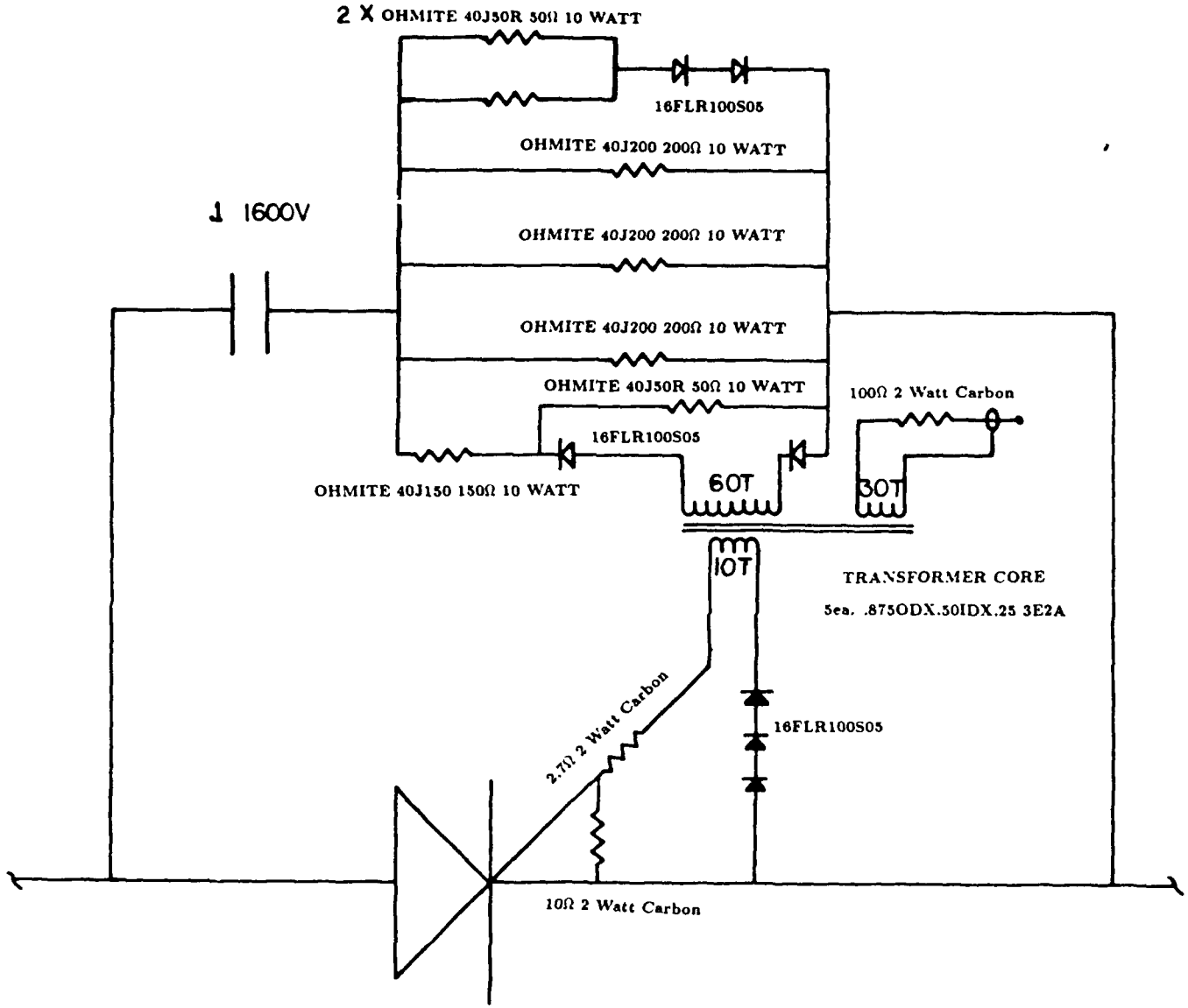

Figure E.1: TRIGGER-I Snubber Board

In summary the TRIGGER-I snubber board is the SCRs final line of defense against destructive partial triggers. TRIGGER-I's responsibility is to see that should an SCR begin to conduct, the SCR is turned on fully and all of the other SCRs are also turned on to share the load. It also performs the less challenging role of feeding charge through the SCR anode during the turn on phase and reducing dV/dt transients, as well as delivering the output of the SSLAM SCR Driver to the SCR gate after transforming the impedance from $\sim$ 100 ohms to $\sim$ 10 ohms. Unfortunately there is one chink in the defensive armour of the TRIGGER-I snubber board. TRIGGER-I relies on the energy stored in the snubber capacitor to perform it regenerative triggering function. If there is insufficient energy stored in this capacitor then TRIGGER-I will not be capable of delivering sufficient trigger to the SCR gates. It is the responsibility of the SCR Driver to assure that the modulator can not be operated in this mode.

A picture of the SCR Driver appears in Fig. E.2. The SCR Driver is housed in a 3 inch high by 15 inch deep standard rack mount chassis. It is a complete self contained unit including control logic, pulse amplifiers and power supplies. The SCR Driver requires only a single TTL level trigger pulse, 115 VAC, and voltage divider inputs to function. The voltage divider inputs allow the Driver chassis to monitor the voltage on the SNOMAD modulator power supply and Intermediate Storage capacitors. The SCR Driver also accepts input from several photodiodes mounted at strategic locations inside the modulator enclosure. The SCR Driver will disable the modulator should the photodiodes indicate an arc, in the case of an overvoltage or undervoltage condition of the Intermediate Storage capacitors, or in the case of insufficient power supply voltage to assure proper functioning of the TRIGGER-I snubber boards. The SCR Driver logic circuit also determines the timing between the Command Resonant Charge (CRC) pulse and the triggering of the main commutator SCRs. It also assures that false input trigger signals to the chassis are ignored by locking out the TTL input trigger for a period of 220 μsecs after receiving each trigger input.

A simplified schematic of the SCR Driver logic circuits appears in Fig. E.3. Referring to this schematic, sensoring inputs are carefully filtered and compared against adjustable references by

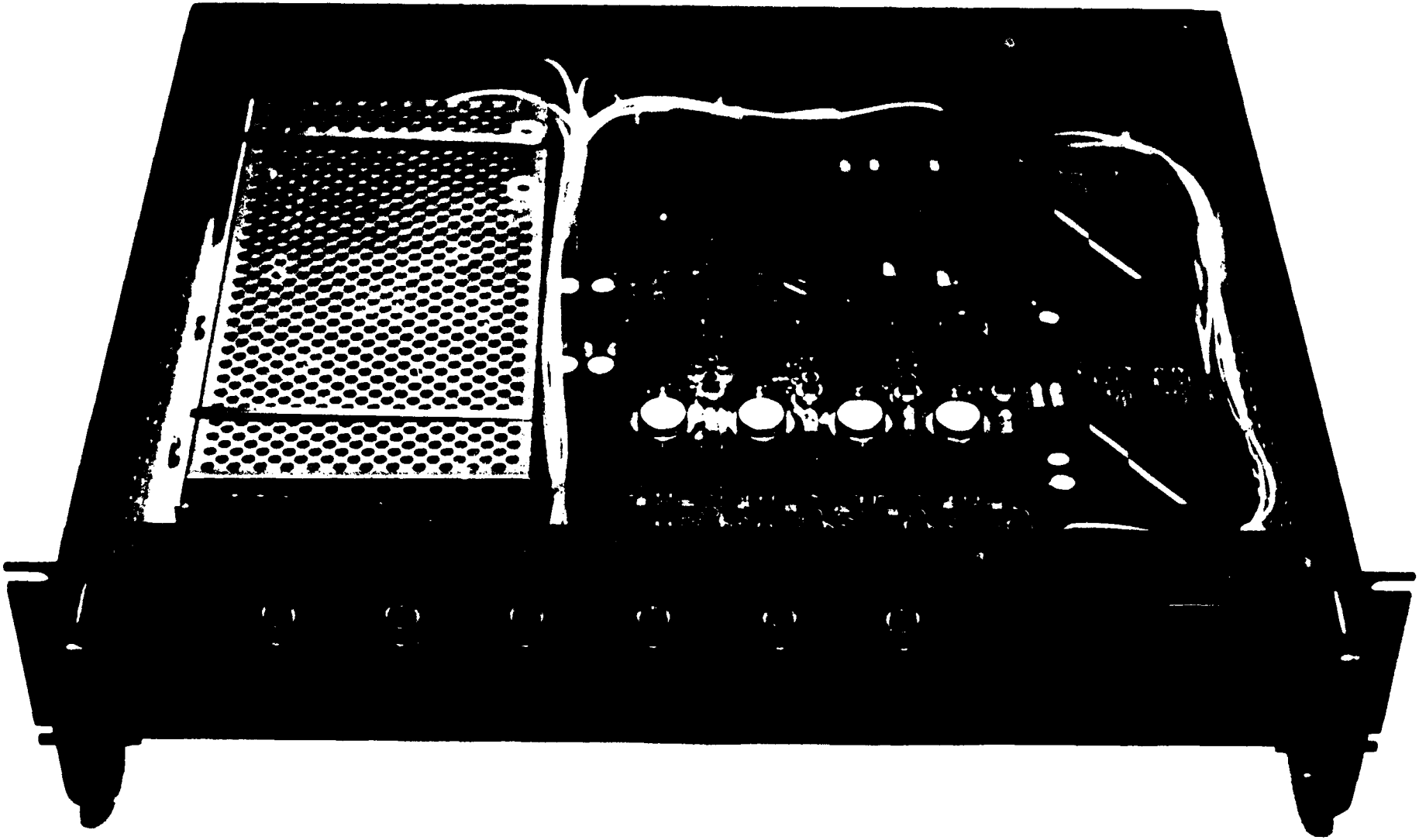

Figure E.2

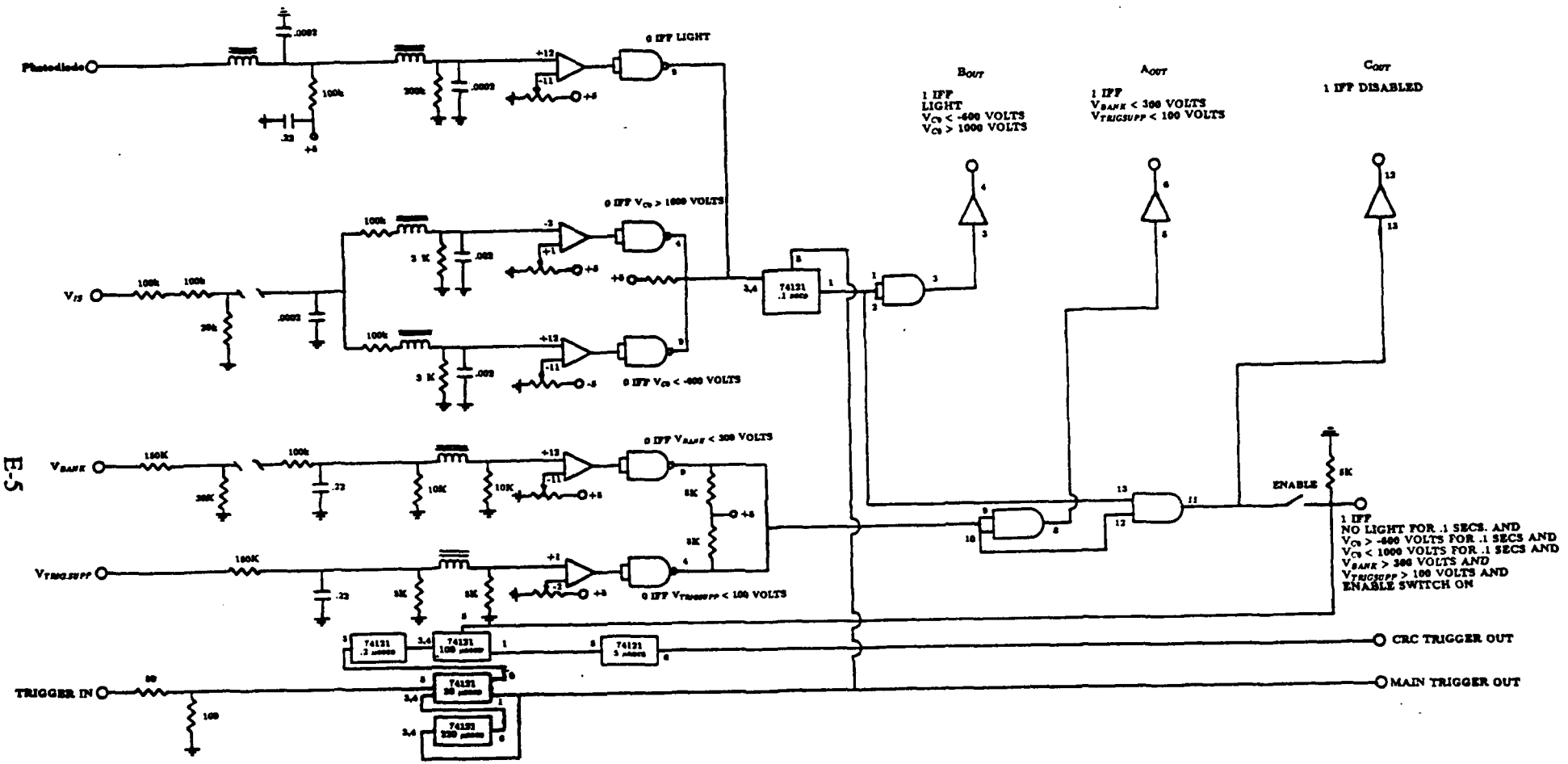

Figure E.3: SSLAM SCR Driver Logic Circuit

high speed NE522 comparators. In case the photodiodes detect an arc or an overvoltage condition is sensed the driver is disabled for .1 seconds to allow breakdown products to disassociate. A series of five 74121's generate the timing sequence, and a set of three buffers provide information to the operating system regarding the modulator status. The SCR Driver logic circuit provides two inputs to the output circuit. These two outputs are the properly timed trigger signals at TTL levels which control the CRC and Main SCR triggering. Referring to Fig. E.4 which shows a simplified schematic of the SCR Driver output circuit, the output trigger signals from the logic circuit are buffered via 75452 peripheral line drivers. The outputs of the 75452's drive IRF-460 MOSFETS which generate the 150 VDC trigger signals via 1:2 isolation transformers. The IRF-460 MOSFETs are protected from transients by a saturable isolation inductor and a diode clipper circuit. A bias circuit is also tied to each MOSFET output to assure that the trigger transformers on the TRIGGER-I snubber board are properly reset between pulses.

Finally in Table E.1 we provide a parts list for the SCR Driver chassis. Negatives for the printed circuit board, SRL-2650, on which all of the component mount are kept on file at SJS and made available to the DoD for reproduction. Silk screened instructions found on this printed circuit board make assembly straightforward. Silk screened front and rear panels for the SCR Driver can also be purchased from this vendor.

In summary, The SCR Driver chassis in conjunction with the TRIGGER-I snubber boards performs an invaluable role in the overall SSLAM modulator system. They monitor the modulator status and control its functioning. They assure both the survival of the modulator and the SCRs.

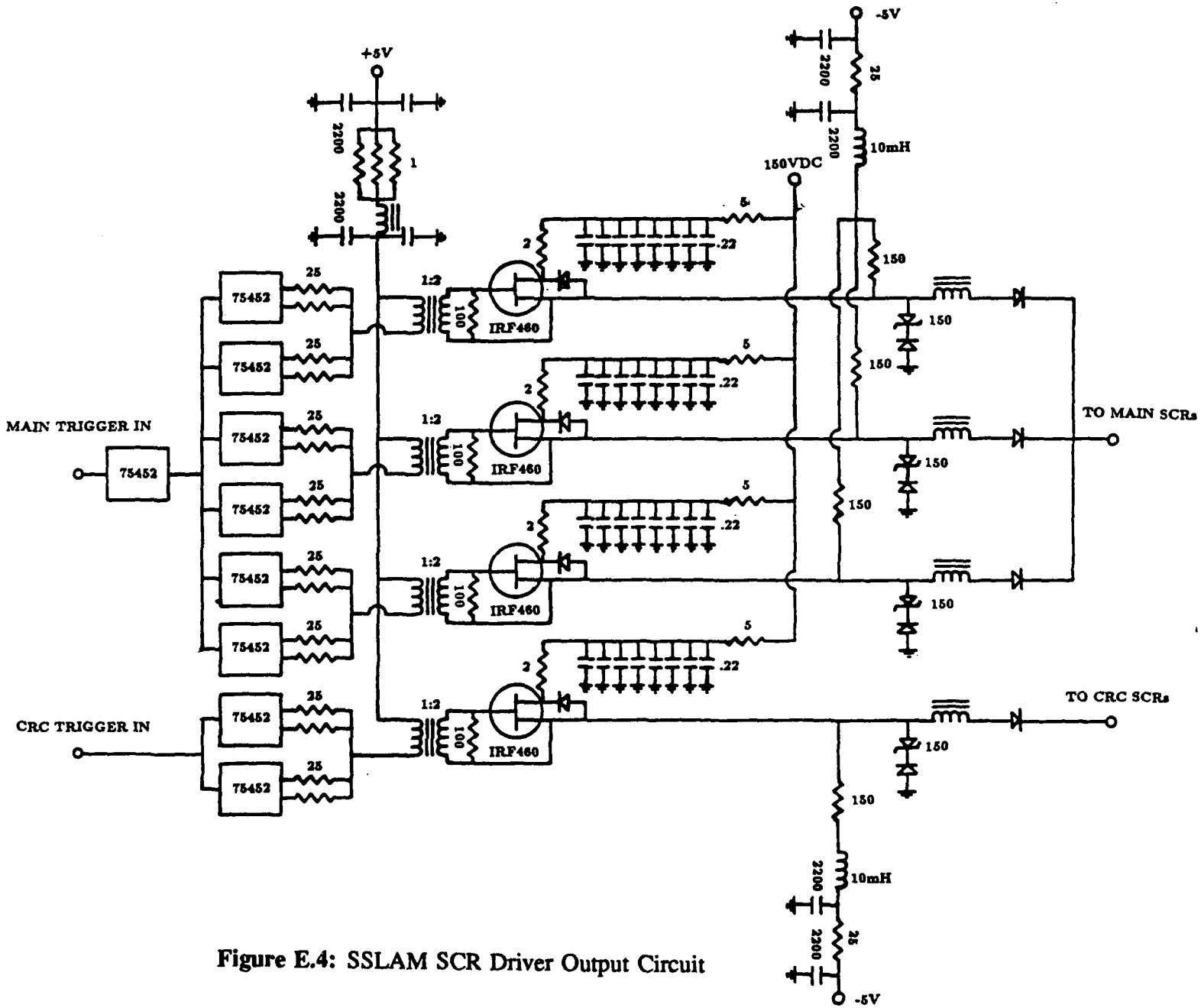

Figure E.4: SSLAM SCR Driver Output Circuit

TABLE E.1: SCR DRIVER COMPONENT LIST

DESCRIPTION	VENDOR	QUANTITY
SRL-2650 PC BOARD	SJS	1 ea.
TECHMAR VCD-3H-13D-BF/H-BP-RFP-1:CBA.R-2:SC-3H-13D-B		1ea.
FMP5-2K 5V,2A	KEPCO/TDK	2 ea.
NEW 44F1642 2200μfd,16V	MALLORY	7 ea.
NEW 59F316 50mH,65ma.	MILLER	4 ea.
NEW 15F2259 .5mH,2A.	MILLER	1 ea.
IR16FL100S05	IR	18 ea.
1N3015RB 200V Zener	MOTOROLA	32
IRF-460	IR	4
MKP-1845-.01,400V	RHOED.	8 ea.
MKP-1841 .22,160V	RHOED.	22 ea.
FKP-1 100pf,1600V	WIMA	1 ea.
FKP-1 680pf,1600V	WIMA	6 ea.
AUGAT 814-AG-10D	NEW 67F1801	10
AUGAT 808-AG-10D	NEW 67F1800	9
NEW 46F1439 SWITCH	2600H11E ARROW HART	1 ea
NEW 46F1858 SWITCH	2600HR11E ARROW HART	1 ea.
SN75452	TI	9
SN74121	TI	4
NE522	SIGNETICS	3
SN7408	TI	1
SN7404	TI	1

25Ω 1/2w CC	Allen-Bradley	16
50Ω 1/2w CC	Allen-Bradley	1
100Ω 1/2w CC	Allen-Bradley	6
200Ω 1/2w CC	Allen-Bradley	1
500Ω 1/2w CC	Allen-Bradley	1
3kΩ 1/2w CC	Allen-Bradley	2
5kΩ 1/2w CC	Allen-Bradley	5
6kΩ 1/2w CC	Allen-Bradley	1
10kΩ 1/2w CC	Allen-Bradley	3
30kΩ 1/2w CC	Allen-Bradley	1
40kΩ 1/2w CC	Allen-Bradley	1
100kΩ 1/2w CC	Allen-Bradley	2
150kΩ 1/2w CC	Allen-Bradley	1
200kΩ 1/2w CC	Allen-Bradley	1
1 MEGΩ 1/2w CC	Allen-Bradley	1
1Ω 3.25W	OHMITE 13F145	3
2Ω 3.25W	OHMITE 13F145	4
5Ω 3.25W	OHMITE 13F145	4
25Ω 3.25W	OHMITE 13F145	1
75Ω 3.25W	OHMITE 13F145	1
20kΩ 1/2w	NEWARK 81F1153 AB	5
.875ODX.5IDX.25 3E2A	846XT250 FERROXCUBE	4
.500ODX.375IDX.25 3E2A	768XT188 FERROXCUBE	4
.375ODX.187IDX.125 3E2A	266CT125 FERROXCUBE	4
RED # 24 AWG 600V TFE	BELDEN	25ft
BLK # 24 AWG 600V TFE	BELDEN	15ft
WHT # 24 AWG 600V TFE	BELDEN	25ft

APPENDIX F

1.0 SCR SELECTION

Understanding the loss mechanisms in SCRs is important in establishing the operating limitations for these devices. If a simple model is assumed where the usable area of the device is a function of the time interval between triggering ($t = 0$) and device turn-on ($t = t_o$), then for an interdigitized gate structure the active area would be given by

$$A(t) = A_0 \cdot \frac{t}{t_0} \qquad t < t_0$$

$$A(t) = A_0 \qquad t > t_0$$

For a center-fire gate structure the time dependence of the conducting area should be

$$A(t) = A_0 \cdot \left(\frac{t}{t_0}\right)^2 \qquad t < t_0$$

$$A(t) = A_0 \qquad t > t_0$$

where A_0 is the total junction area and $A(t)$ is the time dependent region which is fully conductive.

The energy dissipated per pulse will be given by

$$\text{Energy} = \int_0^\tau I^2(t) \cdot R(t)dt$$

where τ is the pulse length and $R(t)$ is the time-varying resistance of the junction. According to this simple model

$$R(t) = R_0 \cdot \frac{A_0}{A(t)}$$

If a current waveform having a sinusoidal time dependence is assumed, then for $t_0 << \tau$

$$\text{Energy Loss} = I_0^2 R_0 \cdot \left(\frac{\pi^2 t_0^3}{6\tau^2} + \frac{\tau}{2}\right) \qquad A(t) = A_0 \left(\frac{t}{t_0}\right)$$

$$\text{Energy Loss} = I_0^2 R_0 \cdot \left(\frac{2\pi^2 t_0^3}{3\tau^2} + \frac{\tau}{2}\right) \qquad A(t) = A_0 \left(\frac{t}{t_0}\right)^2$$

We can therefore define a predicted dynamic resistance given by

$$R(\tau) = R_0 \left[1 + \text{const} \cdot \left(\frac{t_0}{\tau} \right)^3 \right]$$

This predicted energy loss does not adequately describe the experienced time-dependent behavior of SCRs. Immediately following turn-on (<1 μsec), this time dependence may be present, but use of a saturable magnetic assist limits the peak current during this interval to such a low value that little energy is dissipated. Analyses of experimentally-measured time dependent losses in such circuits indicates a behavior given approximately by

$$R = R_0 \left[1 + \frac{\text{const}}{I_0} \cdot \left(\frac{dI}{dt} \right) \right]$$

This would indicate that to first order the actual device turn-on losses are not adequately described by a model where the conduction area is time dependent but rather by a model in which the whole device requires time to react to changing currents. This suggests that so long as the limiting dI/dt is not exceeded (which might result in excessive voltage drops followed by electrical breakdown), the energy absorbed due to rising conduction currents is most likely distributed throughout the device.

It appears that the diffusion of minority carriers across the junction is the dominant loss mechanism. This means that even after an SCR has been conducting low level current indefinitely, dI/dt losses will still be associated with an increase in current. This mechanism also explains why the reverse recovered charge during turn-off is such a strong function of the dI/dt. Saturable inductors to limit turn-on currents will only help if they reduce the current during the first microsecond or so when the conduction area is still expanding.

It is also easy to explain why the voltage drop across the device increases faster than linearly with dI/dt for pulse lengths approaching the carrier lifetime. Rapid fluctuations in the current cause rapid carrier concentration variations at the junction with very little effect on the concentrations far from the junction. This results in a decrease in the effective diffusion capacitance. For sinusoidal waveforms it can be shown that the effective junction diffusion

capacitance defined as $C_d = dQ/dV$ is given by

$$C_d = (1/2)\tau(dI/dV) \qquad \omega\tau << 1$$

$$C_d = (\frac{\tau}{2\omega})^{1/2}(dI/dV) \qquad \omega\tau >> 1$$

After reviewing the test data accumulated in an intensive effort by Ed Cook at LLNL, it appeared redundant to establish our own SCR test stand. Instead, candidate devices whose performance had been thoroughly documented were installed at different times into the modified SNOMAD-I driver. Performance data was collected under actual operating conditions with SNOMAD-I driving a copper vapor laser at full power. Since devices with different case and wafer sizes were tested, in some cases several devices (≤ 4) were installed in an isolated parallel fashion.

The wide variation in performance indicated in the manufacturers specifications is somewhat deceiving. The maximum RMS current is predominately determined by the wafer area while the peak operating voltage is determined by the wafer thickness. The recovery times are determined primarily by the carrier lifetime and the junction diffusion capacitance. The recovery times can be decreased by decreasing the carrier lifetime but at the expense of slightly increased conduction losses.

In summary all of the devices are based on silicon, use similar doping levels, and have similar gate interdigitation levels. All the manufacturers listed sell SCRs with similar operating voltages, RMS current levels, and dI/dt capability. Choosing a device with a lower RMS current rating will require the designer to parallel several devices. The selection of an appropriate SCR is straightforward and, for a given operating envelope, if the appropriate device from one manufacturer fails, it is likely that an equivalent device from any of the other manufacturers will be at least stressed very close to its limit in the same socket.

APPENDIX G

1.0 CAPACITOR SELECTION

As reliability and performance continues to improve, components which initially could be neglected begin to impact the overall reliability. Capacitors are a good example of this phenomenon. Present requirements for low loss operation a 6 kHz reliably and continuously for years eliminates most energy storage media. Mylar, the most common storage medium for pulsed power applications at low duty factors, must be eliminated because of its high loss tangent. Polycarbonate and reconstituted mica also are unusable for this reason.

Aluminized polypropylene with interleaved aluminum foil conductors fully extended appears to be the best dielectric material for the low voltage front end. Strontium titanate ceramic capacitors demonstrate a similar loss tangent and would be used in the front end of the pulser if fabrication in thin sheets were not so difficult. They are an excellent choice at voltages in excess of 20 kV where they can be fabricated as disks.

Candidate polypropylene capacitors are available from several manufacturers. Rhoderstein, WIMA, ByCap, GE, Sprague, and Maxwell are examples. WIMA presents a product line which extends to 2 kV operating voltage and is suitable for operation at CW repetition rates in excess of 100 kHz. SNOMAD-I employs WIMA capacitors while SNOMAD-II utilize ByCap devices and SNOMAD-IV and SNOMAD-V use Rhoderstein capacitors. To date, there has been zero failure of these capacitors in these pulsers. Strontium titanate capacitors are only available from TDK and Murriata-Erie. TDK is the most common supplier and manufactures devices in the range of 20-50 kV. Parameters for the various candidate dielectric materials appear in Table G.1.

Table G.1: The Essential Characteristics of the Plastic Dielectrics Used

Physical Characteristics of the film	Polyester	Polycarbonate	Polypropylene	$SrTiO_2$	Reconstituted Mica
Dielectric Constant 1 kHz/23 C	3.3 (positive as temp. rises)	2.8 (largely constant over temp. range)	2.2 (negative as temp. rises)	~ 5000	
Dielectric Loss factor Tan δ/23°C 1 kHz 10 kHz 100 kHz 1 MHz	5×10^{-3} 11×10^{-3} 18×10^{-3} 20×10	1.5×10^{-3} 5×10^{-3} 10×10^{-3} 10×10	1×10^{-4} 1×10^{-4} 1×10^{-4} 1×10	< 0.1%	0.5%
Specific volume Resistance $\Omega\times$ cm/23°C	10^{18}	2×10^{17}	6×10^{18}	$> 10^{12}$	6×10^{17}
Dielectric strength in V/μm at 23°C	580 V-	535 V-	650 V-	> 10	
Preferred temperature range	-55...+100°C	-55...+100°C	-55...+85°C	-55...-85°C	-65...-125°C
Dielectric absorption in % at 23 C	0.20...0.25	0.12...0.20	0.05...0.10	< 0.1%	< 0.5%
Energy Density	12.7 kJ/m^3	9.5 kJ/m^3	5.4 kJ/m^3	15 kJ/m^3	15 kJ/m^3

APPENDIX H

1.0 INDUCTION CELL DESIGN

1.1 Introduction

Among the family of particle accelerators, the Induction Linear Accelerator is the best suited for the acceleration of high current electron beams. Because the electromagnetic radiation used to accelerate the electron beam is not stored in cavities but is supplied by transmission lines during the beam pulse, it is possible to utilize very low Q (typically < 10) structures and very large beam pipes. This combination increases the Beam Breakup limited maximum currents to several kiloamperes. The micropulse lengths of these machines is measured in 10's of nanoseconds and duty factors as high as 10^{-4} have been achieved. Until recently the major problem with these machines has been associated with the pulse power drive. Beam currents of kiloamperes and accelerating potentials of megavolts required peak power drives of gigawatts since no energy was stored in the structure.

The marriage of linear induction accelerator technology with nonlinear magnetic pulse compressors has produced some unique capabilities. It now appears possible to produce electron beams with average currents measured in amperes, peak currents in kiloamperes and gradients exceeding 1 MeV/meter, with power efficiencies approaching 50%. Nonlinear magnetic pulse compression technology has replaced the spark gap drivers used on earlier accelerators with state-of-the-art, all-solid-state, SCR-commutated compression chains. The reliability of these machines is now approaching 10^{10} shot MTBF.

Unfortunately induction accelerators are still limited to rather modest gradients and are large and expensive. While there has been considerable effort expended in optimizing the pulsed power drive for these accelerators, there have been little investigation into the optimization of the induction accelerator cells themselves. In this proposal we will present a research plan aimed at improving the operating gradients and reducing the weight and cost of the Induction Accelerator cells. This research will culminate in the construction and test of a high gradient, lightweight, 2 MeV linear induction accelerator based on these new design principles.

1.2 Induction Accelerator Cell Design

In the following section we will discuss the considerations involved in conventional induction cell design. We will see the critical role played by the ferrite material properties. We will also show that the accelerator gradients and weight vary linearly with the pulse length. We will then discuss alternative induction cell designs.

Both RF and induction linear accelerators are composed of multiple transmission line transformers. While these transmission lines are all driven in parallel as the electron beam passes through them, their voltages add energy to the electron beam in series. Isolation between the transmission lines is achieved by connecting them with a beam pipe which is below cutoff at the operating frequency for all modes except the TEM_{00}. The electron beam forms the inner conductor for this mode. Early Soviet literature describes RF accelerators as air core induction linacs.

If the accelerator is to be efficient, the losses in the transmission line must be negligible in comparison to the energy coupled into the electron beam. In other words, the effective impedance of the transmission line Z_{eff} must be large compared to V_{LINE}/I_{BEAM}. For an RF accelerator, the characteristic line impedance Z_{LINE} may be low, less than 100 ohms, but it is resonant and therefore the effective impedance becomes $Z_{eff} = Z_{LINE} \cdot Q_L/2\pi$ (lowest order mode) where Q_L is the loaded Q of the resonant cavity.

Resonant RF structures also have the advantage that they provide a voltage step up over the drive voltage by a factor.

$$V_{acc} = V_{driver} \cdot Q_L^*/2\pi$$

where:

$$Q_L^{*-1} = Q_u^{-1} + Q_e^{-1} + Q_{\text{beamloading}}^{-1}.$$

The disadvantage of resonant structures is that a cavity (shorted $\lambda/2$ transmission line) is never simply resonant with a single mode and the wake functions of the electron beam have Fourier components which feed energy into all available modes. Some of these modes are

spatially antisymmetric and act to steer the electrons into the beam pipe wall. This sets an upper limit to the total charge which can be accelerated during an RF cavity decay time ($\tau = Q_L/\omega$).

An induction cell is non-resonant and if designed properly stores neither the drive fields nor the wake fields. This dramatically increases the practical operating current but also places constraints on the minimum efficient operating current. If the induction accelerator cell used vacuum as a transmission line medium, the maximum impedance in practice would be less than a few hundred ohms. In operating induction linacs which provide short pulses ($\sim$ 50 ns), this line is filled with ferrimagnetic material (ferrite); for long pulses (50 nsec $\leq \tau_p \leq 1\mu$sec), ferromagnetic materials (e.g. Si-Fe, Metglass, Superpermalloy) are employed. Most high frequency ferrites have dielectric constants of order $\epsilon_r = 10$ and permeabilities of order $\mu_r = 1000$. With ferrite as a medium, the characteristic transmission line impedance is increased over the vacuum value by a factor of $(\mu_r/\epsilon_r)^{1/2} = 10$, yielding effective shunt impedances as high as several thousand ohms. Also the use of ferrite shortens the length of the transmission line required to provide isolation at the desired drive pulse length. Since the group velocity, $v_g = c/(\mu_r\epsilon_r)^{1/2} \simeq c/100$, the transmission line is shorter than the vacuum equivalent by a factor of order 100. Some low frequency RF accelerators employ ferrite solely for this purpose even though the line is resonant.

In summary the use of ferrite in the accelerator cell increases the practical micropulse length by a factor of 100 and the use of a non-resonant structure (induction linac) increases the maximum electron beam current by not storing wake fields. The penalty accompanying these advantages is centered on the fact that induction accelerators are incapable of efficiently accelerating very low current beams.

Design of an induction accelerator cell is relatively straightforward if these basic operating principles are kept in mind. The following rules must be observed. The variables discussed refer to those pictured in Fig. H.1.

I. The length (h) of the ferrite loaded transmission line is determined by the pulse length and the electrical characteristics of the ferrite.

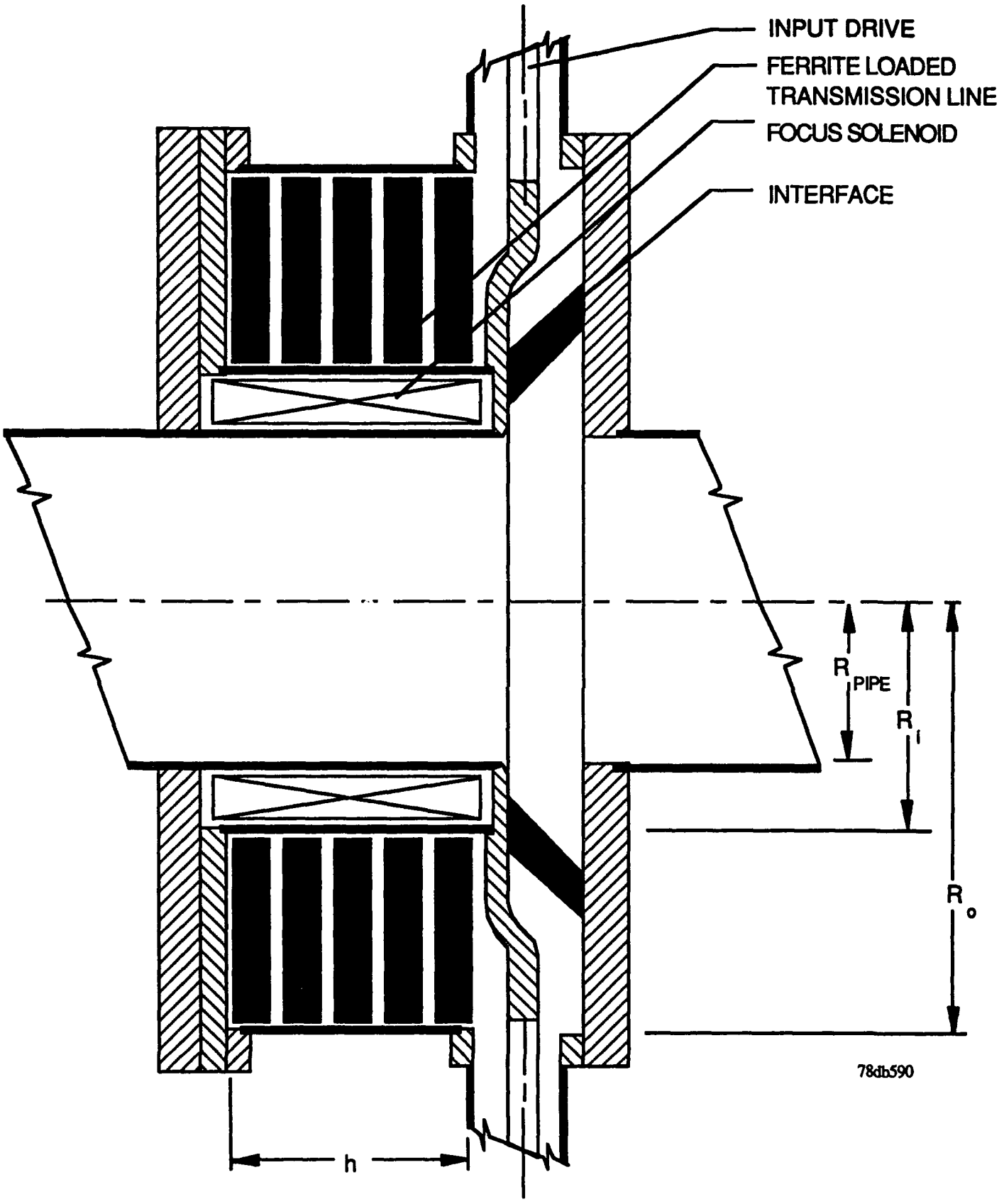

Figure H.1: Simplified cross section of a conventional induction accelerator cell

$$2 \cdot h \geq \tau_p(\text{pulse length}) \cdot \text{velocity}$$

$$= \tau_p \cdot \frac{c}{\sqrt{\epsilon_r \mu_r}} \approx \frac{\tau_p \cdot c}{100}$$

In practice, the best performance is achieved by setting h = t_p· c/100 or in other words setting the line length equal to a single transit time rather than a round trip time. This constraint arises because the ferrite properties are field dependent and the minimum ferrite volume is achieved by designing around a single transit time. Making h longer than a transit time is wasteful as the additional ferrite will never be seen by the pulse. Summarizing, for optimum performance:

$$h \approx \frac{\tau_p \cdot c}{(\epsilon_r u_r)^{1/2}} \approx \frac{\tau_p \cdot c}{100}$$

II. The value for $(R_o - R_i) = \Delta R$ is set by the drive voltage and the maximum flux swing of the ferrite. As the wave generated by the drive pulse is transmitted down the line, the creation of a saturation wave must be avoided or the impedance of the line will appear time dependent.

$$\text{Since : } \int E \cdot dl = -\frac{d}{dt} \int B \cdot da$$

if one assumes μ is constant and B = μH

then

$$B \leq B_{sat}.$$

Two extreme cases may be considered:

A) If B(r) = const, then

$$\text{Voltage} \leq \Delta B_s \cdot \Delta R \cdot v_g$$

B) If B(r)α1/r and if no portion of the line is allowed to saturate

$$B(R_i) \leq B_{sat}$$

and

$$\text{Voltage} \leq \Delta B_s \cdot v_g \cdot R_i \cdot \ln(R_o/R_i)$$

In practice μ is not a constant and is dependent on both dB/dt and H. This causes the real requirement to lie somewhere in between cases (A) and (B) so that $B(r)\alpha r^{-\alpha}$, $0 \leq \alpha \leq 1$.

III. Beam Pipe Radius - R_{PIPE}

Three competing requirements determine the optimum value for R_{PIPE}:

(A) The growth of the beam break-up instability (BBI) is exponentially dependent on R_{PIPE}^{-2}. (i.e. $A = A_o \exp(I_{BEAM} \cdot V_{acc} \cdot \text{Const.}/B_{kg} R_{PIPE}^2 \cdot E_{gap})$)

(B) The impedance of the ferrite loaded transmission line decreases approximately linearly with R_{PIPE}^{-1}.

(C) The weight of the accelerator increases as the square of R_{PIPE}.

In short the losses are increasing with R_{PIPE} linearly while the growth of BBI is decreasing exponentially as R_{PIPE}^2. It is essential in these designs to fully understand the dependence of the growth rate of the BBI on pipe diameter. In past designs, the pipe diameter has been undersized and has resulted in designs which were not compatible with full current operation. This applies to both RF and induction linear accelerators.

1.3 Operating Voltage and Gradient

It has been shown above that the length of the accelerator is set by the choice of core material and pulse length. In addition the beam pipe radius is determined primarily by BBI considerations. It was also shown that the value of $\ln R_o/R_i$ was determined by the core material and the individual gap drive voltage. Indeed once the drive voltage, current and pulse length are selected, then limiting values for the accelerator cell are uniquely determined.

The operating current, total accelerator voltage and pulse length are set by the application. This leaves the individual gap voltage the only unspecified parameter. We have shown above that the accelerator gradient is linearly proportional to the individual gap voltage. What we will show below is that while the coupling coefficient (the fraction of energy deposited in the

beam versus the energy lost in the accelerator cores) is independent of gradient, the accelerator weight and cost becomes exponentially dependent on the gradient in the limit of large gradients. We will also show that for constant BBI gain, accelerator weight and cost in the limit becomes exponentially dependent on $\sqrt{I_{beam}}$.

The equivalent circuit for an induction linac is the same as that for all transformers. One must bear in mind that while the number of secondary turns N_{sec} is unity, the number of primary turns is fractional given by

$$N_{prim} = \frac{1}{\#\text{Acc cells}}$$

$$Z_{out} = \frac{V_{acc}}{I_{beam}}$$

while Z_{in} the input drive impedance to the individual cells is given by

$$Z_{in} = \frac{V_{gap}}{I_{percell}}$$

The shunt impedance to ground is determined by the accelerator cell geometry and choice of core material. It is given '

$$Z_{shunt} = \frac{1}{2\pi}\sqrt{\frac{\mu}{\epsilon}} ln R_o/R_i$$

Under the assumption that no ferrite is allowed to exceed a flux swing of ΔB_s and B(r) α 1/r, we saw that the accelerator gap voltage was given by

$$V_{gap} = \Delta B_s \cdot v_g \cdot R_i ln R_o/R_i$$

where $v_g = c/(\epsilon_r \mu_r)^{1/2}$ is the wave velocity in the ferrite and $R_i(R_o)$ the inner (outer) radius of the ferrite core. The accelerator shunt impedance is then simply determined by the characteristic impedance of this ferrite loaded transmission line

$$Z_{SHUNT} = Z_{LINE} = \frac{1}{2\pi}\sqrt{\frac{\mu}{\epsilon}} ln\left(\frac{R_o}{R_i}\right) = \frac{1}{2\pi}\sqrt{\frac{\mu}{\epsilon}}\frac{V_{gap}}{v_g \cdot \Delta B_s \cdot Ri}$$

$$= \frac{1}{2\pi}\mu \cdot \frac{V_{gap}}{\Delta B_s \cdot Ri}$$

If the electron beam impedance is defined as

$$Z_{beam} = \frac{V_{gap}}{I_{BEAM}}$$

then the coupling coefficient (= energy coupled to the beam/the total energy incident on the accelerator cell) is given by

$$K = \frac{Z_{SHUNT}}{Z_{BEAM} + Z_{SHUNT}} = \frac{1}{\frac{2\pi \Delta B_s R_i}{\mu I_{BEAM}} + 1}$$

A plot of coupling coefficient versus ferrite core inner radius for several different beam currents appears in Fig. H.2. Here we have assumed a ferrite with a $\mu_r = 400$ and $\epsilon_r = 12$.

It should be noted that the coupling coefficient is independent of accelerator gradient but increases with increasing current and decreasing ferrite core inner radius.

The cost and weight of the accelerator structure is to first order linearly dependent on the core volume.

$$\text{Core Volume} = \#\text{cells} \cdot \text{cell core length} \cdot \pi(R_o^2 - R_i^2) \qquad (H.1)$$

and

$$V_{gap} = \frac{V_{acc}}{\#\text{cells}} = \Delta B_s \cdot v_g \cdot R_i ln\left(R_o/Ri\right) \qquad (H.2)$$

if Bα 1/r and no ferrite is allowed to exceed a flux excursion of ΔB_s. We can then rewrite Eq. (H.1) as

$$\text{Core Volume} = \frac{V_{acc}}{V_{gap}} \cdot v_g \cdot \tau_{pulse} \cdot \pi R_i^2 exp\left(\frac{V_{gap} \cdot 2}{\Delta B_s \cdot v_g \cdot R_i}\right)^{-1} \qquad (H.3)$$

where τ_{pulse} is the pulse length. It should be noted that the minimum core volume (d core volume/d V_{gap} = 0) is always achieved when $V_{gap} \approx 0$. Also for $2 \cdot V_{gap}/\Delta B_s \cdot v_g \cdot R_i << 1$, core volume is approximately independent of V_{gap} while for

$$\frac{2V_{gap}}{\Delta B_s \cdot v_g \cdot Ri} >> 1$$

core volume becomes exponentially dependent on V_{gap}.

This becomes obvious upon careful examination of Fig. H.3. Here we have assumed μ_r = 400, ϵ_r = 12, and τ_{pulse} = 50 nsec. Referring to Eq. (H.3), it also appears that core volume is

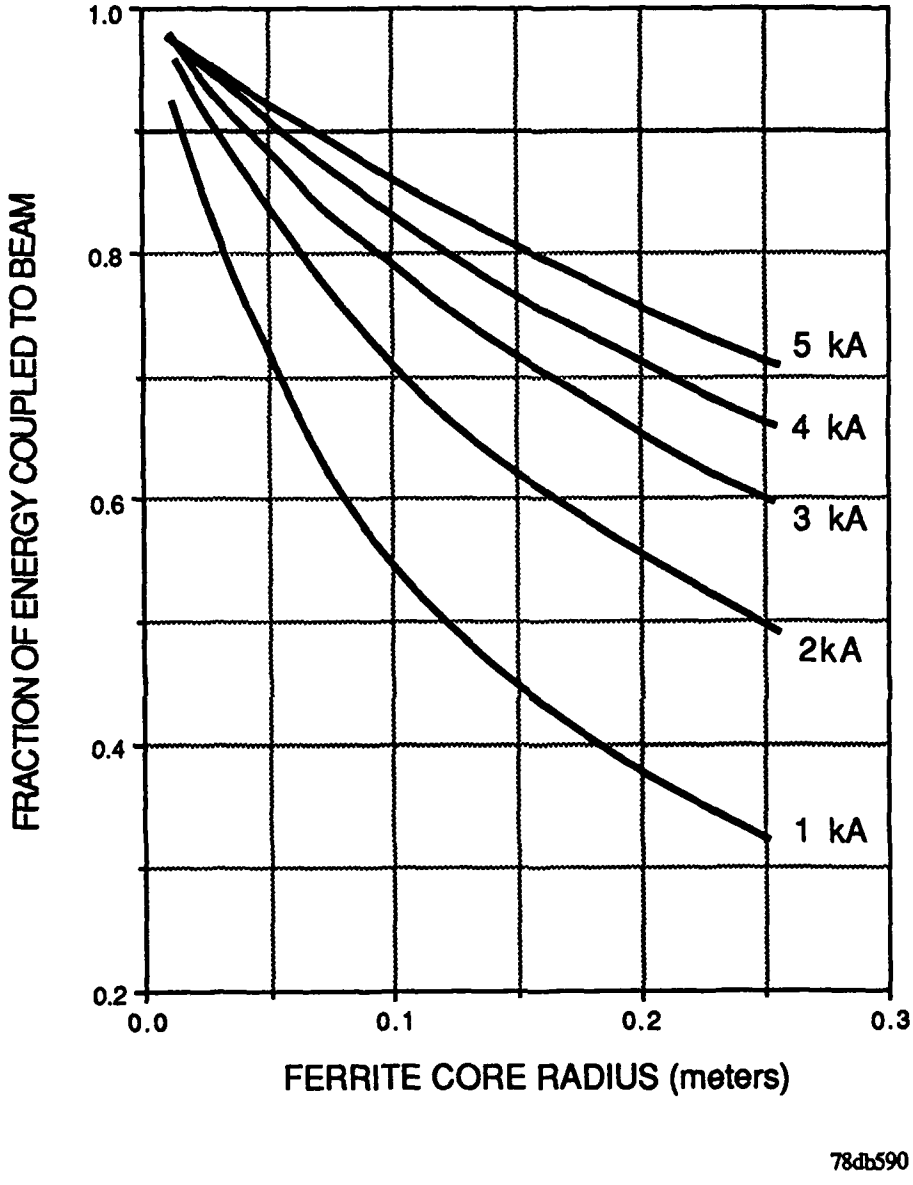

Figure H.2: Coupling coefficent.

linearly dependent on τ_{pulse}. The dependency on $v_g = c/(\mu_r \cdot \epsilon_r)^{1/2}$ is somewhat more subtle. For small values of V_{gap}/R_i the core volume varies as $1/\mu_r^{1/2}$ but as V_{gap}/R_i becomes large, core volume becomes exponentially dependent on $\mu_r^{1/2}$.

It is also obvious from Fig. H.3 that the inner ferrite core radius dramatically impacts the accelerator weight at a given gradient. Referring to Fig. H.2 the efficiency degrades rapidly as the ferrite inner radius is increased. This inner radius is determined primarily by the beam pipe radius and the thickness of the focusing solenoid. Arbitrary reduction of these parameters independently of the current will result in the onset of the Beam Break-up Instability which will drive the accelerator beam current into the walls.

The amplitude of the BBI oscillation throughout the accelerator is given by:

$$A = A_o \exp\left(\frac{\text{const. } NIZ_\perp\omega}{B_{kg}}\right)$$

where

K = $1.16 \cdot 10^{-13}$ kg - sec/(kamp-ohm)

N = Number of accelerator gaps

ω = Mode frequency

I = Accelerator current

B_{kg} = Focusing field

Substituting

$$NZ_\perp = N(Z_\perp/Q) \cdot Q = \frac{\text{const.}_1 \cdot Q \cdot V_{acc}}{E_{gap} \cdot R_{pipe}}$$

where

V_{acc} = Accelerator voltage

E_{gap} = Accelerator gap electric field stress

R_{pipe} = Beam pipe radius

provides the following equation for the BBI amplitude.

$$A = A_o \exp\left(\text{const} \cdot \frac{I \cdot V_{acc}}{B_{kg} R_{pipe}^2 \cdot E_{gap}}\right)$$

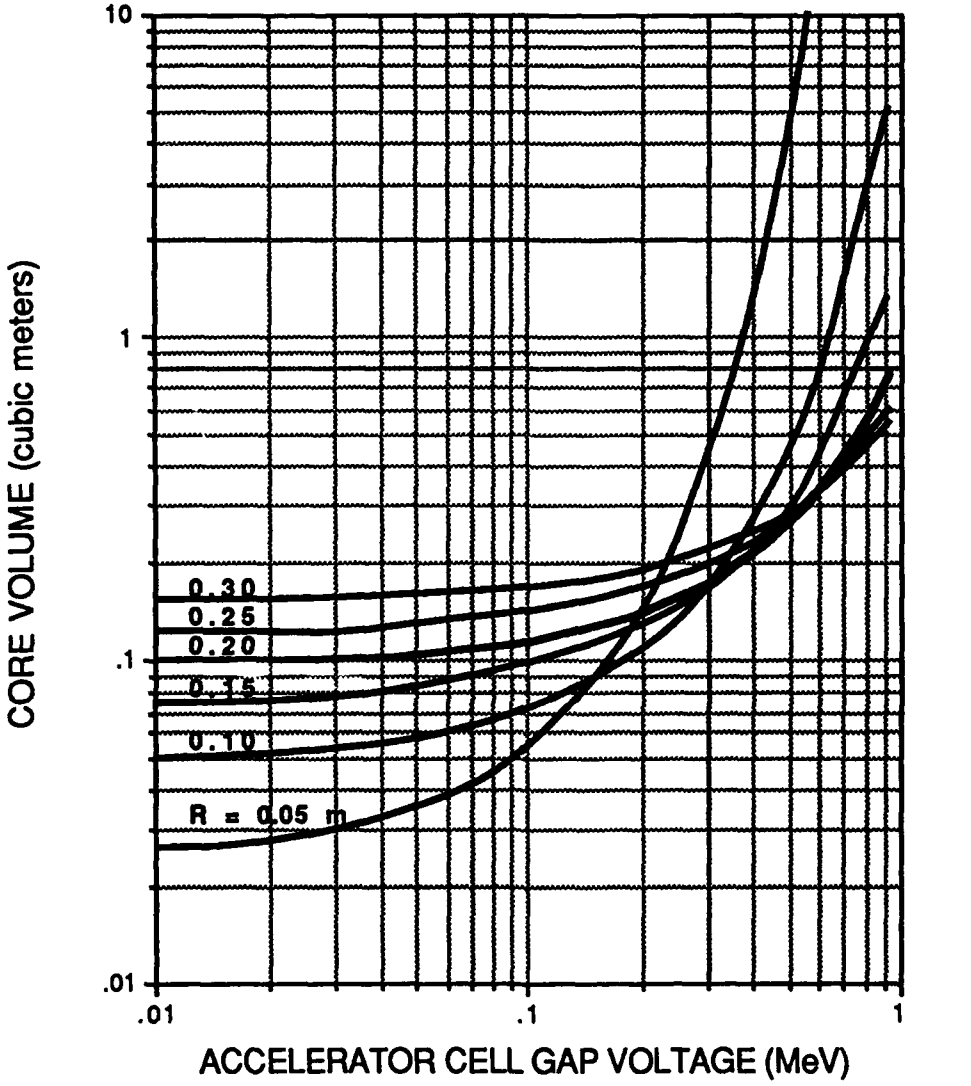

$\mu = 400$, $\Delta B_s = 0.65$ Tesla

78db590

Figure H.3: Accelerator core volume per megavolt

Therefore, the BBI amplitude depends exponentially on the inverse of the accelerator gap stress and the beam pipe radius squared.

In order to minimize both the beam pipe radius and the solenoid thickness ($R_o - R_i$) while holding BBI gain constant at a given current and accelerating potential, the accelerator gap stress must be increased to as high a value as practicable. Unfortunately at the high duty factors required for most of these applications, exceeding the threshold where field emission in the gap occurs is not allowed. Understanding this limit is essential to optimizing the design.

2.0 NEW INDUCTION ACCELERATOR ARCHITECTURES

In the last section, we discussed the impact that the beam pipe diameter places on the required ferrite core volume and losses. The problem arises from the location in which the ferrite is placed in conventional induction accelerators. In conventional induction accelerators the ferrite is wrapped around the beam pipe and solenoid. Referring to Fig. H.4 where we have stripped the induction accelerator schematic to its simplest essentials, we see that some provision must be made to isolate the shields of the coaxial drive cables which would otherwise attempt to float up to the potential of the previous induction cell. Since all of these cables connect to a common ground at the supply source, the accelerator would soon discover it was shorted out at the source. The time required for the accelerator to discover this is one roundtrip travel time along the drive cables. If the drive cables are long enough or the pulse short enough we would need no additional isolation.

In Fig. H.5 we schematically depict the conventional method used to achieve one pulse length worth of isolation. As we discussed above, ferrite is wrapped around the beam pipe and the shields of the drive cables are connected to ground at the outer diameter of the ferrite. Placing the ferrite around the beam pipe uniquely determines the geometry, volume, efficiency and accelerating gradient of an induction cell as a function of only the pulse length, drive voltage per cell, and inherent ferrite properties. The length of each accelerator cell is set by the permeability and permittivity of the ferrite and the pulse length. The inner diameter of the ferrite is set by the beam pipe diameter and the radial extent of the ferrite core is determined by

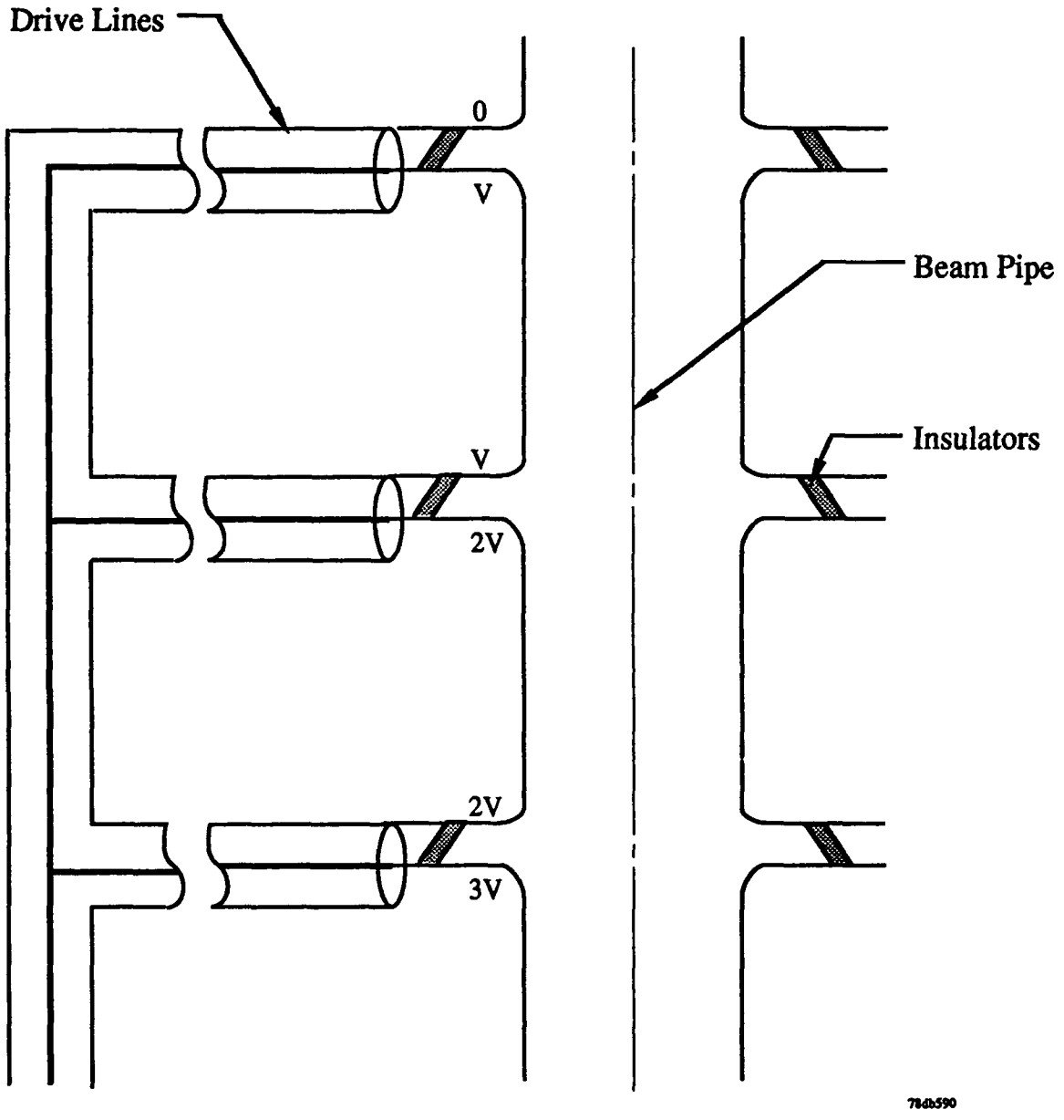

Figure H.4: Simplified induction linear accelerator schematic

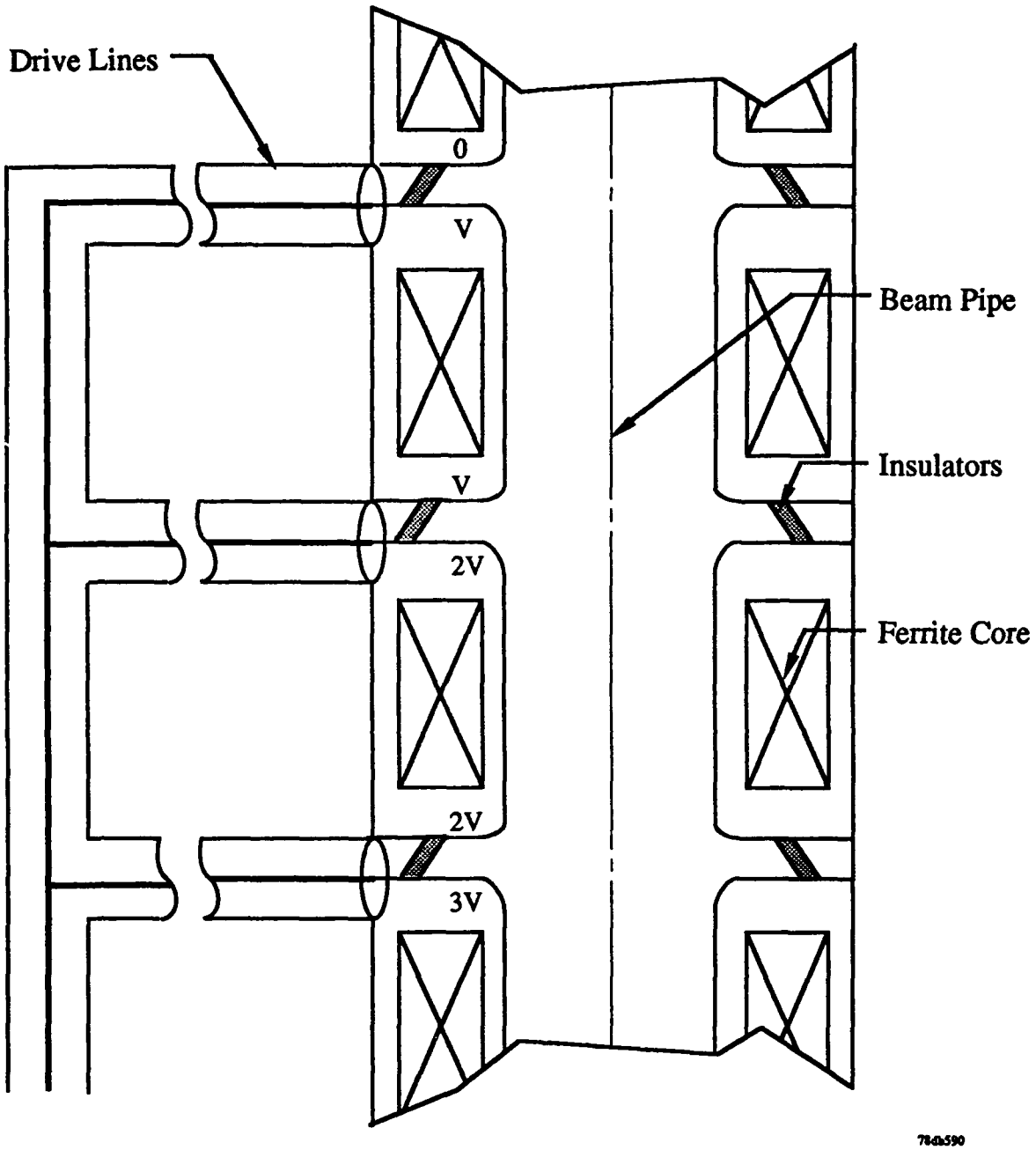

Core Length Set By Pulse Length
Core ID Set By BBU (OD of Beam Pipe and Focussing Magnets)
Core OD Set By Voltage per Cell

Figure H.5: Conventional linear induction accelerator design

the drive voltage and available flux swing in the ferrite. Increasing the beam pipe diameter to reduce beam breakup growth results in increased ferrite volume and increased losses. In order to minimize losses, the ferrite inner diameter should be as small as possible but in order to improve beam stability the inner diameter should be as large as possible. This is the dilemma posed by the conventional linear induction accelerator design. We will however see that placing the ferrite around the beam pipe does have one key advantage. A ground shield can be used to tightly enclose the accelerator structure confining the electric field to the immediate vicinity of the accelerator gaps. No field appears outside this ground shield and no voltages appear at any point which exceed the single cell voltage except inside the beam pipe.

In Fig. H.6 we suggest a new induction linear accelerator configuration which leads to a more compact, lighterweight design. Here the beam pipe can be as large as desired as the ferrite is wrapped around the drive lines. As the drive lines are typically only 1-2 inches in diameter and the beam pipe plus focusing magnet are typically 10 inches or more in diameter, placing the ferrite around the drive lines reduces the ferrite volume requirement by two orders of magnitude. The gradient of the accelerator is no longer determined by the ferrite properties and for short pulses the inductance of a coiled drive line would be sufficient by itself to isolate the shields on the drive cables as depicted in Fig. H.7. In fact the drivelines can be wrapped around ferrite cores several times when ferrite is used. This can further decrease the ferrite volume required in the linear induction accelerator design (Concept I) shown in Fig. H.6.

In the case of this modified induction accelerator design, the outer ground shield is optional. For space-based applications there is probably no reason to shield the accelerator and the accelerating field can simply be allowed to appear on the outside of the accelerator. An observer watching the unshielded accelerator would see an electromagnetic wave traveling down the length of the induction accelerator as the electron beam is accelerated. The length of this electromagnetic wave would simply be the pulse length multiplied by the speed of the accelerating electrons which would essentially by the speed of light. As an example, a 5 nanosecond accelerating pulse would appear as a wave approximately 5 feet in length. The peak amplitude

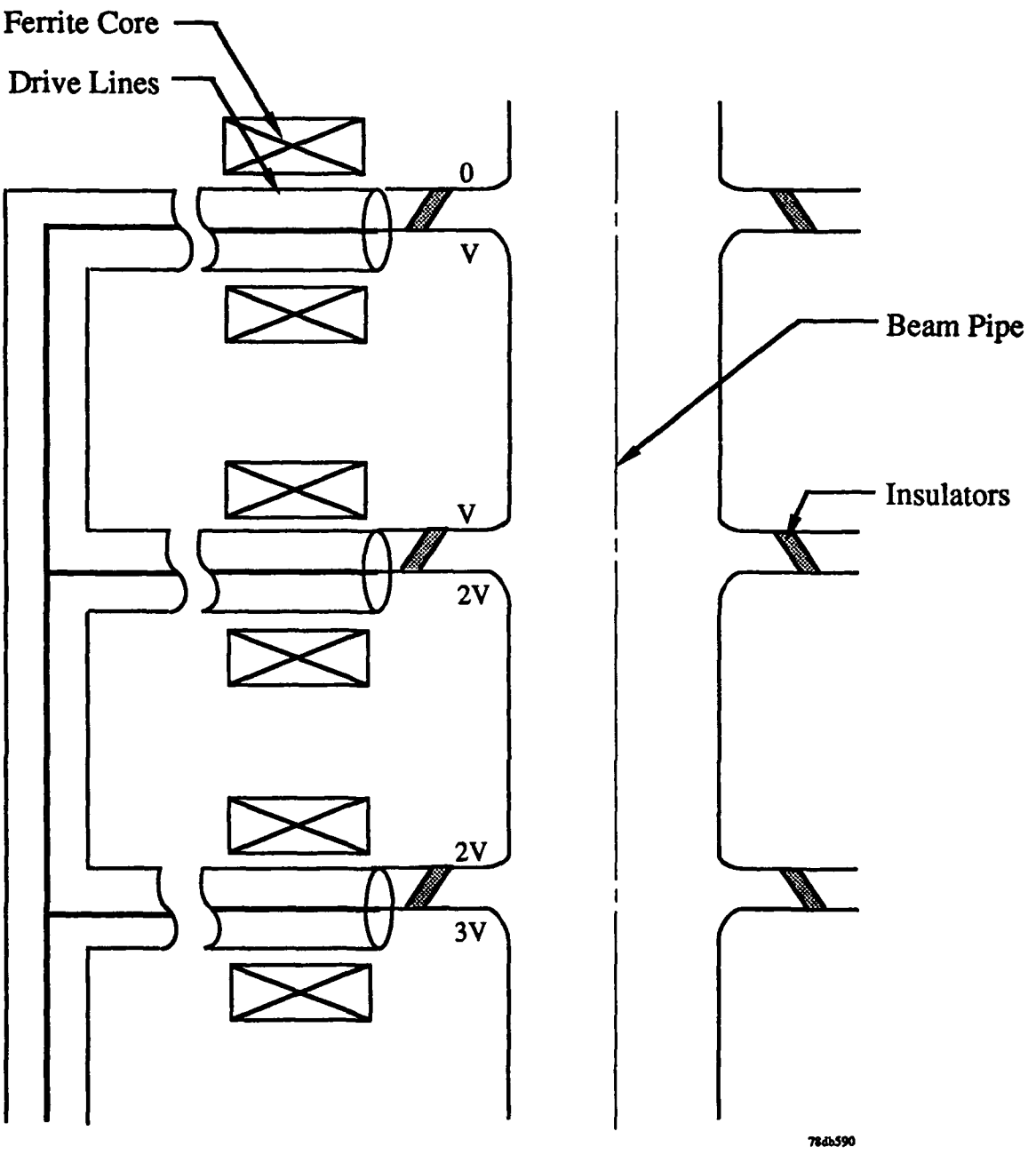

Core ID Determined By Drive Line

$$\text{Core Cross-Section} = \frac{\text{Gradient}}{4} \cdot c \cdot (\text{pulse length})^2$$

Figure H.6: Concept I - Modified linear induction accelerator

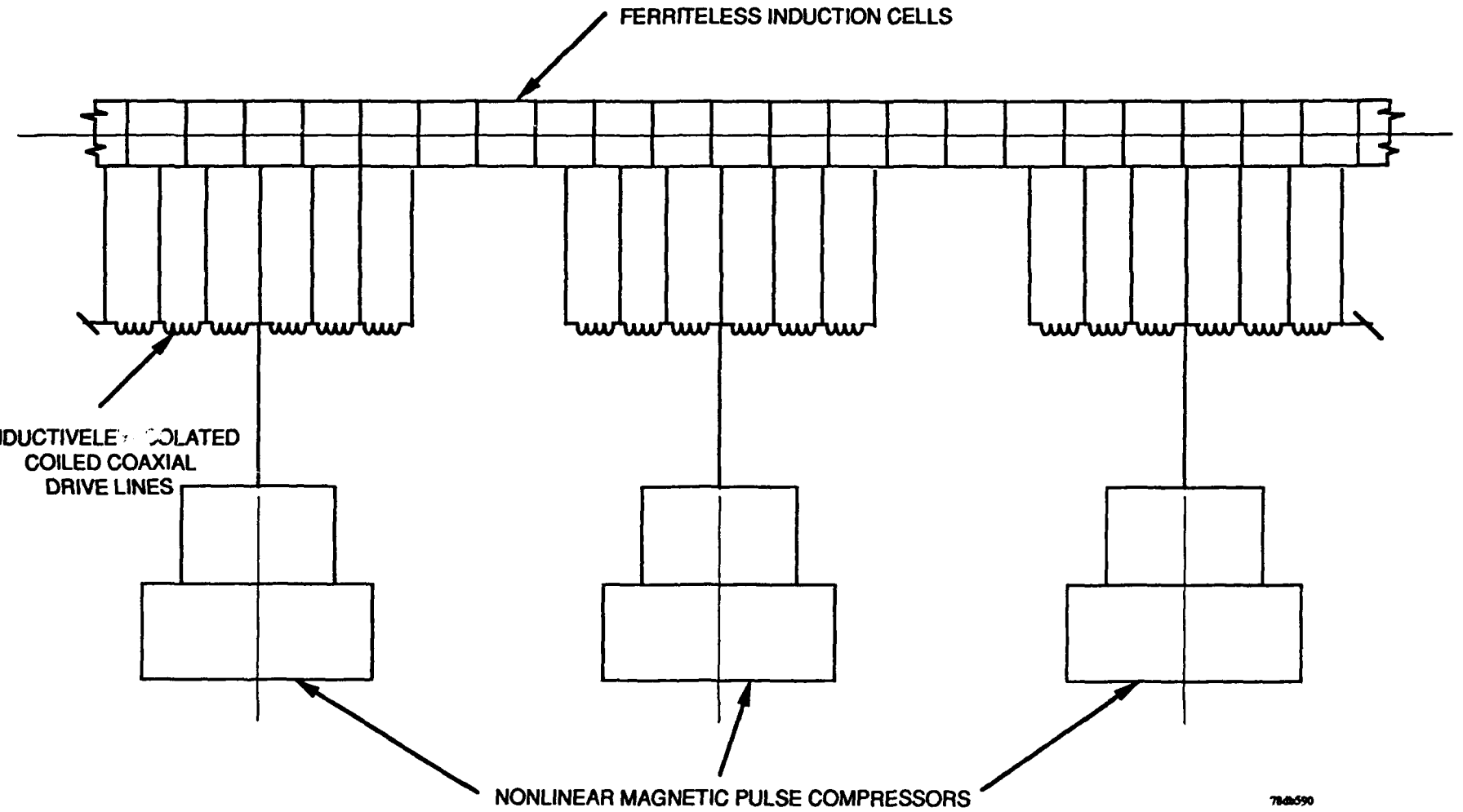

Figure H.7: Concept II: Ferriteless induction accelerator for short pulse operation

of this wave is simply given by multiplying the gradient of the accelerator by the spatial pulse length and dividing by 2. For this reason we will see that it becomes very important to minimize the pulse length as this will determine the maximum voltage that appears on the outside of the accelerator at a given gradient.

This external electromagnetic wave induces a voltage drop on the outer conductor of the drive lines which tie back to a common ground at either the pulsed power drive or optional external ground shield. The inductance associated with either the ferrite isolation cores or coiling the transmission line must be sufficient to prevent significant current from flowing. The efficiency of the accelerating structure is reduced by the ratio of this leakage current to the accelerating electron beam current. The peak voltage drop across the isolation inductors is no longer the single cell voltage as in the case of the conventional linear induction accelerator but is given as

$$V_{peak} = \frac{\text{Gradient} \cdot \text{Pulselength} \cdot v_{electron}(\approx c)}{2}$$

As the wave travels past the isolation inductor, the voltage across the inductor drops to zero at the center of the wave and then reverses reaching a maximum negative voltage equal to the maximum positive voltage. The average voltage drop across the inductor is zero. This means that the ferrite cores are automatically reset and in the case of a conventional air core inductor, created by coiling the transmission line, all of the energy associated with the shunt leakage current is returned to the accelerating electrons.

As the electromagnetic wave travels down the accelerator at approximately the speed of light, the tail of the wave is feeding energy into the tail of the electron beam pulse and the head of the wave is being constantly recreated by the drive pulse to the next accelerator cell in line. Creating this wave front requires charging the stray capacitance between the next accelerator cell and the nearest ground plane to the peak voltage appearing across the isolation inductors.

The maximum one-way volt-second product determines the required ferrite core cross-section and/or the number of turns the drive lines makes around the core. From Faraday's law we derive.

$$N \cdot \text{Area} \cdot \Delta B_s = \int V \cdot dt$$

$$= V_{peak} \frac{\text{PulseLength}}{4} = \frac{\text{Gradient} \cdot (\text{PulseLength})^2 \cdot c}{8}$$

The maximum voltage to ground is identical to the peak voltage across the isolation core, but it is a dipole field and falls off very rapidly with distance in the radial direction.

As an example we will examine the properties of a conceptual accelerator whose specifications appear in Table H.1. In this lightweight accelerator, the gradient is 3 MeV/meter and the pulse length is 5 nanoseconds. If the electron beam is travelling at approximately the speed of light, then the peak voltage across the isolation inductors is 2.25 MeV. The volt·second product appearing across the isolation inductor is only 2.81 volt-milliseconds. The single turn ferrite core cross-section requirement, assuming a ΔB_s of 6000 Gauss, is only 7 square inches. If we assume a drive line diameter of 1 inch operating at 150 kV then a single turn ferrite core with dimensions of 1" ID X 2" OD X 14" long is all that is required. Such a core would weigh approximately 2 kg. If each drive line is supplying 150 kV to the accelerator then there would be 1000 accelerator cells in our 150 MeV accelerator and the total ferrite core weight would be only 2000 kg. We will see that by invoking another design option, it will be possible to reduce the required ferrite volume by a factor of 4 and the weight down to 500 kg. The focusing magnets are wrapped around the beam pipe and power is supplied by wires fed up through the center of the drive line inner conductor.

As an interesting comparison, a 150 MeV induction accelerator of conventional design operating with a 50 nanosecond accelerating pulse and a 1 foot diameter beam pipe would have required over 200,000 kg of ferrite. In the case of the conventional induction accelerator, this weight would increase linearly with the pulse length. In the Concept I induction accelerator design, the weight increases with the square of the pulse length. If the pulse length were decreased even more, the weight savings would be even greater. Conversely if the pulse length is increased, the weight savings are not as great. The development of short pulse driver technology

Table H.1: Compact, Lightweight Induction Linear Accelerator Specifications

Acceleration Potential	- 150 MeV
Beam Current	- 2600 Amperes
Pulse Length	- 5 nsecs
PRF	- 50 kHz
Average Beam Power	- 100 MW
Gradient	- 3 MeV/meter
Beam Energy/Pulse	- 2000 Joules
Overall Accelerator Mass	- 10,000 kg

78db590

is paramount to increasing the utility and decreasing the cost and weight of all induction accelerators, but it is an especially critical issue in the case of these alternate design concepts. For very long pulses of order several hundred nanoseconds, the conventional induction accelerator design will always be the preferred approach, but any induction accelerator operating for these pulse lengths would be prohibitively large and of very limited utility.

As we mentioned above the drive pulse to each accelerator cell must charge up the stray capacitance between the cell and the nearest ground plane to the peak voltage across the isolation inductor. In our 5 nanosecond pulse length, 3 MeV/meter accelerator we found the peak voltage to ground was 2.25 MeV. If we assume a 150 kV/cell drive voltage then each accelerator cell is 5 centimeters in length. If we were to place our 1 foot diameter beam pipe inside of a 6 foot diameter thin walled metal tube or aluminized balloon for shielding purposes, then the capacitance per unit length is given as

$$C = \frac{2\pi\epsilon_0}{ln(R_o/R_i)} = 30\text{pf/meter}$$

For our 5 centimeter long accelerator cell, the incremental capacitance to ground is 1.5 picofarads. Charging this capacitance to 2.25 MeV would require approximately 3.4 microcoulombs. Referring to Table H.1 we see that we are planning to accelerate an electron beam current of 2600 amperes. At this drive level, it would require 1.25 nanoseconds to charge the stray capacitance. This should pose very little problem as the energy corresponding to this 1.25 nanoseconds of electron beam pulse will be fed into the beam at the tail of the pulse. The accelerating pulse must simply arrive at the accelerating cells 1.25 nanoseconds ahead of the electron beam pulse for optimum coupling efficiency. Both the drive pulse and the electron beam pulse would still be 5 nanoseconds in duration.

Finally in Fig. H.8 we present a third design option known as Concept III. The Concept III induction accelerator design can be combined with the Concept I accelerator design. By grouping the accelerator cells in blocks fed by a common drive line we can further reduce the ferrite requirement. For instance if we were to block accelerator cells together in groups of 10 in our example, then only one primary stem drive line would have to be isolated from ground

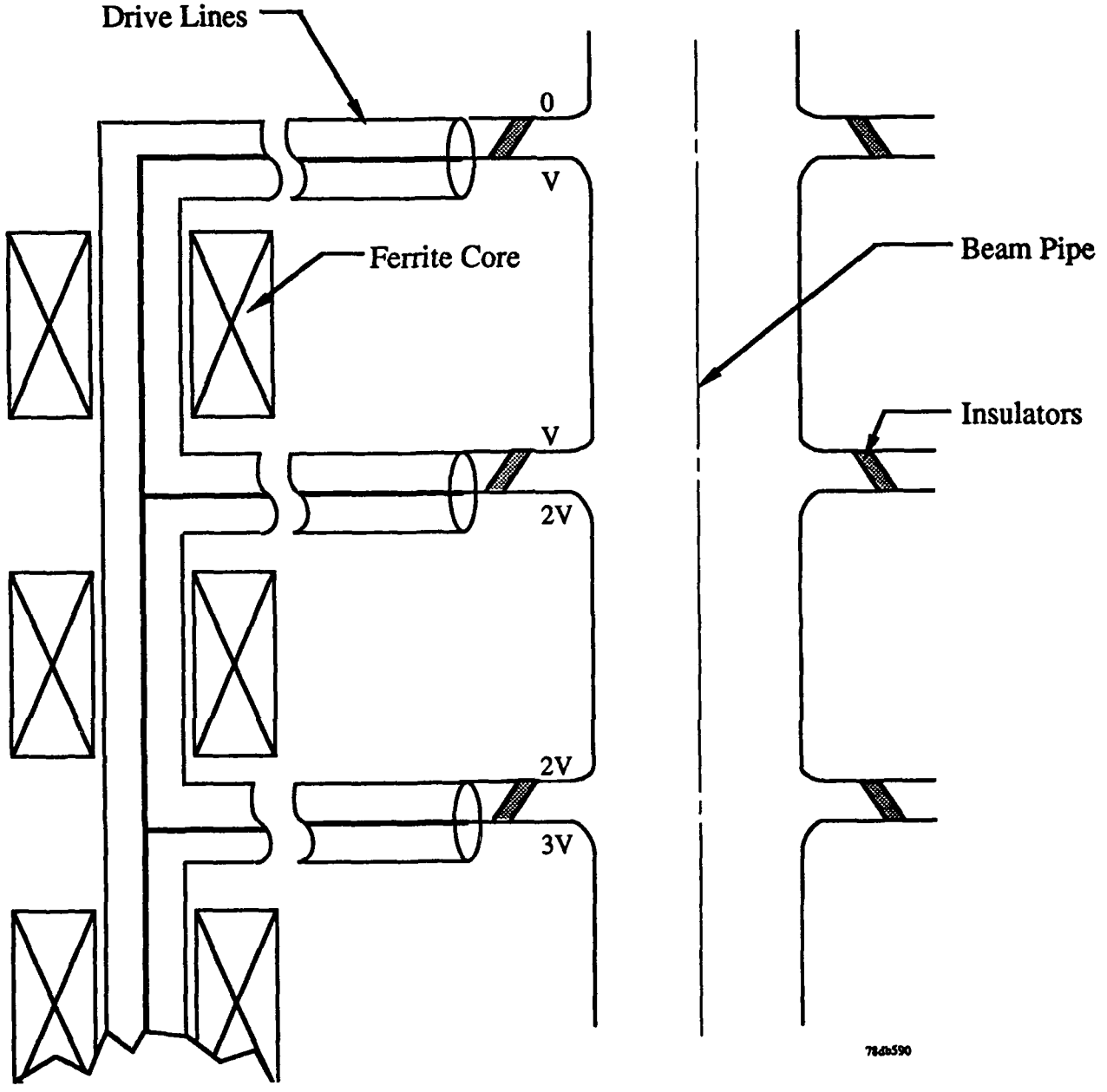

Core Volume Reduced By $\frac{(\text{Drive Line Diam.})^2}{(\text{Beam Pipe + Magnet Diam.})^2} \sim 100$

Over Conventional Induction Accelerator

Figure H.8: Concept III - Modified induction accelerator

for each group of 10 accelerator cells. The isolation inductors placed between the individual cells need only be sufficient to provide 150 kV isolation for the 5 nanosecond drive pulse. As these cores are wrapped around the 1 inch drive line rather than the 1 foot diameter beam pipe the ferrite volume requirement is reduced by more than two orders of magnitude for these 150 kV isolation inductors over the conventional induction linear accelerator design. Employing this design in our example accelerator would reduce the ferrite weight to less than 500 kg.

In summary we have described some alternate induction linear accelerator designs which offer significant weight and cost savings over conventional induction accelerator designs while decreasing the length of the accelerator by a factor of 6. These alternate designs are not the optimum choice for all applications but offer many advantages in short pulse and/or space based applications.

3.0 THE GAP FIELD

An investigation of the limiting electric field stress as a function of various surface conditioning techniques has been undertaken at SRL. This study was aimed at both documenting maximum usable electric field levels as well as searching for new gap electrode processing techniques that might extend these limits. This work was primarily performed at SRL and was supplemented by additional support from the LLNL Beam Research Program due to its impact on cell design for all induction linacs.

The results (Fig. H.9) indicate that operation at electric field levels up to 300 kV/cm may be possible. Previous induction linacs have been designed around peak stresses of $\sim$ 150 kV/cm which is probably reasonable since little surface conditioning was attempted. It was also found that simple mechanical polishing of a surface does not yield much benefit. Dielectric occlusions (imbedded polishing compound) which can lead to large electric field enhancements are probably responsible for this result. These enhancement factors can be just as significant and detrimental as the emission sites found on an unpolished surface.

Electropolishing will remove most of these impurities and therefore helps considerably. Unfortunately electropolishing also exposes basic impurities found in the stainless steel such as

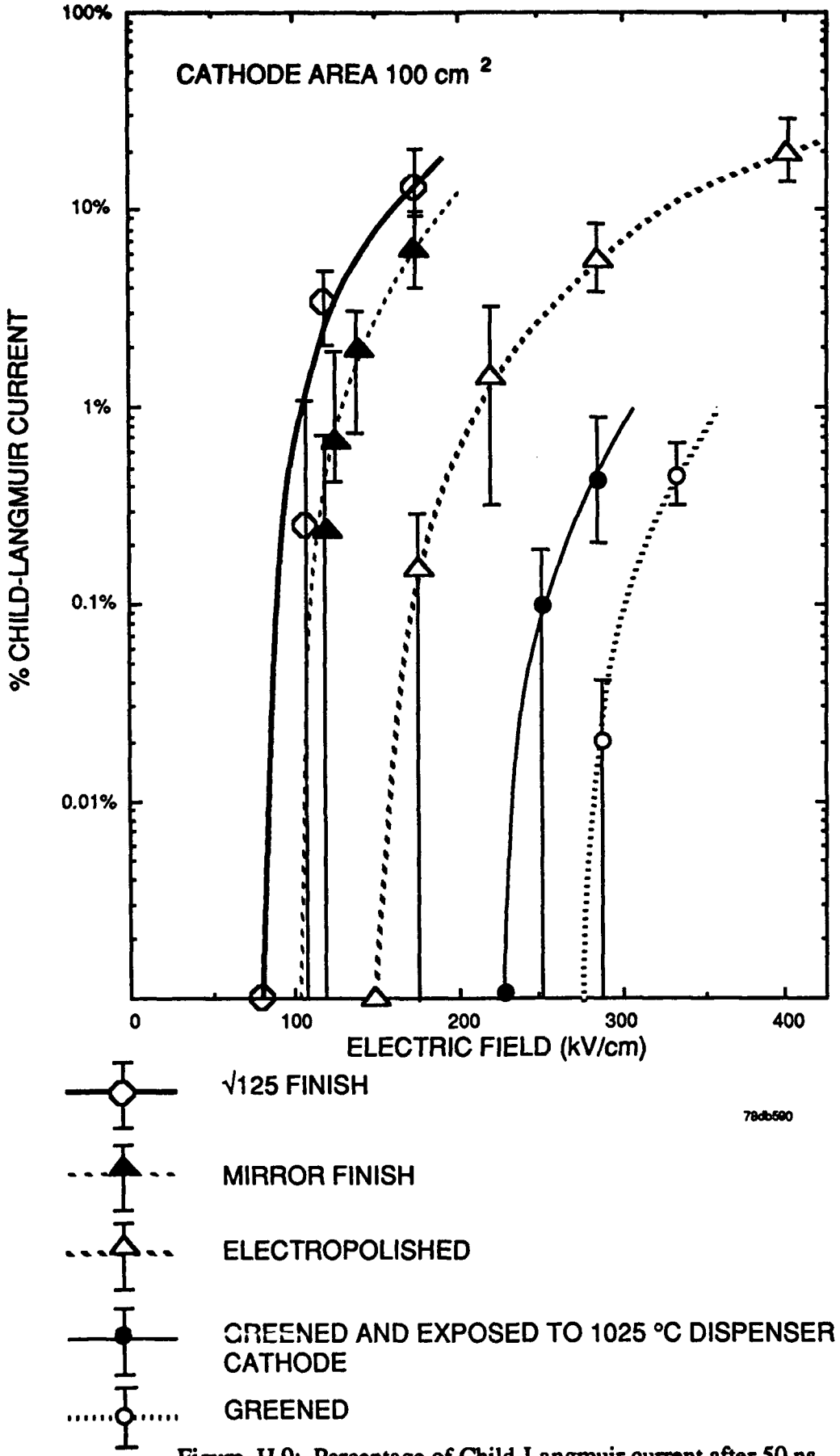

Figure H.9: Percentage of Child-Langmuir current after 50 ns

carbon particles. A process known as "Greening" (firing an electropolished stainless steel surface in wet hydrogen for $\sim$ 1 hour at 950°C) improves the situation considerably. Electropolishing etches away the iron atoms leaving a surface primarily composed on metallic chromium. The "Greening" process leaves the remaining iron in the metallic state but oxidizes this chromium surface forming O^- doped Cr_2O_3 and Cr^+ doped Cr_2O_3. The resulting high permittivity semi-conducting coating tends to shield high permittivity occlusions eliminating the enhancement factor. As mentioned above the field stress achievable on these surfaces exceed 300 kV/cm with greening. Similar field stress levels have been achieved on anodized aluminum surfaces probably for similar reasons.

Care must be taken when employing coated surfaces. A breakdown involving an arc can reduce the surface breakdown field back to levels between 100 and 200 kV/cm. These coatings can be used to advantage if reasonable safety factors are employed and several vacuum tube manufacturers (e.g. EG&G, Varian) have actually marketed devices operating at $\sim$ 200 kV/cm.

4.0 THE FOCUSING SOLENOID

In theory it should be possible to offset the effects of an undersized beam pipe diameter by arbitrarily increasing the focusing field. In practice two considerations limit the practicality of this approach. First we have shown above that for constant BBI gain $B_z \alpha 1/R_{pipe}^2$. The thickness of a solenoid is proportional to B_z and therefore $\Delta R_{solenoid} \alpha 1/R_{pipe}^2$. Secondly, as the focusing field is increased to suppress the beam break-up instability, the number of Betatron wavelengths in the accelerator increases. This leads to cork screwing and increased BBI excitation. Tuning becomes more complicated as the radial position of the beam becomes a rapidly oscillating function of time and energy. It is best to use the minimum required focusing level. This minimum focusing field requirement can be determined from the beam envelope equation.

In cylindrical coordinates, the equation of motion for an electron,

$$\gamma m \frac{d\vec{v}}{dt} = -e(\vec{E} + \vec{v} \times \vec{B}) \qquad (H.4)$$

may be written as

$$\ddot{r} - r\dot{\phi}^2 = -\frac{e}{\gamma m}(E_r + rB_z\dot{\phi}) \qquad (H.5)$$

$$r\ddot{\phi} + 2\dot{r}\dot{\phi} = \frac{e}{\gamma m}B_z\dot{r} \qquad (H.6)$$

$$\dot{z} = \beta_z c \qquad (H.7)$$

if we assume zero emittance and an axial magnetic guide field. E_r is simply derived from Gauss law $\left(\vec{\nabla}\cdot\vec{E} = \rho/\epsilon_o\right)$ as

$$E_r = \frac{r\rho}{2\epsilon_o} \qquad (H.8)$$

If we assume that $\ddot{\phi} = 0$, then from Eq. (H.6) we find

$$\dot{\phi} = \frac{eB_z}{2\gamma m} \qquad (H.9)$$

A simple substitution of

$$\ddot{r} = \frac{d^2r}{dz^2}\beta^2c^2 \qquad (H.10)$$

allows us to rewrite Eq. (H.5) as

$$\frac{d^2r}{dz^2} + kB_z^2r + \frac{2I}{I_\alpha(\gamma\beta)^2} \qquad (H.11)$$

where

$$k = \frac{e^2}{4\gamma^2\beta^2m^2c^2} \qquad (H.12)$$

and

$$I_\alpha = \frac{4\pi\epsilon_o mc^3\gamma\beta}{e} = 17kA\beta\gamma \qquad (H.13)$$

It can also be shown that for electron beams of finite emittance

$$\frac{d^2r}{dz^2} + kB_z^2r = \frac{2I}{I_\alpha(\gamma\beta)^2} + \frac{\epsilon^2}{r^3} \qquad (H.14)$$

If $d^2r/dz^2 = 0$, then as $\epsilon \rightarrow 0$

$$B_z = \sqrt{\frac{2I}{I_\alpha}}\frac{1}{r}\frac{2\gamma m_0 c}{e} \qquad (H.15)$$

The focusing solenoid (which supplies this axial magnetic field) itself can be constructed a number of ways. The most conventional and rugged approach is coils wound from square hollow

tubing insulated by fiberglass and epoxy. This approach is not compact and the conductor sizes are typically large. Because the impedance to coolant flow is linearly proportional to the length of the conductor and to the inverse cube of the coolant channel diameter it is not possible to arbitrarily shrink the conductor size. Large conductor sizes with high current levels per conductor introduce large dipole fields near the leads. This can be avoided by using smaller conductors immersed in an insulating coolant such as Fluorinert or freon but because these coolants only cool effectively by vaporization, large channels must be provided to remove vapor and the magnet housing gets bulky. This problem can be eliminated if the magnet can be exposed to the same coolant medium as the ferrite accelerator core. Simply placing the magnet in a perforated housing inside the ferrite ID will accomplish this. Freon and Fluorinert provide an order of magnitude better cooling than forced air. Immersed in freon, copper conductors, which can handle for 2×10^6 amps/m^2 in air, are capable of handling 2×10^7 amps/m^2.

For a pure solenoidal field

$$B = \mu_o N' I = \mu_o \left(\frac{I}{m^2}\right) \times \Delta R \approx 8\pi \times \Delta R(m)(tesla)$$

$$B_z = 8\pi \times \Delta R(m)\, Tesla \; at \; J = I/m^2 = 2 \times 10^7 amps/m^2.$$

To develop a focusing field of 0.25 Tesla, $\Delta R \approx 1$ cm. A four layer magnet of #10 solid square conductor should easily achieve this requirement. In order to leave room for insulation and coolant passages, the final ΔR of the complete package is estimated to be $\sim$ 1.5 cm.

As the electron beam is compressed to a small diameter, the emittance term can no longer be neglected and the equilibrium condition of the beam envelope equation takes the form

$$r^4 = \frac{\left((2I/I_\alpha)r^2 + \epsilon^2\right)\beta^2 c^2}{\Omega_L{}^2}$$

where for the condition of Brillouin flow

$$\Omega_L = \frac{-eB_z}{2\gamma m_0}.$$

APPENDIX I

1.0 THE SNOMAD TRANSFORMER DESIGN

In conventional magnetic compressor design transformers are frequently interspaced between compression stages. When the operating impedance becomes difficult to handle a transformer is used to change the value to something felt to be optimum. This avoids compression reactors with thousands of turns or a number of turns less than unity. In high performance magnetic switches which operate on submicrosecond time scales these transformers must be carefully designed as continuous transmission lines. Great care is taken to both confine the leakage magnetic fields and simultaneously to avoid breakdown level electric fields. As an example the total combined inductance of both the saturated first stage compression reactor and 1:100 transformer primary in SNOMAD-IV is less than 2 nH.

Unfortunately every time a pair of transformers is introduced into a magnetic compressor it creates a resonant circuit. As the duty factor increases understanding the behavior of this resonant circuit becomes increasingly important. Damping must be introduced so that positive reset can be achieved between compression cycles. Referring to Fig. I.1, if there is no damping present (ie. R=0) then the circuit appears as a shorted secondary to the bias winding and reset can never be achieved. If R is made arbitrarily large than the compression pulse is significantly damped and the efficiency is adversely affected. In the specific application of driving Induction accelerators it is almost impossible to avoid the problem as the induction cell load appears as a transformer.

If multiple transformers must be used than it is convenient to keep the step- up ratios per transformer as small as possible. Damping is almost impossible until the cores have been reset. Once reset the inductance is low enough that a small amount of resistance in series with the secondary of the first transformer will damp oscillations rapidly. This resistance should be installed where the current is lowest during the compression cycle. A convenient method for implementing this resistor is to construct some of the secondary transmission lines of the transformer using thin walled stainless steel tubing as an inner conductor. This method is

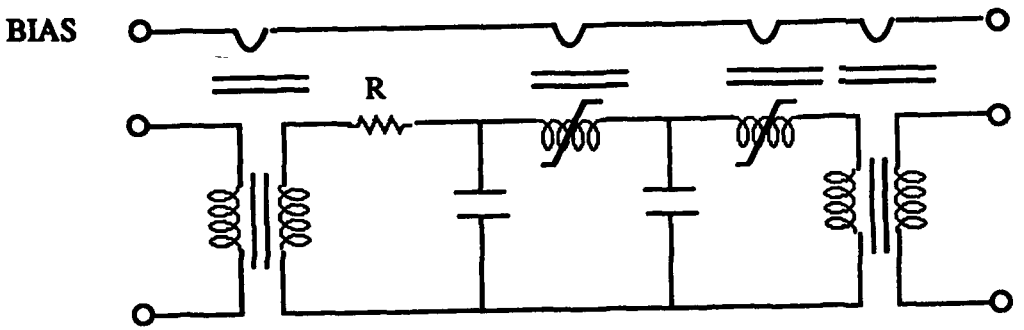

Conventional Magnetic Compressor With Multiple Transformers

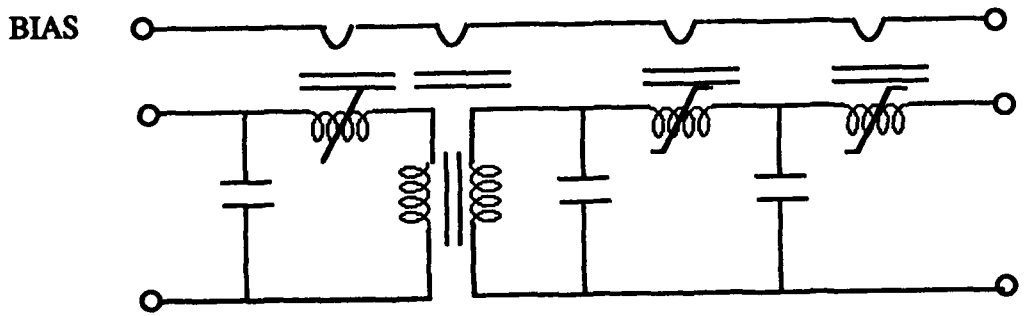

Open Ended Magnetic Compressor With Single Transformer

78db590

Figure I.1: Magnetic compressor

employed in all of the SNOMAD pulse compressors.

The maximum required value of this resistance is determined from the number of shorted turns presented to the bias winding. The current induced by the single turn bias winding in the secondary of the transformer is determined by multiplying the bias current by the inverse of the number of shorted turns. The voltage appearing across the shorted turns is simply the IR drop across the resistance. At a minimum this voltage should be sufficient to fully reset the core volume enclosed by the shorted turns during the intrapulse period.

As an example, SNOMAD-I laser, has a 50 turn secondary on the input transformer. Between this transformer and the primary of the output transformer are a nine turn 2^{nd} stage and a one turn 3^{rd} stage. The number of shorted turns is then simply given by $50 - (9 + 1 + 1) = 39$. A resistance of .5 ohms has be installed in series with the secondary. A bias current of 28 amperes will induce a voltage of .4 volts across these shorted turns. The volt-second requirement to reset the cores is $\sim 10^{-4}$ volt-seconds/turn. In this worst case scenario 250 μsecs. would be required to fully reset and damp the resonances in this circuit. This does not take into account the efforts employed to use the reverse voltage afterpulse to contribute most of the reset.

Step-up transformers can be constructed by either using multiple secondary turns, using fractional numbers of primary turns, or any combination thereof. At first the concept of fractional primary turns may seem somewhat foreign but it is the basis of all induction linacs where forcing the electron beam to make several secondary turns would be very difficult.

An equivalent circuit for a transformer using a fractional turn primary appears in Fig. I.2. a Simplified cross-sectional view appears in Fig. I.3. Here multiple primary windings are all fed in parallel while the secondary is a single turn formed by the series connection of the same windings. The equivalent circuit for the more conventional multiple secondary turn transformer appears in Fig. I.4, while a simplified cross-section is shown in Fig. I.5. Here a single high permeability core is used for isolation and the secondary makes multiple passes around the core adding on the primary voltage with each pass. As an example transformer employed in SNOMAD-IV is a hybrid with a 20 turn secondary and 1/5 turn primary providing a 100:1

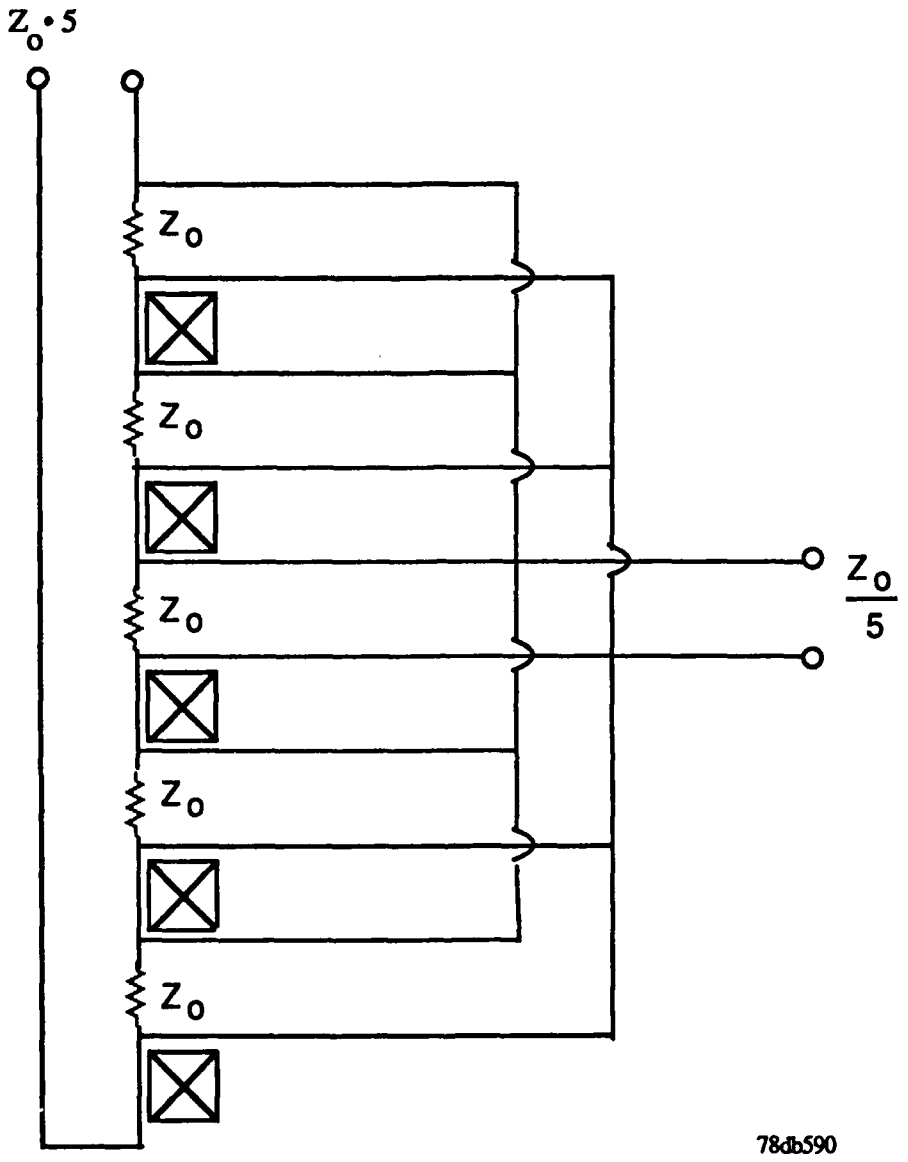

Figure I.2: Equivalent circuit of induction style transformer

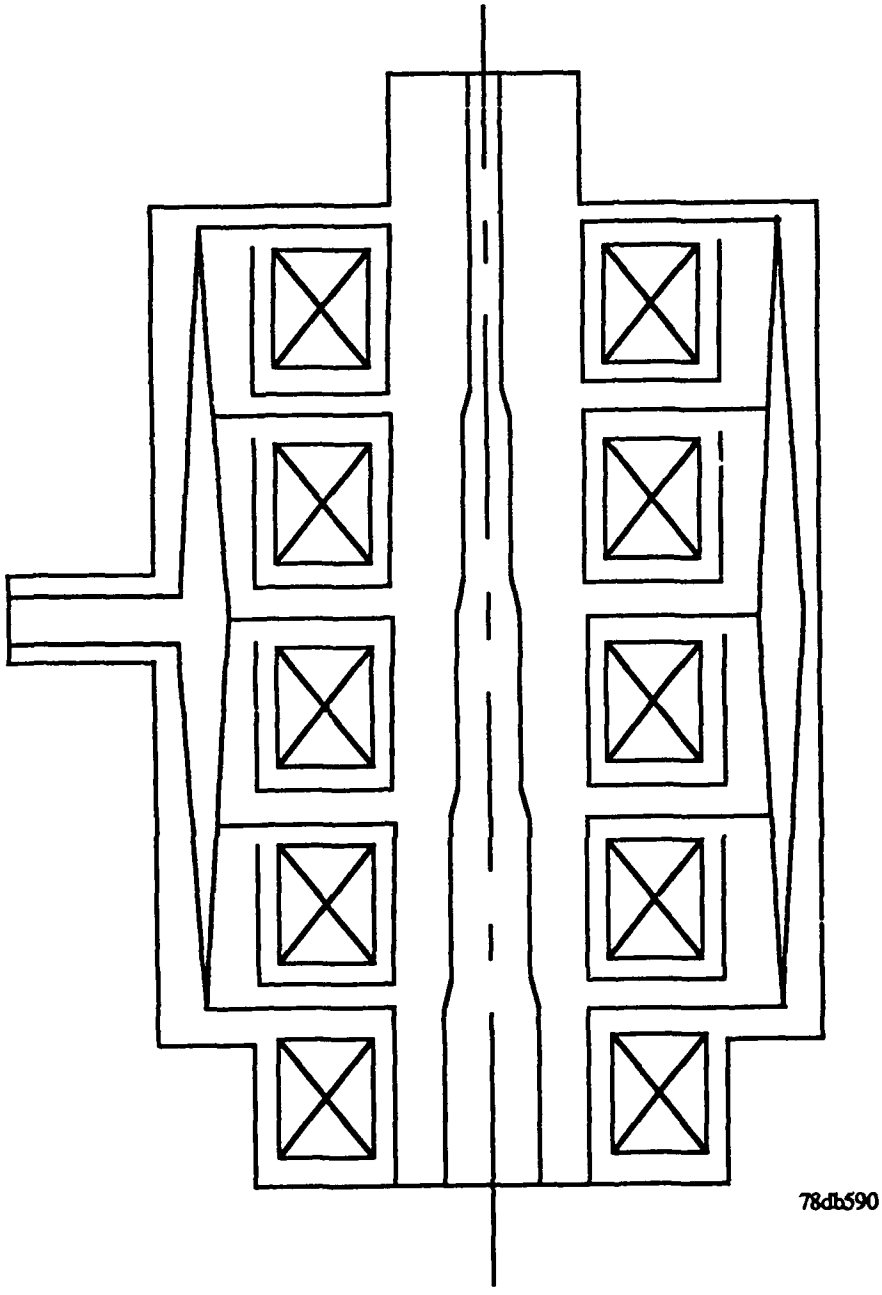

Figure I.3: Simplified fractional turn primary transformer

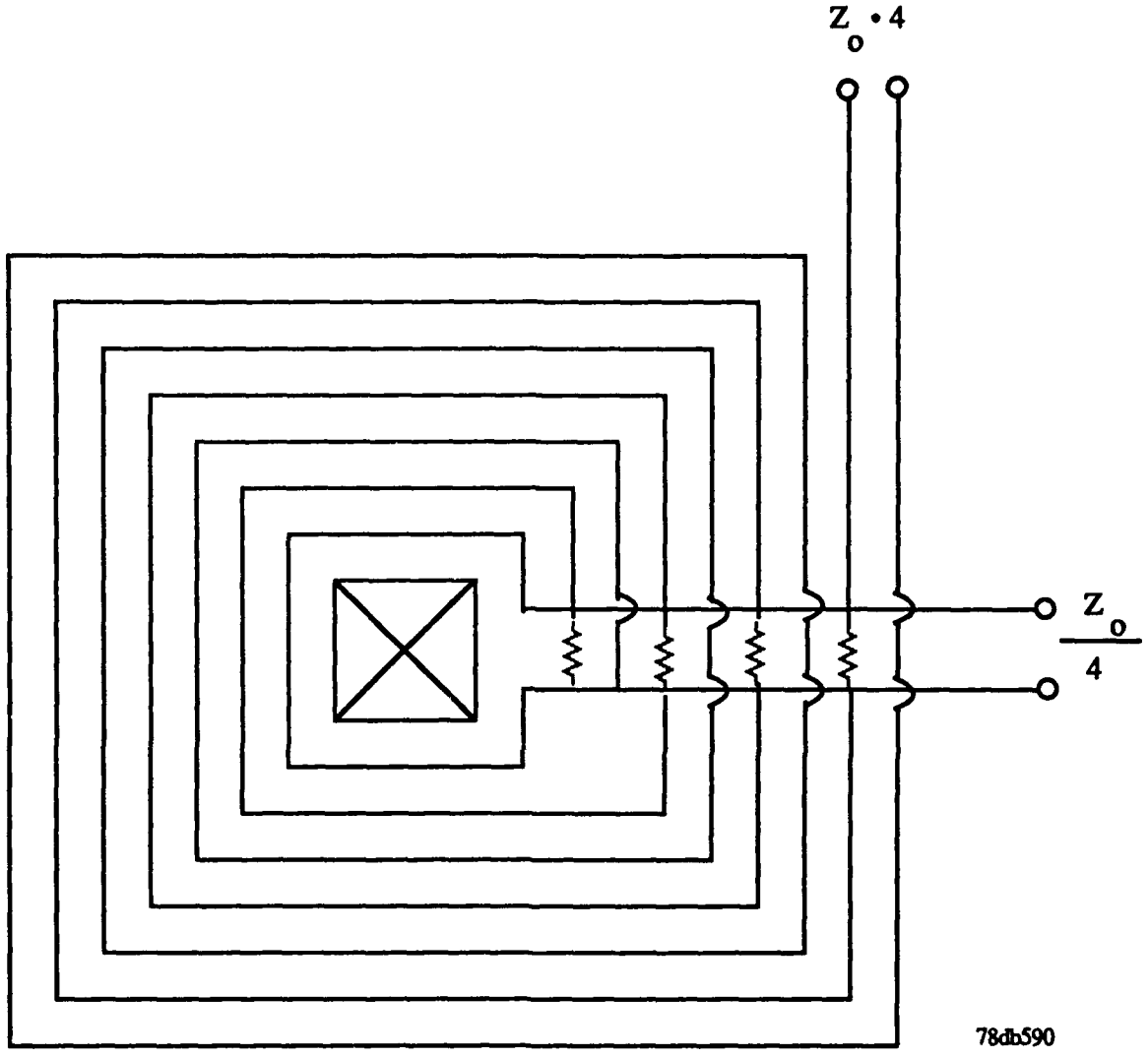

Figure I.4: Equivalent circuit of multiple turn secondary transformer

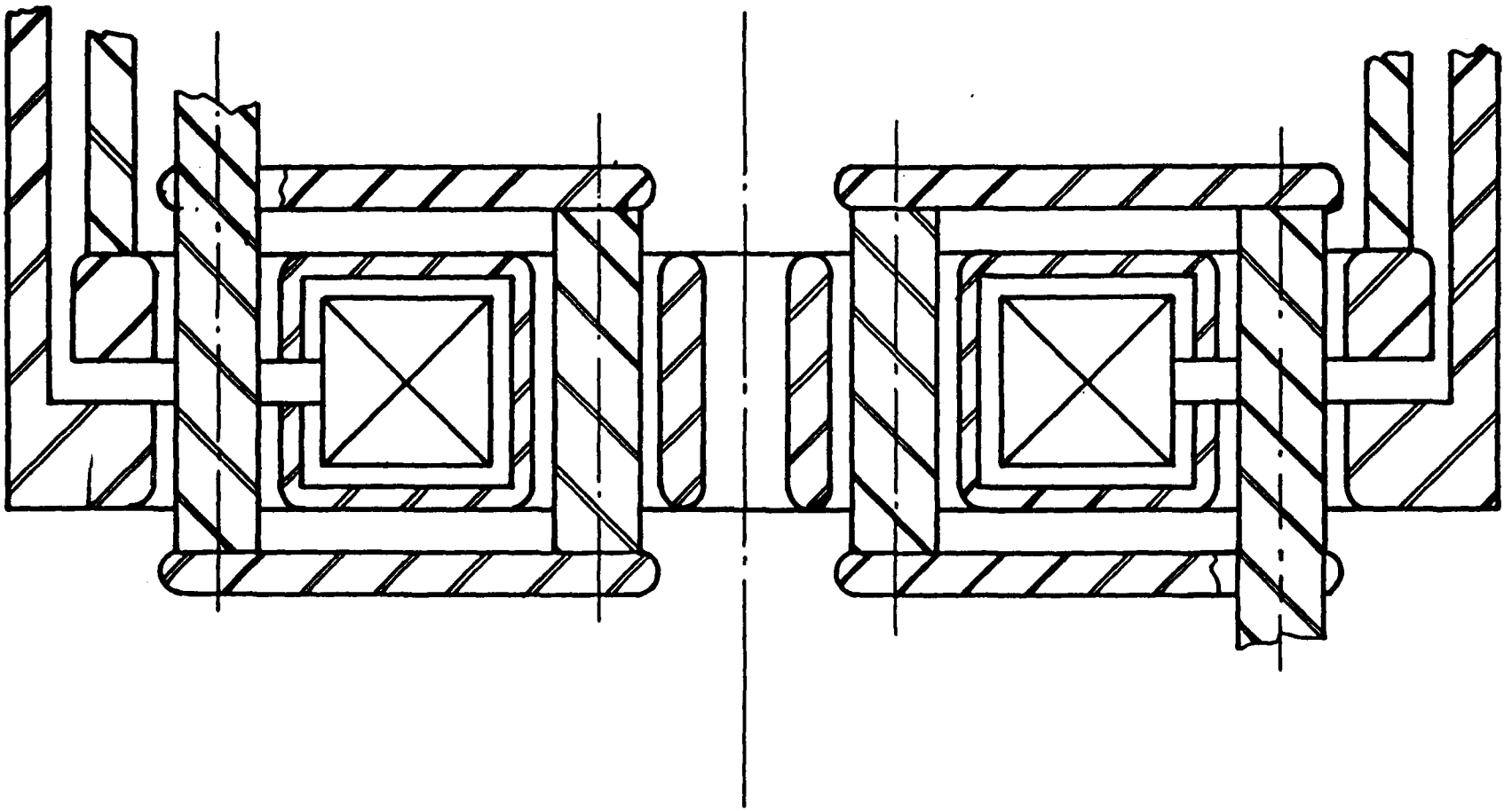

Figure I.5: Simplified multiple turn secondary transformer

step-up, while the transformer used in the SNOMAD-V achieves an 60:1 step-up ratio via a 30 turn secondary and a 1/2 turn primary.

In the case of either transformer it is extremely important to understand where currents are flowing and which regions the fields are confined to. An example of this is presented in Fig. I.6. Here the regions occupied by the magnetic fields has been shaded in. We will assume that the permeability of the magnetic core is infinite and therefore the shunt inductance is infinite and no net current flows around the core. In order for the currents to exactly cancel the ratios of the currents in the primary and secondary are equal to the ratio of the number of turns. This can be understood more intuitively by thinking of the primary transmission line as feeding into the secondary transmission lines all in parallel.

Another interesting feature common to all the transformers in the recent SNOMAD modulator designs is a floating secondary. By floating the secondary of the transformer and forcing the center tap to zero voltage with respect to ground, only half of the up to 100 kV potential appears between any of the windings and the grounded coaxial housing. This further reduces the size of the transformer and reduces electrical stresses. The center tap is held at zero voltage by carefully designing the second and third stages of the compression reactor with bipolar windings. The stray capacitance to the core housings will complete the job.

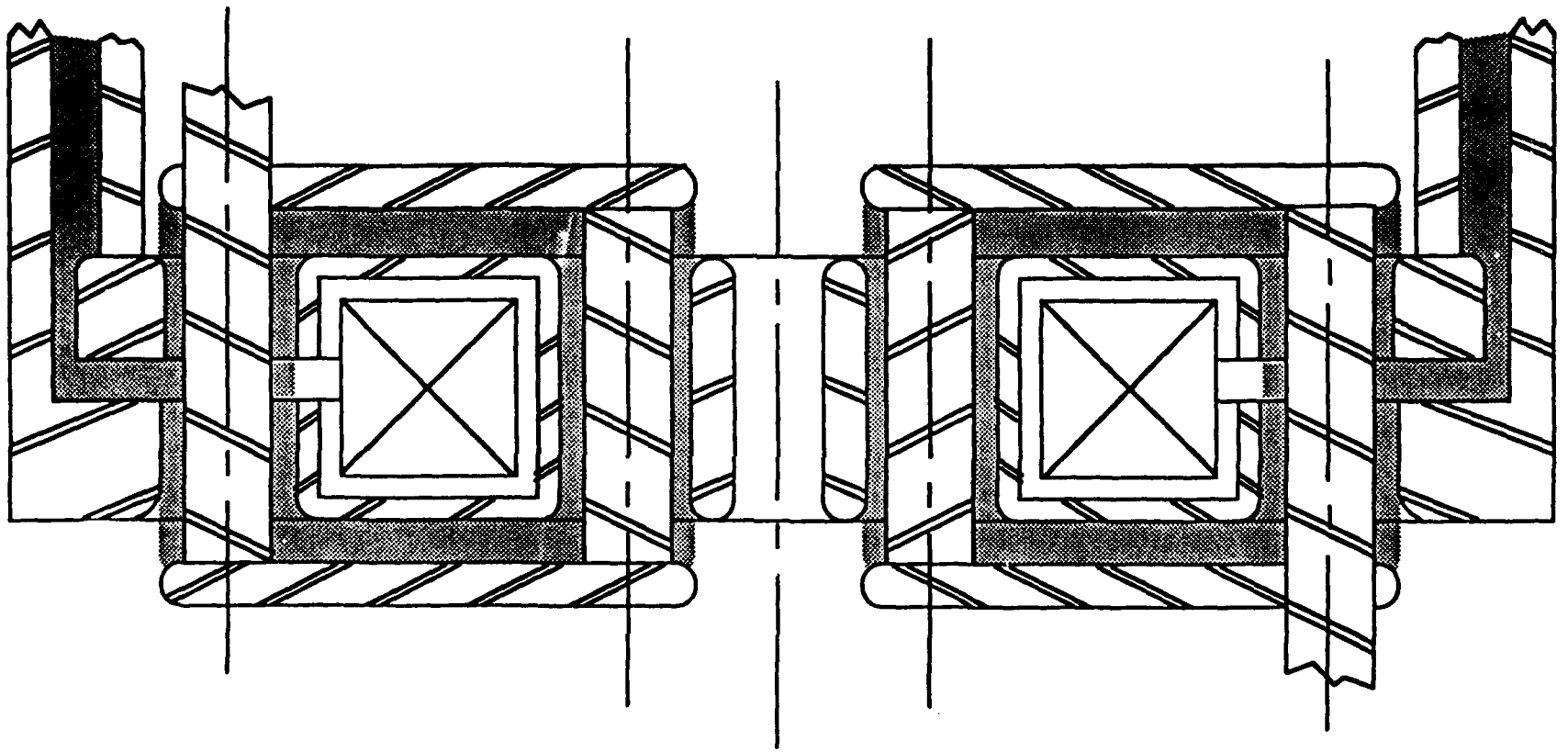

Figure I.6: Simplified multiple turn secondary transformer with volume occupied by leakage field shown shaded.

APPENDIX J

1.0 THE SNOMAD TIMING CONTROL SYSTEM

Minimization of output timing variations or jitter is crucial to operation of a large scale facility which may employ hundreds of modules. Jitter is derived from several sources. Non-repeatable reset conditions can have the most dramatic effect and can cause output timing variations of several microseconds. Incomplete reset during the intrapulse interval is caused primarily by resonances designed into the compression chain. This is further discussed in the preceding section which discusses transformer design.

Another source of output timing variations is associated with the temperature dependant behavior of the SCRs, capacitors, and compression cores. As the temperature rises the SCR turn-on time decreases, the capacitance values drop increasing the resonant frequency, and the saturation flux decreases shortening the compression time. Unfortunately all these factors act in the same direction so there is no inherent compensation. However, the exteriors of all these components are thermally anchored to the boiling temperature of liquid freon and therefore following a warm-up cycle encompassing several thermal time constants (~30 minutes) there will be a minimum of temperature variation. Any variations which still occur will appear as slow drifts and simply monitoring the output pulse timing and comparing it against a reference time will allow a very simple control system to adjust the low level trigger input appropriately.

The DRIFT COMPENSATOR chassis was designed to eliminate the drift problem. This chassis includes a circuit which senses the time of the laser output pulse and the adjusts a delay in the SCR trigger circuit until the timing of the laser output pulse corresponds to an chosen reference time. The DRIFT COMPENSATOR chassis pictured in Fig. J.1 relies on a commercially available ECL logic pulse generator with two output channels to generate the actual timing pulses. Referring to the simplified schematic provided in Fig. J.2, the computer generated initial timing pulse triggers the pulse generator. The pulse generator delays are automatically adjusted by the drift compensator circuit. The desired time of the laser output pulse is entered into the second channel of the pulse generator. The output pulse from the first channel triggers

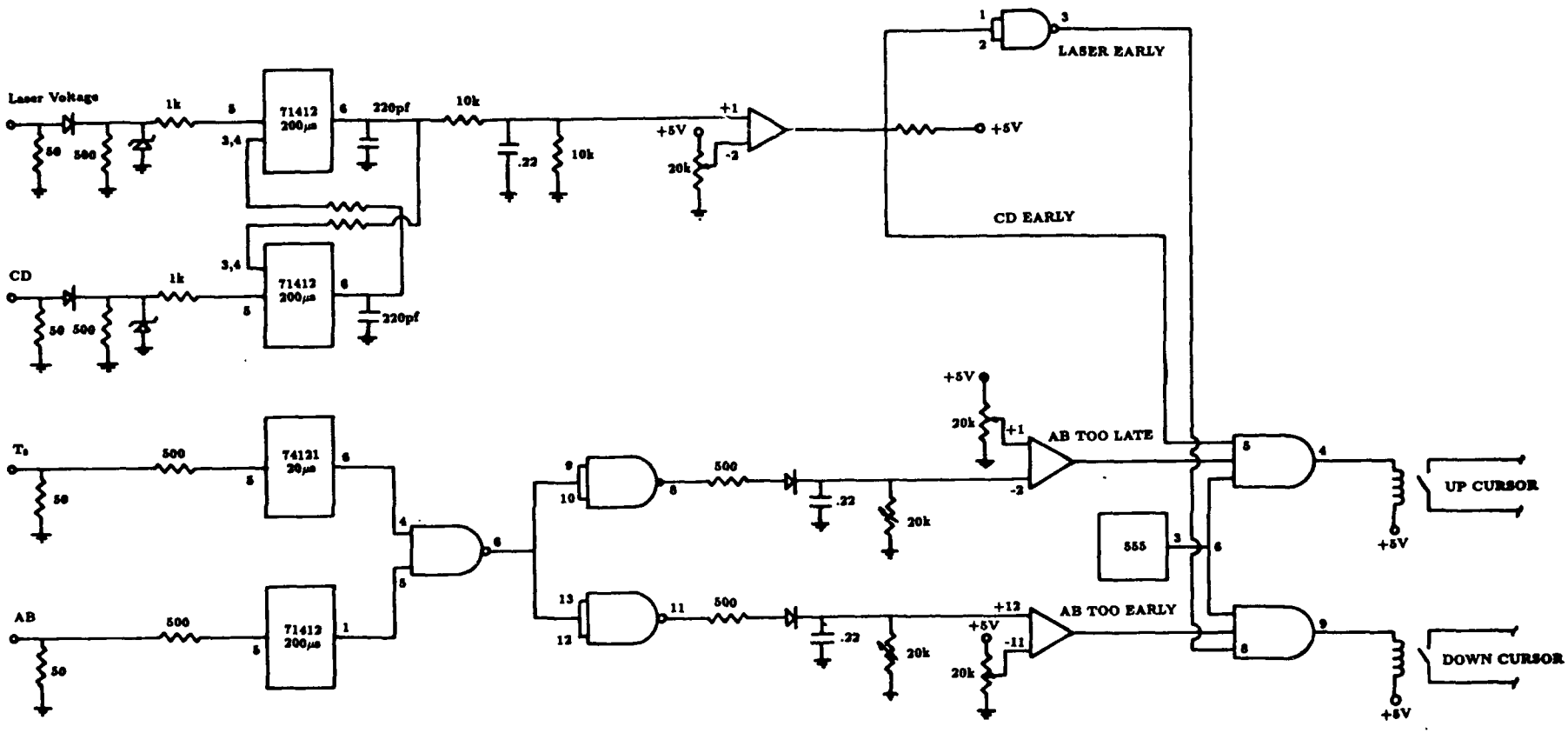

Figure J.1: SSLAM Drift Compensator

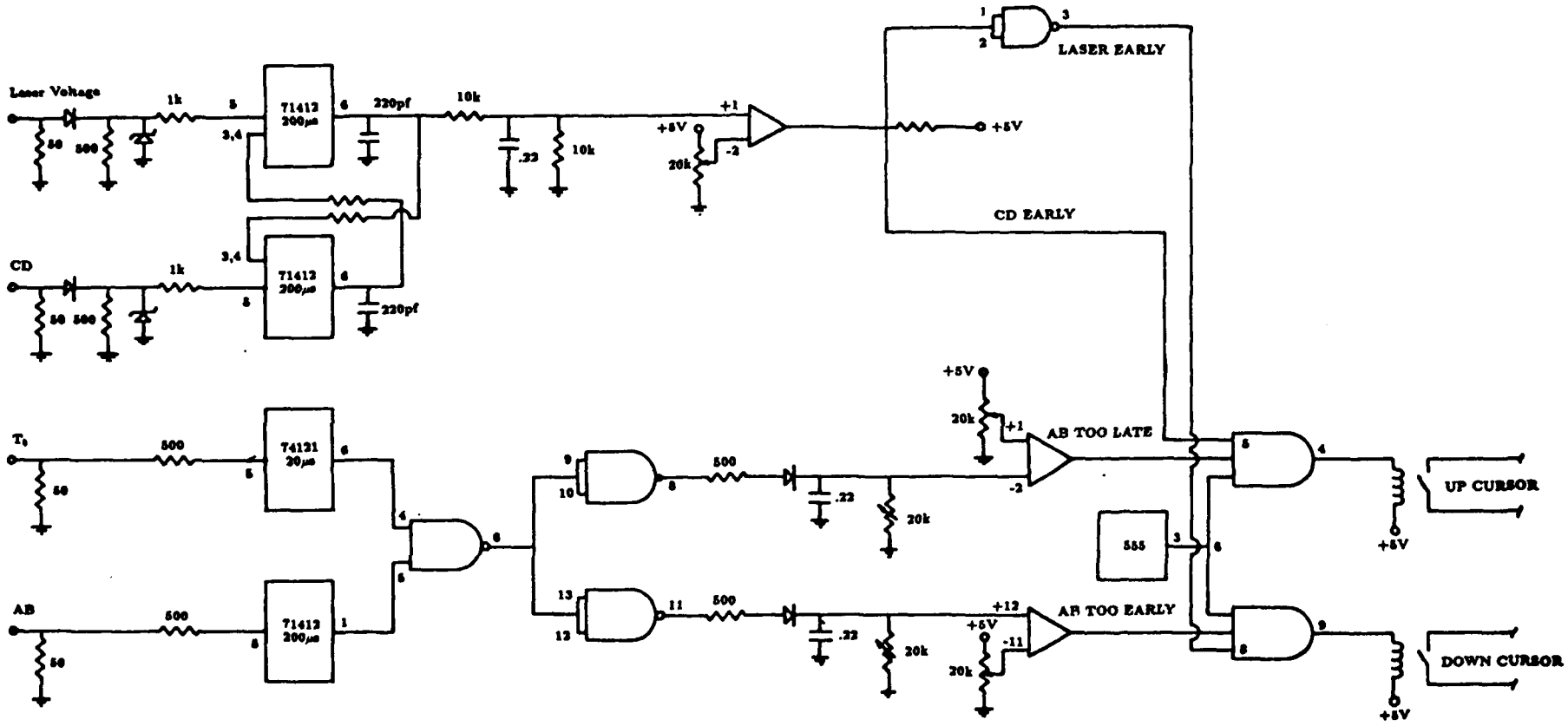

Figure J.2: Simplified schematic of SSLAM Drift Compensator

the SCR DRIVER. The timing of the first channel output pulse is varied by the drift compensator. If the laser output pulse occurs later than it should as indicated by the second channel output pulse, the first channel output pulse is moved forward to compensate and vise versa if the laser pulse is early. The timing is adjusted in 100 picosecond steps at a slew rate of 4 nanoseconds per second.

The DRIFT COMPENSATOR will not compensate for instantaneous voltage variations on the intermediate storage capacitors but will remove the effects of long term thermal drift. Input voltage variations leads to output timing variations which are not as simple to correct. Nonlinear magnetic compressors obey Faraday's law which simply states

$$\int V \cdot dt = N \cdot AREA \cdot \Delta B_s$$

If we assume the charging waveshape is sinusoidal until time τ with a possible period of constant voltage before core saturation at time T i.e.

$$V = \frac{V_0}{2}(1 - \cos\omega t) \qquad if \quad t < \tau$$

$$V = V_0 \qquad if \quad t > \tau$$

then

$$\int_0^T V \cdot dt = V_0 (T - \tau) + \frac{V_0 \cdot \tau}{2}$$

therefore

$$dT = \left[\frac{-T}{V_0} + \frac{\tau}{2 \cdot V_0}\right] dV$$

If the core compression time is adjusted to be exactly equal to the charging time then we have

$$\frac{dT}{T} = \frac{1}{2}\frac{dV}{V}$$

For a typical SCR commutated copper vapor laser driver design the overall compression period is $\sim$7 μsecs and therefore a 1% voltage variation would correspond to a 35 nsec shift in the output pulse timing. In a system where the jitter is required to have a standard deviation of

less than 350 psecs the voltage regulation would have to be maintained better than .01% if no other corrective measures were taken. It is possible to tolerate poorer voltage regulation if the input voltage can be monitored and the SCR trigger timing adjusted so as to compensate for the change in compression time do to voltage variations.

The best place to regulate the input charging voltage is at the intermediate energy storage capacitor. The voltage appearing here before the main SCRs are fired is what determines the output pulse timing. To attempt to control this voltage solely by regulating the DC supply voltage and ignoring the effects of the pulse charging circuit would be foolish. The regulation scheme currently in use is a simple but effective shunt regulation scheme.

The oversimplified circuit diagram presented in Fig. J.3 outlines the basic principle of this pulsed, shunt, post regulator. The intermediate storage capacitor is charged resonantly from the unregulated DC power supply output filter capacitor. After the charging cycle is completed the voltage appearing on the intermediate storage capacitor is compared against a reference level. The DC supply is adjusted so that the voltage will always initially exceed this reference level. Energy is inductively transferred back into the filter capacitor until the voltage corresponds to the reference level. If we assume the DC supply voltage can be regulated to within 1% of its nominal value then the intermediate storage capacitor voltage can be adequately regulated if the nominal initial charging level is 101% of the desired value. The post regulation circuit will then need to transfer at most 4% of the intermediate storage energy back into the filter capacitor. In the case of SNOMAD-V this corresponds to only 240 millijoules. At 1 kV input voltages if we can afford 50 μsecs for the post regulation process the peak currents would only be on the order of a few amperes. Commercially available MOSFETs or silicon Darlingtons are available with this power handling capability.

Finally after doing as good a job as practicable of controlling the input voltage we still have the option of readjusting the SCR trigger timing to account for any remaining voltage changes. As we noted above, to first order the output pulse timing varies linearly with changes in the input voltage. Referring to Fig. J.4, if the input charging voltage is compared against a reference

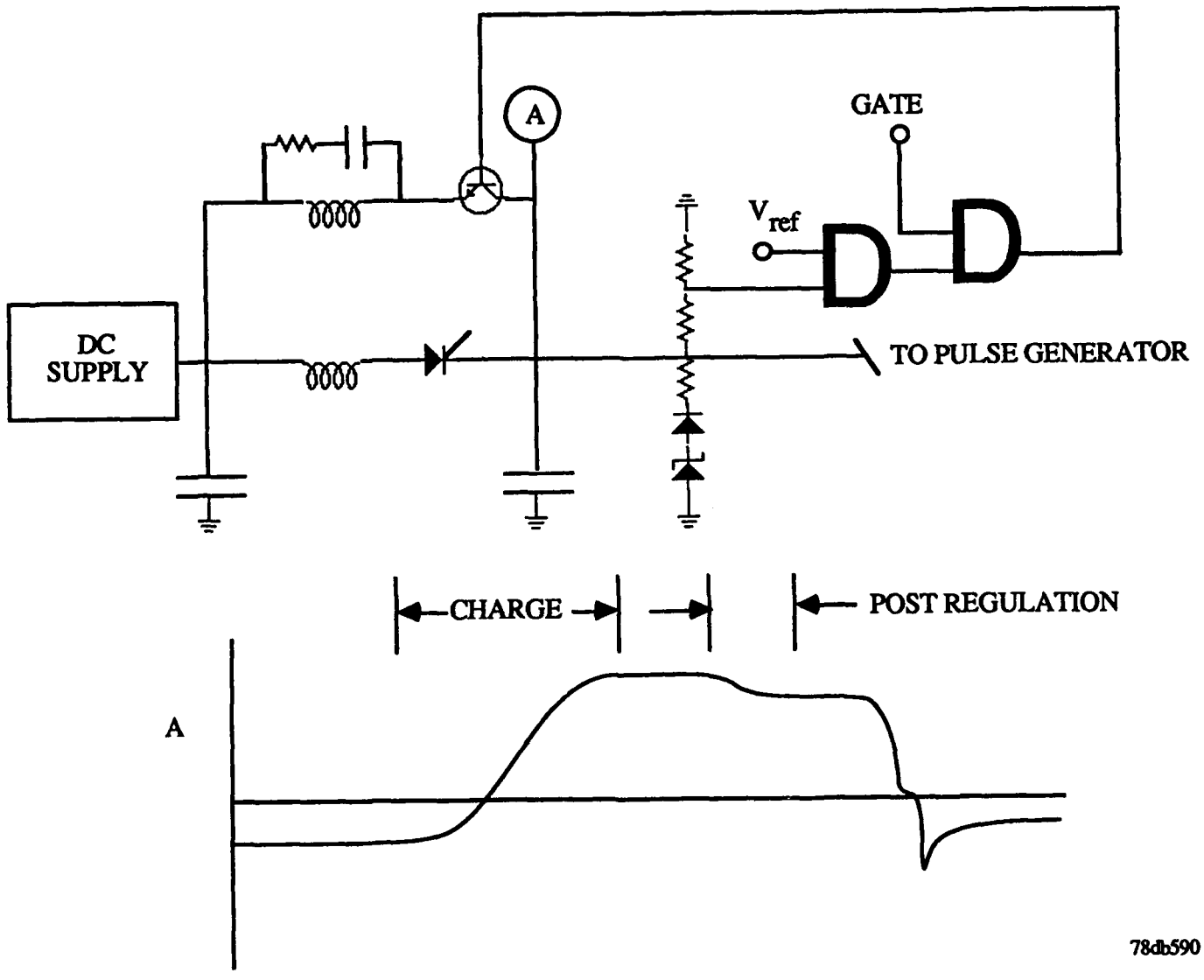

Figure J.3: Post Regulation Circuit

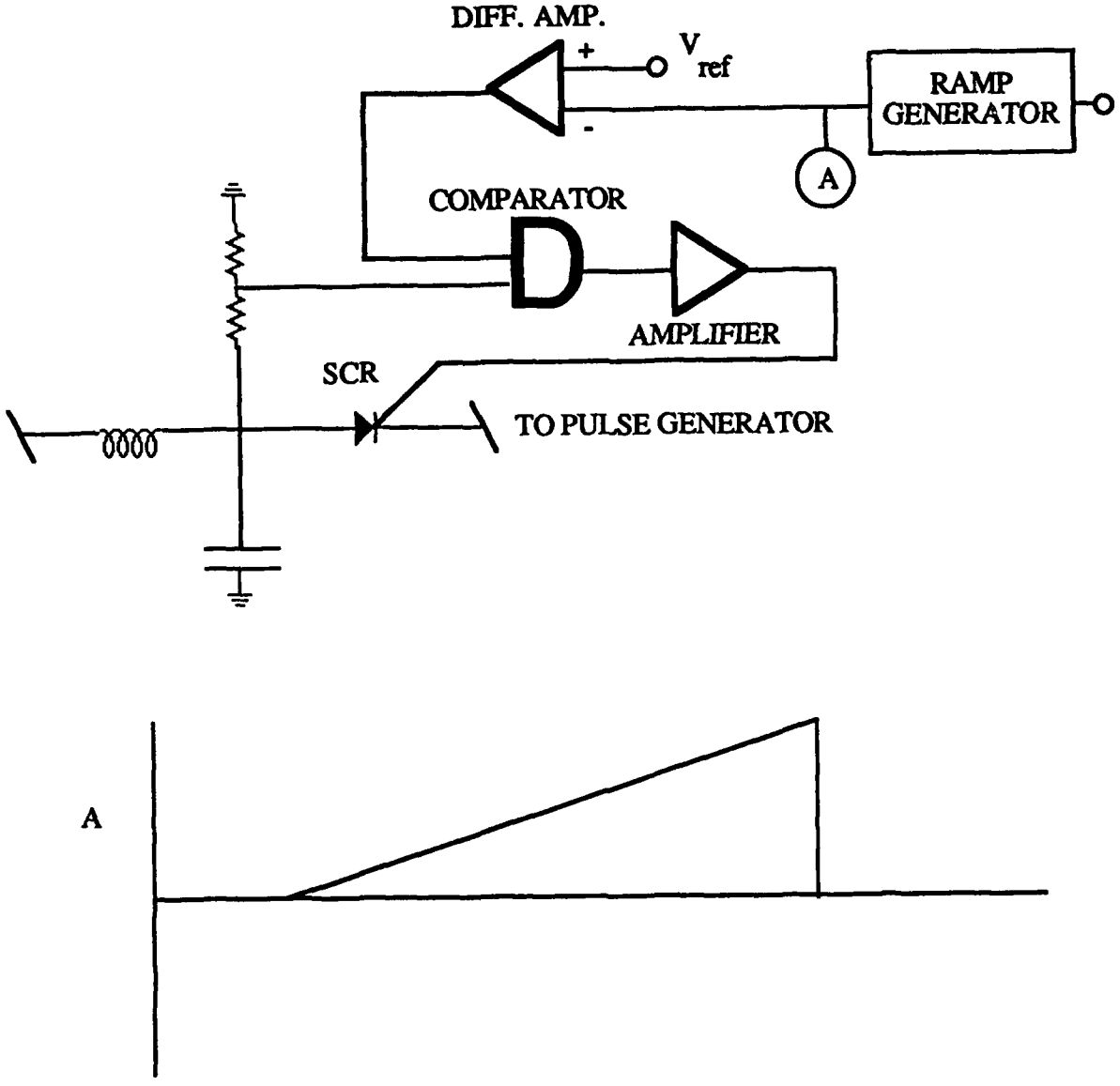

Figure J.4: Voltage variable delay circuit

voltage which has a linear time dependence, then if the slope of the reference voltage is correctly adjusted and the SCR is triggered when the two voltages are equal then the output pulse timing is automatically adjusted to compensate for voltage drifts.

In practice these circuits acting together have been adequate to maintain the jitter within the desired specifications. In fact, as there is some overlap in capability of the three timing control circuit, it has been found that it is not necessary to employ all three concurrently. Adequate jitter reduction has been achieved through the use of any one of the three circuits individually.

END